Advancing Point-of-Care Applications through

Ultraviolet Protective Mechanisms and Disease Diagnostics

by

Kenneth Benjamin Morabito

B.S. Drexel University, Philadelphia, PA, 2007

Sc.M. Brown University, Providence, RI, 2008

Submitted in partial fulfillment of the requirements

for the degree of Doctor of Philosophy in the

Division of Biology and Medicine at Brown University

School of Engineering

and

Center for Biomedical Engineering

Providence, Rhode Island

May 2013

This dissertation by Kenneth B. Morabito is accepted in its present form by the Division of Biology and Medicine as satisfying the dissertation requirement for the degree of Doctor of Philosophy.

Date_____ _____
Anubhav Tripathi, Ph.D., Advisor

Date_____ _____
Edith Mathiowitz, Ph.D., Reader

Date_____ _____
Jeffrey Morgan, Ph.D. Reader

Date_____ _____
Robert Hurt, Ph.D., Reader

Date_____ _____
Rami Kantor, M.D., External Reader

Approved by the Graduate Council

Date_____ _____
Peter Weber, Ph.D., Dean of the Graduate School

CURRICULUM VITAE

Name: Kenneth Benjamin Morabito

Date of Birth: March 17, 1984

Place of Birth: Philadelphia, PA, USA

I. EDUCATION

- Ph.D., Biomedical Engineering. Thesis title: Advancing Point-of-Care Applications through UV Protective Mechanisms and Disease Diagnostics. Brown University, Providence, RI, May 2013.
- Sc.M. Biomedical Engineering. Brown University, Providence, RI, May 2008.
- B.S. Biomedical Engineering. Drexel University, Philadelphia, PA, June 2007.

II. ABSTRACTS

- K Morabito, T Erkers, J Lee, A Tripathi. *Separation and Isolation of Biomolecules Using Motion of Magnetic Spheres in Microfluidic Channels*. Accepted to American Institute of Chemical Engineers (AiChE) Annual Meeting. Pittsburgh, PA. November 2012.
- K Steeley, K Morabito, A Tripathi, N Shapley. *The Effect of Particle Structure and Formulation On the Protection of Photosensitive Molecules*. Accepted to American Institute of Chemical Engineers (AiChE) Annual Meeting. Pittsburgh, PA. November 2012.
- J Wang, K Morabito and A Tripathi. *Isolation of RNA Using Microfluidic Motion of Magnetic Beads*. Accepted to American Institute of Chemical Engineers (AiChE) Annual Meeting. Pittsburgh, PA. November 2012.

- K Morabito, J Colgan, S Opal, A Artenstein, R Kantor, A Tripathi. *Simple Method for Amplifying RNA Targets.* Presented at Life Sciences Technology Showcase. Providence, RI. October 2011.
- K Morabito, K Gilida, N Shapley, A Tripathi. *Proximal Effects of Ultraviolet Light Absorbers and Polymer Matrix in the Photo-Protection of Beta-Carotene.* Presented at Biomedical Engineering Society (BMES) Annual Meeting. Austin, TX. October 2010.
- K Gilida, K Morabito, M Huang, A Tripathi, N Shapley. *Uniform Composite Nanoparticles for the Protection of Ultraviolet Sensitive Molecules.* Presented at American Institute of Chemical Engineers (AiChE) Annual Meeting. Salt Lake City, UT. October 2010.
- K Gilida, K Morabito, M Huang, A Tripathi, N Shapley. *Tunable Core-Shell Nanoarchitectures Containing Encapsulated Beta-Carotene.* American Institute of Chemical Engineers (AiChE) Annual Meeting. Nashville, TN. November 2009.

III. PUBLICATIONS

- K Morabito, L Schreier, R Kantor, A Tripathi. A simple method for quantifying mutant variant nucleic acids. Submitted to *Journal of Molecular Diagnostics*. (2012).
- K Morabito, C Wiske, A Tripathi. Inhibitory dimer formation during real time nucleic sequence based amplification. Submitted to *of Molecular Diagnosis and Therapy* (2012).
- J Wang, K Morabito, A Tripathi. Isolation of nucleic acids using motion of beads in a microfluidic channel. In preparation.
- J Wang, K Morabito, A Tripathi. Isolation of nucleic acids using motion of beads in a microfluidic channel. In preparation.
- K Morabito, T Erkers, J Lee, A Tripathi. Separation and isolation of biomolecules using motion of magnetic spheres in microfluidic channels. Submitted to *Biomicrofluidics*. (2012).

- KG Steeley, B Kuestermeyer, C Stanton, J Yu, K Morabito, D Li, C Mello, P Calvert, A Tripathi, and NC Shapley. Uniform Polymer Particles Formulated with Sunscreens for the Protection of Ultraviolet Sensitive Molecules. Submitted to *Microencapsulation.* (2012).
- D Li, P Calvert, C Mello, K Morabito, A Tripathi, N Shapley, K Gilida. Stabilization of Natural Dyes by High Levels of Antioxidants. *Advanced Materials Research* 441, 192-99 (2012).
- K Morabito, KG Steeley, N Shapley, C Mello, D Li, P Calvert, A Tripathi. Proximal effects of ultraviolet light absorbers and polymer matrix in the photostability of β-Carotene. *Dyes and Pigments* 92(1), 509-16 (2011).
- K Morabito, NC Shapley, KG Steeley, A Tripathi. Review of sunscreen and the emergence of non-conventional absorbers and their applications in ultraviolet protection. *International Journal of Cosmetic Science* 33(5), 385-90 (2011).

IV. INVITED SEMINARS AND LECTURES

- K Morabito. *Introduction to UV Biosensors.* Invited Lecture for Biosensors and Applied Microfluidics. Brown University, Providence, RI. April 2012.
- K Morabito. *Food and Drug Administration: Device Regulations*. Invited Lecture for Biomedical Engineering Design, Research and Modeling. Brown University, Providence, RI. November 2011.

V. AWARDS AND LEADERSHIP

- NASA Rhode Island Space Grant Fellowship. 2009 - 2010
- Graduate Biomedical Engineering Society (gBMES). Secretary October 2009 – August 2010.
- Corinna Borden Keen Research Fellowship. 2008 - 2009
- AJ Drexel Scholarship 2002 - 2007
- Order of Omega National Honor Society 2006 - 2007

- Drexel Inter-fraternity Council President 2006
- TKE Leadership Scholarship 2005 - 2006

VI. TRAINING

- Laboratory: HPLC, GC, refractometry, distillation, photolithography, soft lithography, PCR, nucleic acid sequence based amplification, DNA ligation amplification, SEM, fluorescence microscopy, DNA/RNA sizing and quantification, molecular beacon detection, ELISA, spectrophotometry.
- Software: Adobe Photoshop, AutoCAD, Solidworks, LabView, Comsol, Origin, Sigmaplot, MATLAB, Endnote, MS Office.

VII. PROFESSIONAL DEVELOPMENT

- Second International Wyss Symposium Microfluidics and Medicine. Boston, MA. 2011
- Harvard Global Health Institute 5th Annual Global Health Infectious Diseases Program Scientific Symposium. Boston, MA. 2011

ACKNOWLEDGEMENTS

I would like to thank Professor Anubhav Tripathi for his guidance and for his mentorship throughout my years at Brown. Professor Tripathi has taught me the importance of conducting good science, how to ask complex questions and follow through by designing experiments to answer them. I am very fortunate to have had Professor Tripathi as an advisor because he genuinely cares about my success, both career and personal life, and the success of all of my lab members. Despite his other commitments as a Professor, husband and father, he was always available to meet with me on a given day and he quite literally worked around the clock to ensure that he was fulfilling and exceeding his obligations as an advisor. Professor Tripathi is not just a great advisor, he is truly an exceptional one and I am very lucky and thankful to have had the privilege to work with him. I look forward to any collaboration we may have in the future.

Thank you also to my thesis committee members, Jeffrey Morgan, Edith Mathiowitz, Robert Hurt, and Rami Kantor for providing me with thought-provoking discussion, scientific insight, and encouragement, and for pushing me to improve through this process. I value your mentorship and am honored to have you as my thesis committee.

Thank you to Carol Folan, Jeff Brown, and all of the faculty and staff who made any and all logistical maneuvers seem like a walk in the park. You are the nuts and bolts of the program and I am thankful for your assistance and support through it all.

Thank you to my labmates, past and present, for your insights, discussions, and camaraderie. Thank you Carmichael Ong, Aartik Sarma and Stephanie McCalla for laying the groundwork for a large portion of my research involving SMART. Thank you Stephanie

Angione, Glareh Azadi and Pamela Storlazzi for your support and helping me troubleshoot problems and discover new ways of approaching my work. Thank you Jingjing Wang for your help with all of the projects that we have worked on together. You have been an outstanding addition to our lab and I am happy to pass the torch onto you as I leave.

Thank you to my family- Mom, Dad, Andy and Kaitlyn and soon-to-be extended family- Steve, Linda, Gina and Alex for supporting me in every way possible.

Finally, thank you Julie. You have been my number one supporter, always celebrating my small research achievements along the way, and you are always there to help me figure things out when I find myself lost in my work. “Doing a Ph.D.” was mentally challenging as expected, but it was unexpectedly emotionally challenging and often times left me feeling isolated from the “real” world, but you are always there to put things into perspective and offer a bird’s eye view when I needed it most. I am truly lucky to have had a partner to go through this academic journey with together. We have understood each other’s research in great detail, providing each other with constant feedback and brainstorming of new ideas. Some may say that I have been cursed (or blessed) with a short fuse and you are always there to help extinguish the flame during my most stressful times. Thank you for listening to me and reassuring me that everything will work out well in the end as long as I keep working hard and pushing forward. This would not have been possible without your reassurance and loving support.

CONTENTS

ABSTRACT **1**

OVERVIEW OF CHAPTERS **3**

PART ONE - UV PROTECTIVE MECHANISMS **5**

1 INTRODUCTION **6**

1.1. Relevance 6

1.2. Background and significance 7

1.3. Conventional sunscreen ingredients 7

1.4. Active organic ingredients 8

1.4.1. Advantages and disadvantages of organics 8

1.4.2. Organic UVA ingredients 9

1.5. Active inorganic ingredients 10

1.5.1. Nanoparticles 10

1.5.2. Titanium dioxide and zinc oxide 11

1.5.3. Advantages and disadvantages of inorganics 11

1.6. Emergence of solid lipid nanoparticles 12

1.7. Polymeric nanoencapsulation 13

1.8. Novel UV protection approaches 14

1.8.1. Cyclodextrin complexation 14

1.8.2. UV absorbers in textiles 14

1.8.3. Antioxidants 16

1.8.4. Carotenoids 17

1.8.5. Mycosporine-like amino acids 17

1.9. Summary 18

1.10. References 19

2 UNDERSTANDING THE PROXIMITY OF UV ABSORBERS AND PHOTOSTABILIZERS **26**

2.1. Abstract 26

2.2. Introduction 27

2.3. Materials 29

2.3.1. Sensor molecule 29

2.3.2. Photostabilizer molecule 30

2.3.3. Polymer matrix 30

2.4. Methods 31

2.4.1. Macroscopic configurations 31

2.4.2. Experimental device 32

2.4.3. FTIR analysis of β–carotene degradation 33

2.4.4. UV-Vis analysis of β–carotene degradation 34

2.4.4. UV-Vis analysis of 2-ethylhexyl 4-methoxycinnamate degradation 34

2.5. Results and discussion 34

2.5.1. β–carotene degradation 35

2.5.2. Effect of 2-ethylhexyl 4-methoxycinnamate on β–carotene degradation 40

2.5.3. Proximal effect 45

2.5.4. Addition of poly(methyl methacrylate) 48

2.6. Conclusion 50

2.7. Acknowledgement 51

2.8. References 52

3 STABILIZATION OF NATURAL DYES IN SOLUTION AND THIN FILMS USING HIGH CONCENTRATIONS OF ANTIOXIDANTS **56**

3.1. Abstract 56

3.2. Introduction 57

3.3. Experimental 58

3.3.1. Materials 58

3.3.2. Sample preparation 58

3.3.3. Thickness measurement 60

3.4. Results 60

3.4.1. Photostabilization of indigo and MB solution 60

3.4.2. Film thickness 64

3.4.3. Photostabilization of MB in films 66

3.4.4. Additional dye/stabilizer combinations 68

3.5. Discussion 68

3.6. Conclusion 69

3.7. Acknowledgments 69

3.8. References 70

4 UNIFORM POLYMER SUNSCREEN PARTICLES FOR THE PROTECTION OF ULTRAVIOLET SENSITIVE MOLECULES 71

4.1. Abstract 71

4.2. Introduction 72

4.3. Experimental 77

4.3.1. Production of uniform particles 77

4.3.2. Particle exposure to UV light and analysis using UV/Vis 80

4.3.3. UV/Vis spectra 81

4.3.4. Decay of β-carotene in solution 82

4.4. Results and discussion 82

4.4.1. β-carotene decay 82

4.4.2. Effect of UV protectants individually 84

4.4.3. Effect of protectant concentration 86

4.4.4. Effect of polymer matrix 88

4.4.5. Effect of multiple UV protectants 89

4.4.6. Decay Rate Constants 92

4.4.7. Determining spacing between beta-carotene and UV absorber 94

4.4.8. Effect of spacing 96

4.5. Conclusion 97

4.6. Acknowledgements 98

4.7. References 99

5 UNDERSTANDING UV PROTECTIVE MECHANISMS: KEY CONTRIBUTIONS 106

PART TWO – DISEASE DIAGNOSTICS 108

6 INTRODUCTION 109

6.1. Relevance 109

6.2. Background 109

6.2.1. Influenza background 109

6.2.2. HIV background 110

6.3. Current diagnostic assays 111

6.3.1. Current influenza diagnostics 111

6.3.2. Current HIV diagnostics 111

6.3.3. Disadvantages of current HIV diagnostic assays 112

6.4. Nucleic acid sequence based amplification (NASBA) 113

6.5. Microfluidic assays using NASBA 114

6.6. Simple method for amplifying RNA targets (SMART) 115

6.7. Details of SMART 117

6.7.1 RNA Isolation 118

6.7.2. Capture 119

6.7.3. Microfluidic separation 121

6.7.4. Nucleic acid sequence based amplification of SMART probes 122

6.7.5. Real time detection of K103N RNA RC 124

6.8. Development of SMART and applications in subsequent chapters 125

6.9. References 126

7 CAPTURE AND SEPARATION OF BIOMOLECULES USING MAGNETIC BEADS IN A SIMPLE MICROFLUIDIC CHANNEL WITHOUT AN EXTERNAL FLOW DEVICE 133

7.1. Abstract 133

7.2. Introduction 134

7.3. Experimental 136

7.3.1. Materials 136

7.3.2. Microchip device 137

7.3.3. Microscope apparatus 137

7.3.4. Percent bead transfer procedures 138

7.3.5. Three assays: non-specific adsorption, capture and separation 139

7.4. Results and discussion 141

7.4.1. Magnetic bead movement 141

7.4.2. Alkaline Phosphatase (AP) kinetics 143

7.4.3. Non-specific adsorption and/or carryover of DiFMUP 147

7.4.4. Capture of alkaline phosphatase (AP) 150

7.4.5. Separation of alkaline phosphatase (AP) 151

7.5. Conclusion 153

7.6. Acknowledgments 155

7.7. References 156

8 ENGINEERING INSIGHTS IN MULTIPLEXING REAL-TIME NUCLEIC ACID SEQUENCE BASED AMPLIFICATION (NASBA) 160

8.1. Abstract 160

8.2. Introduction 161

8.3. Design constraints 164

8.3.1. Inhibitory and non-inhibitory dimer formations 164

8.3.2. Dimer formation caused by T7 promoter sequence 165

8.3.3. Optimizations to reduce inhibitory structures 165

8.3.4. Molecular beacon design for NASBA 166

8.4. Materials and methods 167

8.5. Results 169

8.6. Discussion 172

8.6.1. Thermodynamic evaluation of oligonucleotides using hybridization and melting predictions 172

8.6.2. Redesigning the primer avoids inhibitory dimer formation 176

8.6.3. Real-time NASBA using molecular beacon detection 177

8.7. Conclusion 178

8.8. Acknowledgment 179

8.9. References 179

9 SMART ASSAY TO DETECT HIV-1 K103N MUTATIONS AND DEVELOP NOVEL VIRAL LOAD TECHNIQUE 182

9.1. Abstract 182

9.2. Introduction 183

9.2.1. Capture 183

9.2.2. Amplification 185

9.2.3. Real-time detection of K103N and WT RNA RC 186

9.3. Materials 188

9.3.1. Engineered oligonucleotide sequences 188

9.3.2. Microchip device 190

9.3.3. NASBA reaction mix 190

9.3.4. Heating devices 191

9.3.5. Optical equipment 191
9.4. Methods 192
9.4.1. Theoretical hybridizations 192
9.4.2. SMART experiments 192
9.4.3. Determining K103N concentration using SMART probes 194
9.5. Results and discussion 195
9.5.1. Hybridization theory predications 195
9.5.2. Validation of SMART using on-chip amplification 196
9.5.3. SMART using off-chip amplification with real time detection 200
9.5.4. Determining K103N concentration using SMART probes 202
9.6. Conclusion 208
9.7. Acknowledgments 211
9.8. References 212
10 SMART ASSAY TO DETECT ISOLATED H3 INFLUENZA SAMPLES 213
10.1. Abstract 213
10.2. Introduction 213
10.3. Materials 214
10.3.1. Engineered oligonucleotide sequences 214
10.3.2. Microchip device 215
10.3.3. NASBA reaction mix 216
10.3.4. Heating devices 216
10.3.5. Optical equipment 216
10.4. Methods 216
10.4.1. Theoretical hybridizations 216
10.4.2. Redesigning the biotinylated oligonucleotide and molecular beacon 217

10.4.3. SMART experiments 217

10.5. Results and discussion 218

10.5.1. Hybridization theory predications 218

10.5.2. Redesigned molecular beacon 219

10.5.3. SMART detection of H3 influenza 220

10.6. Conclusion 222

10.7. Acknowledgments 222

11 CONCLUSIONS AND FUTURE DIRECTIONS FOR SMART 223

FIGURES AND TABLES

Table 1.1. Commonly used organic sunscreen components. 8

Figure 1.1. UV radiation pathway. 10

Figure 1.2. Liposome vs. SLN. 12

Table 1.2. Australian/New Zealand UV Protection factor (UPF) standard. 15

Figure 2.1. UV absorber molecules. 31

Figure 2.2. Macroscopic configurations. 32

Figure 2.3. Fluorescence and UV apparatuses. 33

Figure 2.4. Fluorescence decay of β–carotene. 36

Figure 2.5. Fluorescence based upon concentration of β-carotene at time = 60 minutes. 38

Figure 2.6. FTIR spectrum of16.65uM β–carotene solution before and after 60 minute UVA exposure. 39

Figure 2.7. UV-Vis Spectra of 16.65uM β–carotene solution before and after UV exposure. 40

Figure 2.8. UV-Vis Spectra of 2-ethylhexyl 4-methoxycinnamate solution before and after UV exposure. 41

Figure 2.9. β–Carotene decay at 16.65uM fixed concentration mixed with varying 2-ethylhexyl 4-methoxycinnamate concentrations in the core/shell configuration. 42

Figure 2.10. β–Carotene decay at 16.65uM fixed concentration mixed with varying 2-ethylhexyl 4-methoxycinnamate concentrations in the homogenous configuration. 43

Figure 2.11. β–Carotene decay at 16.65uM fixed concentration mixed with 2-ethylhexyl 4-methoxycinnamate [217mM] for all three configurations. 45

Figure 2.12. Fluorescence of β–carotene 16.65uM after 60 minute exposure in the homogeneous configuration vs. concentration of 2-ethylhexyl 4-methoxycinnamate. 47

Figure 2.13. UV-Vis spectra of 16.65uM β–carotene when mixed with 434mM 2-ethylhexyl 4-methoxycinnamate in the homogeneous configuration, before and after 60 minute UVA exposure. 48

Figure 2.14. β–Carotene [16.65uM] decay when mixed with 2-ethylhexyl 4-methoxycinnamate [217mM] alone versus β–carotene decay when mixed with 2-ethylhexyl 4-methoxycinnamate and poly(methyl methacrylate) [1.67mM] in the core/shell configuration. 49

Figure 2.15. β–Carotene [16.65uM] decay when mixed with 2-ethylhexyl 4-methoxycinnamate [217mM] alone versus β–carotene decay when mixed with 2-ethylhexyl 4-methoxycinnamate and poly(methyl methacrylate) [1.67mM] in the homogeneous configuration. 50

Figure 3.1. β-carotene containing film samples prepared on quartz slides. 60

Figure 3.2. Photodegradation profiles of different dyes in solution with stabilizers in one or two separate cuvettes. 61

Table 3.1. Experimentally determined photodegradation rate constants of different dye/stabilizer combinations in solution. 62

Figure 3.3. Photodegradation kinetics of different dyes in solution with stabilizers in one or two separate cuvettes. 63

Figure 3.4. Schematic of AFM scan for thickness measurement. 65

Figure 3.5. Photodegradation kinetics of MB in single- and dual-layer films in absence or presence of TEA. 67

Figure 3.6. Change in β-carotene photodegradation rate constant as a function of stabilizer. 68

Figure 4.1. Particle size distributions. 78

Figure 4.2. Beta-carotene and PMMA particles. 79

Figure 4.3. Spectra. 81

Figure 4.4. Decay of beta-carotene shown through normalized absorbance with respect to time, both encapsulated (in PMMA) and not encapsulated. 83

Figure 4.5. The decay of the beta-carotene absorbance spectrum when beta-carotene is encapsulated in a polymer matrix made up of PMMA and exposed to UV light. 84

Figure 4.6. Beta-carotene decay when encapsulated in a PMMA polymer matrix with **(a)** oxybenzone, **(b)** OMC, **(c)** avobenzone, or **(d)** vitamin E. 86

Figure 4.7. The effect of protectant amount by comparing the absorbance at different times when beta-carotene and PMMA particles also contain **(a)** oxybenzone, **(b)** OMC, **(c)** avobenzone, or **(d)** vitamin E. 87

Figure 4.8. A comparison between the UV protection of PMMA, PLGA (50:50), and PLGA (75:25) polymer matrices when beta-carotene or beta-carotene and 0.03g oxybenzone are added. 89

Figure 4.9. Beta-carotene decay profiles when two protectants are used such as **(a)** OMC and oxybenzone, **(b)** avobenzone and oxybenzone, **(c)** oxybenzone and vitamin E, **(d)** OMC and vitamin E, **(e)** avobenzone and vitamin E, and **(f)** all combinations. 91

Figure 4.10. Ratio of the rate constants when an absorber is added and the rate constant of beta-carotene in polymer particles and the affect of the corresponding ratio of amount of absorber and amount of beta-carotene. 93

Table 4.1. Rate constants for particles of each composition. 94

Figure 4.11. The relationship between the rate constant and the spacing between beta-carotene and the absorbers. 97

Figure 6.1. Key design elements of SMART. 116

Figure 6.2. SMART probe design. 116

Figure 6.3. Overview of SMART from sample-to-result. 118

Figure 6.4. Z-chip for isolation of RNA from patient sample. 119

Figure 6.5. SMART capture step. 120

Figure 6.6. SMART microchip device. 121

Figure 6.7. SMART amplification step using cyclic only NASBA. 123

Figure 6.8. Molecular beacon hybridization and real-time detection. 124

Figure 7.1. (a) Schematic showing the main forces acting on a magnetic bead **(b)** Comsol simulated magnetic field created by the permanent magnet. 138

Figure 7.2. Substrate conversion assays. 140

Figure 7.3(a). 1μL of 1μg/μL (~65,000 beads) magnetic beads progressing through the microchannel at 0.7±0.04 mm/s. 142

Figure 7.3(b). Percentage of magnetic beads transferred between the wells as a function of increasing velocity of the magnet**.** 143

Table 7.1. Properties of streptavidin coated magnetic beads and binding capacity of AP = 71.4μM. 144

Figure 7.4. Off-chip DiFMUP added to AP in cuvette. 145

Figure 7.5(a). Non-specific adsorption assay. 147

Figure 7.5(b). Capture assay. 150

Figure 7.5(c). Separation assay. 153

Figure 8.1. Traditional NASBA. 163

Figure 8.2. T7 promoter sequence. 165

Figure 8.3. Molecular beacon designs. 166

Table 8.1. Poorly designed HIV-1 K103N oligonucleotide set (OLD), redesigned HIV-1 K103N oligonucleotide set (NEW), and H3 Influenza oligonucleotide set. 168

Figure 8.4. T7 promoter sequence dimer theoretical hybridization energies simulated with DINAMelt. 169

Figure 8.5. Primer dimer formations (OLD). 170

Table 8.2. Theoretical hybridization ΔG and T_m values for all potential primer dimers and/or non-specific hybridizations in HIV-1 K103N oligonucleotide set (OLD). 170

Table 8.3. Theoretical hybridization ΔG and T_m values for potential RNA product hybridizations with HIV-1 K103N oligonucleotide set (OLD). 170

Table 8.4. Theoretical hybridization ΔG and T_m values for all potential primer dimers and/or non-specific hybridizations using redesigned HIV-1 K103N oligonucleotide set (NEW). 171

Table 8.5. Theoretical hybridization ΔG and T_m values for all potential primer dimers and/or non-specific hybridizations in H3 Influenza oligonucleotide set. 171

Figure 8.6. Real-time NASBA of poorly designed HIV-1 K103N oligonucleotide set (Old) vs. redesigned HIV-1 K103N set (New) vs. H3 Influenza oligonucleotide set. 172

Figure 8.7. T7 polymerization of unexpected P1-P1 RNA. 175

Figure 9.1. SMART capture using K103N and WT sDNA. 184

Figure 9.2. Modified real-time nucleic sequence based amplification (NASBA). 186

Figure 9.3. Real time fluorescence detection using molecular beacons. 187

Table 9.1. Oligonucleotides used in SMART assay. 189

Figure 9.4. Microfluidic separation microchip design. 190

Table 9.2. Theoretical hybridization energies. 196

Figure 9.5. SMART gel plot after using on-chip amplification. 197

Figure 9.6. SMART electropherogram after using on-chip amplification. 198

Figure 9.7. SMART assay results using off-chip amplification with real-time detection. 200

Figure 9.8. Time to positivity (T_p) values are plotted versus the logarithmic scale of starting K103N sDNA concentration. 201

Figure 9.9. Histogram of normalized fluorescence of all sDNA and controls after 180 minutes reaction time. 202

Figure 9.10. Off-chip real time fluorescence of amplified K103N probe as a function of time. 203

Figure 9.11. Real time fluorescence of amplified WT probe as a function of time. 204

Figure 9.12. Off-chip modeling of fluorescence versus K103N SMART probe concentration at high concentrations (30,000 – 150,000 copies/μL K103N SMART probe). 205

Figure 9.13. Off-chip modeling of fluorescence versus K103N SMART probe concentration at low concentrations (less than 30,000 copies/μL K103N SMART probe). 206

Figure 9.14. On-chip K103N viral load quantification at high concentrations (6.25% to 25% K103N). 207

Figure 9.15. On-chip K103N viral load quantification at low concentrations. 207

Table 10.1. Successfully used influenza PCR primers. 214

Table 10.2. Engineering oligonucleotide sequences for SMART influenza detection. 215

Table 10.3. Redesigned oligonucleotide sequences for H3 SMART detection. 215

Table 10.4. Theoretical hybridization ΔG and T_m values for predicted H3 oligonucleotide set hybridization during capture phase of SMART. 218

Table 10.5. Theoretical hybridization ΔG and T_m values for predicted hybridizations of the original oligonucleotide set during NASBA. 219

Table 10.6. Theoretical hybridization ΔG and T_m values for predicted hybridizations during NASBA using the redesigned molecular beacon. 219

Figure 10.1. Comparison of hair-pin structure of molecular beacons. 220

Figure 10.2. Original biotinylated oligo and molecular beacon vs. redesigned biotinylated oligo and redesigned molecular beacon. 221

Figure 11.1. SMART disease diagnostic POC device. 224

ABSTRACT

We strive to achieve advancements in point-of-care (POC) diagnostics. Within this vast field, our work has taken two distinct paths. First, we worked towards understanding protective mechanisms for improving sunscreens through the study of ultraviolet light absorbers. Second, we developed a novel separation, amplification and detection technique for infectious diseases; specifically influenza sub-typing, HIV mutation detection and viral load quantification. These pathways are uniquely different but both seek solutions for engineering problems with global health implications.

Understanding UV protective mechanisms focuses on environmental health and improving disease diagnostics focuses on microbiological global health. Non-toxic sunscreens must be used around the world as a preventative POC treatment, generating new pathways for new UV protection products that will help everyone globally. First we investigate the spatial relationship of sunscreen components, absorber and photostabilizer, to better understand improving sunscreens and textiles through positioning of molecules rather than increasing the concentration of active UV absorber ingredients. Next we use our gained knowledge of absorber/photostabilizer proximity to assess the photostability of sunscreen nanoparticles and sensitive natural dyes doped with large concentrations of antioxidants. Overall, this work gives new insights to designing safer, photostable sunscreens and more photostable textiles.

Developing new diagnostic technology for infectious diseases is critical in both the developed and developing world. HIV is non-discriminatory; however drug resistance mutation monitoring is much more readily available in the developed world. The drug resistant K103N strain is concentrated in rural regions of Africa and subsequently it is often undiagnosed and mistreated. It is of global importance to help those infected with proper diagnosis so that HIV positive patients with drug resistant strains are medicated properly and the drug resistant population declines at its root before it has the opportunity to expand. Similarly, influenza is a

widespread pathogen in the developed world resulting in approximately 36,000 deaths annually in the Unites States. Rapid POC diagnostics for influenza helps to prevent influenza pandemics by giving health care workers information to contain the outbreak at the source of the infection locally.

We developed a novel method for RNA detection called Simple Method for Amplifying RNA Targets (SMART). We detail the advantages of SMART over conventional methods of detection, particularly its practicality in POC settings. We give a systematic approach to understanding all of the steps of SMART and the important design parameters to consider when using SMART. We also show the applications of SMART by 1) detecting and quantifying synthetic samples of HIV-1 K103N within a wild type HIV-1 population and 2) detecting clinical samples of influenza with various subtypes. Overall, we give a detailed approach to the design and engineering of our novel POC infectious disease diagnostic assay and show its use in mutation detection and sub-typing.

OVERVIEW OF THESIS CHAPTERS

The work presented in this thesis covers the understanding and development of UV protective mechanisms and disease diagnostics and as such is divided into two parts; part one (chapters 1through 5) covers UV protective mechanisms and part two (chapters 6 through 11) covers disease diagnostics.

Part one begins with chapter 1, which gives an introduction and details the background information and motivation relevant to UV protection. Chapter 2 reports on a study which investigated the proximal relationship of a photosensitive UV absorbing dye paired with a photostabilizer when exposed to a UV light source. Chapter 3 details a study which investigated the photo-protection of combinations of natural dyes when paired with antioxidants in solution and in thin films. Chapter 4 investigates the use of several UV absorber/photostabilizer combinations within polymeric nanospheres and the resulting photostability when exposed to a UV light source. Chapter 5 concludes part one of this thesis, summarizing the conclusions of our work to better understand UV protective mechanisms and how we can utilize what we have learned for future UV protective applications.

Part two begins with chapter 6, which gives an introduction to disease diagnostics, background on current detection methods for infectious disease and our motivation for a novel disease diagnostics assay. Chapter 7 reports on a study which investigated the use of our novel microfluidic device for the capture and separation of a model biomolecule, alkaline phosphatase. This study served as the proof of concept platform for our novel diagnostic assay. Chapter 8 introduces our novel diagnostics assay, Simple Method for Amplifying RNA Targets (SMART) and details critical design parameters particularly during the amplification process. Chapter 9 reports on a study which utilizes SMART for the detection and quantification of synthetic HIV-1 K103N RNA. Chapter 10 reports on our results using SMART for the detection and sub-typing of clinical influenza samples. Chapter 11 concludes part two of the thesis, summarizing the

conclusions of our work, the accomplishments of the assay development and the future applications for SMART.

UV PROTECTIVE MECHANISMS

I

CHAPTER 1

INTRODUCTION

1.1. Relevance

Protection against ultraviolet (UV) radiation is the major function of sunscreen lotions and UV protective coatings for vehicles, homes, equipment and clothing. Sunscreen formulations have been optimized over time to become protective over a broader spectrum of UV radiation and maintain greater photostability. They are comprised of organic and inorganic components which act as chemical and physical UV protectors, respectively. Some of the organic components limit sunscreen effectiveness due to suboptimal spectrum of protection and photostability. Studies using solid lipid nanoparticles (SLNs), recently explored organic molecules, inorganic molecules, and antioxidants as an attempt to further optimize UV protection. In this introduction, we examine traditional and emerging nanoparticle components and highlight novel ideas in UV protection which may provide pathways for future studies and safer, more natural forms of UV protection.

1.2. Background

Frequent exposure to solar ultraviolet (UV) radiation is well known to cause damage to exposed surfaces. Fading and aging of paints, fabrics, and plastic coatings as well as sun-related skin cancer are major industrial, environmental, and health concerns. Advancing the field of UV protection is achieved by protecting surfaces against the broadest possible spectrum of UV radiation, including the ultraviolet-A (UVA; 400-320nm) and ultraviolet-B (UVB; 320-290nm), wavelengths of sunlight, optimizing photostability of protective molecules, and trapping reactive species before photochemical damage occurs. Hence, improved UV protection can potentially make a major impact in a wide range of applications, including paints and coatings, cosmetics, textiles, pharmaceuticals, and environmental remediation. This introduction presents some of the recent innovations in UV protective technology involving nanoparticles, nanoencapsulation, and nanocomplexation, recent novel applications, and potential future directions incorporating antioxidants and natural products.

1.3. Conventional sunscreen ingredients

A familiar example of UV protective technology is sunscreen lotion. Most sunscreen products are composed of organic and inorganic components. The organic, such as oxybenzone, usually acts as a chemical sunscreen by absorbing UV radiation. The inorganic component, such as titanium dioxide, usually acts as a physical sunscreen by absorbing, reflecting and scattering UV radiation. Sunscreen is applied to the skin topically, covering the stratum corneum and shielding the multiple layers of the skin. While the direct cause of most skin cancers (melanoma and non-melanoma) is still under debate[1-3], the predominant function of the sunscreen components is to shield the skin

from UV radiation as effectively as possible. An optimal sunscreen contains multiple elements which reflect and scatter UV radiation, absorb UV wavelengths, contain stabilizing mechanisms such as encapsulation or complexation for sustained efficacy, and trap free radicals, for example with antioxidants, in order to limit photochemical damage.

1.4. Active organic ingredients

Organic Ingredient	Description
Avobenzone	Oil soluble and used to absorb the full spectrum of UVA rays. Since avobenzone is highly degradable in the presence of sunlight it is often paired with a photo stabilizer in sunscreen formulations[4,5].
Oxybenzone	Absorbs UVA radiation. Potentially harmful and a likely photocarcinogen. Derivative of benzophenone, a known photo-carcinogen[1].
Ensulizole	Protects against UVB and minimally against UVA. Water soluble and is used in formulations for a light, non-greasy feeling[6].
Octinoxate	Absorbs UVB radiation. Reduces the appearance of scars. Water insoluble, making it useful in waterproof formulations[7].
Octisalate	Formed by condensation of salicylic acid with 2-ethylhexanol. The salicylate portion of the molecule absorbs UV radiation, while the ethylhexanol adds water resistant properties[8].

Table 1.1. Commonly used organic sunscreen components.

1.4.1. Advantages and disadvantages of organics

Organic components used in sunscreen formulations are fairly abundant and diverse in comparison to inorganic components. This gives manufactures flexibility with characteristics of the formulation such as the sun protection factor (SPF), water

resistance, and product feel. Organic components could be considered less effective because they absorb UV radiation rather than reflecting or causing it to scatter. This makes them vulnerable to photo-degradation and prone to generating free radicals. However, the main concern with organic sunscreens is the potential for photo-irritant or photo-sensitizing reactions in susceptible individuals. The use of p-aminobenzoic acid (PABA), one of the earliest active ingredients used in sunscreens, has come under heavy scrutiny because of skin sensitivity issues and has been removed from a majority of sunscreen products.

1.4.2. Organic UVA ingredients

A problem associated with current on-the-shelf sunscreens is that, in many cases, the only indicator of product efficacy is the sun protection factor (SPF). This is an incomplete measure, because SPF is primarily dependent on UVB protection and does not adequately reflect the degree of UVA protection offered by the product [9]. However protection against both ranges of UV radiation is critical because both are implicated in skin cancer[1].

For some time avobenzone was the predominant UVA protector in most sunscreen formulations. However, several new organic sunscreen ingredients have been developed in recent years. Most of these new ingredients, such as ecamsule, bemotrizinol and bisoctrizole protect against UVA and act as a photostabilizer when paired with avobenzone, creating a synergistic effect for superior UVA protection. With the rise of new organic UVA sunscreen ingredients, the FDA has proposed that test methods and labeling of UVA protection to be used in addition to the current SPF rating system [9].

1.5. Active inorganic ingredients

1.5.1. Nanoparticles

Inorganic pigments with a high refractive index, such as titanium dioxide (TiO_2) and zinc oxide, also block UV light. Nanoparticle grades of these materials are often incorporated into sunscreen formulations because, by virtue of their small particle size, they are more effective than the bulk pigments in absorbing and scattering UV light. Figure 1.1. illustrates this effect.

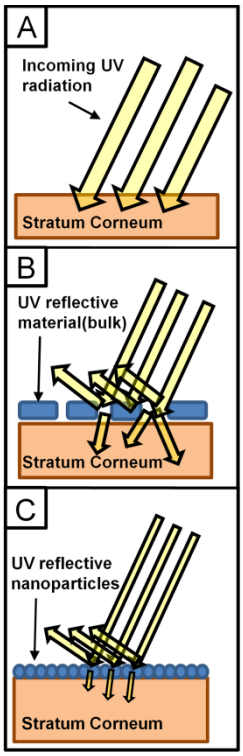

Figure 1.1. UV radiation pathway. **(A)** Incoming UV radiation penetrates the stratum corneum. **(B)** UV reflective material in bulk form (ex. ZnO) is applied to the surface of the stratum corneum. Some incoming UV radiation is blocked by reflection/scattering and some UV radiation is unblocked/deflected to the stratum corneum. **(C)** UV reflective nanoparticles (ex. ZnO) are applied to the surface of the stratum corneum. Most of the incoming UV radiation is reflected by the nanoparticles, leaving less UV radiation to penetrate to stratum corneum.

1.5.2. Titanium dioxide & zinc oxide

TiO_2 is a mineral which is prepared as ultra-fine nanoparticles. Sunscreen grades of TiO_2 have primary particle sizes ranging from about 10 to 60 nm [10]. These particles form aggregates which reflect UV radiation most efficiently with aggregates typically sized from 30 to 150 nm. In sunscreens TiO_2 is usually treated with coating materials such as silicon oils, SiO_2, or Al_2O_3 in order to make it more passive with the organic components and improve its dispersion and UV absorption in the overall formulation[10,11].

Zinc oxide (ZnO) is a mineral and prepared in particles that have a typical size ranging from 20 to 80 nm[12]. ZnO is usually coated with silicon oils, SiO_2, or Al_2O_3 in sunscreen formulations. It can be considered a better sunscreen ingredient than TiO_2 depending on the formulation requirements, because ZnO is more transparent and covers a broader UVA spectrum[13]. Alternatively, TiO_2 can be considered superior because it delivers a much greater SPF than ZnO.

1.5.3. Advantages and disadvantages of inorganics

Inorganics used in sunscreen are beneficial because they have been shown to absorb reflect and scatter UV radiation, which is generally considered more effective than absorption of UV radiation. Inorganics cover a broad spectrum, so their addition can simplify the sunscreen formulation by minimizing the necessary number of organic components. This can be beneficial for those with sensitivity or skin irritation issues. Inorganic UV sunscreens have relatively high consumer acceptance because of their transparency, which increases the usage of sunscreen[3]. A drawback of using inorganics is their dispersion issues, which often require an additional material for coating the inorganic material[11]. Coatings are also used to reduce the photoreactive nature of

inorganics protecting in part against the dominant drawback which is the potential risk caused by the generation of free radicals through oxidation when exposing inorganic molecules to UV radiation[1-3,14].

1.6. Emergence of solid lipid nanoparticles

In the mid 1980s Dior introduced the liposome in their product, *Capture*. This product opened the door for the research and production of micro and nanoparticles in the pharmaceutical and cosmetic industries[15]. Solid lipid nanoparticles (SLNs) were developed a few years after in the early 1990s and are advantageous in comparison to liposomes because of their protection against chemical degradation and controlled drug release properties[15]. Figure 1.2. depicts the structural differences between liposomes and SLNs.

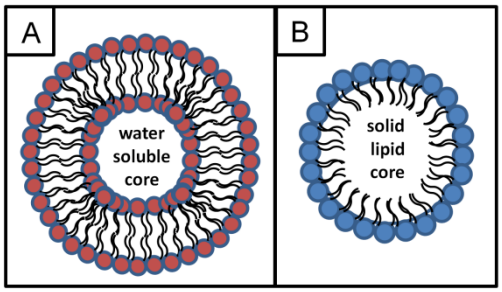

Figure 1.2. Liposome vs. SLN. **(A)** The liposome is a spherical lipid bi-layer (bi-layer of polar hydrophilic head groups attached to non-polar hydrophobic fatty acid tails) which encapsulates a water soluble core. **(B)** The SLN is a spherical lipid monolayer (polar hydrophilic head groups attached to non-polar hydrophobic fatty acid tails) which encapsulates a solid lipid core.

SLNs are established in the field of pharmaceuticals and drug delivery[15,16]. Many drugs have been incorporated into SLNs and are effective within the body because of their structural stability, drug release profile, high loading capacity and biocompatibility[16]. SLNs are used in cosmetic applications because of favorable

characteristics including skin hydration, lubrication, skin whitening effect, chemical stability, and UV protection[15,17,18].

SLNs have been emerging as a carrier system for sunscreens. SLNs are advantageous in comparison to conventional o/w emulsions because they have been shown to exhibit a zero-order release profile of organic components. Thus, SLNs release less of the sunscreen formulation over a given period of time resulting in a longer lasting sunscreen[19].

Although the use of SLNs solely as UV filters is neither recognized nor commercially available, they have been shown to have a synergistic effect when paired with UV filters with regards to overall UV protection and photostability. This results in a reduced need for high concentrations of potentially photo-carcinogenic sunscreen formulations without sacrificing the sun protection factor[20]. This advantage of the SLNs is based upon their ability to reflect and scatter incoming UV radiation. It has been shown that the scattering properties of SLNs depend on their degree of crystallinity. More crystalline SLNs have a greater ability to reflect and scatter radiation[21].

1.7. Polymeric nanoencapsulation

Similar to SLNs, poly($_{D,L}$-lactide) (PLA), is an established polymer in the drug delivery industry. Nanoencapsulation of octinoxate using PLA results in increased photostability[22]. Similarly, a study by the same research group showed that encapsulating octinoxate with poly-D,L-lactide-co-glycolide (PLGA) also has greater photostability than octinoxate alone[23]. Lee et al. showed avobenzone encapsulated by poly(methyl methacrylate) (PMMA) to have improved photostability, thermal stability and UV protection. PMMA/avobenzone nanoparticles can be applied to develop very stable

sunscreens[24]. All three of these nanoencapsulations are promising because of their polymer biocompatibility. Polymeric encapsulation holds great promise as an emerging sunscreen technology because of the great variety and versatility of polymers and detailed understanding of the polymer properties.

1.8. Novel UV protection approaches

1.8.1. Cyclodextrin complexation

Cyclodextrins are cyclic oligiosaccharides composed of 5 or more α-D-glucopyranoside units. They exist in three natural forms, α, β and γ. They can entrap appropriately sized molecules into the hydrophobic lumen of their ringed structure[25]. Cyclodextrins are complexed with compounds to increase aqueous solubility and dissolution rate of poorly soluble drugs. They are also used to protect against oxidation and improve photostability[25,26]. Cyclodextrins complexed with ibuprofen have been shown to be effective in reducing the damage caused by UV radiation after sun exposure. Godwin et al. show that topically applying ibuprofen immediately following UV exposure is crucial in reducing epidermal lipid damage. Complexing ibuprofen with hydroxypropyl-β-cyclodextrin provided enhanced protection[27].

1.8.2. UV absorbers in textiles

A new idea in UV protection is to incorporate UV protective nanoparticles into fabric used for clothing in order to reduce the fading of colors. ZnO nanoparticles have been incorporated into the surface of cotton and wool fabrics. The addition of ZnO increases the mechanical strength of both fabrics and results in an UV absorbing fabric[28,29]. Another study by Sun et al. incorporated ZnO nanoparticles into polyester

fabric. This study had mixed results; while a polymer/ZnO coating not in direct contact with the fabric decreased the fading rate of the dyed fabric, the polymer/ZnO coating increased the fading rate of one dye used when in direct contact with the fabric. Sun et al. attributes this increased fading rate to the generation of free radicals when ZnO is exposed to UV radiation[30].

Another approach to protecting fabric is to incorporate multiwall carbon nanotubes (MWNT). Mondal et al. developed a polyurethane coating containing UV protective MWNT. Several weight percentages of the coating were applied to cotton fabric and the transmission of UV radiation through the fabric was measured. An UV protection factor (UPF) of the fabric was calculated based upon the transmission of UV radiation. UPF ratings are listed according to the Australian/New Zealand standard.

UPF Rating	**UV Radiation Transmission (%)**	**UPF Description**
15 - 24	6.7 - 4.2	Good
25 - 39	4.1 - 2.6	Very Good
40 - 50, 50+	Less than 2.6	Excellent

Table 1.2. Australian/New Zealand UV Protection factor (UPF) standard.

This coating applied to cotton fabric achieved a UV protection factor of 174 for only 1 wt % of MWNT used in the cotton fabric [31]. Because of the UV protective benefits and nil effect on clothing comfort, the addition of trace amounts of UV protective material into textiles is a likely trend to continue to be studied.

1.8.3. Antioxidants

Antioxidants and other natural products such as carotenoids are currently being explored as UV protective additives to limit photochemical damage. The new molecules, applied in conjunction with nanoencapsulation and nanocomplexation have the potential for powerful new sunscreen ingredients.

Antioxidants are found naturally in plant species. Excessive exposure to UV radiation triggers production of non-photosynthetic pigments, cinnamic acid derivatives and flavanoids which are responsible for blocking UV radiation in addition to their antioxidant activity[32]. Incorporation of antioxidants into sunscreen formulations is a logical approach to combat potentially hazardous photogenerated free radicals. Antioxidants contain many free electrons which are donated to unpaired electrons present in free radicals. Antioxidants are used in the cosmetic industry to prevent the formation of new wrinkles and reduce skin aging caused by UV radiation. These antioxidants, such as vitamin C, vitamin E and pycnogenol, have been shown to have a synergistic effect when combined for UV protection[33]. Photostabilizers have also been shown to exhibit antioxidant properties. Chaudhuri et al. showed that diethylhexyl syringylidene malonate (DESM) can be used as a photostabilizer for avobenzone as well as an effective antioxidant[5]. Synthetic antioxidants are also a possibility, as Otani et al. developed a new UV-B radiation absorbent molecule with efficient antioxidant activity by modification of the glycoside. This new molecule is expected to be commercially available for sunscreen formulations[34].

1.8.4. Carotenoids

Carotenoids are produced in plants and other photosynthetic organisms. The yellow, orange and red color of many fruits is due to the carotenoid content. Green plants also contain carotenoids, but their color is masked by their chlorophyll content. Humans cannot self-produce carotenoids and depend on a dietary supplement[35-38]. Carotenoids are important because they play a role in protecting plants from UV damage. They are effective natural antioxidants because of their singlet oxygen quenching ability and scavenging of peroxyl radicals[39-41]. When incorporated into daily dietary intake, carotenoids have been shown to have a variety of positive health effects. A decreased risk for prostate cancer has been associated with the consumption of lycopene found in tomatoes[42]. Carotenoids have potential in skin protection applications. Heinrich et al. showed that a dietary mixture of the β-carotene, lutein and lycopene protects against UV induced erythema[43]. In homogenous solution, carotenoids are efficient blue light (near UVA) filters[44]. When complexed with β-glycyrrhizic acid, a cyclodextrin, their antioxidant activity increases (increased scavenging rate of peroxyl radicals by carotenoids)[45]. Because of their antioxidant function and blue light filtering, carotenoids are plausible components to use in a sunscreen formulation.

1.8.5. Mycosporine-like amino acids

Marine algae are able to synthesize mycosporine-like amino acids (MMAs) which effectively absorb UV radiation between 310-360 nm[46,47]. MMAs have been shown to be photostable and require light, oxygen and a strong photosensitizing agent such as riboflavin and/or sea water for photo-degradation to occur[48-50]. Additionally, MMAs will photo-degrade slower under high irradiance conditions without the presence of a

photosensitizer[48]. MMAs are a promising natural sunscreen additive because of their high UV radiation absorbance and strong photostability.

1.9. Summary

We have introduced the traditional components, the use of nanoparticles and the emerging technologies of UV protection. This section also summarized recent studies which presented novel ideas in UV protection applications, as well as the incorporation of antioxidants and natural products in UV protection. New techniques offer improved UV protection, safety and enhanced photostability. Particularly promising is the polymeric encapsulation of UV absorbers, and the divergence from chemical absorbers towards the use of antioxidants and other natural product additives. In the following chapters we detail our research in which we explored these very areas of interest, specifically investigating (1) the role of proximity of UV absorber and photostabilizer (2) the use of large concentrations of antioxidants paired with sensitive UV absorbing dyes and (3) polymeric nanoencapsulation of UV absorber/photostabilizer combinations and the resulting effect on photostability.

1.10. References

1 Westerdahl, J., Ingvar, C., Masback, A. & Olsson, H. Sunscreen use and malignant melanoma. *Int J Cancer* **87**, 145-150, doi:10.1002/1097-0215(20000701)87:1<145::AID-IJC22>3.0.CO;2-3 [pii] (2000).

2 Dunford, R. *et al.* Chemical oxidation and DNA damage catalysed by inorganic sunscreen ingredients. *FEBS Lett* **418**, 87-90, doi:S0014-5793(97)01356-2 [pii] (1997).

3 Nohynek, G. J. Nanotechnology, cosmetics and the skin: is there a health risk? *Skin Pharmacol Physiol* **21**, 136-149 (2008).

4 Chatelain, E. & Gabard, B. Photostabilization of butyl methoxydibenzoylmethane (Avobenzone) and ethylhexyl methoxycinnamate by bis-ethylhexyloxyphenol methoxyphenyl triazine (Tinosorb S), a new UV broadband filter. *Photochem Photobiol* **74**, 401-406 (2001).

5 Chaudhuri, R. K., Lascu, Z., Puccetti, G., Deshpande, A. A. & Paknikar, S. K. Design of a photostabilizer having built-in antioxidant functionality and its utility in obtaining broad-spectrum sunscreen formulations. *Photochem Photobiol* **82**, 823-828, doi:2005-07-15-RA-612 [pii]10.1562/2005-07-15-RA-612 (2006).

6 Stanley B Levy, M. *Sunscreens and Photoprotection*, <http://www.emedicine.com/derm/topic510.htm> (2006).

7 Todorov, D. G. *Chemical UVB sunscreen/sunblock: octyl methoxycinnamate (octinoxate)*,<http://www.smartskincare.com/skinprotection/sunblocks/sunblock_octinoxate.html> (1999).

8 M. Singh, M. H. B. Octyl salicylate: a new contact sensitivity. *Contact Dermatitis* **56**, 48-48 (2007).

9 R. Bissonnette, M., FRCPC. Update on Sunscreens *Skin Therapy Letter* **13**, 5-7 (2008).

10 Popov, A. P., Lademann, J., Priezzhev, A. V. & Myllyla, R. Effect of size of TiO2 nanoparticles embedded into stratum corneum on ultraviolet-A and ultraviolet-B sun-blocking properties of the skin. *J Biomed Opt* **10**, 064037, doi:10.1117/1.2138017 (2005).

11 A. Jaroenworaluck, W. S. N. K. R. S. Characteristics of silica-coated TiO2 and its UV absorption for sunscreen cosmetic applications. *Surface and Interface Analysis* **38**, 473-477 (2006).

12 Cross, S. E. *et al.* Human skin penetration of sunscreen nanoparticles: in-vitro assessment of a novel micronized zinc oxide formulation. *Skin Pharmacol Physiol* **20**, 148-154, doi:000098701 [pii]10.1159/000098701 (2007).

13 Sheldon R. Pinnell, D. F. R. G. M. A. M. N. K. Microfine Zinc Oxide is a Superior Sunscreen Ingredient to Microfine Titanium Dioxide. *Dermatologic Surgery* **26**, 309-314 (2000).

14 Hanson, K. M., Gratton, E. & Bardeen, C. J. Sunscreen enhancement of UV-induced reactive oxygen species in the skin. *Free Radic Biol Med* **41**, 1205-1212, doi:S0891-5849(06)00413-8 [pii]10.1016/j.freeradbiomed.2006.06.011 (2006).

15 Muller, R. H., Radtke, M. & Wissing, S. A. Solid lipid nanoparticles (SLN) and nanostructured lipid carriers (NLC) in cosmetic and dermatological preparations.

Adv Drug Deliv Rev **54 Suppl 1**, S131-155, doi:S0169409X02001187 [pii] (2002).

16 Muller, R. H., Mader, K. & Gohla, S. Solid lipid nanoparticles (SLN) for controlled drug delivery - a review of the state of the art. *Eur J Pharm Biopharm* **50**, 161-177, doi:S0939-6411(00)00087-4 [pii] (2000).

17 Souto, E. B. & Muller, R. H. Cosmetic features and applications of lipid nanoparticles (SLN, NLC). *Int J Cosmet Sci* **30**, 157-165, doi:ICS433 [pii]10.1111/j.1468-2494.2008.00433.x (2008).

18 Wissing, S. A. & Muller, R. H. Cosmetic applications for solid lipid nanoparticles (SLN). *Int J Pharm* **254**, 65-68, doi:S0378517302006841 [pii] (2003).

19 Wissing, S. A. & Muller, R. H. Solid lipid nanoparticles as carrier for sunscreens: in vitro release and in vivo skin penetration. *J Control Release* **81**, 225-233, doi:S0168365902000561 [pii] (2002).

20 M. E. Carlotti, S. S., D. Vione, E. Pelizzetti, E. Ugazio, S. Morel. Study on the Photostability of Octyl-p-Methoxy Cinnamate in SLN. *Journal of Dispersion Science and Technology*, 809–816 (2005).

21 Wissing, S. & Muller, R. The development of an improved carrier system for sunscreen formulations based on crystalline lipid nanoparticles. *Int J Pharm* **242**, 373-375, doi:S0378517302002193 [pii] (2002).

22 Vettor, M. *et al.* Poly(D,L-lactide) nanoencapsulation to reduce photoinactivation of a sunscreen agent. *Int J Cosmet Sci* **30**, 219-227, doi:ICS443 [pii]10.1111/j.1468-2494.2008.00443.x (2008).

23 Perugini, P. *et al.* Effect of nanoparticle encapsulation on the photostability of the sunscreen agent, 2-ethylhexyl-p-methoxycinnamate. *Int J Pharm* **246**, 37-45, doi:S0378517302003563 [pii] (2002).

24 Lee, J.-S., Kim, J.-W., Kim, J., Han, S.-H. & Chang, I.-S. Photochemical properties of UV-absorbing chemicals in phase-controlled polymer microspheres. *Colloid & Polymer Science* **283**, 194-199 (2004).

25 Loftsson, T. & Brewster, M. E. Pharmaceutical applications of cyclodextrins. 1. Drug solubilization and stabilization. *J Pharm Sci* **85**, 1017-1025, doi:10.1021/js950534b10.1021/js950534b [pii] (1996).

26 Scalia, S., Casolari, A., Iaconinoto, A. & Simeoni, S. Comparative studies of the influence of cyclodextrins on the stability of the sunscreen agent, 2-ethylhexyl-p-methoxycinnamate. *J Pharm Biomed Anal* **30**, 1181-1189, doi:S0731708502004338 [pii] (2002).

27 Godwin, D. A., Wiley, C. J. & Felton, L. A. Using cyclodextrin complexation to enhance secondary photoprotection of topically applied ibuprofen. *Eur J Pharm Biopharm* **62**, 85-93, doi:S0939-6411(05)00182-7 [pii]10.1016/j.ejpb.2005.06.002 (2006).

28 Yadav A, P. V., Kathe AA, Raj S, Yadav D, Sundaramoorthy C, Vigneshwaran N. Functional finishing in cotton fabrics using zinc oxide nanoparticles. *Bull Mater Science* **29**, 641-645 (2006).

29 A. Becheri, M. D., P. Lo Nostro, P. Baglioni. Synthesis and characterization of zinc oxide nanoparticles: application to textiles as UV-absorbers. *Journal of Nanoparticle Research* **10**, 679-689, doi:10.1007/s11051-007-9318-3 (2008).

30 Sun, L. Effects of undoped and manganese-doped zinc oxide nanoparticles on the colourfading of dyed polyester fabrics. *Chemical Engineering Journal*, 391-398 (2009).

31 Mondal, S. & Hu, J. L. A novel approach to excellent UV protecting cotton fabric with functionalized MWNT containing water vapor permeable PU coating. *Journal of Applied Polymer Science* **103**, 3370-3376, doi:Doi 10.1002/App.25437 (2007).

32 Edreva, A. The importance of non-photosynthetic pigments and cinnamic acid derivatives in photoprotection. *Agriculture, Ecosystems & Environment* **106**, 135-146 (2005).

33 Cho, H. S. *et al.* Anti-wrinkling effects of the mixture of vitamin C, vitamin E, pycnogenol and evening primrose oil, and molecular mechanisms on hairless mouse skin caused by chronic ultraviolet B irradiation. *Photodermatol Photoimmunol Photomed* **23**, 155-162, doi:PPP298 [pii]10.1111/j.1600-0781.2007.00298.x (2007).

34 Otani, T. *et al.* Synthesis of new UV-B light absorbents: (Acetylphenyl)glycosides with antioxidant activities. *Bioorg Med Chem Lett* **18**, 3582-3584, doi:S0960-894X(08)00489-7 [pii]10.1016/j.bmcl.2008.05.006 (2008).

35 Britton, G. Structure and properties of carotenoids in relation to function. *FASEB J* **9**, 1551-1558 (1995).

36 Demmig-Adams, B. & Adams, W. W., 3rd. Antioxidants in photosynthesis and human nutrition. *Science* **298**, 2149-2153, doi:10.1126/science.1078002298/5601/2149 [pii] (2002).

37 Olson, J. A. & Krinsky, N. I. Introduction: the colorful, fascinating world of the carotenoids: important physiologic modulators. *FASEB J* **9**, 1547-1550 (1995).

38 Stahl, W. & Sies, H. Bioactivity and protective effects of natural carotenoids. *Biochim Biophys Acta* **1740**, 101-107, doi:S0925-4439(04)00280-7 [pii]10.1016/j.bbadis.2004.12.006 (2005).

39 Stahl, W. & Sies, H. Antioxidant activity of carotenoids. *Mol Aspects Med* **24**, 345-351, doi:S009829970300030X [pii] (2003).

40 Conn, P. F., Schalch, W. & Truscott, T. G. The singlet oxygen and carotenoid interaction. *J Photochem Photobiol B* **11**, 41-47, doi:1011-1344(91)80266-K [pii] (1991).

41 Burton, G. W. & Ingold, K. U. beta-Carotene: an unusual type of lipid antioxidant. *Science* **224**, 569-573 (1984).

42 Giovannucci, E. A review of epidemiologic studies of tomatoes, lycopene, and prostate cancer. *Exp Biol Med (Maywood)* **227**, 852-859 (2002).

43 Heinrich, U. *et al.* Supplementation with beta-carotene or a similar amount of mixed carotenoids protects humans from UV-induced erythema. *J Nutr* **133**, 98-101 (2003).

44 Junghans, A., Sies, H. & Stahl, W. Macular pigments lutein and zeaxanthin as blue light filters studied in liposomes. *Arch Biochem Biophys* **391**, 160-164, doi:10.1006/abbi.2001.2411S0003-9861(01)92411-7 [pii] (2001).

45 Polyakov, N. E., Leshina, T. V., Salakhutdinov, N. F., Konovalova, T. A. & Kispert, L. D. Antioxidant and redox properties of supramolecular complexes of

carotenoids with beta-glycyrrhizic acid. *Free Radic Biol Med* **40**, 1804-1809, doi:S0891-5849(06)00058-X [pii]10.1016/j.freeradbiomed.2006.01.015 (2006).

46 Bandaranayake, W. M. Mycosporines: are they nature's sunscreens? *Nat Prod Rep* **15**, 159-172 (1998).

47 Karsten, U., Wiencke, C. Factors controlling the formation of UV-absorbing mycosporing-like amino acids in the marine red alga Palmaria palmata from Spitsbergen (Norway). *J. Plant Physiol.*, 407-415 (1999).

48 Whitehead, K. & Hedges, J. I. Photodegradation and photosensitization of mycosporine-like amino acids. *J Photochem Photobiol B* **80**, 115-121, doi:S1011-1344(05)00067-9 [pii]10.1016/j.jphotobiol.2005.03.008 (2005).

49 Conde, F. R., Carignan, M. O., Churio, M. S. & Carreto, J. I. In vitro cis-trans photoisomerization of palythene and usujirene. Implications on the in vivo transformation of mycosporine-like amino acids. *Photochem Photobiol* **77**, 146-150 (2003).

50 Conde, F. R., Churio, M. S. & Previtali, C. M. The deactivation pathways of the excited-states of the mycosporine-like amino acids shinorine and porphyra-334 in aqueous solution. *Photochem Photobiol Sci* **3**, 960-967, doi:10.1039/b405782a (2004).

CHAPTER 2

UNDERSTANDING THE PROXIMITY OF UV ABSORBERS AND PHOTOSTABILIZERS

2.1. Abstract

β-Carotene was used as a probe to investigate the protection offered by 2-ethylhexyl 4-methoxycinnamate, a photostabilizer, upon ultraviolet-A photodegradation. β-Carotene and 2-ethylhexyl 4-methoxycinnamate were arranged in two distinct macroscopic configurations (core/shell and homogenous) in solution with tandem and single cuvettes. 2-Ethylhexyl 4-methoxycinnamate was also combined with poly(methyl methacrylate) in solution to investigate the protective synergy between the photostabilizer and the polymer matrix. The choice of configuration played a more dominant role than the concentration of 2-ethylhexyl 4-methoxycinnamate in the degradation of β-carotene, with β-carotene remaining more stable in the homogeneous configuration. Changing configurations yielded different proximities of 2-ethylhexyl 4-methoxycinnamate to β-carotene; closing the proximity increased the potential close interactions (<1nm) where transfer of excited state energy from β-carotene to 2-ethylhexyl 4-methoxycinnamate could occur resulting in increased photostability. The addition of poly(methyl methacrylate) had a negligible impact on the decay of β-carotene in both configurations.

2.2. Introduction

Approximately 40% of the solar energy which reaches Earth is allowed to pass through the atmosphere to reach the surface. The atmosphere allows visible light to pass through while blocking hazardous light, by use of stratospheric oxygen and ozone molecules which absorb 97-99% of the sun's high frequency ultra-violet radiation (wavelengths of 150 - 300 nm). The ultra-violet light that successfully reaches the earth's surface is predominantly ultraviolet-A (UVA) radiation (wavelengths of 320 – 400 nm), with a smaller component of ultraviolet-B (UVB) radiation (wavelengths of 280-320 nm). UVA radiation is of particular interest because of its prevalence in sunlight and being of relatively high energy it is important to investigate the harmful effects of UVA radiation [1]. Among fillers and other inactive ingredients, traditional sunscreens are comprised of primary UV absorbers and additional UV absorbers dedicated to protect the primary UV absorber, which serve as photostabilizers [2,3].

Many structural and spectroscopic studies [4,5] have been performed in order to understand the specific interactions such as hydrogen bonding, solvent-solute complexation, changes in the electronic charge distribution following photoexcitation, and excited-state reactions. Several studies have been performed to understand the influence of polymer matrices on photophysical properties of intermolecular hydrogen bridged UV absorbers [6,7]. In these UV absorbers an excited state intramolecular proton transfer in the excited singlet state opens a pathway for the transformation of harmful ultraviolet radiation into thermal energy[8]. The migration of UV absorber molecules out of the polymer matrix is influenced by the free volume of the polymer as well as by the size and shape of the diffusing molecules[9]. The systematic investigation on the photophysical

properties of molecules in the condensed phase and their molecular structure provides insight into the impact of interactions between the solvent and solute[10]. For example, the proximity of the carbonyl and hydroxyl groups in UV absorbers can allow for the formation of intra- and intermolecular hydrogen bonds. The interaction of UV light and UV absorber begins when a photon of UV light interacts with a ground state molecule of the UV absorber by encountering a pair of electrons. The photon energy is transferred to one of the electrons promoting it to the singlet excited state. This singlet state electron intersystem crosses to a less energetic triplet excited state. In the triplet excited state, the absorbed energy is dissipated as heat before the electron returns to its ground state pairing. Once in the ground state, the molecule is free to repeat the absorption process which is of the order of a few milliseconds. As the cycle of absorption and dissipation progresses, molecules may be damaged by photochemical reactions and no longer able to repeat the cycle. This typically occurs in the triplet excited state, where a competition exists between the excited state electrons fighting to return to ground state and reactive oxygen species searching for donor electrons. With prolonged exposure to UV light, more UV absorber molecules become damaged and the overall effectiveness, or photostability, of the absorber decreases. Photostabilizers are added to maintain the photostability of the UV absorber. They are able to quench and dissipate the excited state energy of the UV absorber before any damaging photochemical reactions occur. [11,12]

Recently, polymer nanocomposites have been formulated to achieve increased photostability and UV protection [13-21]. These studies showed the significance of UV absorbing activity in zinc oxide (ZnO) treated matrices and ZnO-polyethylene terephthalate (PET) nanocomposites. In addition, photo-oxidation studies on polyethylene

containing nanoparticle and pigmentary grade titanium dioxide pigments showed that in general the former are more photoactive. It was argued that the proximity of nanoparticle pigments induce oxidation of the polymer during processing and the formation of hydroperoxide and carbonyl groups. Similarly, composites of titanium oxides and silicon dioxide hybrid capsules showed good UV protective properties. Although these studies showed the role of the proximity of metal oxides on UV protection, there are almost no systematic studies performed which delineate the proximity of absorbers and matrices.

Most previous studies used small concentrations of UV absorber paired with a weak UV absorbing polymer. In this paper high concentrations of absorber were paired with a strongly absorbing dye. A new experimental method was introduced to understand the proximal effects of high levels of UV absorbers and polymer matrices. The relationship between molecule proximity and photostability was examined. Additionally, a polymer matrix was added to consider the photoprotective synergy between absorber and polymer. Overall, the role of the proximity of absorbers and polymer matrix in the protection against UVA radiation was investigated.

2.3. Materials

2.3.1. Sensor molecule

β-Carotene (M_w =536.8g/mol), was selected as an UVA sensitive probe molecule to investigate the proximal effect on photostability when paired with other absorbers and a polymer matrix. β-Carotene is not typically used as a sunscreen active ingredient, but it serves as an ideal probe molecule because it absorbs UVA light, photodegrades and undergoes a fluorescence shift. As shown in figure 2.1, the β-carotene molecule contains a long conjugated hydrocarbon chain, consisting of many C=C bonds which serve as a

chromophore for the molecule. This chromophore is responsible for the light absorption and gives β-carotene its deep orange color. Based upon the Planck-Einstein equation, $E = hc/\lambda$, UV light has more energy than visible light. When exposed to an abundant UVA light source, the C=C and C-C bonds of the hydrocarbon chain break, the molecule degrades and loses its deep orange color, becoming transparent.[22]

2.3.2. Photostabilizer molecule

The known UV absorber 2-ethylhexyl 4-methoxycinnamate (EHMC) (M_w =290.3g/mol) was selected to serve as a photostabilizer (structure shown in figure 2.1). Its peak absorption when dissolved in acetone was between 325 and 375 nm, thus validating its use as a UVA absorber. The photoprotective effects of 2-ethylhexyl 4-methoxycinnamate when mixed with β–carotene in two distinct configurations were investigated. These two configurations are shown in figure 2.2.

2.3.3. Polymer matrix

Poly(methyl methacrylate) is often used as a polymer matrix for producing microparticles. It is important to evaluate its effect (structure shown in figure 2.1) on the overall photostability of each configuration tested. Poly(methyl methacrylate) of M_w = 120,000 (Sigma Aldrich) was dissolved in acetone and was mixed with 2-ethylhexyl 4-methoxycinnamate in a ratio of 2-ethylhexyl 4-methoxycinnamate: poly(methyl methacrylate) (4:1).

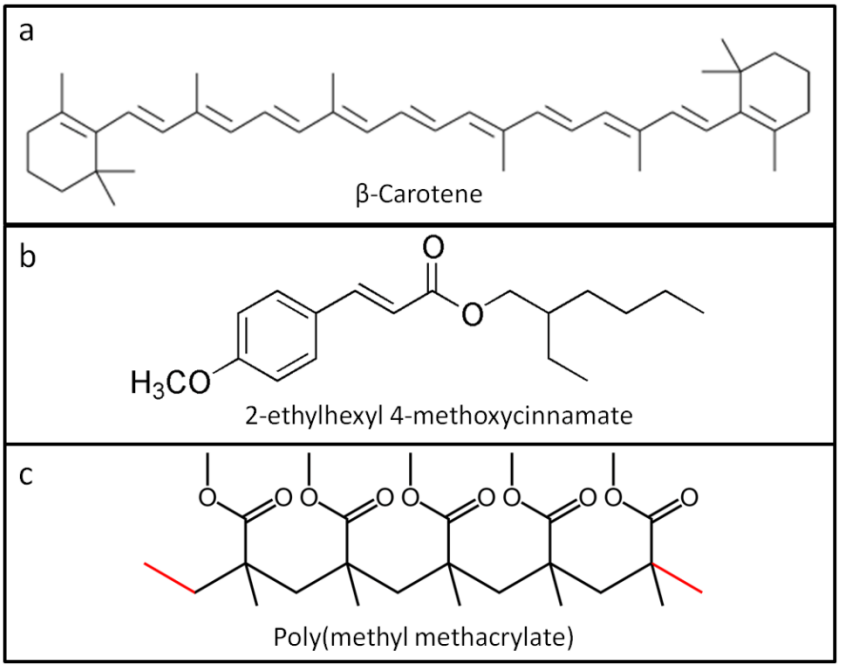

Figure 2.1. UV absorber molecules. **(a)** β–Carotene molecule. **(b)** 2-ethylhexyl 4-methoxycinnamate. **(c)** Poly(methyl methacrylate).

2.4. Methods

2.4.1. Macroscopic configurations

β–Carotene solutions were mixed with each dilution of 2-ethylhexyl 4-methoxycinnamate in two distinct configurations using a standard or tandem cuvette cell (NSG Precision Cells Inc., Farmingdale NY). The tandem cell uses a quartz divider which has no effect on the fluorescence signal. The cuvette cells were chosen to macroscopically replicate the physical orientation of microparticles containing the UV sensitive molecule (β-carotene) and the photostabilizer (2-ethylhexyl 4-methoxycinnamate). For both configurations the total concentration (i.e. no tandem divider) of β–carotene equaled 16.65uM and the total concentration of 2-ethylhexyl 4-methoxycinnamate was equal to one of 868mM, 434mM, 217mM or 108mM. The total sample volume equaled 2 mL. It is important to note that the homogeneous configuration

used a single well cuvette, rather than a tandem well cuvette. By eliminating the divider, the free motion of β–carotene and 2-ethylhexyl 4-methoxycinnamate throughout the entire 2 mL sample occurs. This is analogous to a completely homogenous microparticle of the same radius as the core/shell configuration, rather than a core-shell particle. Each mixture of 2-ethylhexyl 4-methoxycinnamate/poly(methyl methacrylate) was configured with β–carotene in the two configurations shown in figure 2.2. The overall β–carotene, 2-ethylhexyl 4-methoxycinnamate and poly(methyl methacrylate) concentrations for each configuration were fixed at 16.65uM, 217mM, and 1.67mM respectively.

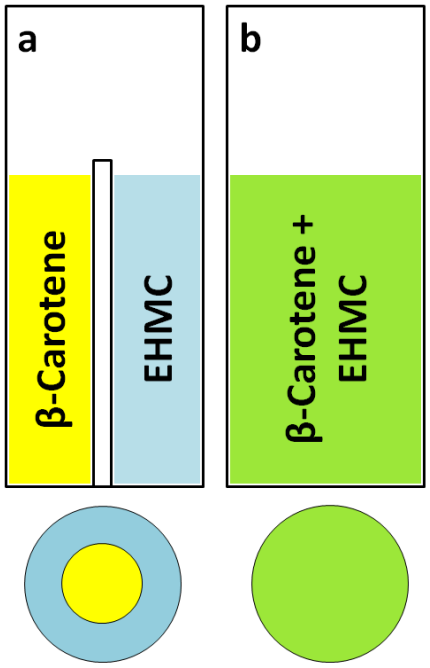

Figure 2.2. Macroscopic configurations. **(a)** Core/shell configuration of β–carotene and 2-ethylhexyl 4-methoxycinnamate in tandem cuvette cell. **(b)** Homogenous configuration of β–carotene solution and 2-ethylhexyl 4-methoxycinnamate in standard cell.

2.4.2. Experimental device

Fluorescence was measured for 30 seconds using QuantaMaster UV VIS fluorometer (PTI, Birmingham NJ) shown in figure 3(a). For consistency and optimal

fluorescence, the right well of the cuvette (tandem only) was adjacent to the light source. After fluorescence was recorded, the sample was removed from the fluorometer and placed 18.5mm from UVA light (λ=365 nm, I=1900μW/cm^3) for 10 min using a Pen Ray Mercury lamp (UVP, Upland CA) as shown in figure 3(b). The right well of the cuvette (tandem only), representing the outer surface of a particle was always adjacent to the lamp. The entire apparatus was enclosed in a black box to minimize any background radiation and reflection. After exposure the cuvette was returned to the fluorometer and the fluorescence was measured again for 30 seconds. This cycle was repeated for a total exposure time of 60 minutes.

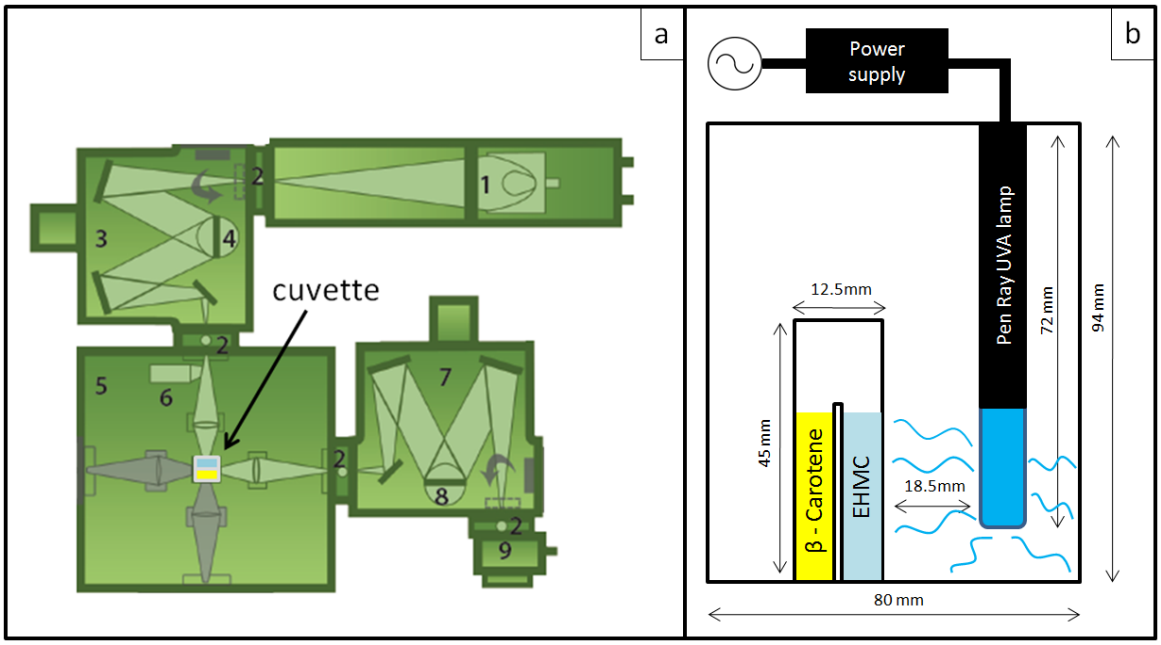

Figure 2.3. Fluorescence and UV apparatuses. **(a)** QuantaMaster UV VIS fluorometer. **(b)** UVA exposure chamber.

2.4.3. FTIR analysis of β–carotene degradation

A 2 mL solution of β–carotene [16.650uM] in a standard cuvette was exposed to UVA light for 60 minutes. At the beginning and end of exposure a Spectrum One FTIR

(PerkinElmer, Waltham MA) was used to measure the absorption bands associated with C=C and C-C bonds, which range from 1600-1680 cm^{-1}.

2.4.4. UV-Vis analysis of β–carotene degradation

A 2 mL solution of β–carotene [16.650uM] in a standard cuvette was exposed to UVA light for 60 minutes. At the beginning and end of the exposure time, the absorbance of the solution was measured using a NanoDrop 1000 UV-Vis Spectrophotometer (Wilmington, DE).

2.4.5. UV-Vis analysis of 2-ethylhexyl 4-methoxycinnamate degradation

A 2mL solution of 2-ethylhexyl 4-methoxycinnamate [868mM] in a standard cuvette was exposed to UVA light for 60 minutes. At the beginning and end of the exposure time, the absorbance of the solution was measured using a NanoDrop 1000 UV-Vis Spectrophotometer (Wilmington, DE).

2.5. Results and discussion

β–Carotene solution excitation and emission spectra were determined. β–Carotene dissolved in acetone showed a maximum excitation at 350nm and a maximum emission at 525nm. The 2-ethylhexyl 4-methoxycinnamate solution excitation and emission spectra were also determined; a maximum excitation at 380nm and a maximum emission at 413nm, although it had a fairly broad emission spectrum. Because of this broad emission, it was important to compare the emission spectra of both 2-ethylhexyl 4-methoxycinnamate and β–carotene to ensure that 2-ethylhexyl 4-methoxycinnamate did not interfere with the fluorescence signal of β–carotene. A comparison of 2-ethylhexyl 4-methoxycinnamate and β–carotene emission spectra, when excited with 350nm light,

revealed that the 2-ethylhexyl 4-methoxycinnamate fluorescence was insignificant when compared to β–carotene fluorescence. This ensured that 2-ethylhexyl 4-methoxycinnamate fluorescence did not interfere with measuring β–carotene fluorescence.

2.5.1. β–carotene degradation

The solution of β–carotene contained in a single well cuvette was bleached when exposed to the UVA light source in 10 minute intervals for a total of 60 minutes. Figure 2.4. illustrates the decay of the fluorescence signal, measured in photons/sec. The data was normalized by dividing each data point in a set by its initial data point at time = 0 minutes. As the concentration of β–carotene was reduced, a higher percentage of β–carotene molecules were interacting with a fixed number of UVA photons which caused more rapid photodegradation, thus a less photostable sample. Conversely if the concentration of β–carotene increased, a smaller percentage of β–carotene molecules were interacting with a fixed number of UVA photons resulting in greater photostability. This is analogous to sunscreen manufacturers increasing the concentration of active ingredient (UV absorber) in a formulation to increase the photostability of the sunscreen.

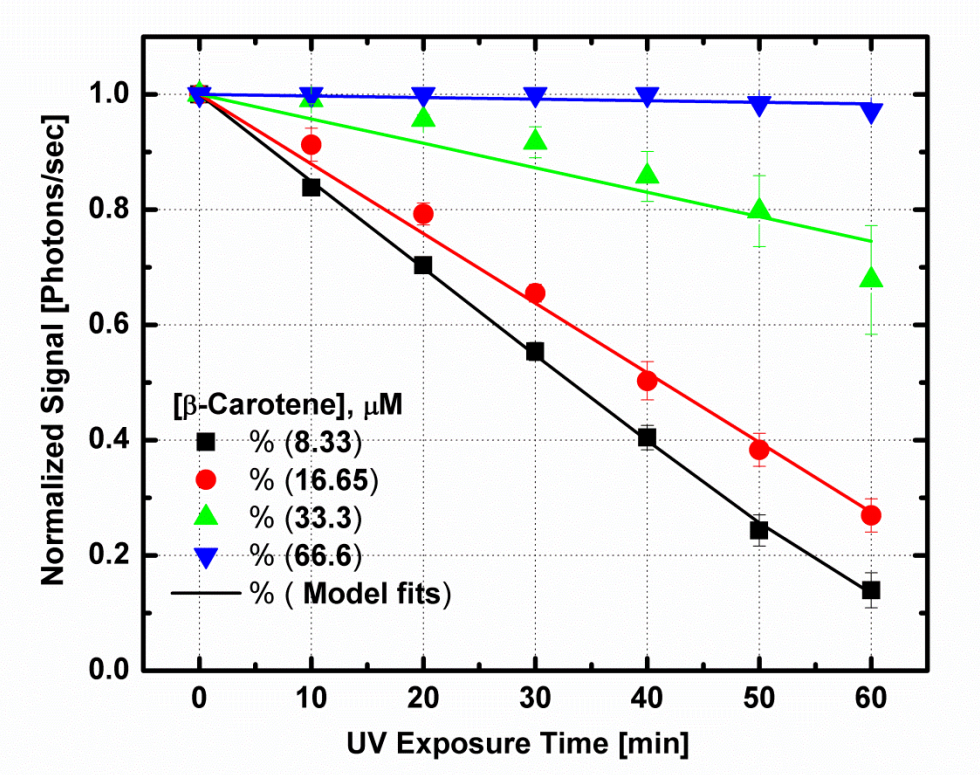

Figure 2.4. Fluorescence decay of β–carotene.

The photoreaction of β-carotene (A) is often described by the following equation[2]

$$A \xrightarrow{hc/\lambda} P \qquad (1)$$

where P refers to product(s) formed. Assuming instant mixing of samples, the rate of photodegradation can be described by

$$-\frac{d[A]}{dt} = \varphi_A I_A = \varphi_A I_0 (1 - \exp(-\chi[A]d)) \qquad (2)$$

where [A] is the concentration of β-carotene at after UV exposure time t, φ_A is the quantum yield for excitation of A, I_0 is the lamp intensity, I_A is the absorbed intensity,

χ is the molar excitation coefficient and *d* is the optical path length. The general solution of this equation is

$$\frac{[A]}{[A_0]} = \frac{1}{[A_0]\chi d} \ln\{1 + \exp([A_0]\chi d - \varphi_A I_0 \chi dt) - \exp(-\varphi_A I_0 \chi dt)\}$$

(3)

where $[A_0]$ is the known initial concentration of β-carotene. With $d = 1.25cm$ in our experiments, [A] can be evaluated given the values of χ and $\varphi_A I_0$. The fits of this equation are plotted in figure 2.4. For $\chi = 8.6 \times 10^8 \, cm^2/mole$ and $\varphi_A I_0 = 2.09 \times 10^{-12} \, mole/cm^3 s$, the fluorescence data for $[A_0] = 8.33 \mu M$ fits very well with the model. However, the model does not accurately capture the entire experimentally observed decay profiles for concentrations higher than $[A_0] = 8.33 \mu M$. It is likely that at high concentrations, the interactions between molecules protected β-carotene degradation from UV exposure. To understand this behavior of β-carotene fluorescence, an average distance between β–carotene molecules can be evaluated. Figure 4(b) shows that when the average proximity of individual β–carotene molecules was less than approximately 60nm, the fluorescence stabilized. This corresponds to β–carotene solutions with a concentration greater than 67uM. The normalized fluorescence of β–carotene after 60 minutes of exposure is plotted in figure 2.5.

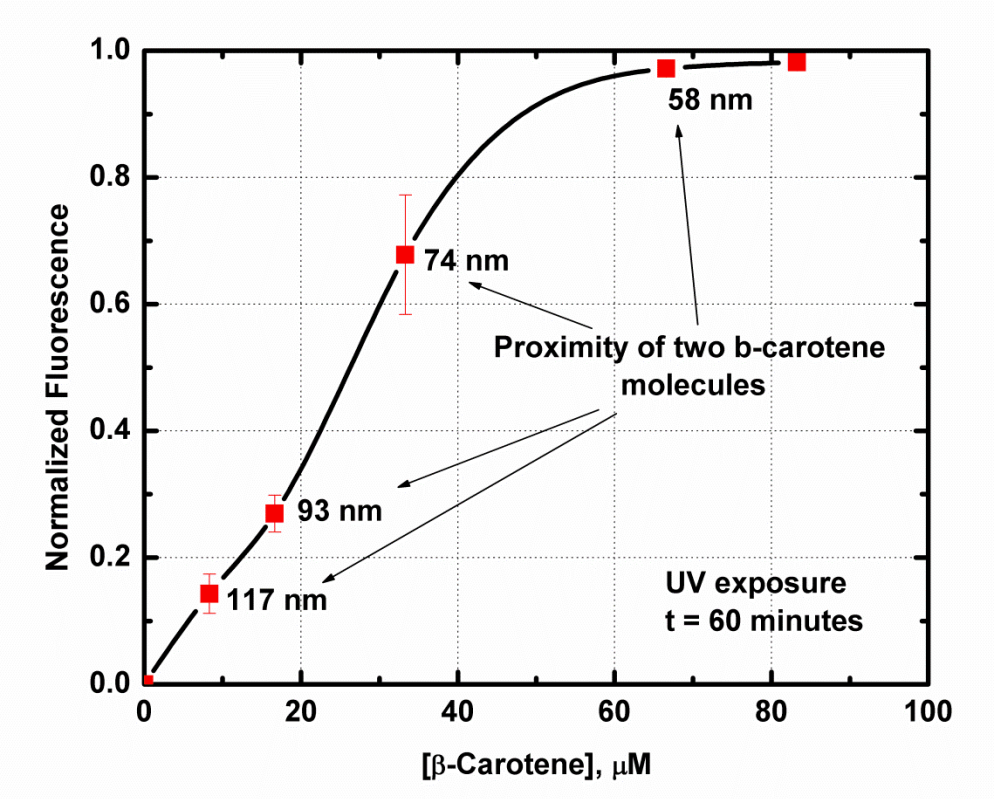

Figure 2.5. Fluorescence based upon concentration of β-carotene at time = 60 minutes.

Figure 2.6. shows an FTIR spectrum of 16.65uM β–carotene solution before and after 60 minute UVA exposure. The FTIR spectra obtained after degrading β–carotene solution with UVA light for one hour showed a significant decrease in absorbance (red ovals) associated with C=C and C-C bonds (1600 – 1680 cm^{-1}) indicating color loss and degradation of the hydrocarbon chain chromophore. However, the spectrum showed no significant decrease in absorbance for aromatic C-H bonds (3070cm^{-1}).

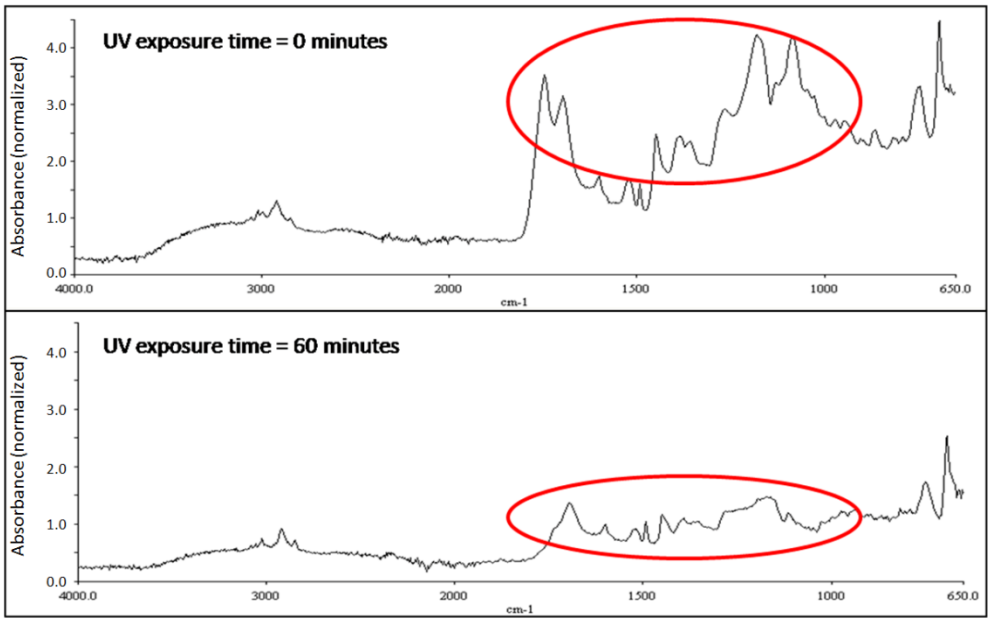

Figure 2.6. FTIR spectrum of16.65uM β–carotene solution before and after 60 minute UVA exposure.

Figure 2.7. shows a UV-Vis Spectra of 16.65uM β–carotene solution before and after UV exposure. The UV-Vis spectrum before irradiation (time = 0 minutes) for β-carotene showed absorbance in the UV range as well as in the visible spectrum. The UV-Vis spectrum after irradiation (time = 60 minutes) showed only absorbance in the UV range. The red oval region corresponds to loss of absorbance in the visible spectrum after 60 minutes. This was supported by FTIR results and verified by pre and post UV exposure visual observation.

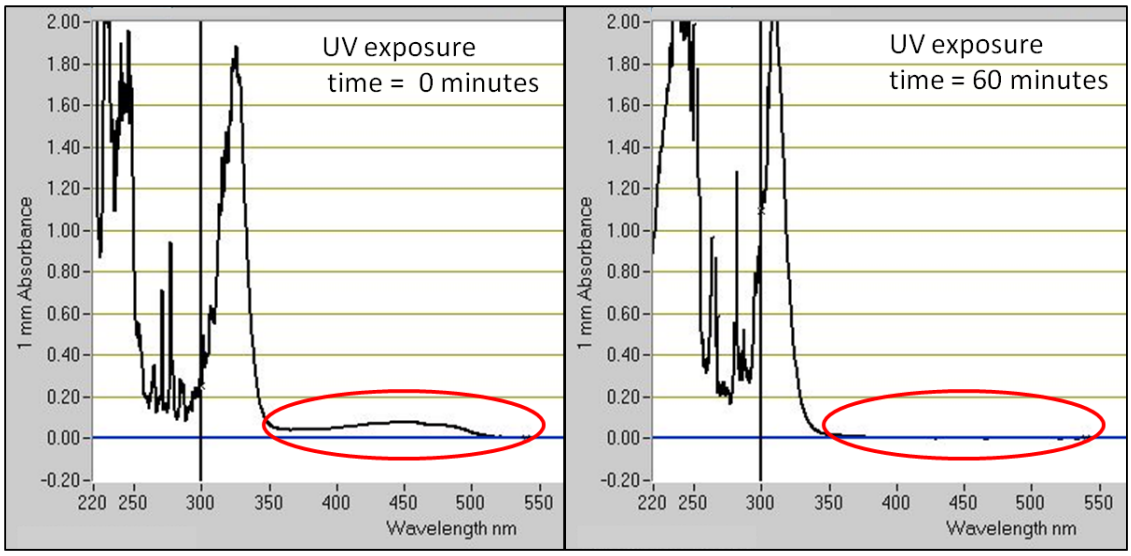

Figure 2.7. UV-Vis Spectra of 16.65uM β–carotene solution before and after UV exposure.

2.5.2. Effect of 2-ethylhexyl 4-methoxycinnamate on β–carotene degradation

Next, we attempted to understand the varying photostability of β-carotene and 2-ethylhexyl 4-methoxycinnamate molecular configurations. 2-Ethylhexyl 4-methoxycinnamate 98% by volume [3.47M], stabilized with 0.05 to 0.1% butylated hydroxytoluene (Acros Organics, Morris Plains NJ) was diluted in acetone to four concentrations: 868mM, 434mM, 217mM and 108mM. Preliminary experiments confirmed that butylated hydroxytoluene had no stabilizing effect on β-carotene. The 24.5% by volume [868mM] solution of 2-ethylhexyl 4-methoxycinnamate was comparable to the 20% maximum concentration by volume regulated in Japanese sunscreen formulations. The 12.25% by volume [434mM] solution was comparable to the 10% maximum concentration by volume regulated in European and Australian sunscreen formulations. The 6.125% by volume [217mM] solution was comparable to the 7.5% maximum concentration by volume regulated in the USA. The 3% by volume [108mM] fell below any maximum concentration regulation. The UV-Vis spectrum before

irradiation (time = 0 minutes) for 2-ethylhexyl 4-methoxycinnamate showed absorbance in the UV range. The UV-Vis spectrum after irradiation (time = 60 minutes) also showed absorbance in the UV range. Figure 2.8. shows UV-Vis spectra of 2-ethylhexyl 4-methoxycinnamate solution before and after UV exposure. The maximum absorbance was between 325 and 375 nm, suggesting its use as an effective UVA absorber.

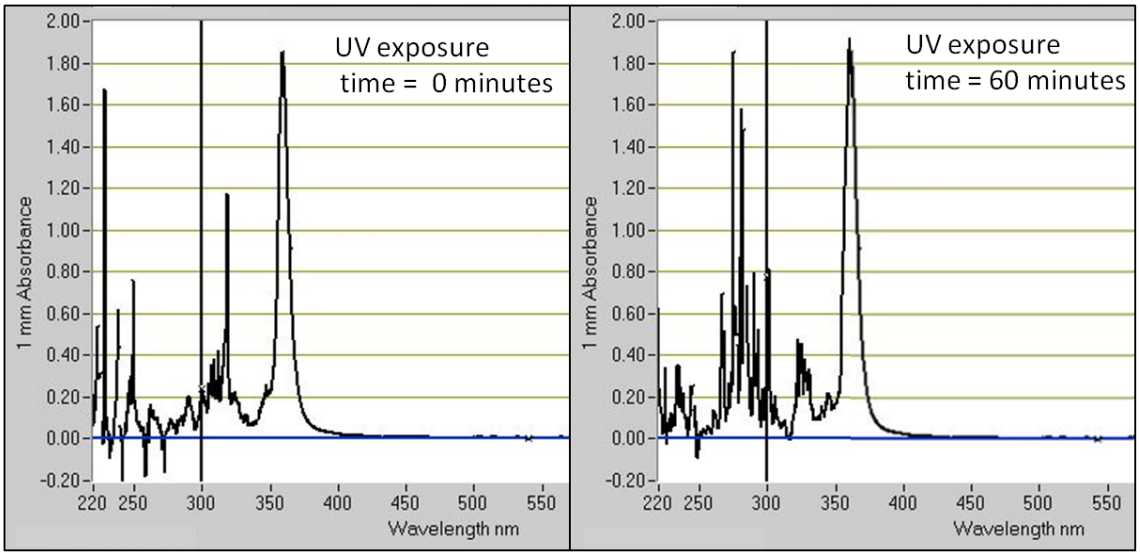

Figure 2.8. UV-Vis Spectra of 2-ethylhexyl 4-methoxycinnamate solution before and after UV exposure.

Figure 2.9. shows the results of the core/shell configuration. The data was normalized by dividing each data point in a set by its initial data point at time = 0 minutes. Increasing the concentration of 2-ethylhexyl 4-methoxycinnamate had a minor effect on the photostability of β–carotene in the core/shell configuration. The limiting factor of photostability in this configuration was that an interface existed, preventing close interactions between β–carotene and 2-ethylhexyl 4-methoxycinnamate molecules. Figure 2.10 shows the results of the homogeneous configuration; in which all of the β–carotene and 2-ethylhexyl 4-methoxycinnamate molecules are in close contact, a feature which resulted in optimal quenching and dissipating of excited state energy and the most

photostable configuration. 390uM and 790uM concentrations of 2-ethylhexyl 4-methoxycinnamate were also included to show that increasing the concentration of 2-ethylhexyl 4-methoxycinnamate resulted in greater photostability of β–carotene in this configuration. However, the fluorescence results showed that for the same overall concentration of 2-ethylhexyl 4-methoxycinnamate in the core/shell and homogenous configurations, the homogenous configuration offered much more effective photoprotection. Therefore the proximity of 2-ethylhexyl 4-methoxycinnamate to β–carotene had a greater impact than the concentration of 2-ethylhexyl 4-methoxycinnamate on the photostability, whereby closing the proximity of 2-ethylhexyl 4-methoxycinnamate and β–Carotene yielded substantial benefits to photostability.

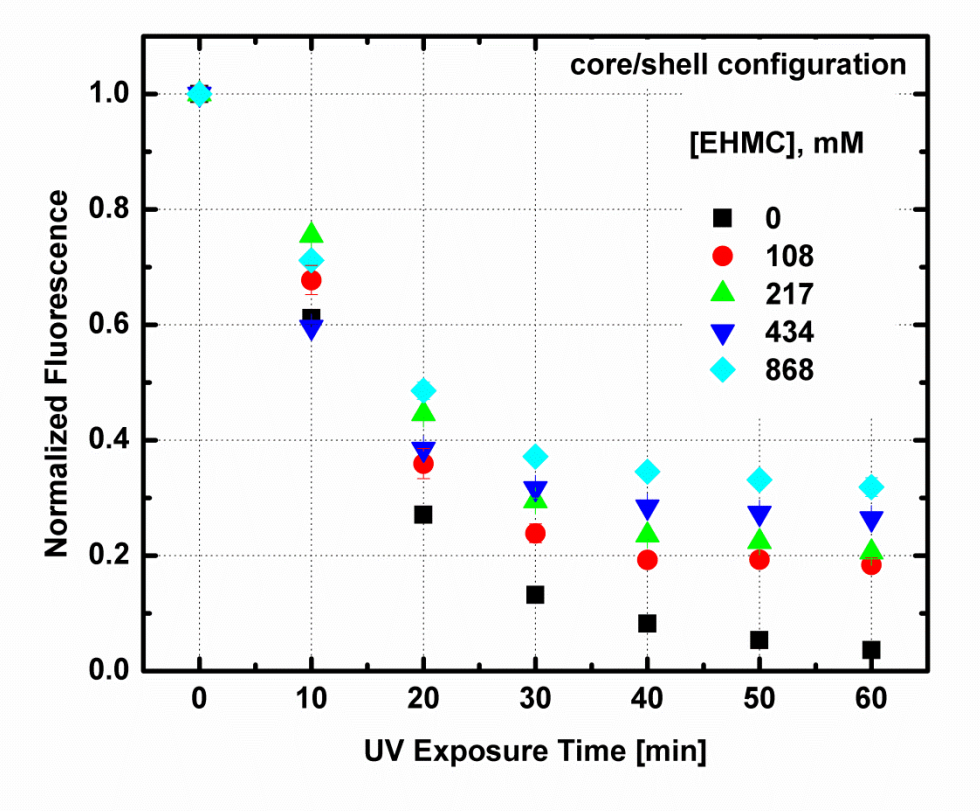

Figure 2.9. β–Carotene decay at 16.65uM fixed concentration mixed with varying 2-ethylhexyl 4-methoxycinnamate concentrations in the core/shell configuration.

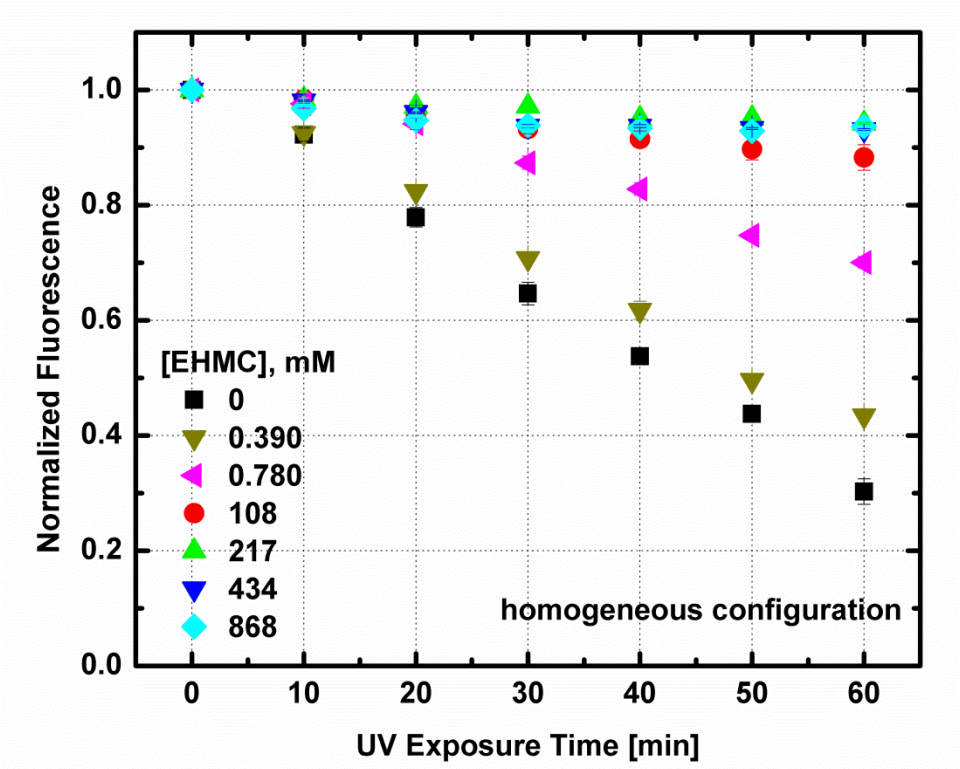

Figure 2.10. β–Carotene decay at 16.65uM fixed concentration mixed with varying 2-ethylhexyl 4-methoxycinnamate concentrations in the homogenous configuration.

β–Carotene retained the most fluorescence when mixed with the highest concentration of 2-ethylhexyl 4-methoxycinnamate and it retained the least fluorescence when mixed with the lowest concentration of 2-ethylhexyl 4-methoxycinnamate in both molecular configurations. Comparing the two configurations to one another for a given concentration of 2-ethylhexyl 4-methoxycinnamate we found that the homogeneous configuration retained the most fluorescence when exposed to UVA light for the duration of one hour for all concentrations of 2-ethylhexyl 4-methoxycinnamate. This result was most apparent for the 2-ethylhexyl 4-methoxycinnamate of concentration 217mM shown in figure 2.11. Here we added a hybrid configuration which used 2-ethylhexyl 4-methoxycinnamate in both wells of the tandem cuvette. Note that the total amount of 2-ethylhexyl 4-methoxycinnamate in the system was equal for all three configurations, but

the 2-ethylhexyl 4-methoxycinnamate was distributed differently among the compartments in each configuration. In the core/shell configuration all of the 2-ethylhexyl 4-methoxycinnamate was in front of the β–carotene and should reduce the UV irradiation level for all the β–carotene molecules according to Beer's law. In the homogenous configuration, with conditions constant, one would expect less stability (Beer's law) because half of the 2-ethylhexyl 4-methoxycinnamate molecules were behind the β–carotene and only half were in front, while in the core/shell configuration all 2-ethylhexyl 4-methoxycinnamate molecules were in front of β–carotene molecules. However the homogenous configuration showed greater stability than the core/shell, which is strong evidence for a proximity effect between β–carotene and 2-ethylhexyl 4-methoxycinnamate.

Increasing the concentration of 2-ethylhexyl 4-methoxycinnamate did increase the photostability, but the configuration played a more dominant role in the photostability. With the concentrations of β–carotene and 2-ethylhexyl 4-methoxycinnamate fixed, changing from core/shell to hybrid to homogeneous yielded very significant improvements in the overall photostability. The homogeneous configuration was approximately 1.5 times more stable than the hybrid configuration and 5 times more stable than the core/shell configuration based upon β–carotene fluorescence after 60 minutes of UVA exposure.

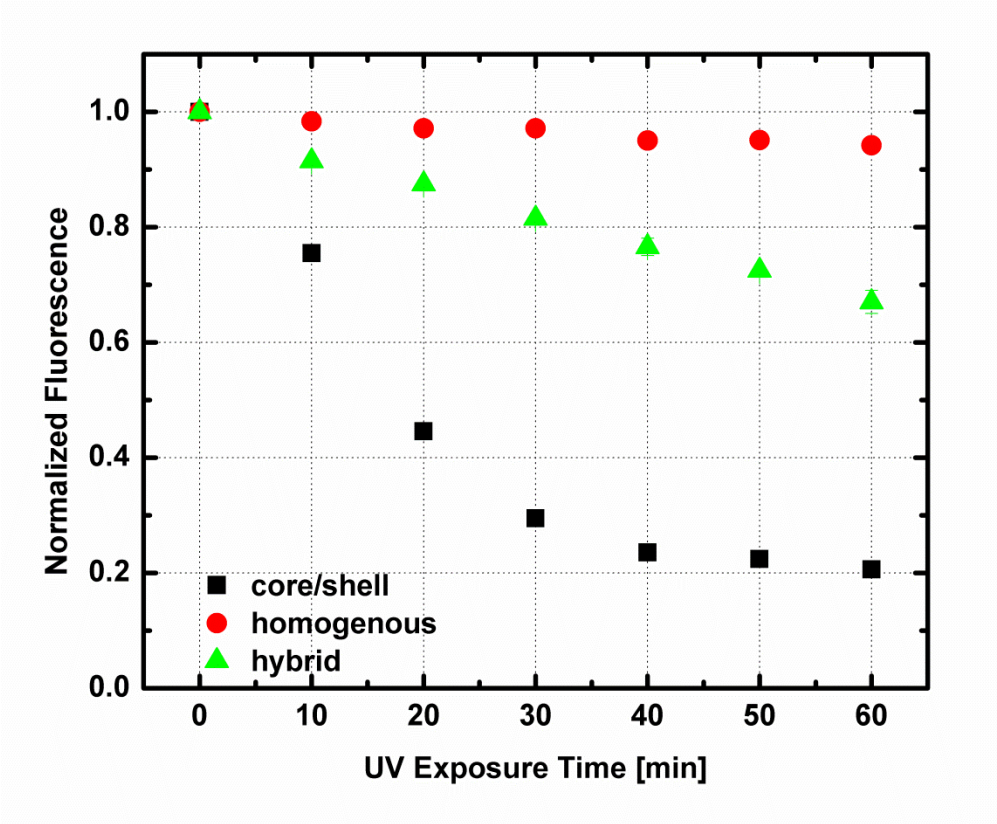

Figure 2.11. β–Carotene decay at 16.65uM fixed concentration mixed with 2-ethylhexyl 4-methoxycinnamate [217mM] for all three configurations.

2.5.3. Proximal effect

We also attempted to understand the proximal effect of β-carotene and 2-ethylhexyl 4-methoxycinnamate in the homogeneous configuration. When β–carotene molecules and 2-ethylhexyl 4-methoxycinnamate molecules were freely allowed to mix, the highest level of fluorescence was retained over an exposure period of 60 minutes. This led to the hypothesis that a proximal relationship existed at the molecular level between the β–carotene and 2-ethylhexyl 4-methoxycinnamate with regard to the photostability of β–carotene. Since the β–carotene concentration was constant [16.65uM], the distance between one β–carotene molecule to an adjacent 2-ethylhexyl 4-methoxycinnamate molecule could be approximated using a body centered cubic unit

cell. There were exceedingly more 2-ethylhexyl 4-methoxycinnamate molecules than β–carotene molecules present; therefore we assumed that one unit cell containing a β–carotene molecule would also contain eight 2-ethylhexyl 4-methoxycinnamate molecules. This assumption was valid for our data since the number of molecules in solution from the lowest concentration of 2-ethylhexyl 4-methoxycinnamate used [390uM] far exceeded the number of β–carotene molecules in solution, by over a factor of 23. This model would be valid for solutions with 2-ethylhexyl 4-methoxycinnamate concentration of less than approximately 133uM for the given β–carotene concentration of 16.65uM. As the concentration of 2-ethylhexyl 4-methoxycinnamate increased, the average distance between 2-ethylhexyl 4-methoxycinnamate and β–carotene decreased, hence the probability of 2-ethylhexyl 4-methoxycinnamate closely interacting with β–carotene increased. More relevant was the relationship between fluorescence and proximity. Figure 2.12. shows that increasing the distance between the β–carotene/2-ethylhexyl 4-methoxycinnamate molecules resulted in a decrease in fluorescence after the 60 minute exposure. By closing the proximity between 2-ethylhexyl 4-methoxycinnamate and β–carotene, we effectively increased the probability of close interactions (<1nm) between 2-ethylhexyl 4-methoxycinnamate and β–carotene. These close interactions allow for effective energy transfer, i.e. quenching of excited state molecules. Interpolating the data, there appears to be a threshold value on the magnitude of 15nm. For molecules spaced closer than this value, fluorescence was maintained, while for molecules spaced further than this value, there was considerable decay in the fluorescence. The proximity of β–carotene/2-ethylhexyl 4-methoxycinnamate in the core/shell configuration was fixed because of the divider in the tandem cuvette. In its microparticle analogue, β–carotene

and 2-ethylhexyl 4-methoxycinnamate would only physically interact minimally at the core-shell interface. The proximal effect, fluorescence versus proximity, could be calculated for the hybrid configuration, but only for the core (left well of the cuvette).

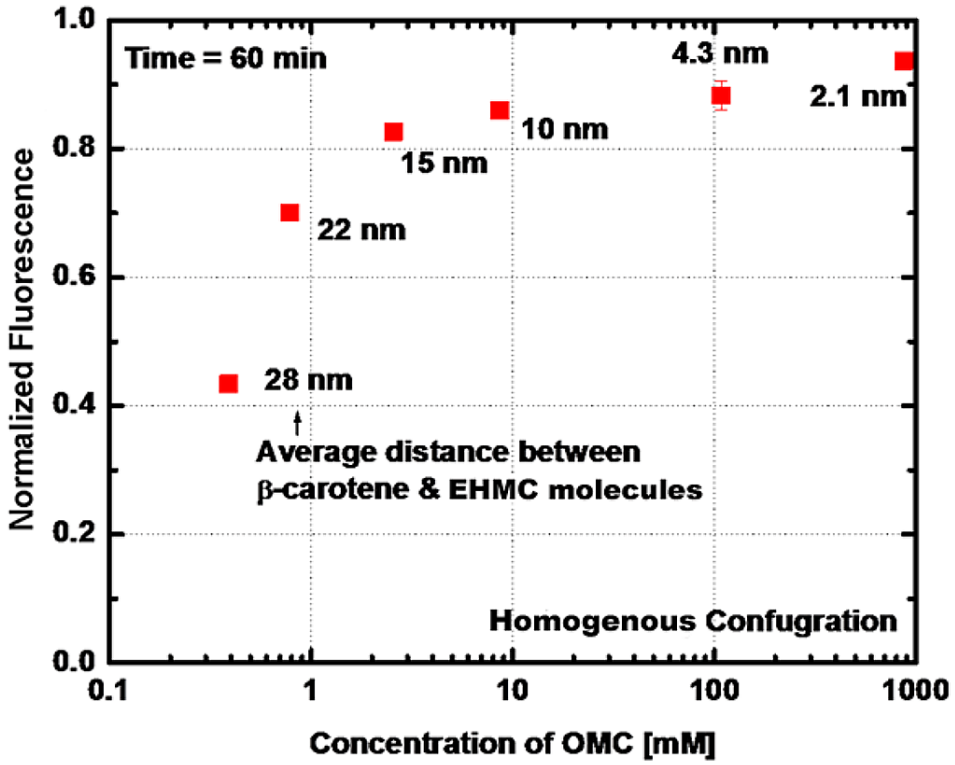

Figure 2.12. Fluorescence of β–carotene 16.65uM after 60 minute exposure in the homogeneous configuration vs. concentration of 2-ethylhexyl 4-methoxycinnamate.

An additional UV-Vis analysis was performed for the homogeneous configuration (2-ethylhexyl 4-methoxycinnamate = 434mM, β-carotene = 16.65uM) to compare the absorbance before and after UV exposure. Both pre and post exposure spectra showed strong peaks from 350nm to 400nm resulting from the absorbance of 2-ethylhexyl 4-methoxycinnamate as shown in figure 2.13. There was also a faint absorbance band from 400nm to 500nm due to the absorbance of β-carotene. UV-Vis results from figure 2.7. clearly showed that absorbance in the visible light region of β–carotene decreased with exposure to UVA radiation. This corresponds with the visible observation of the orange

colored solution decaying to a clear solution after one hour of exposure to UVA radiation. However, figure 2.13 shows that when β–carotene was homogenously mixed with 2-ethylhexyl 4-methoxycinnamate [434mM], absorbance in the visible light region of β–carotene was maintained throughout the 60 minutes of UV exposure (red ovals). This is verified by visual observation of the orange colored solution remained orange throughout the duration of exposure and this further supports that the homogeneous configuration effectively maintained photostability.

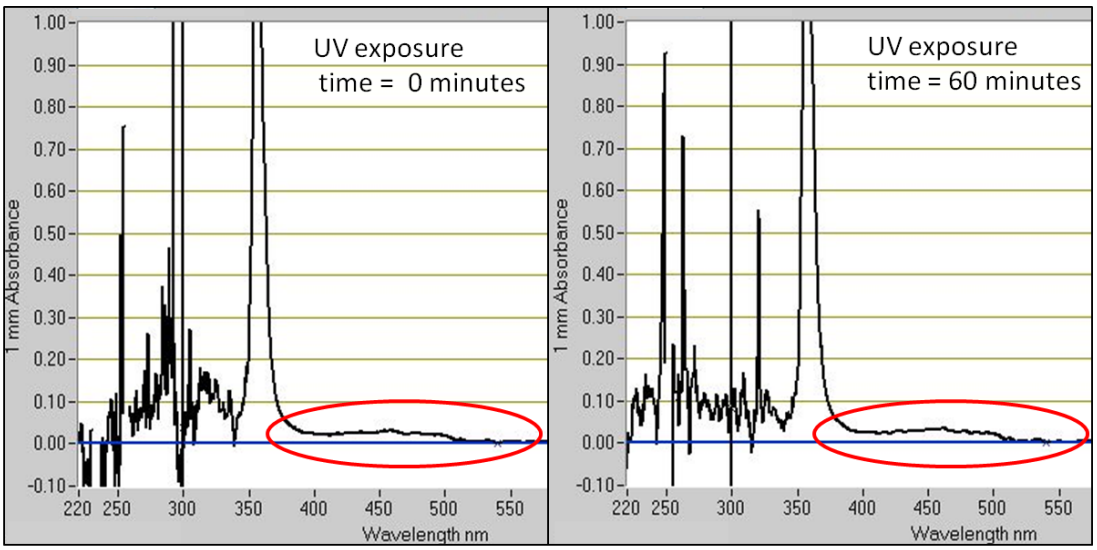

Figure 2.13. UV-Vis spectra of 16.65uM β–carotene when mixed with 434mM 2-ethylhexyl 4-methoxycinnamate in the homogeneous configuration, before and after 60 minute UVA exposure.

2.5.4. Addition of poly(methyl methacrylate)

The fluorescence decay of β–carotene was compared when using 2-ethylhexyl 4-methoxycinnamate alone as the UV photostabilizer versus using 2-ethylhexyl 4-methoxycinnamate mixed with poly(methyl methacrylate) (PMMA). Figures 2.14. and 2.15. show this comparison. The addition of PMMA appeared to have only a minor inhibitory or synergistic effect on the fluorescence decay of β–carotene in our three

configurations, without a clear trend. In future assays we plan to use several different concentrations of PMMA, thus affecting the overall viscosities of our formulations. We would like to elucidate the effect of viscosity on the proximal interactions between β–carotene and 2-ethylhexyl 4-methoxycinnamate in our system.

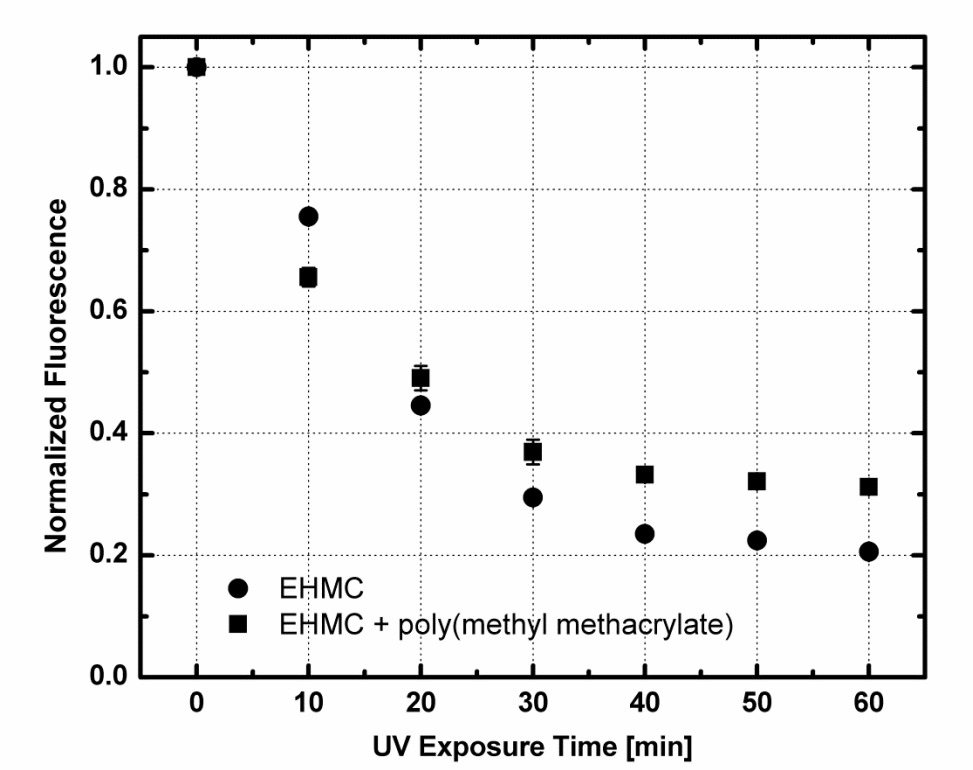

Figure 2.14. β–Carotene [16.65uM] decay when mixed with 2-ethylhexyl 4-methoxycinnamate [217mM] alone versus β–carotene decay when mixed with 2-ethylhexyl 4-methoxycinnamate and poly(methyl methacrylate) [1.67mM] in the core/shell configuration.

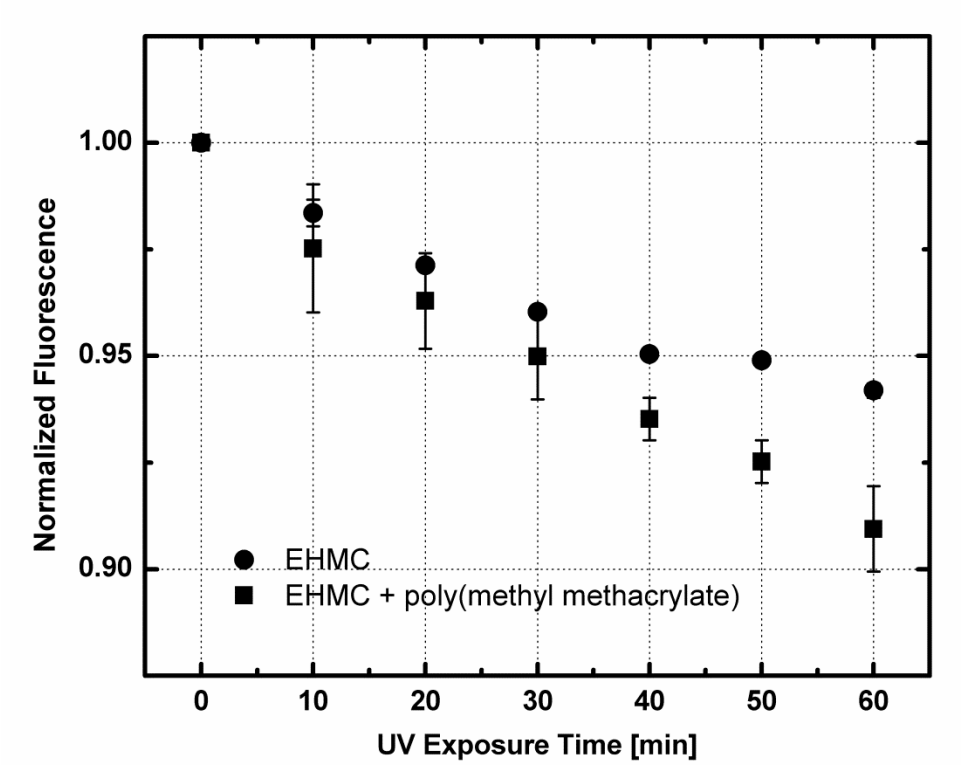

Figure 2.15. β–Carotene [16.65uM] decay when mixed with 2-ethylhexyl 4-methoxycinnamate [217mM] alone versus β–carotene decay when mixed with 2-ethylhexyl 4-methoxycinnamate and poly(methyl methacrylate) [1.67mM] in the homogeneous configuration.

2.6. Conclusion

The proximity of the 2-ethylhexyl 4-methoxycinnamate to β–carotene played a significant role in the photostability of β–carotene exposed to UVA irradiation. Closing the proximity increased β–carotene photostability. This was achieved by first homogenously mixing β–carotene and 2-ethylhexyl 4-methoxycinnamate and then increasing the concentration of 2-ethylhexyl 4-methoxycinnamate. The body centered cubic cell model effectively showed that by increasing the concentration of 2-ethylhexyl 4-methoxycinnamate in the homogeneous configuration, we effectively decreased the average spacing between 2-ethylhexyl 4-methoxycinnamate and β–carotene molecules in solution thus increasing the probability of 2-ethylhexyl 4-methoxycinnamate and β–

carotene molecules having close interactions in solution where photostabilizing energy transfers could occur. Based upon our model there appeared to be a threshold separation of 15 nm, where below this average distance greater photostability was achieved. Furthermore, changing the proximity of 2-ethylhexyl 4-methoxycinnamate to β–carotene yielded very different fluorescence decay profiles for the same given concentration of 2-ethylhexyl 4-methoxycinnamate in the core/shell, homogenous and hybrid configurations, in which the homogenous configuration offered the best photoprotection. The addition of poly(methyl methacrylate) showed no clear trend with regard to the photostability of the configurations in this study. Moving forward, we may incorporate 2-ethylhexyl 4-methoxycinnamate with other UVA absorbers to explore synergistic effects.

2.7. Acknowledgement

We acknowledge the support of the National Science Foundation (Contract No. NSF-CBET 0755946) for this research.

2.8. References

1 Gallagher, R. P. & Lee, T. K. Adverse effects of ultraviolet radiation: A brief review. *Progress in Biophysics & Molecular Biology* **92**, 119-131, doi:DOI 10.1016/j.pbiomolbio.2006.02.011 (2006).

2 Herzog, B., Wehrle, M. & Quass, K. Photostability of UV Absorber Systems in Sunscreens. *Photochemistry and Photobiology* **85**, 869-878, doi:DOI 10.1111/j.1751-1097.2009.00544.x (2009).

3 Parejo, P. G., Zayat, M. & Levy, D. Highly efficient UV-absorbing thin-film coatings for protection of organic materials against photodegradation. *Journal of Materials Chemistry* **16**, 2165-2169, doi:Doi 10.1039/B601577h (2006).

4 Pospisil, J. & Nespurek, S. Photostabilization of coatings. Mechanisms and performance. *Progress in Polymer Science* **25**, 1261-1335 (2000).

5 Chou, P. T., Chen, Y. C., Yu, W. S. & Cheng, Y. M. Spectroscopy and dynamics of excited-state intramolecular proton-transfer reaction in 5-hydroxyflavone. *Chemical Physics Letters* **340**, 89-97 (2001).

6 Stein, M. *et al.* Influence of polymer matrixes on the photophysical properties of UV absorbers. *Journal of Physical Chemistry A* **106**, 2055-2066, doi:Doi 10.1021/Jp012134k (2002).

7 Otterste.Ja. Photostability and Molecular-Structure. *Journal of Chemical Physics* **58**, 5716-5725 (1973).

8 Wu, Y. G. *et al.* Excited state intramolecular proton transfer in 2-(2 '-arylsulfonamidophenyl)benzimidazole derivatives: Insights into the origin of

donor substituent-induced emission energy shifts. *Journal of Physical Chemistry A* **111**, 4584-4595, doi:Doi 10.1021/Jp068832s (2007).

9 Sobolewski, A. L. & Domcke, W. G. Computational studies of the photophysics of hydrogen-bonded molecular systems. *Journal of Physical Chemistry A* **111**, 11725-11735, doi:Doi 10.1021/Jp075803o (2007).

10 Baughman, B. M., Stennett, E., Lipner, R. E., Rudawsky, A. C. & Schmidtke, S. J. Structural and Spectroscopic Studies of the Photophysical Properties of Benzophenone Derivatives. *Journal of Physical Chemistry A* **113**, 8011-8019, doi:Doi 10.1021/Jp810256x (2009).

11 Montalti, M. *Handbook of Photochemistry 3rd Edition*. (CRC/Taylor & Francis, 2006).

12 Sangermano, M., Borlatto, E., Bytner, F. D. D., Priola, A. & Rizza, G. Photostabilization of cationic UV-cured coatings in the presence of nanoTiO(2). *Progress in Organic Coatings* **59**, 122-125, doi:DOI 10.1016/j.porgcoat.2007.01.020 (2007).

13 He, J. Q., Shao, W., Zhang, L., Deng, C. & Li, C. Z. Crystallization Behavior and UV-Protection Property of PET-ZnO Nanocomposites Prepared by In Situ Polymerization. *Journal of Applied Polymer Science* **114**, 1303-1311, doi:Doi 10.1002/App.30614 (2009).

14 Gorensek, M. & Sluga, F. Modifying the UV blocking effect of polyester fabric. *Textile Research Journal* **74**, 469-474 (2004).

15 Liauw, C. M. *et al.* Effect of interactions between stabilisers and silica used for anti-blocking applications on UV and thermal stability of polyolefin film 2. Degradation studies. *Polymer Degradation and Stability* **65**, 207-215 (1999).

16 Nasu, A. & Otsubo, Y. Rheology and UV-protecting properties of complex suspensions of titanium dioxides and zinc oxides. *Journal of Colloid and Interface Science* **310**, 617-623, doi:DOI 10.1016/j.jcis.2007.02.012 (2007).

17 Yang, H. Y., Zhu, S. K. & Pan, N. Studying the mechanisms of titanium dioxide as ultraviolet-blocking additive for films and fabrics by an improved scheme. *Journal of Applied Polymer Science* **92**, 3201-3210, doi:Doi 10.1002/App.20327 (2004).

18 Becheri, A., Durr, M., Lo Nostro, P. & Baglioni, P. Synthesis and characterization of zinc oxide nanoparticles: application to textiles as UV-absorbers. *Journal of Nanoparticle Research* **10**, 679-689, doi:DOI 10.1007/s11051-007-9318-3 (2008).

19 Katangur, P., Patra, P. K. & Warner, S. B. Nanostructured ultraviolet resistant polymer coatings. *Polymer Degradation and Stability* **91**, 2437-2442, doi:DOI 10.1016/j.polymdegradstab.2006.03.018 (2006).

20 Allen, N. S. *et al.* Degradation and stabilisation of polymers and coatings: nano versus pigmentary titania particles. *Polymer Degradation and Stability* **85**, 927-946, doi:DOI 10.1016/j.polymdegradstab.2003.09.024 (2004).

21 Zhang, Y., Wu, Y. F., Chen, M. & Wu, L. M. Fabrication method of TiO2-SiO2 hybrid capsules and their UV-protective property. *Colloids and Surfaces a-Physicochemical and Engineering Aspects* **353**, 216-225, doi:DOI 10.1016/j.colsurfa.2009.11.016 (2010).

22 Hideki Kandori, H. S., Mamoru Mimuro. Direct Determination of a Lifetime of the S2 State of B-Carotene by Femtosecond Time-Resolved Fluorescence Spectroscopy. *American Chemical Society*, 2671-2672 (1994).

CHAPTER 3

STABILIZATION OF NATURAL DYES IN SOLUTION AND THIN FILMS USING HIGH CONCENTRATIONS OF ANTIOXIDANTS

3.1. Abstract

Natural dyes are normally unstable due to photo-oxidation by UV light. We have measured the stability of a number of natural dyes in combination with high concentrations of antioxidants, excited state quenchers, and UV absorbers. We found that certain combinations, including indigo/BHT, methylene blue/*p*-benzoquinone, and methylene blue/triethylamine show enhanced stability in solution and/or in thin polymer films. By comparing solutions and films of the mixed components with solutions and films of the antioxidant placed between the dye and UV source, we can show that the effect is not UV screening but is due to some form of intermolecular chemistry. This effect may account for the high stability of natural dyes in plant tissues, such as the skins of fruit, and may be usable to stabilize natural dyes in foods or textiles, especially if suitable nanoparticle structures can be developed.

3.2. Introduction

Mechanisms of photostabilization have been well established as a result of extensive studies on photodegradation and photo-oxidation of synthetic polymers especially in the 1970's mainly for the concern of the durability of these polymers in their outdoor applications [1-4]. There are typically three photostabilization mechanisms [4]: UV screening or absorbing, excited state quenching, and free radical scavenging, and they could interact synergistically, additively, or antagonistically when two of them coexist in one system [4,5]. The latter two mechanisms depend on the distance between the UV sensitive moiety and the stabilizer molecule at the nanoscale [3]. In polymer stabilization, very low levels of stabilizers, typically a fraction of 1 wt%, are used. The polymers are very weakly UV absorbing but become brittle due to chain breakage after very low levels of oxidation, typically a 0.1 wt% reaction.

Natural dyes are vulnerable to photo-oxidation but present a very different case. They are strongly UV absorbing and oxidize very rapidly but only discolor when a large fraction of the dye has been oxidized. In polymers, low concentrations of antioxidants are effective because the reaction between free radicals and polymer is very inefficient, whereas antioxidants rapidly trap and remove free radicals when they do collide. Similar arguments apply to the action of excited state quenchers. In dyes, the rate of generation of excited states is much higher and consequently they cannot be stabilized by low levels of antioxidants.

Natural dyes in fruit skins are well known to be associated with high levels of antioxidants and are quite stable. This suggests that there may be a different stabilization regime where the dyes are closely associated with antioxidants or excited state quenchers.

In this paper we describe the stabilization of natural dyes in solution and in polymers films. In each case we compare the stability of the dye under intense UV when mixed with high concentrations of stabilizer, with that of the same dye placed behind a film or solution of the stabilizer. In this way we show that the effect is not simply due to UV absorption but does occur when the molecules are in close proximity.

3.3. Experimental

3.3.1. Materials

β-carotene, indigo, methylene blue (MB), 2,6-di-*tert*-butyl-4-methylphenol (BHT), oxybenzone (98%), (+/-) α-tocopherol, *p*-benzoquinone (BQ), triethylamine (TEA), chloroform (anhydrous, 99+%), N,N-dimethylformamide (DMF), toluene (99%), acetone (99.5%), polymethyl methacrylate (PMMA, MW=120,000), and polyvinylpyrrolidone (PVP, MW=10,000) were purchased from Sigma-Aldrich and used without further treatment.

3.3.2. Sample preparation

Solution samples were prepared in either dye/stabilizer mixed solutions or two separate solutions of the dye and the stabilizer, respectively, and were tested by UV irradiation in quartz cuvettes for possible proximity effects. The two cuvettes were placed back to back, with the stabilizer cuvette in front of the dye cuvette. Samples were irradiated by a 254 nm Pen-Ray UV lamp (Cole Parmer, Vernon Hills, IL) at 4 cm fixed distance for different times unless otherwise specified. Dye photodegradation was measured with a Hach DR 4000 UV-vis spectrophotometer (Loveland, CO).

To prepare mixed or separated polymer films containing dye, it is necessary to have two polymers and solvents such that the first film does not re-dissolve in the second. A film of polymer containing stabilizer can then be layered over a film of polymer containing dye. Polymer thin films containing a dye and/or a stabilizer were prepared on acetone pre-cleaned 2.5 cm × 7.5 cm quartz slides (EM Science, Hatfield, PA) through a dipping process (dipping and withdrawal speed = 0.99 cm/s) controlled by a robotic Automove® system (Asymtek, Carlsbad, CA). The dye and the stabilizer were encapsulated either in one single layer (i.e. single-layer films; coded as "dye+stabilizer (x:y)/polymer1" in which x:y indicates the dye:stabilizer molar ratio) or in two separate layers (i.e. dual-layer films in which the first layer is named the base layer that contains the dye and the second layer is named the cover layer that contains the stabilizer, coded as "stabilizer/polymer2 + dye/polymer1"). For example, BHT/PVP + β-carotene/PMMA dual-layer films were prepared from solutions for the base layer (1 mM β-carotene in 5 wt% PMMA/toluene) and the cover layer (10 mM BHT in 10 wt% PVP/ethanol), respectively. Quartz slides were dipped into the 1 mM β-carotene in 5 wt% PMMA/toluene solution at 1 cm/s speed for a 4.7 cm travel distance, let stay in the solution for 5 sec, and then retracted and let dry in air for 30 min. The slides were then dipped into the 10 mM BHT in 10 wt% PVP/ethanol solution in the same way to form the cover layer. As controls, β-carotene/PMMA and BHT/PVP single-layer films were also prepared. A picture of typical β-carotene containing film samples prepared on quartz slides by the dipping process is shown in figure 3.1.

Figure 3.1. β-carotene containing film samples prepared on quartz slides. The rectangle is the area that was examined by the UV-vis spectrophotometer for photodegradation.

3.3.3. Thickness measurement

A JEOL JSM-5610 scanning electron microscope (SEM) and an XE100 atomic force microscope (AFM) (Park Systems Inc., CA) were used to examine the thickness of the films.

3.4. Results

3.4.1. Photostabilization of indigo and MB in solution

Cuvette test on indigo and MB combining with three different stabilizers, BHT, BQ, and TEA, was performed and the results are shown in figure 3.2.

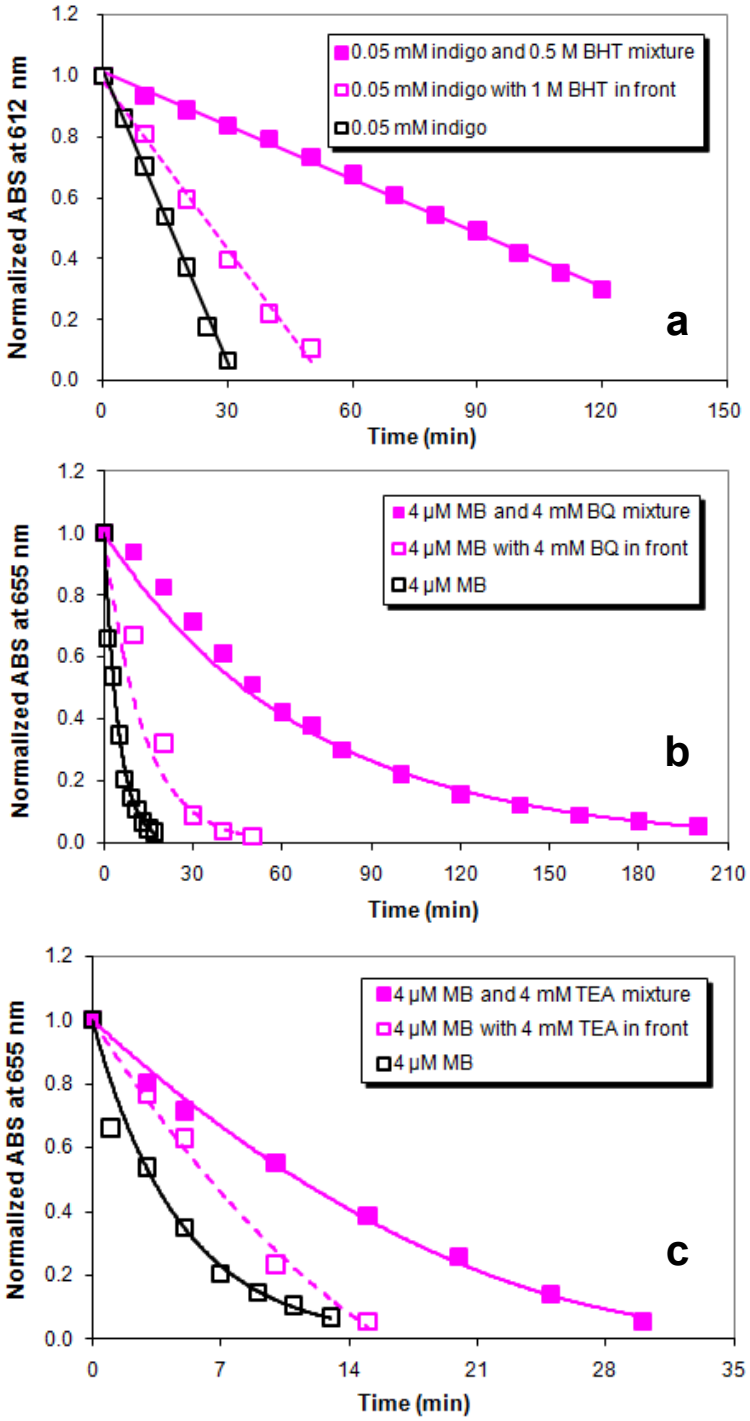

Figure 3.2. Photodegradation profiles of different dyes in solution with stabilizers in one or two separate cuvettes. **(a)** Indigo and BHT in DMF (UV light filtered at a cut-off wavelength 270 nm); **(b)** MB and BQ in ethanol and; **(c)** MB and TEA in ethanol.

Both types of dyes exhibit slower photodegradation when mixed with the stabilizer than when they remained a distance away from the stabilizer. The enhanced photostability is apparently due to the close spatial proximity between the dye molecules and the stabilizer molecules.

The photodegradation of indigo and MB in solution follows different kinetic routes (figure 3.3.), i.e. zero order kinetics for indigo and 1st order for MB, regardless the presence of stabilizer. The photodegradation rate constants obtained from these plots are summarized in Table 3.1.

Dye/Stabilizer System	**Rate Constant**		
	Dye alone	**Dye with stabilizer in front**	**Dye/stabilizer mixture**
Indigo/BHT (DMF) *	0.0315	0.0189	0.0057
MB/TEA (ethanol) **	0.205	0.171	0.0809
MB/HQ (ethanol) **		0.0753	0.0148

Table 3.1. Experimentally determined photodegradation rate constants of different dye/stabilizer combinations in solution. *The rate constant unit for this system is mM/s; ** The rate constant unit for these systems is 1/s.

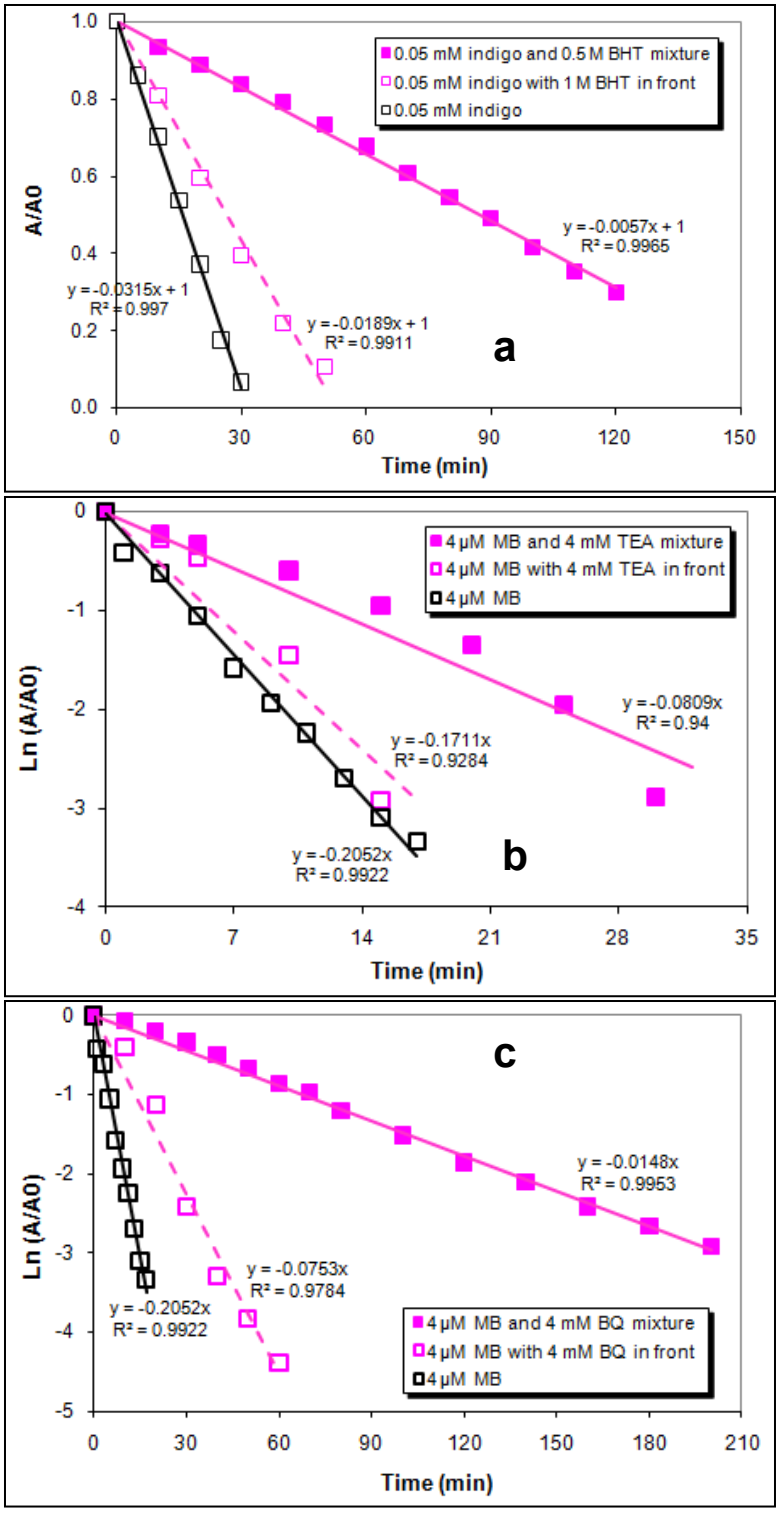

Figure 3.3. Photodegradation kinetics of different dyes in solution with stabilizers in one or two separate cuvettes. **(a)** Indigo and BHT in DMF (UV light filtered at a cut-off wavelength 270 nm); **(b)** MB and BQ in ethanol and; **(c)** MB and TEA in ethanol.

3.4.2. Film thickness

The thickness measurement of a typical polymer film made by the dipping process is shown in figure 3.4. AFM scans and SEM imaging appear to be agreed with each other. The thickness of the cover layer of the dual-layer films was also measured the same way and turned out to be in a range of 1.3 to 3 μm. Besides, the thickness of such polymer films varied according to the polymer concentration and solvent used in the initial dipping solution. These results indicate that by tuning the preparation conditions the dipping process may allow us to prepare films of micron or submicron thick.

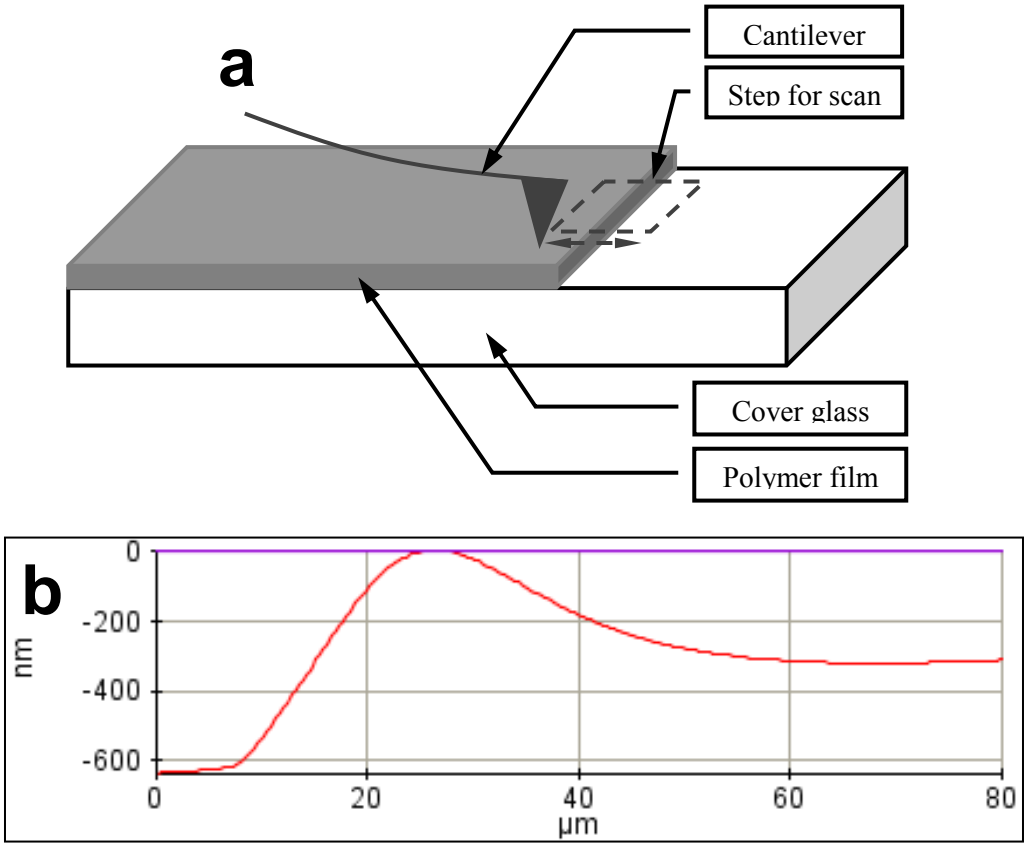

Figure 3.4. Schematic of AFM scan for thickness measurement. **(a)** The dashed parallelogram indicates the scan area, while the double arrow indicates the scan direction. Thickness of polymer films measured by **(b)** AFM scan and **(c)** SEM imaging: β-carotene/PMMA films made from the 1 mM β-carotene in 5 wt% PMMA/toluene solution.

3.4.3. Photostabilization of MB in films

The photodegradation kinetics of MB in single- and dual-layer films with TEA as the stabilizer is shown in figure 3.5. First of all, the photodegradation of MB in films follows 1st order kinetics, regardless the presence of TEA. More importantly, the single-layer films that contain both the dye and the stabilizer show a slower degradation than either the single-layer films with the dye alone or the dual-layer films where the dye and the stabilizer are isolated and in distance. In contrast, the dual-layer films do not seem to provide any protection on MB photodegradation. Besides, increasing the TEA/MB molar ratio from 1000:1 to 3000:1 in the single-layer films further enhances the MB photostability, as indicated by the further lowered rate constant.

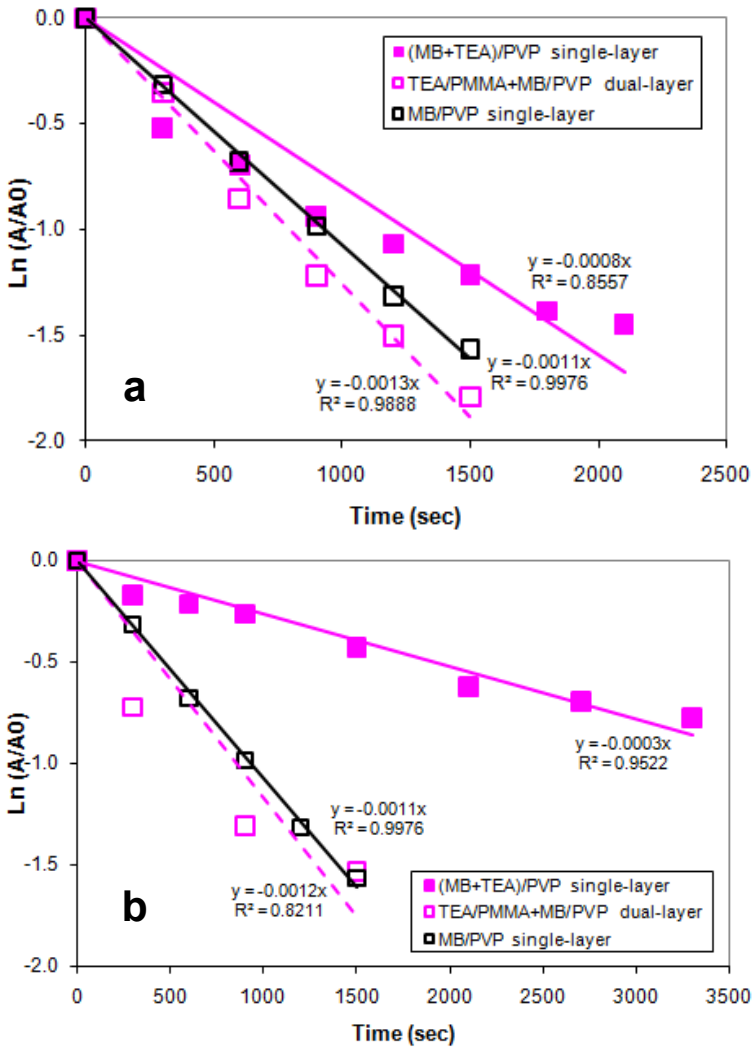

Figure 3.5. Photodegradation kinetics of MB in single- and dual-layer films in absence or presence of TEA. MB/PVP single-layer films were made from a 10 % PVP/ethanol solution that contains 1 mM MB; (MB+TEA)/PVP single-layer films were made from a 10 % PVP/ethanol solution that contains **(a)** 1 mM MB and 1 M TEA or **(b)** 1 mM MB and 3 M TEA. TEA/PMMA+MB/PVP dual-layer films were made from a 3 wt% PMMA/toluene solution that contains **(a)** 1 M TEA or **(b)** 3 M TEA as the cover layer, and a 10 wt% PVP/ethanol solution that contains 1 mM MB as the base layer.

3.4.4. Additional dye/stabilizer combinations

Photodegradation of β-carotene/BHT, β-carotene/α-tocopherol, and β-carotene/oxybenzone were also performed in solution and/or in films, yet no proximity effect was observed in any of these systems. On the other hand, it was found that the photodegradation of β-carotene in single-layer films as a function of stabilizer: β-carotene molar ratio follows a pattern (figure 3.6.). The three types of stabilizers behave quite similarly in providing protection on β-carotene degradation in the single-layer films and 100:1 molar ratio appears to be a critical point at which a significant level of stabilization begins to take place.

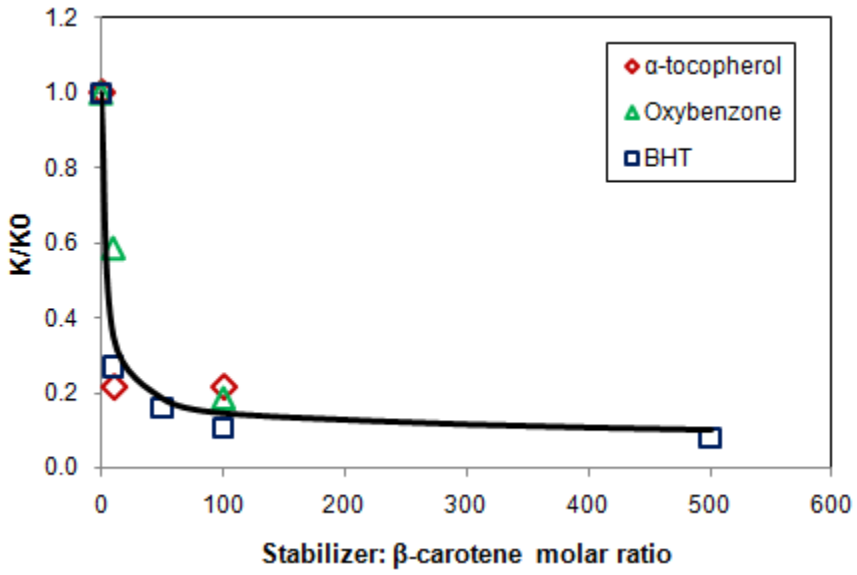

Figure 3.6. Change in β-carotene photodegradation rate constant as a function of stabilizer. β-carotene molar ratio in single-layer films made from 1 mM β-carotene and varied stabilizer types and concentrations in 5 wt% PMMA/toluene solution.

3.5. Discussion

These results clearly show that high levels of BHT (a phenolic antioxidant) stabilize indigo *via* a proximity effect in solution and that MB is stabilized by both benzoquinone (a UV absorber) and TEA (an excited state quencher). In films we have

been able to show that TEA stabilizes MB. Neither indigo nor BQ is amenable to dissolution in the polymers. As a result, no data is available for indigo/BHT or MB/BQ in films. The single- and dual-layer film tests are able to distinguish between UV absorption effects where the dye is protected by screening and any effects that could be attributed to free radical trapping or excited state quenching where the compounds need to be in proximity.

Although particular stabilizers are regarded as acting through one mechanism, it is very likely that the mechanisms of action will be mixed at these very high concentrations of stabilizer. It must also be remembered that diffusional motion is very limited in polymer films and this would be expected to significantly reduce the effectiveness of free radical traps in the solid films. Excited state quenchers, however, depend on very close proximity between the stabilizer and dye and this would be especially effective if the two molecules formed an intermolecular complex.

3.6. Conclusion

We have shown that very high levels of stabilizers can slow photodegradation of natural dyes both in solution and in polymer films. We postulate that this may be part of the role of antioxidants in fruit skins and suggest that this approach might be applied to stabilization of natural dyes in commercial systems.

3.7. Acknowledgments

This work is funded by the National Science Foundation (NSF, CBET # 0755926). We are grateful to Dr. Dapeng Li for taking the lead; working on the photodegradation profile and kinetics. We also thank Dr. Chen-Lu Yang, Mr. Nandula

Wanasekara, and Dr. Vijaya Chalivendra at the University of Massachusetts Dartmouth for their help in the UV-vis measurement and AFM scan.

3.8. References

1 Scott, G. PHOTODEGRADATION AND PHOTOSTABILIZATION OF POLYMERS. *Journal of Photochemistry* **25**, 83-90 (1984).

2 Wiles, D. M. & Carlsson, D. J. PHOTOSTABILIZATION MECHANISMS IN POLYMERS - A REVIEW. *Polymer Degradation and Stability* **3**, 61-72 (1980).

3 Heller, H. J. & Blattmann, H. R. Some aspects of stabilization of polymers against light. *Pure and Applied Chemistry* **36**, 141-162 (1973).

4 Mckellar, J. F. & Allen, N. S. (Applied science publishers LTD, 1979).

5 Scott, G. ANTIOXIDANT ROLE OF UV STABILIZERS. *Pure and Applied Chemistry* **52**, 365-387 (1980).

CHAPTER 4

UNIFORM POLYMER SUNSCREEN PARTICLES FOR THE PROTECTION OF ULTRAVIOLET SENSITIVE MOLECULES

4.1. Abstract

Ultraviolet (UV) radiation can cause significant degradation of skin, pharmaceuticals, paints, dyes and other materials. Previous work has shown that encapsulation of UV sensitive molecules or proximity to protective molecules can provide effective protection from the degradation caused by photo-oxidation. This study explores the protection capacity of polymeric particles containing both UV sensitive and UV protective materials. β-carotene was studied as a model ultraviolet sensitive biomolecule in order to determine the dependence of UV photostability on the composition of uniform polymer particles containing protective molecules. Particles were exposed to UV radiation via a UV lamp and the amount of β-carotene remaining was measured using an Ultraviolet/Visible Spectrophotometer. Common sunscreen agents (i.e. UV absorbers) such as oxybenzone, avobenzone, and octyl-4-methoxycinnamate and the antioxidant vitamin E (alpha-tocopherol) were selected for the model protective molecules. Each protective substance was examined alone and in several combinations. Oxybenzone and avobenzone were found to provide the most protection from photo-oxidation when used singly, and both absorbers provided the best protection overall when

paired with vitamin E, preserving over 80% of the unexposed signal intensity after 60 minutes of exposure. In contrast, combinations of absorbers with oxybenzone did not show a synergistic effect, likely due to photosensitization. Finally, varying the polymer matrix between PMMA and the biocompatible polymer PLGA yielded nearly identical results.

4.2. Introduction

Increased exposure to sunlight has been shown to cause damage to many materials, including human skin, pharmaceuticals, paints, and textiles. As a result, protection from sunlight, specifically ultraviolet (UV) radiation, has become a topic of increasing interest. Methods for protecting ultraviolet sensitive materials from photo-oxidation include physically shielding the material from light (as with clothing shielding skin), physical blockers such as titanium dioxide that scatter light, and chemical absorbers that absorb the radiation and emit it at a lower frequency.

In the short term exposing the skin to UV radiation may cause erythema. Long term exposure has been linked with the rise in incidents of skin cancer[1]. Exposure of skin to UV light depletes the antioxidant defenses of the skin[2], increasing the risk of skin cancer[3] due to DNA alterations[4]. Numerous academic and industrial studies focus on skin protection. Books and articles have been published on sunscreen mechanisms[5-9], regulations[5,7], vehicles[10], and increasing sun protection through diet[11]. Sunscreen regulation is a continuing concern; in June 2011 the United States Food and Drug Administration released new guidelines regarding UVA testing and sunscreen labeling that must be implemented by June 2012.

Clothing comprised of modified or coated fabrics have been created to protect human skin from exposure to UV light. Derivatives of the UV absorber monochlorotriazine have been applied to cotton using the exhaust method, which increased UV protection while only minimally altering the whiteness of the fabric[12]. Zinc oxide and titanium oxide (often found in sunscreens) have been used to coat cotton, polyester, and a cotton-polyester blend, which has been effective in increasing the UV protection of the fabric[13]. The natural dyes *Rheum* and *Lithospermum erythrorhizon* have been shown to have similar effectiveness to the UV absorber benzophenone, absorbing approximately 80% of UV rays[14]. Characteristics of a fabric also lend to the amount of UV protection they provide. Increasing fabric thickness increases UV protection, darker colors protect skin more than lighter colors, and different fabrics offer different levels of protection. For example, synthetic fabrics are more protective than natural fabrics[15].

Pharmaceuticals are also affected by possible exposure to sunlight. The International Conference on Harmonisation, a body whose aim is to establish international pharmaceutical guidelines, has released procedures for testing the photostability of new drug products, ICH Q1B. Many drugs are sensitive to light and have a tendency to photodegrade[16], which causes a decrease in available drug and an increase in potentially hazardous decay products. The formulation and manufacture of a drug product has been shown to also affect its photostability[17]. For these reasons there have been many studies determining processes for estimating the photostability of new drugs. High-performance Liquid Chromatography following exposure to light[18], Ultraviolet Visible Spectrophotometry (UV/Vis) to determine molar extinction coefficients[19], and exposure to light followed by UV/Vis measurements[20] are all proposed

methods for determining drug photostability. Pharmaceutical excipients are also at risk for photostability issues; for example the sustained release properties of a polyethylene oxide matrix are compromised after extended exposure to UV light[21].

Automotive paints require protection from UV rays since they are often exposed to long periods of sunlight. Methods to track and/or quantify the photo-oxidation occurring in paints are challenging. Time-of-flight secondary mass spectrometry has been used to detect which layers of paint undergo photo-oxidation[22]. Ultraviolet microspectroscopy can be used on the complete paint system, measuring how much absorber is left in each layer of paint[23]. Computational models have also been compiled to estimate the effect of UV and weather on automotive clear coats[24]. One method to improve weatherability of the coatings includes adding titanium dioxide nanoparticles modified with aminopropyl trimethoxy silane to polyurethane coatings[25].

Encapsulation of a UV sensitive material in a polymer matrix can provide some UV protection due to light scattering[26,27] and restriction of movement due to lack of available free volume[28]. UV absorbers, the type of materials often used in sunscreens, are another means of protection from UV light[29]. A combination of both methods should offer superior protection for materials prone to degradation from exposure to UV light[30]. It has also been found that a particle containing protective materials of different mechanisms, for example a UV absorber and an antioxidant, increased the photostability of both the UV absorber and antioxidant[31]. Polymer films containing UV protective materials have also been shown to provide UV protection[32]. This study explores the protection capacity of polymeric particles containing both UV sensitive and UV protective materials.

The decay of beta-carotene when exposed to UV light has been well documented due to its inclusion in the human diet and UV protective properties as an antioxidant when located in the skin[33,34]. Beta-carotene located in the skin acts as a natural defense against UV light, such that abnormally low concentrations of beta-carotene in the skin have been linked to skin cancer as well as precancerous lesions[34]. Even in other cancers, such as breast cancer, beta-carotene oxidation products have been found to inhibit cancer cell growth[35]. The wealth of information available on beta-carotene and its oxidative decay makes it a prime candidate for determining how much protection can be provided by the proposed particles. The products[36-39] and mechanisms[36,37,40,41] of beta-carotene decay by photo-oxidation have been determined repeatedly in previous studies.

Four sunscreen agents were used in this study to protect beta-carotene from degradation due to UV exposure. Three of the sunscreen materials (oxybenzone, octyl-4-methoxycinnamate (OMC), avobenzone) utilized are classified as "ultraviolet absorbers." These materials provide protection by absorbing the light to prevent it from reaching an ultraviolet sensitive material. The fourth materialis vitamin E (alpha-tocopherol), an antioxidant, which protects by eliminating the free radicals produced by exposure to ultraviolet light. Free radicals encourage oxidation, or the breakdown of the UV sensitive substance.

UV absorbers protect substances from UV light by absorbing the energy before it reaches the sensitive material. All three absorbers used have an aromatic ring, which aids in stabilizing an excited molecule by delocalizing the additional energy[6]. The absorber molecule can then emit the excess energy three different ways, depending on the amount of energy. Low energies can be emitted as heat, moderate energies can be given off by

fluorescence, and high energies dissipate by causing a photochemical reaction[7]. Heat and fluorescence are the preferred mechanisms for emitting the excess energy. Photochemical reaction usually leads to degradation of the UV absorber, loss of effectiveness, and the potential to create toxic byproducts.

One of the ways the human body defends itself against oxidation, such as that from UV radiation, is by maintaining a blood plasma concentration of vitamin E. Vitamin E is known as a chain-breaking antioxidant, meaning it intervenes in the propagation reactions of oxidation. In this mechanism the vitamin E lends its hydrogen atom to the radical of the substance it is protecting, becoming a radical itself that is stabilized by resonance. Vitamin C has been found to restore the vitamin E radical to its original state by giving it a hydrogen atom, allowing it to continue to protect the body[42]. Vitamin E has even been shown capable of protecting organisms as a sunscreen by topical application in cream form[43].

Many UV protective systems are designed to be protective on a macro scale, such as sunscreens being formulated to be spread across the skin. This work focuses on UV protection provided on a molecular scale by encapsulating small amounts of a UV sensitive substance with UV protective substances. The protection provided is limited by the amount of materials that can be contained within the particle. Further proof is also provided that encapsulation alone can offer enhanced photostability[26,27,44], especially when photoprotective mechanisms are combined[31]. Beyond simply photostabilizing sunscreens, the goal of this study is to utilize the methods of encapsulation and proximity to a UV stabilizer to protect a UV sensitive material within a particle. Encapsulating a UV sensitive molecule with a UV absorber or an antioxidant increased the amount of

material left undegraded after exposure to UV radiation. A combination of two absorbers did not enhance the protection, but an absorber and antioxidant combination offered considerable UV protection.

4.3. Experimental

4.3.1. Production of uniform particles

Uniform particles composed of a polymer (poly(methyl methacrylate) (PMMA)), a light sensitive material (β-carotene), and a UV absorber (oxybenzone, octyl-4-methoxycinnamate (OMC), avobenzone) or antioxidant (vitamin E) were synthesized using the solvent evaporation method. The solvent evaporation method, specifically that utilizing an oil-in-water (O/W) emulsion as implemented in this study, has been extensively reviewed by O'Donnell and McGinity[45]. Briefly, 3 milligrams of β-carotene, 0.2 grams of PMMA, and varied amounts of a UV absorber were dissolved in 3 milliliters of toluene. This oil phase was blended into an aqueous solution containing 0.05 wt% poly(vinyl alcohol) (PVA) (a surfactant) at 15000rpm using an Ultra-Turrax T 25 basic (IKA). This process created an O/W emulsion. The emulsion was stirred overnight at least 16 hours at approximately 200rpm on a magnetic stir plate to allow the toluene to move from the emulsion droplets into the aqueous phase before evaporating out of the mixture entirely. The particles were collected by centrifuging for 10 minutes at 10000rpm and disposing of the supernatant. Fresh deionized water was added and the pellet was resuspended by sonication. The result of the process is spherical particles with an average size of approximately 900 nanometers (found using Zetasizer Nano ZS90, Malvern Instruments) in diameter (figure 4.1a) whose composition is determined by the materials

dissolved in the oil phase. Bright field images of the particles were taken using an Olympus IX81 confocal microscope and are shown in figure 4.2.

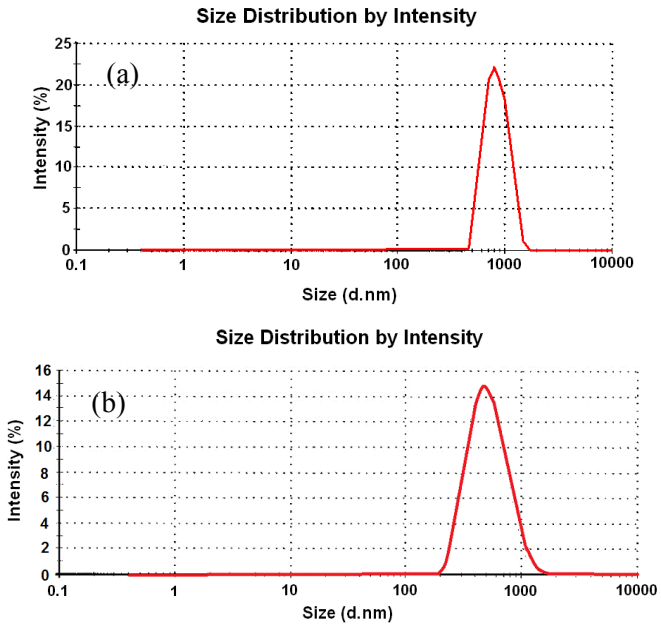

Figure 4.1. Particle size distributions **(a)** particles made of PMMA, β-carotene, and 0.03g oxybenzone and **(b)** particles made of PLGA (50:50) and β-carotene.

Similar particles made of poly(lactic-co-glycolic acid) (PLGA), a copolymer of polylactic acid (PLA) and polyglycolic acid (PGA), were examined for comparison between PMMA and a biocompatible polymer. A 50:50 ratio of PLA:PGA was explored, along with a 75:25 ratio. The solvent evaporation method was again used, this time in a similar process to that reported by Ito *et al.*[46]. The main difference between these two procedures is the solvent (chloroform for PLGA) and evaporation time (four hours instead of overnight). The PLGA particles had an average size of approximately 460 nanometers in diameter (figure 4.1b).

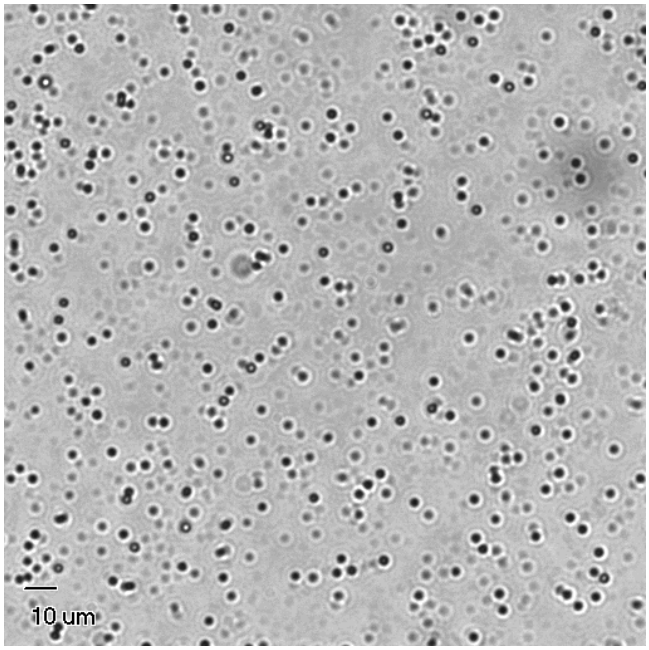

Figure 4.2. β-carotene and PMMA particles. Image taken with an Olympus IX81 confocal microscope.

It appeared that almost all of the highly hydrophobic β-carotene and absorbers were encapsulated inside of the particles. After centrifuging, the remaining supernatant was only a faint orange color characteristic of a very low concentration of β-carotene. Moreover, particles are assumed to be uniform due to use of the solvent evaporation method. The oil phase from which the particles are made is a homogeneous solution, and therefore the droplets in the emulsion are also homogeneous. The leaching of the solvent into the aqueous phase is not likely to cause the β-carotene, polymer, and absorber to segregate within the droplets since they are all hydrophobic. As long as the droplet composition remains homogeneous during the transition to solid form, the assumption that the product is uniform particles is valid.

4.3.2. Particle exposure to UV light and analysis using UV/Vis

Particles suspended in deionized water were diluted to the micromolar range for β-carotene before exposure to UV light. The suspensions contained approximately 19 μM of β-carotene, that is the suspension contained enough particles to equal the β-carotene content of a 19 μM solution. It is evident from figure 4.3a that protection provided by encapsulation alone is mostly due to light scatter and not absorption, since PMMA absorbs very little light. The spectrum of the UV lamp (365nm Pen Ray Mercury Lamp by UVP) along with the absorbers' spectra are shown in figure 4.3b. Dilution assured that light reached most particles and that the absorption peaks were within the operating range of the UV/Vis (Lambda XLS+ by PerkinElmer). A quartz cuvette with a 10.00 millimeter path-length was used for exposures and UV/Vis. The cuvette was filled with 3.7mL of particle suspension and placed in the center of an opaque box, approximately 2 centimeters from the UV lamp described. The particles were exposed for predetermined amounts of time, ranging from 0 to 60 minutes.

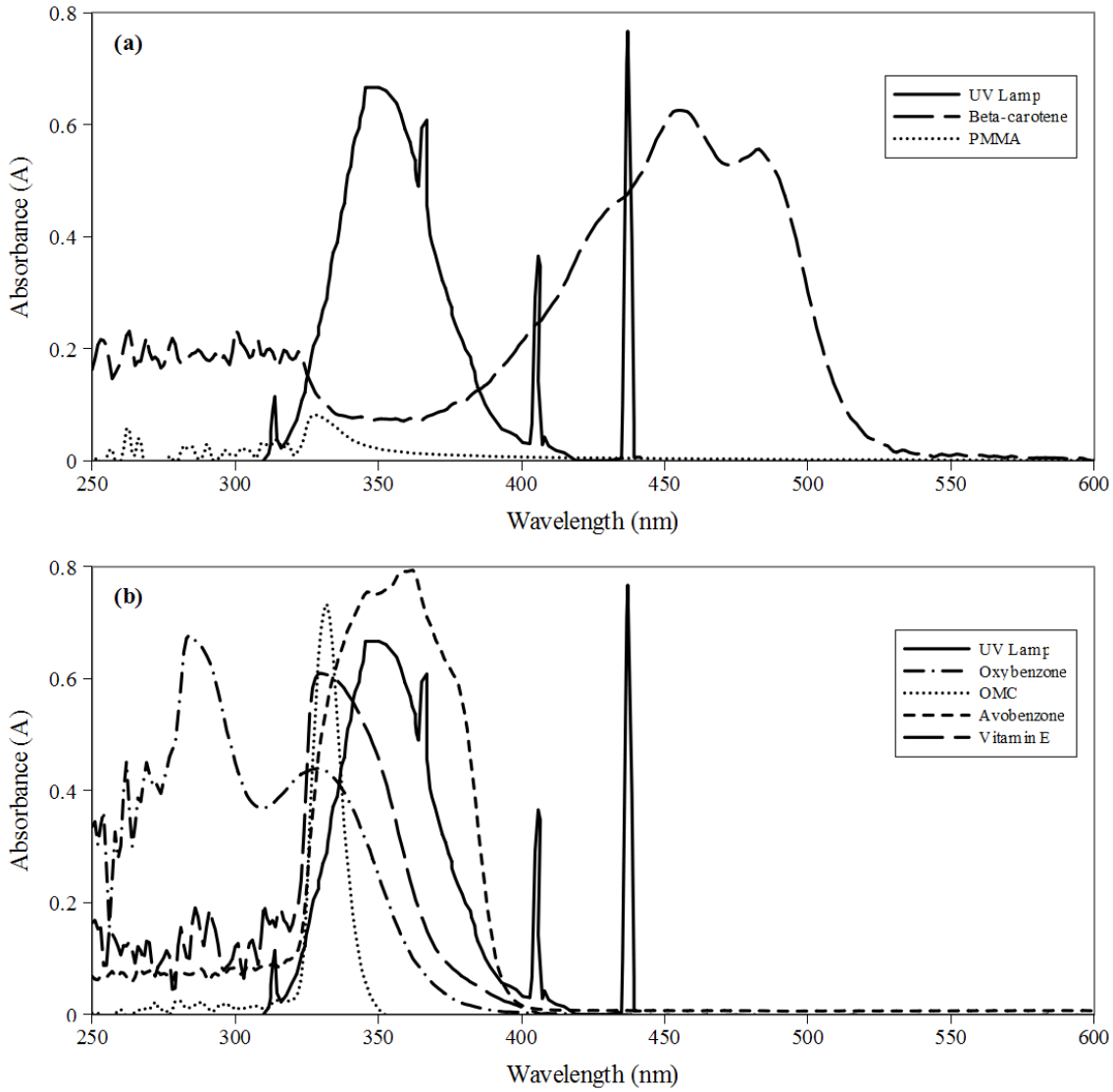

Figure 4.3. Spectra. **(a)** the UV lamp, β-carotene, and PMMA; and **(b)** the UV lamp, oxybenzone, OMC, avobenzone, and vitamin E.

4.3.3. UV/Vis spectra

β-carotene has three recognizable absorbance peaks as seen in figure 4.3b, the middle and most prominent occurring at approximately 465nm. The UV/Vis results are extremely concentration dependent. As β-carotene is exposed to ultraviolet radiation and the amount of β-carotene that has not undergone photodegradation decreases, the

absorbance peaks decrease also. This method allows for the degree of β-carotene decay to be quantified.

After exposure to the UV lamp, particles were centrifuged at 10000rpm and resuspended in Triton X-100 in preparation for UV/Vis measurements. As with the particle exposures, the Triton X-100 suspensions also contained 19 μM β-carotene. Triton X-100 was used to match the refractive index of the PMMA and PLGA. The particles were sonicated to disperse the pellet. Pure Triton X-100 was used as a blank (reference) sample. The middle β-carotene peak was noted for each exposure time, the baseline intensity was subtracted, and then the peak height was normalized with the 0 minutes exposure reading.

4.3.4. Decay of β-carotene in solution

A solution of beta-carotene in acetone similar in concentration to the solutions of particles was exposed to UV light and the decay mapped. The solution was placed into a quartz cuvet and capped for exposure to minimize evaporation. Evaporated acetone was replaced to ensure consistent concentrations. Data from the UV/Vis was collected and analyzed in the same manner as the particles, except with acetone as a blank (reference) sample.

4.4. Results and discussion

4.4.1. β-carotene decay

Previous studies have shown that encapsulation alone can decrease the decay rate of an UV sensitive material when exposed to UV light[26,27,44]. For comparison, a series of exposures of a solution of β-carotene in acetone were analyzed and compared to the

decay of β-carotene encapsulated in a PMMA particle (figure 4.4). β-carotene in solution underwent complete decay in 22 minutes, whereas β-carotene encapsulated in PMMA reached a plateau of approximately 80% degradation after 30 minutes and maintained the plateau to the 45 minutes exposure mark. This data supports similar findings by Perugini *et al*[26]. As shown in figure 4.3a, PMMA slightly absorbs UV radiation as well. The decay curves can be fit fairly well by a single exponential function to obtain an average decay rate constant.

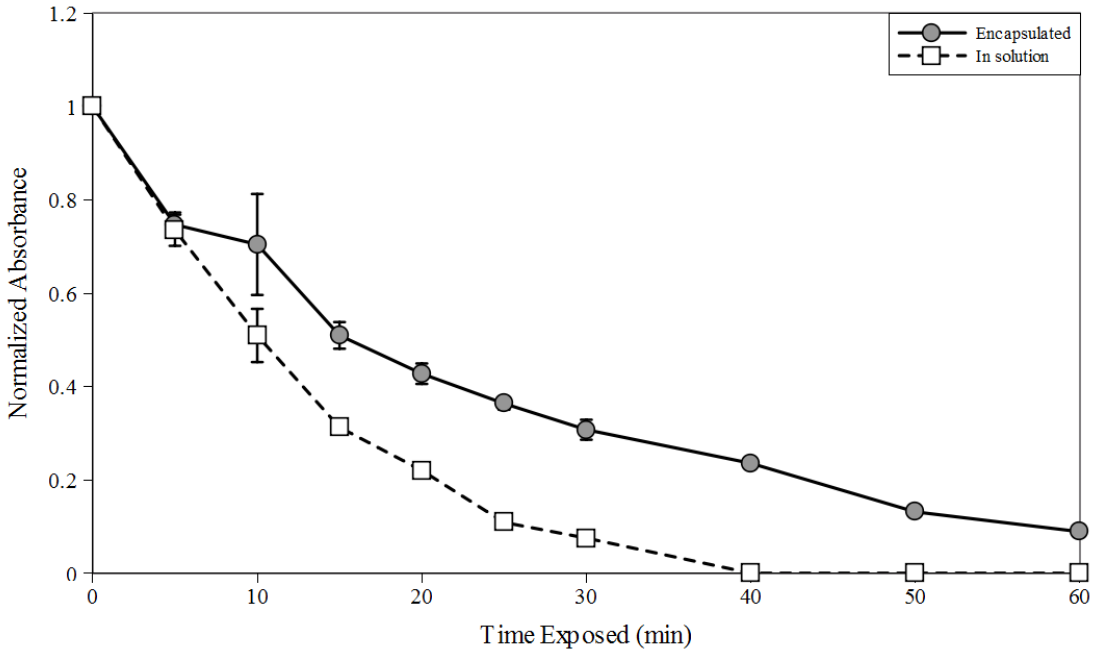

Figure 4.4. Decay of beta-carotene shown through normalized absorbance with respect to time, both encapsulated (in PMMA) and not encapsulated.

β-carotene encapsulated in PMMA was used as a comparison for all particles containing a UV absorber or antioxidant. A decay of the β-carotene spectrum can be seen in figure 4.5. As mentioned previously, the absorbance peaks decrease as the particles are exposed to UV light. Both figures 4.4 and 4.5 also exhibit the trend that the most rapid rate of decay takes place early in the exposure.

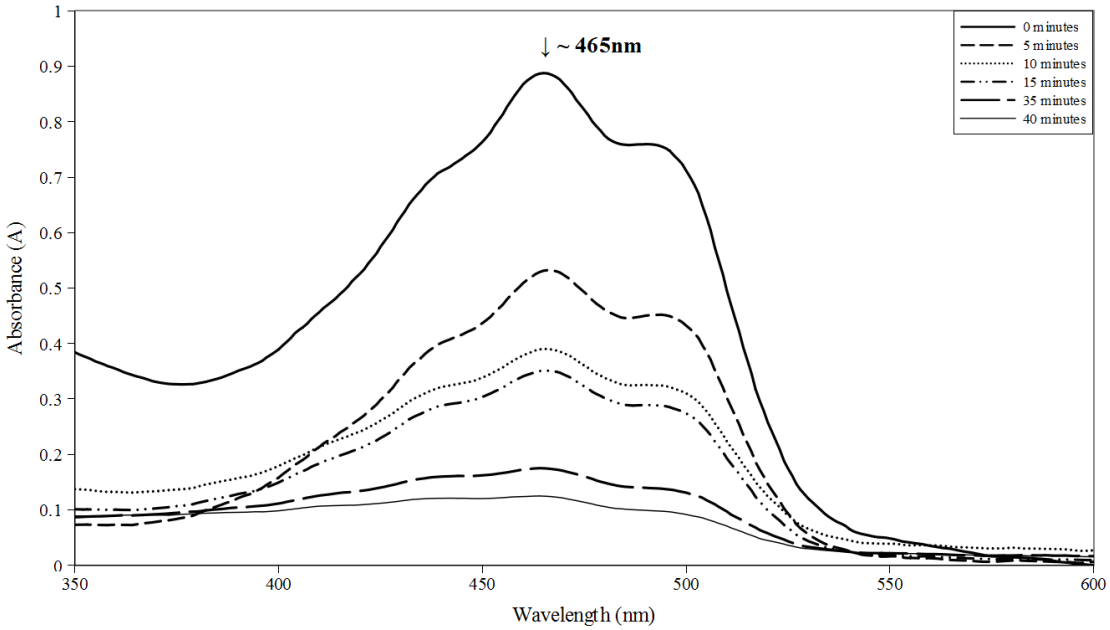

Figure 4.5. The decay of the β-carotene absorbance spectrum when β-carotene is encapsulated in a polymer matrix made up of PMMA and exposed to UV light.

4.4.2. Effect of UV protectants individually

Decay of β-carotene when paired with a UV absorber or antioxidant was found to be dependent on the UV protective species, and the absorber concentration (or spacing between the β-carotene and absorber molecules). Effectiveness of the absorbers or antioxidants was examined both singly and with a second absorber or antioxidant by a comparison of decay charts. Each single absorber or antioxidant was also analyzed by comparing the absorbance of β-carotene at certain times for each concentration, and by calculating the rate constants of decay. Error bars were determined by three data points for all concentrations of oxybenzone and for each absorber or antioxidant when 0.03 grams of absorber were used to make the particles. These points were chosen to estimate the error for all concentrations and all absorbers and antioxidants.

β-carotene decay when coupled with each absorber or antioxidant singly is shown in figure 4.6. Oxybenzone and avobenzone (figures 4.6a and 4.6c, respectively) were

found to be the most effective absorbers especially in high concentrations, leaving approximately 70% of β-carotene intact after 60 minutes of exposure. OMC (figure 4.6b) offered little to no protection, so that beta-carotene concentrations after 60 minutes of exposure were similar to those of β-carotene encapsulated alone in all cases. The ineffectiveness of OMC may be due to its instability when exposed to UVA and UVB light[8]. Vitamin E (figure 4.6d) showed protective capabilities, especially at the highest concentration, when approximately 50% of β-carotene was left after an hour of UV exposure.

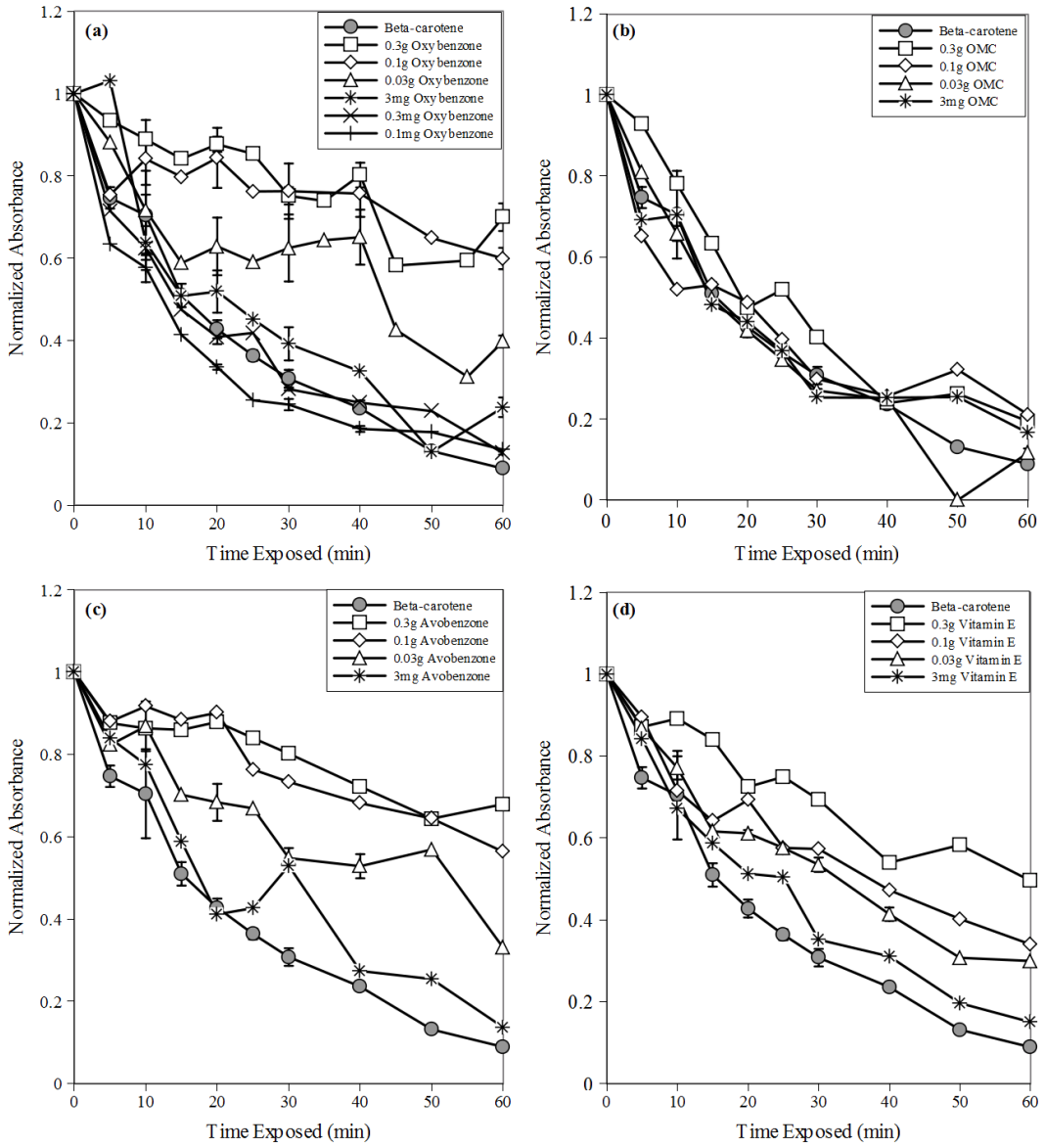

Figure 4.6. β-carotene decay when encapsulated in a PMMA polymer matrix with **(a)** oxybenzone, **(b)** OMC, **(c)** avobenzone, or **(d)** vitamin E.

4.4.3. Effect of protectant concentration

The decay of all particles was dependent upon the protectant concentration with the exception of OMC, whose decay curves appear in a cluster. The largest two concentrations of oxybenzone, particles made with 0.3 grams and 0.1 grams of the

absorber, are very close in decay and final percentage of β-carotene left intact. The similarity of the decay curves corresponding to the two highest concentrations suggest that a plateau is reached where additional absorber will not offer additional UV protection either because the β-carotene molecules are already surrounded by protective molecules or because the particle is not able to encapsulate any additional material since the polymer amount is fixed. Very small concentrations of oxybenzone were shown to have the same protective capacity as β-carotene protected by encapsulation alone. Avobenzone displayed similar behavior to oxybenzone. The dependence of vitamin E on concentration was more gradual, as each increase of concentration was matched with an increase in protection, with the highest concentration providing the best protection.

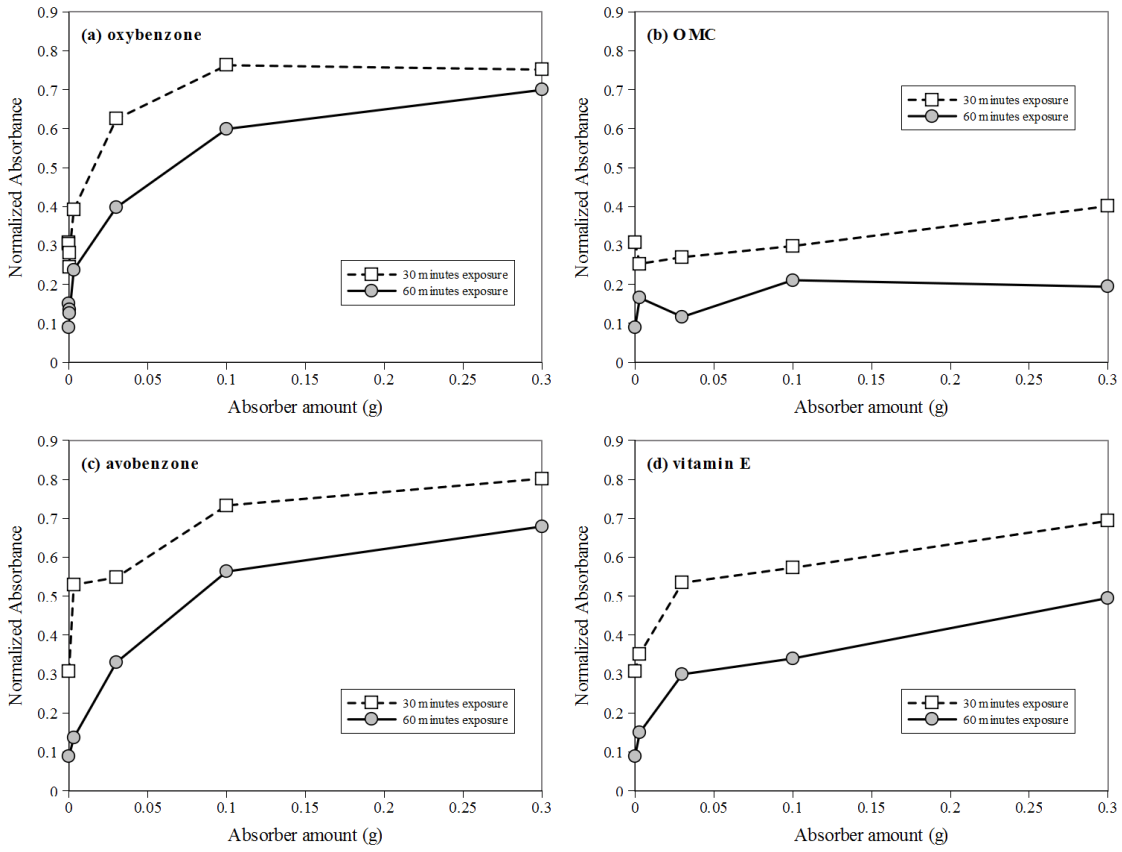

Figure 4.7. The effect of protectant amount by comparing the absorbance at different times when β-carotene and PMMA particles also contain **(a)** oxybenzone, **(b)** OMC, **(c)** avobenzone, or **(d)** vitamin E.

While the decay curves themselves give some insight on concentration effect, a comparison between amount of absorber and absorbance, such as in figure 4.7, provides a clearer picture. As mentioned previously, the decay curves for the two largest oxybenzone concentrations overlap. In figure 4.7a the absorbance at 30 minutes exposure stays almost constant between the two highest concentrations of oxybenzone, and there is only a slight difference at 60 minutes. All of the protectants except OMC behave in a similar fashion, where the initial increase in concentration is very beneficial, while there is a plateau after the absorber amount of 0.1 grams. No clear trend can be found in the OMC case (figure 4.7b). In most cases it is desired to have the greatest effect for the smallest amount of material, and it can be determined from figure 4.7 that 0.1 grams of protectant would be ideal in such a case, given 3 mg of β-carotene.

4.4.4. Effect of polymer matrix

The results from individual protectants in PMMA particles were compared to those of a biocompatible polymer, PLGA. Figure 4.8 shows the comparison of particles made of the two polymers. The particles containing only β-carotene appear in the lower cluster of curves, while particles containing both β-carotene and oxybenzone can be seen in the upper group of curves. All polymers showed similar effectiveness; approximately 40% of the beta-carotene is left non-degraded after an hour using each of the polymers with oxybenzone.

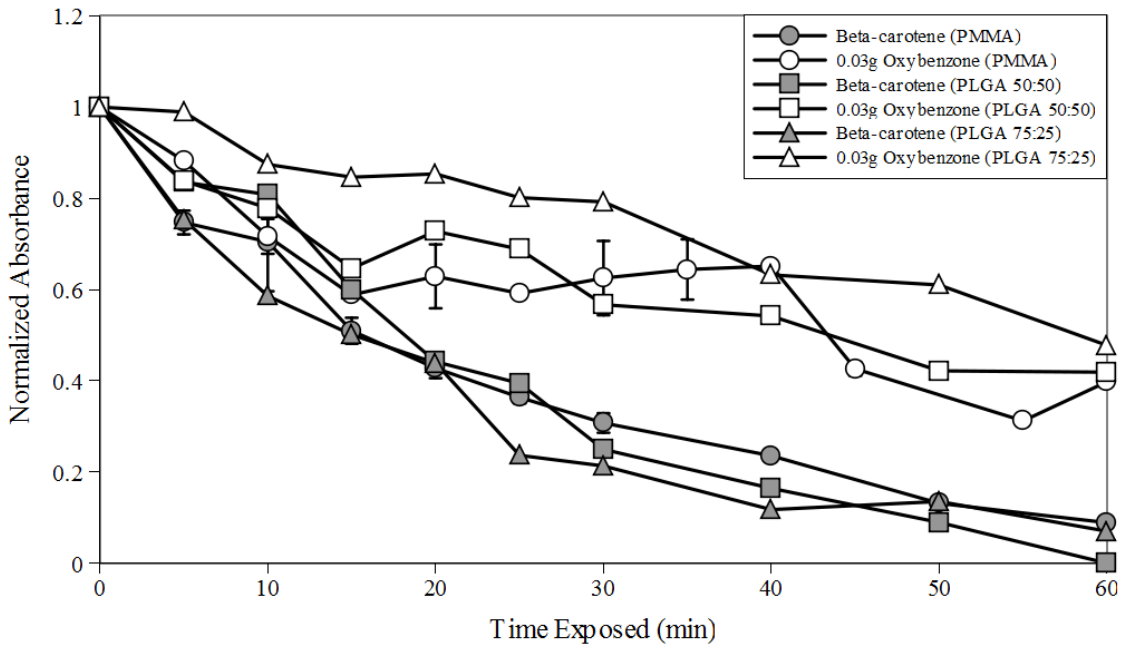

Figure 4.8. A comparison between the UV protection of PMMA, PLGA (50:50), and PLGA (75:25) polymer matrices when β-carotene or β-carotene and 0.03g oxybenzone are added.

4.4.5. Effect of multiple UV protectants

Oxybenzone and vitamin E were chosen for use as stabilizers to determine whether a combination of protectant species would be more beneficial than a single absorber or antioxidant. Absorber combinations are often used in sunscreens to increase the sun protection factor (SPF), while an absorber and antioxidant combination has already been found to be effective in increasing photostability when encapsulated[31]. Each combination was made with 0.03 grams of an absorber along with 0.03 grams of either oxybenzone or vitamin E; the decay profiles are shown in figure 4.9. The addition of oxybenzone had a neutral or negative impact on the protection provided by particles containing another absorber or antioxidant, which was opposite of expectations. The

combination of OMC and oxybenzone (figure 4.9a) offered little to no protection in comparison to β-carotene alone in a polymer particle. The absorbance curve of avobenzone as a single absorber mimics the absorbance curve of the combination of avobenzone and oxybenzone, indicating that the addition of oxybenzone offered no extra protection (figure 4.9b). Oxybenzone has been shown to sensitize other molecules when in a polar environment [8], such is the case with these particles. The increased UV sensitivity of the additional absorber can explain the minimal increase of protection when oxybenzone is paired with another absorber.

Adding vitamin E to particles containing an absorber was advantageous in every case, reducing the decay rate and increasing the amount of β-carotene remaining after 60 minutes of UV exposure. This enhanced photostability agrees with what has been found previously for encapsulated absorber and antioxidant combinations[31]. The combinations of vitamin E with oxybenzone and avobenzone (figures 4.9c and 4.9e, respectively) have the least decay of any particles examined and both show improvement over the absorbers alone. Approximately 80% β-carotene is left intact in both cases after 60 minutes of exposure, which rivals larger concentrations of one protectant alone. The addition of vitamin E also increases the protection offered by particles containing OMC (figure 4.9d), which is consistent with the idea that OMC stability is an important requirement for effective UV protection. The most likely explanation for the behavior of absorber-vitamin E combinations is that the vitamin E and absorber particles utilize two different methods of UV protection, that of an absorber and an antioxidant, and the two mechanisms complement each other, leading to a synergistic protective effect.

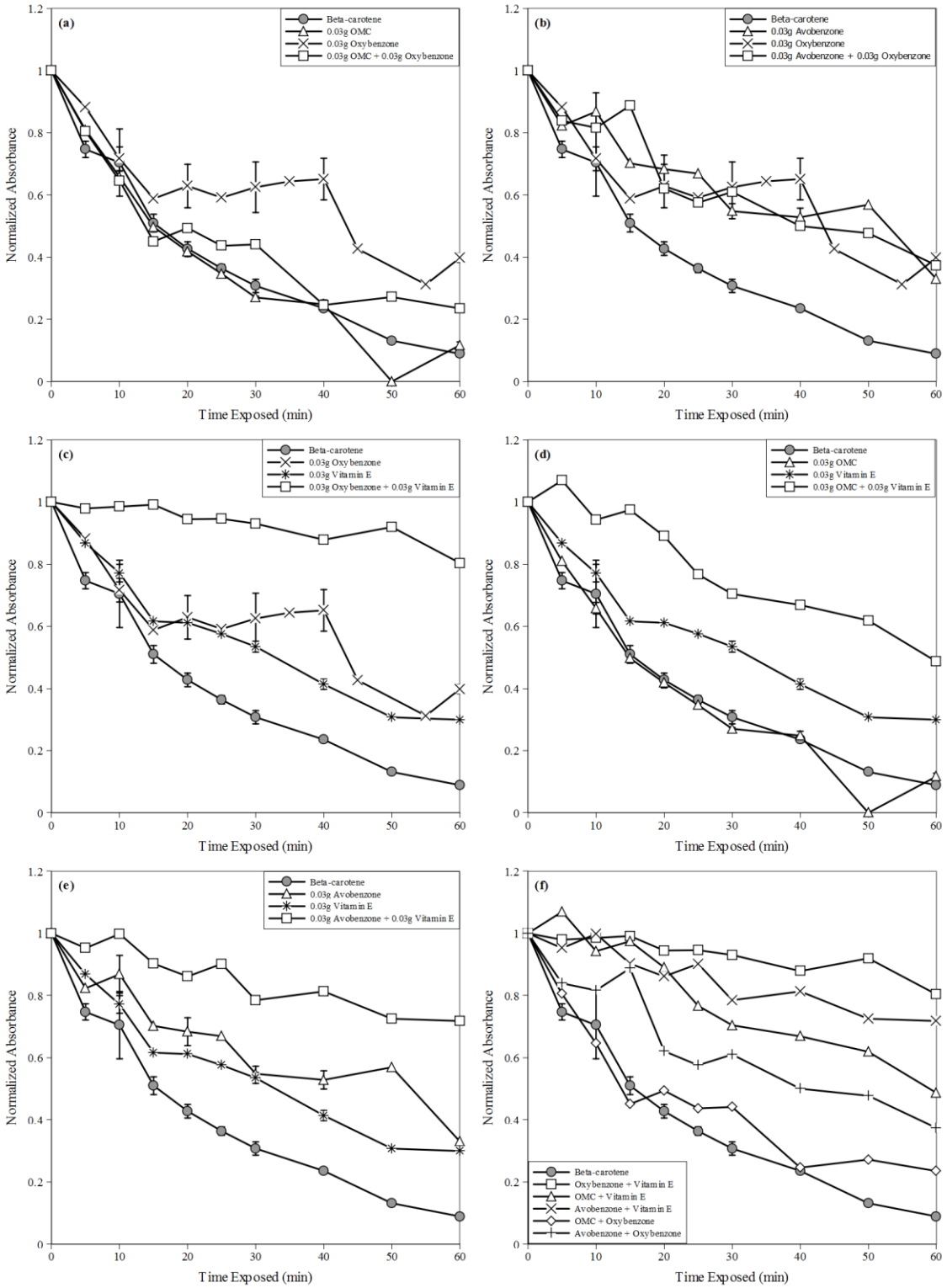

Figure 4.9. β-carotene decay profiles when two protectants are used such as **(a)** OMC and oxybenzone, **(b)** avobenzone and oxybenzone, **(c)** oxybenzone and vitamin E, **(d)** OMC and vitamin E, **(e)** avobenzone and vitamin E, and **(f)** all combinations.

4.4.6. Decay Rate Constants

Decay rate constants were calculated to quantitatively compare the decay in each case, assuming a single exponential decay. Rate constants were determined by plotting the natural log of the normalized absorbance versus the exposure time, the slope of each line being the rate constant. The rate constant for β-carotene encapsulated alone was used to normalize all of the curves. Figure 4.10 compares the ratio of β-carotene and absorber amount to the ratio of the rate constants, while table 4.1 provides the rate constants numerically. This plot confirms the minimal change noted earlier when absorber amount increases above the 0.1 grams mark. Figure 4.10 also confirms that avobenzone and oxybenzone offer the most protection, followed closely by vitamin E. OMC, which offered little to no protection as seen in the decay curves, does not adhere to the trend put forth by the other absorbers in that the addition of more absorber offers more protection. The fluctuation of the OMC rate constants confirms that it is not a good choice of absorber in this application.

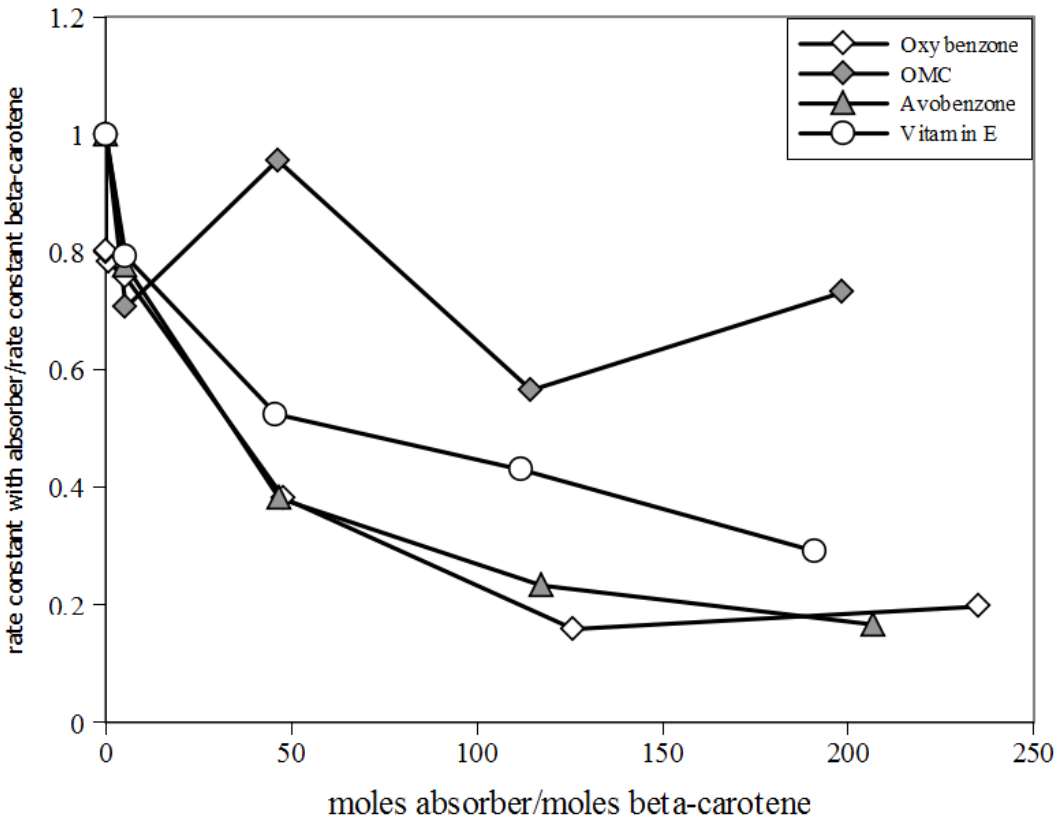

Figure 4.10. Ratio of the rate constants when an absorber is added and the rate constant of β-carotene in polymer particles and the affect of the corresponding ratio of amount of absorber and amount of β-carotene.

Decay Rate Constants		
Material	**Amount (g)**	**Rate constant (s^{-1})**
β -carotene (not encapsulated)	0.003	-1.5E-03
β -carotene (encapsulated)	0.003	-6.5E-04
Oxybenzone	0.3	-1.3E-04
	0.1	-1.0E-04
	0.03	-2.5E-04
	0.003	-4.9E-04
	0.0003	-5.1E-04
	0.0001	-5.2E-04
	0.00001	-5.2E-04
OMC	0.3	-4.8E-04
	0.1	-3.7E-04
	0.03	-6.2E-04
	0.003	-4.6E-04
Avobenzone	0.3	-1.1E-04
	0.1	-1.5E-04
	0.03	-2.5E-04
	0.003	-5.1E-04
Vitamin E	0.3	-1.9E-04
	0.1	-2.8E-04
	0.03	-3.4E-04
	0.003	-5.2E-04
Combinations		
Oxybenzone + OMC	0.03g each	-3.9E-04
Oxybenzone + Avobenzone		-2.6E-04
Oxybenzone + Vitamin E		-5.2E-05
OMC + Vitamin E		-2.1E-04
Avobenzone + Vitamin E		-9.8E-05

Table 4.1. Rate constants for particles of each composition.

4.4.7. Determining spacing between beta-carotene and UV absorber

The distance between particles can be approximated using a body-centered cubic unit cell model because the amount of absorber molecules is significantly larger than that of the β-carotene in most cases. In this model one β -carotene molecule is placed at the center of the unit cell and it is surrounded by 8 protectant molecules, each situated at a corner. To calculate the distance, the overall particle volume is first established by

summing the individual volumes of the protectant, PMMA, and β-carotene, based on the known mass added and literature values of the density. The particle volume is divided by the number of absorber molecules, which is determined through the use of the absorber's mass, molecular weight and Avogadro's number. This value is then multiplied by 8, the number of absorber molecules found in each unit cell, and the product is raised to the 1/3 power to determine the length of the cube's side. Finally, the distance between beta-carotene and absorber molecules is found by multiplying the cube's length by $\sqrt{3}/2$. The complete process is demonstrated in Equation 1 below[29].

$$\left\{\left[\frac{Mass_{PMMA}}{\rho_{PMMA}}+\frac{Mass_{Beta-carotene}}{\rho_{Beta-carotene}}+\frac{Mass_{\mathrm{Pr}otectant}}{\rho_{\mathrm{Pr}otectant}}\Big/\frac{Mass_{\mathrm{Pr}otectant}}{MW_{\mathrm{Pr}otectant}}\times Avogadro's\#\right]\times 8\right\}^{1/3}\times\frac{\sqrt{3}}{2}$$

(1)

It is also possible to estimate β-carotene to β-carotene proximity without absorbers present through geometric relationships. The procedure is akin to the method described earlier. However, in this model a simple cubic unit cell structure, is applied and the distance is determined by calculating the length of the unit cell's edge.

$$\left\{\left[\frac{Mass_{PMMA}}{\rho_{PMMA}}+\frac{Mass_{Beta-carotene}}{\rho_{Beta-carotene}}+\frac{Mass_{\mathrm{Pr}otectant}}{\rho_{\mathrm{Pr}otectant}}\Big/\frac{Mass_{Beta-carotene}}{MW_{Beta-carotene}}\times Avogadro's\#\right]\times 8\right\}^{1/3}$$

(2)

4.4.8. Effect of spacing

Spacing calculations were completed as described above, except in the cases where there were fewer absorber molecules than β-carotene molecules (the extra dilute data points for oxybenzone). In such cases, the unit cell was inverted to have eight β-carotene molecules around one absorber molecule. Spacing is proportional to absorber amount, and therefore provided similar information to previous data, as shown in figure 4.11. Once again, oxybenzone, avobenzone, and vitamin E show similar trends while OMC exhibits an unclear trend. For oxybenzone, avobenzone, and vitamin E at small spacing, each rate constant varied approximately linearly with the separation distance. However the extra oxybenzone points (at absorber amounts less than 3 milligrams) show that when the distance between a β-carotene molecule and an absorber molecule is in excess of 5 nanometers, UV protection is limited. When the distance between β-carotene and the protectant is above 5 nanometers, the β-carotene is not near enough in proximity for the protective mechanism to reach the molecule.

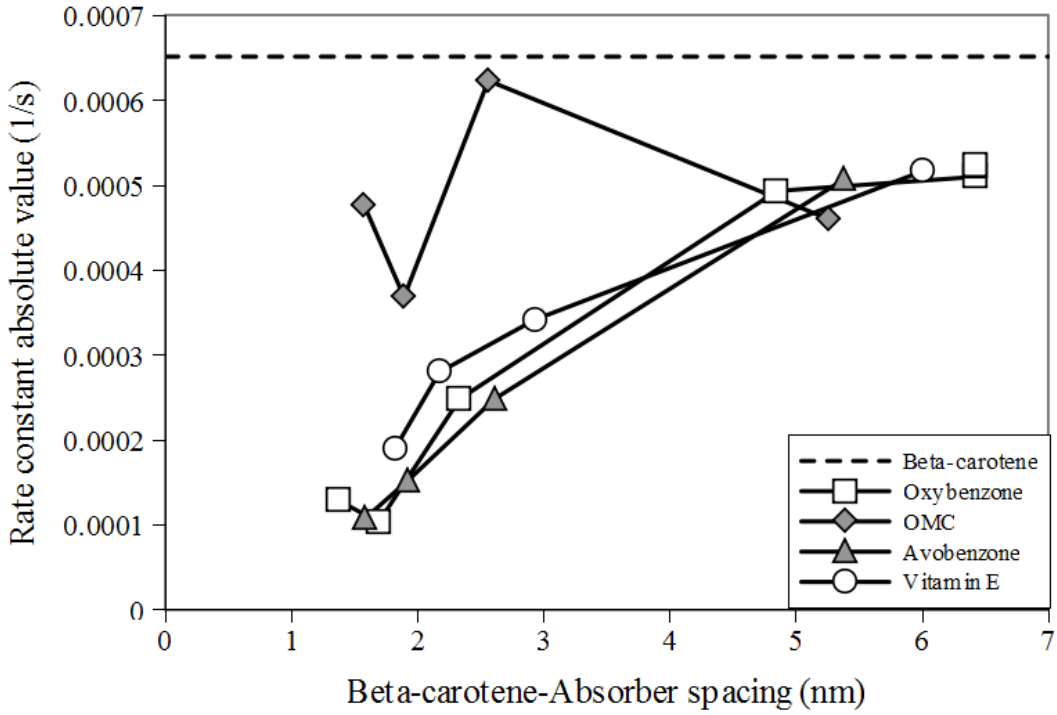

Figure 4.11. The relationship between the rate constant and the spacing between β-carotene and the absorbers.

4.5. Conclusion

Encapsulation of β-carotene, a UV sensitive substance, with UV protective molecules in a polymer matrix was determined to be an effective method of protection from UV light. β-carotene was chosen as the sensitive molecule since its photodegradation is well mapped. Oxybenzone, OMC, and avobenzone were selected as UV absorbers and used along with vitamin E, an antioxidant. Particles were exposed to ultraviolet light and then were suspended in Triton X-100 so that their UV/Vis absorbance spectra could be collected. Decay curves and rate constants revealed the extent of UV protection. Oxybenzone and avobenzone provided sufficient protection, followed by vitamin E. OMC provided only minimal protection in all cases. A plateau in absorber concentration was also observed, where addition of more absorber after 0.1

grams (~50-100 moles absorber per mole β-carotene) offered no increase in protection. Absorber-absorber and absorber-antioxidant combinations also provided UV protection. Oxybenzone sensitized the absorbers it was paired with, leading to equal or less protection than that of the absorber alone. Vitamin E increased protection in all cases, likely due to the complementary effect of two distinct protection mechanisms, light absorption and free radical trapping. The vitamin E combination with oxybenzone and avobenzone provided the best protection overall. It was also noted that the spacing between β-carotene and the protective molecule had a significant effect on protection. Spacing of less than 5 nanometers offered adequate protection while spacing above 5 nanometers offered little protection.

This work can potentially provide guidelines to further protect materials sensitive to UV radiation. Sunscreens have been stabilized by encapsulation[26,27,44], but may be further stabilized by encapsulating with complementary materials such as a UV absorber and an antioxidant. Other photosensitive substances that can benefit from encapsulation with UV protective molecules include pharmaceuticals, dyes and pigments.

4.6. Acknowledgements

We gratefully acknowledge support provided by the National Science Foundation (NSF-CBET 1005778), Kristin Steeley and Nina Shapely at Rutgers University for taking the lead; their work creating the particles, collecting and analyzing results. We also thank the lab of Kathryn Uhrich at Rutgers University for use of the Zetasizer Nano ZS90.

4.7. References

1 Donaldson, M. R. & Coldiron, B. M. No End in Sight: The Skin Cancer Epidemic Continues. *Seminars in Cutaneous Medicine and Surgery* **30**, 3-5, doi:10.1016/j.sder.2011.01.002 (2011).

2 Shindo, Y., Witt, E., Han, D., Epstein, W. & Packer, L. Enzymic and Non-Enzymic Antioxidants in Epidermis and Dermis of Human Skin. *J Investig Dermatol* **102**, 122-124 (1994).

3 Diepgen, T. L. & Mahler, V. The epidemiology of skin cancer. *British Journal of Dermatology* **146**, 1-6, doi:10.1046/j.1365-2133.146.s61.2.x (2002).

4 Brash, D. E. *et al.* A role for sunlight in skin cancer: UV-induced p53 mutations in squamous cell carcinoma. *Proceedings of the National Academy of Sciences* **88**, 10124-10128 (1991).

5 Wolf, R., Tüzün, B. & Tüzün, Y. Sunscreens. *Dermatologic Therapy* **14**, 208-214, doi:10.1046/j.1529-8019.2001.01027.x (2001).

6 Gasparro, F. P. 194 (Springer-Verlag, Georgetown, Texas, 1997).

7 Lowe, N. J. & Shaath, N. A. in *Cosmetic Science and Technology Series* Vol. 10 624 (Marcel Dekker, New York, 1990).

8 Tarras-Wahlberg, N. *et al.* Changes in Ultraviolet Absorption of Sunscreens After Ultraviolet Irradiation. **113**, 547-553 (1999).

9 Kimbrough, D. R. The Photochemistry of Sunscreens. *Journal of Chemical Education* **74**, 51-null, doi:10.1021/ed074p51 (1997).

10 Chatelain, E., Gabard, B. & Surber, C. Skin Penetration and Sun Protection Factor of Five UV Filters: Effect of the Vehicle. *Skin Pharmacology and Physiology* **16**, 28-35 (2003).

11 Sies, H. & Stahl, W. NUTRITIONAL PROTECTION AGAINST SKIN DAMAGE FROM SUNLIGHT. *Annual Review of Nutrition* **24**, 173-200, doi:doi:10.1146/annurev.nutr.24.012003.132320 (2004).

12 Czajkowski, W., Paluszkiewicz, J., Stolarski, R., Kazmierska, M. & Grzesiak, E. Synthesis of reactive UV absorbers, derivatives of monochlorotriazine, for improvement in protecting properties of cellulose fabrics. *Dyes and Pigments* **71**, 224-230, doi:10.1016/j.dyepig.2005.07.004 (2006).

13 Zohdy, M. H., El Hossamy, M. B., El-Naggar, A. W. M., Fathalla, A. I. & Ali, N. M. Novel UV-protective formulations for cotton, PET fabrics and their blend utilizing irradiation technique. *European Polymer Journal* **45**, 2926-2934, doi:10.1016/j.eurpolymj.2009.06.018 (2009).

14 Feng, X., Zhang, L., Chen, J. & Zhang, J. New insights into solar UV-protective properties of natural dye. *Journal of Cleaner Production* **15**, 366-372, doi:10.1016/j.jclepro.2005.11.003 (2007).

15 Ghazi, S., Couteau, C. & Coiffard, L. J. What level of protection can be obtained using sun protective clothing? Determining effectiveness using an in vitro method. *Int J Pharm* **397**, 144-146, doi:10.1016/j.ijpharm.2010.06.022 (2010).

16 Albini, A. & Fasani, E. Photochemistry of drugs: An overview and practical problems. 1-73, doi:10.1039/9781847550712-00001 (1998).

17 Aman, W. & Thoma, K. The influence of formulation and manufacturing process on the photostability of tablets. *Int J Pharm* **243**, 33-41, doi:10.1016/s0378-5173(02)00110-2 (2002).

18 Abdel-Moety, E. M., Al-Rashood, K. A., Rauf, A. & Khattab, N. A. Photostability-indicating HPLC method for determination of trifluoperazine in bulk form and pharmaceutical formulations. *Journal of Pharmaceutical and Biomedical Analysis* **14**, 1639-1644, doi:10.1016/0731-7085(96)01778-5 (1996).

19 Henry, B., Foti, C. & Alsante, K. Can light absorption and photostability data be used to assess the photosafety risks in patients for a new drug molecule? *J Photochem Photobiol B* **96**, 57-62, doi:10.1016/j.jphotobiol.2009.04.005 (2009).

20 Zhan, X., Deng, Z., Yin, G. & Ma, B. Cumulative illuminometer and shelf life of drugs in daylight indoors. *Int J Pharm* **167**, 7-11, doi:10.1016/s0378-5173(98)00034-9 (1998).

21 Maggi, L. Photostability of extended-release matrix formulations. *European Journal of Pharmaceutics and Biopharmaceutics* **55**, 99-105, doi:10.1016/s0939-6411(02)00126-1 (2003).

22 Gerlock, J. L., Prater, T. J., Kaberline, S. L. & deVries, J. E. Assessment of photooxidation in multi-layer coating systems by time-of-flight secondary ion mass spectrometry. *Polymer Degradation and Stability* **47**, 405-411, doi:10.1016/0141-3910(95)00007-0 (1995).

23 Smith, C. A., Gerlock, J. L. & Carter, R. O. Determination of ultraviolet light absorber longevity and distribution in automotive paint systems using ultraviolet

micro-spectroscopy. *Polymer Degradation and Stability* **72**, 89-97, doi:10.1016/s0141-3910(00)00207-x (2001).

24 Bauer, D. R. Interpreting weathering acceleration factors for automotive coatings using exposure models. *Polymer Degradation and Stability* **69**, 307-316, doi:10.1016/s0141-3910(00)00074-4 (2000).

25 Mirabedini, S. M., Sabzi, M., Zohuriaan-Mehr, J., Atai, M. & Behzadnasab, M. Weathering performance of the polyurethane nanocomposite coatings containing silane treated TiO2 nanoparticles. *Applied Surface Science* **257**, 4196-4203, doi:10.1016/j.apsusc.2010.12.020 (2011).

26 Perugini, P. *et al.* Effect of nanoparticle encapsulation on the photostability of the sunscreen agent, 2-ethylhexyl-p-methoxycinnamate. *Int J Pharm* **246**, 37-45, doi:10.1016/s0378-5173(02)00356-3 (2002).

27 Koo, B.-M. *et al.* Encapsulation and Stabilization of Photo-Sensitive Antioxidants by Using Polymer Microcapsules with Controlled Phase Heterogeneity. *Macromolecular Rapid Communications* **29**, 498-502, doi:10.1002/marc.200700759 (2008).

28 Naito, T., Horie, K. & Mita, I. Photochemistry in polymer solids. 11. The effects of the size of reaction groups and the mode of photoisomerization on photochromic reactions in polycarbonate film. *Macromolecules* **24**, 2907-2911, doi:10.1021/ma00010a042 (1991).

29 Morabito, K. *et al.* Proximal effects of ultraviolet light absorbers and polymer matrix in the photostability of β-carotene. *Dyes and Pigments* **92**, 509-516, doi:10.1016/j.dyepig.2011.06.031 (2012).

30 Morabito, K., Shapley, N. C., Steeley, K. G. & Tripathi, A. Review of sunscreen and the emergence of non-conventional absorbers and their applications in ultraviolet protection. *International Journal of Cosmetic Science* **33**, 385-390, doi:10.1111/j.1468-2494.2011.00654.x (2011).

31 Weiss-Angeli, V. *et al.* Nanocapsules of Octyl Methoxycinnamate Containing Quercetin Delayed the Photodegradation of Both Components Under Ultraviolet A Radiation. *Journal of Biomedical Nanotechnology* **4**, 80-89, doi:10.1166/jbn.2008.004 (2008).

32 Li, D. *et al.* Stabilization of Natural Dyes by High Levels of Antioxidants. *Advanced Materials Research* **441**, 192-199 (2012).

33 Darvin, M. E., Gersonde, I., Albrecht, H., Sterry, W. & Lademann, J. In vivo Raman spectroscopic analysis of the influence of UV radiation on carotenoid antioxidant substance degradation of the human skin. *Laser Physics* **16**, 833-837, doi:10.1134/s1054660x06050148 (2006).

34 Hata, T. R. *et al.* Non-Invasive Raman Spectroscopic Detection of Carotenoids in Human Skin. **115**, 441-448 (2000).

35 Hu, X., White, K. M., Jacobsen, N. E., Mangelsdorf, D. J. & Canfield, L. M. Inhibition of growth and cholesterol synthesis in breast cancer cells by oxidation products of [beta]-carotene. *The Journal of Nutritional Biochemistry* **9**, 567-574, doi:10.1016/s0955-2863(98)00048-5 (1998).

36 El-Tinay, A. H. & Chichester, C. O. Oxidation of .beta.-carotene. Site of initial attack. *The Journal of Organic Chemistry* **35**, 2290-2293, doi:10.1021/jo00832a040 (1970).

37 Kennedy, T. A. & Liebler, D. C. Peroxyl radical oxidation of .beta.-carotene: formation of .beta.-carotene epoxides. *Chemical Research in Toxicology* **4**, 290-295, doi:10.1021/tx00021a005 (1991).

38 Stratton, S. P., Schaefer, W. H. & Liebler, D. C. Isolation and identification of singlet oxygen oxidation products of .beta.-carotene. *Chemical Research in Toxicology* **6**, 542-547, doi:10.1021/tx00034a024 (1993).

39 Yamauchi, R., Miyake, N., Inoue, H. & Kato, K. Products formed by peroxyl radical oxidation of .beta.-carotene. *Journal of Agricultural and Food Chemistry* **41**, 708-713, doi:10.1021/jf00029a005 (1993).

40 Burton, G. W. Antioxidant Action of Carotenoids. *The Journal of Nutrition* **119**, 109-111 (1989).

41 Foote, C. S. & Denny, R. W. Chemistry of singlet oxygen. VII. Quenching by .beta.-carotene. *Journal of the American Chemical Society* **90**, 6233-6235, doi:10.1021/ja01024a061 (1968).

42 Burton, G. W. & Ingold, K. U. Vitamin E: application of the principles of physical organic chemistry to the exploration of its structure and function. *Accounts of Chemical Research* **19**, 194-201, doi:10.1021/ar00127a001 (1986).

43 McVean, M. & Liebler, D. C. Inhibition of UVB induced DNA photodamage in mouse epidermis by topically applied alpha-tocopherol. *Carcinogenesis* **18**, 1617-1622, doi:10.1093/carcin/18.8.1617 (1997).

44 Lee, J.-S., Kim, J.-W., Kim, J., Han, S.-H. & Chang, I.-S. Photochemical properties of UV-absorbing chemicals in phase-controlled polymer microspheres.

Colloid and Polymer Science **283**, 194-199, doi:10.1007/s00396-004-1122-3 (2004).

45 O'Donnell, P. B. & McGinity, J. W. Preparation of microspheres by the solvent evaporation technique. *Advanced Drug Delivery Reviews* **28**, 25-42, doi:10.1016/s0169-409x(97)00049-5 (1997).

46 Ito, F. *et al.* Study of types and mixture ratio of organic solvent used to dissolve polymers for preparation of drug-containing PLGA microspheres. *European Polymer Journal* **45**, 658-667, doi:10.1016/j.eurpolymj.2008.12.037 (2009).

CHAPTER 5

UNDERSTANDING UV PROTECTIVE MECHANISMS: KEY CONTRIBUTIONS

Conventional UV sunscreens are making way for novel UV protection techniques. Part one of this thesis began in chapter 1 by highlighting UV protective mechanisms and introducing various new approaches to UV protection, resulting in often more natural, safer methods of protection.

Our research explored this very topic, by understanding the mechanisms of UV protection in order to engineer new, safer sunscreens. In chapter 2, we started by exploring the relationship of UV absorber and photostabilizer to better understand the proximal relationship and its effect on transfer of excited state energy from absorber to photostabilizer. Our results gave us a better understanding on the minimum distance required absorber and photostabilizer for optimal photostability. In chapter 3, we explored the use of sensitive natural dyes paired with high concentrations of antioxidants, which gave us a better understanding of naturally occurring UV protection, such as the skin of a fruit protecting the flesh/core. Finally in chapter 4, we combined and applied the knowledge gained from the previous chapters. We explored the use of polymer nanoparticles for enhanced photostability of sensitive UV absorbers. Using nanoparticles we effectively reduced the proximity of the sensitive absorber to the photostabilizer and we also incorporated the antioxidant vitamin E for improved photostability.

In the future we would like to incorporate cultured keratinocytes and melanocytes into our UV protection assays. We would quantify the cell health and melanin produced for various absorber/photostabilizer combinations to learn more about the UV protection factor rather than just gaining knowledge about the photostability of the sunscreen. Overall, this research increases the general understanding of UV protective mechanisms and provides knowledge for future UV protective applications.

DISEASE DIAGNOSTICS

II

CHAPTER 6

INTRODUCTION

6.1. Relevance

In an ever evolving planet, new strains and sub-types of viruses are constantly sprouting increasing the demand for effective point-of-care (POC) disease diagnostics. Many areas of the world now require diagnostics to be used beyond the laboratory setting, in resource-limited-settings (RLS) so that patients in remote locations can receive the best diagnoses possible. Influenza and HIV diagnostic devices are widely used and developed because of their global importance. In this introduction first we detail the current detection and drug resistance monitoring (DRM) methods for HIV and then the current detection and sub-typing methods for influenza. At the end, we introduce a novel diagnostics assay to improve upon existing detection, DRM and sub-typing.

6.2. Background

6.2.1. Influenza background

Influenza is a widespread pathogen that results in approximately 36,000 deaths in the US [1] with the World Health Organization estimating 250,000-500,000 annual deaths worldwide [2]. Influenza has a variety of subtypes, which are classified by the antigenic subtype of hemagglutinin (H1-16) and neuraminidase (N1-9) expressed on the viral particles [3]. Seasonal influenza is caused by H1N1, H3N2, and H1N2 viruses [4], while highly pathogenic avian flu is caused by the H5N1 subtype [5]. A recurrent pandemic

influenza would result in millions of worldwide deaths [6]. Such a catastrophic event may be avoided if rapid point of care diagnostics were available to health workers at the source of the infection, such that they could contain the infection before it spreads into the global community [7,8]. Additionally, rapid diagnosis of influenza would prevent excessive antibiotic use, which leads to antibiotic resistant bacterial strains and is a large financial burden due to the extra cost of unnecessary treatment, hospitalization, and medication [9,10].

6.2.2. HIV background

HIV is a daunting global pandemic[11]. The development of resistance to antiretroviral medications is the main cause for treatment failure of HIV-infected individuals[12]. K103N, a point mutation of lysine to asparagine at position 103 of the HIV reverse transcriptase (RT), is the most common drug resistance mutation that causes high level resistance to first generation non-nucleoside reverse transcriptase inhibitors (NNRTIs), such as nevirapine and efavirenz[13]. HIV-infected patients receiving NNRTI-based treatment who harbor K103N will most likely fail therapy and will require alternative antiretroviral treatment[13]. Detection of K103N and other drug resistance mutations is of great importance, especially in resource-limited-settings (RLS), where NNRTI-based regimens serve as first-line treatments and subsequent options are limited[14]. A sensitive method to detect drug resistance in a small rural clinic with no advanced laboratory infrastructure or the use of a field deployable device to detect resistance with quick treatment are lacking, though extremely beneficial. Success of any field deployable device will depend on variables such as the cost per test, the need for specialized equipment, staff expertise, refrigeration of reagents during shipping and shelf

life. It would be beneficial if the device would also use minimal sample volume and provide excellent assay sensitivity. Presently available assays, some with significant strengths, do not meet all these considerations [15,16].

6.3. Current diagnostic assays

6.3.1. Current influenza diagnostics

A number of approaches have been investigated for influenza diagnostics, but each of these has associated limitations. Viral culture is specific and provides more viable virus for further testing [17], but it takes 3-14 days for a result, limiting its use for rapid diagnostics [18]. Immunospecific tests, such as rapid antigen tests and immunofluorescence microscopy, lack sensitivity and do not provide sequence specific information for subtyping [19]. Viral nucleic acid amplification and detection can generate subtype or strain specific information, but these tests are also complex and expensive. Polymerase Chain Reaction (PCR) requires expensive benchtop thermal cyclers and trained technicians [18].

6.3.2. Current HIV diagnostics

Various field deployable assays to detect HIV and/or measure its RNA levels (viral load; VL) are under development[20], although, to our knowledge, none incorporate drug resistance testing. For example, progress has been made on a device for HIV detection via immunoassay intended for resource limited settings (RLS)[21] and a successful antibody based HIV-1/2 test device has recently been granted FDA approval for at home use [22]. Many commercial HIV-1 detection and VL kits are currently available including the COBAS TaqMan assay (Roche), RealTime HIV-1 Assay (Abbot), and

Ultrasensitive p24 Assay (PerkinElmer) to name a few[23]. These kits utilize a variety of blood markers for detection and directly monitor VL by measuring HIV-1 RNA or indirectly by measuring p24 antigen, HIV antibodies or CD4 counts. However, none of these HIV detection devices and/or VL kits are capable of testing for drug resistant mutations.

Two main commercial HIV genotyping assays are available to monitor drug resistance, ViroSeq (Abbott) and TRUGENE (Siemens)[23-27]. ViroSeq is a PCR based DNA sequencing technique requiring a full scale ABI sequencer with multiple primers. It requires an initial preparation of a plasma sample using a viral RNA isolation kit, followed by RNA reverse transcription, DNA PCR amplification and sequencing amplified products using ViroSeq equipment in preparation for data analysis. This assay saves time by only genotyping the HIV protease and a segment of RT (codons 1-335), the most common HIV drug targets. Similarly, TRUGENE is an approved DNA sequencing based technique, targeting the protease and reverse transcriptase (codons 40 -247). Both methods require a HIV VL in the range of 2000 to 750,000 copies/mL[26,28] for successful amplification and resistance detection and both can detect K103N mutations in samples containing about 20 to 25% K103N variants[29]..

6.3.3. Disadvantages of current HIV diagnostic assays

Recent research-only assays have been developed to increase the sensitivity of resistance detection, which seems to be important for clinical care [30]. Such assays include next generation sequencing pyrosequencing[31], allele-specific PCR[28,32-34] and single genome sequencing[35], which can detect resistance mutations at levels as low as 0.1%. Despite high sensitivity, pyrosequencing and single genome sequencing are costly and

time consuming, requiring sequencing of multiple genomes; and allele-specific PCR is mutation specific and limited by occurrences of false negatives from nucleotide polymorphisms that can destabilize primer binding. Other novel approaches use ligation of probe molecules as an indicator of mutation detection[36]. Ligation amplification depends on two single stranded DNA probes hybridizing adjacently with a target mutation sequence, which could yield a specificity issue. In addition to PCR amplification, rolling circle amplification is also used in conjunction with this ligation approach[37]. These approaches have been shown to be effective and sensitive but may have limited functionality in diverse HIV-1 genomes because of the variability of target sequences, resulting in mismatch recognition and inherent copying error of the amplicon during PCR amplification[38], and loss of specificity. The aforementioned commercial and non-commercial techniques can sensitively detect HIV resistance mutations such as K103N, however they still require laboratory infrastructure and expertise, at times limited in RLS. Application of a new method in RLS will require comparable sensitivity to existing methods with reduction of duration of sample-to-result time and less equipment restrictions based upon the amplification technique.

6.4. Nucleic acid sequence based amplification (NASBA)

Most of the aforementioned drug resistance detection techniques depend upon polymerase chain reaction (PCR) or another form of temperature cycling. PCR requires expertise and equipment, and can be challenging when amplifying a small population of mutant viral sequences due to non-specific amplification. As an alternative, Nucleic Acid Sequence Based Amplification (NASBA), used in HIV VL testing can be faster than PCR for certain RNA amplification and compares favorably with PCR for HIV RNA

detection[23,39,40]. Since NASBA is an isothermal and exponential process, it avoids rapid degradation of enzymes and undesirable hybridization of participating nucleic acids [41]. NASBA also has its limitations; it can be limited by the secondary structure of RNA, making primer design and multiplexing difficult. Clinically relevant hybridization sites on long, RNA strands may require stringent oligonucleotide design, with only a small fraction of sequences hybridizing efficiently to RNA thus reducing the efficiency of the amplification process[42]. To combat these issues, NASBA usually begins with a 65°C heating step before the addition of enzymes to disrupt full-length RNA secondary structure[43]; and expose primer binding sites, typically 100-250 nucleotides apart, to avoid products with inhibitory secondary structure[44]. An additional disadvantage, is the fact that NASBA initiates with a non-cyclic reverse transcription phase resulting in a relatively long initial step[45]. NASBA has been used in a variety of non-commercial HIV-1 VL assays[40,46,47] and in commercially available kits such as the NASBA HIV-1 RNA QT amplification system[48] or the NucliSens HIV-1 QT[49] and its more rapid, convenient and reliable version, NucliSens EasyQ[50]. However the NASBA principle has not used in detection of drug resistant mutations.

6.5. Microfluidic assays using NASBA

Recently, diagnostic NASBA assays integrated with microfluidic systems have shown improvements over conventional benchtop techniques. These reactors decrease reagent use and further decrease energy consumption of the isothermal system by decreasing the reaction volume. Additionally, these small reaction volumes inherent in microfluidic chips (10nL - 2μL) concentrate the target molecule of interest to improve primer binding and reaction kinetics. A preliminary study showed the efficacy of small

(10-50nL) reaction volumes in silicon-glass reaction chamber [51], followed by a reactor containing 10 parallel 80nL chambers that filled using capillary action [52]. A final reactor design contained 11 parallel channels with two separate chambers for each heating step separated by hydrophobic burst valves. The second chamber included dehydrated enzymes, which were shown to function in a real-time NASBA reaction upon the addition of off-chip heated NASBA mix. Although the full reaction was not run on chip, the sample was purified off-chip, and the capillary loading resulted in the loss of sample, this study shows several advantages of a microfluidic diagnostic system. The reactor was made to be simple, multiplexed, automated, shelf-stable, and consume fewer reagents and energy than its benchtop counterpart [53]. Another assay integrated purification and amplification of RNA using a PDMS chamber reactor [54]. Two reactors were contained on one chip, which would allow two RNA samples to be simultaneously purified from bacterial lysate, mixed with reaction mix, heated, mixed with enzyme, and detected real-time using sequence-specific molecular beacons. Both systems show the ability of microfluidics to create a closed, efficient, automated system that would decrease technician time, human error, and potential for contamination. These papers show the viability and advantages of incorporating a microfluidic platform with NASBA.

6.6. Simple method for amplifying RNA targets (SMART)

Here we implement a new approach[55] for mutation detection, termed Simple Method for Amplifying RNA Targets (SMART), for the application of **(1)** influenza detection and subtyping and **(2)** HIV drug resistant mutation detection using the K103N mutation as our model. SMART is a significant deviation from currently used methods, namely PCR and NASBA, specifically focused on cost-constrained and low laboratory

infrastructure settings. SMART amplification and detection, which do not depend on target RNA variability, but rather on the specific hybridization of a small single stranded DNA probe, termed "SMART probe", is the basis of the new approach.

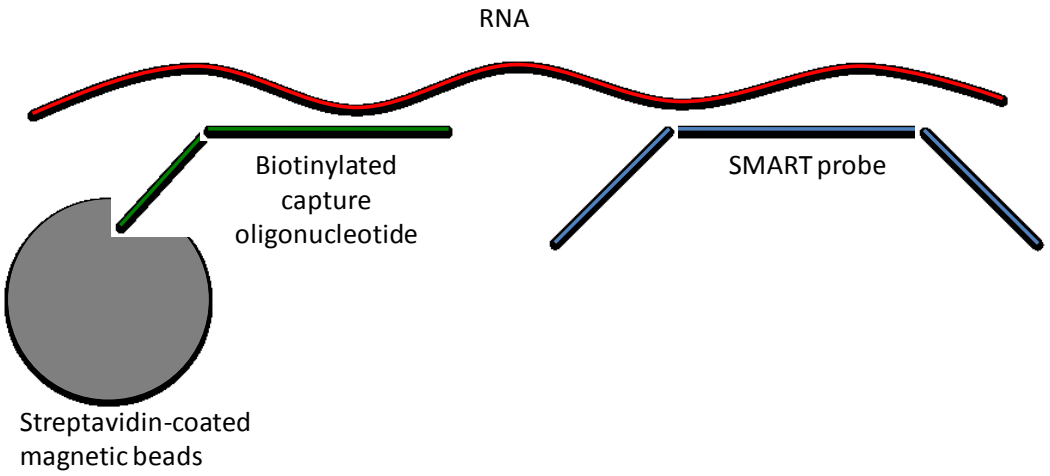

Figure 6.1. Key design elements of SMART. vRNA is captured on magnetic beads using a sequence specific biotinylated oligo. An amplifiable probe is also specifically captured on the RNA molecule, and beads are washed to remove unbound probe.

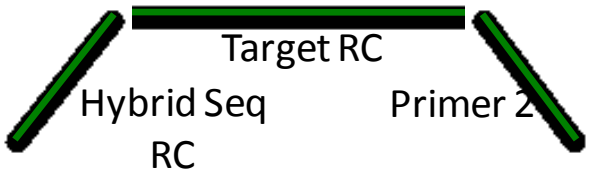

Figure 6.2. SMART probe design. The amplifiable probe includes a central sequence for vRNA hybridization and two ends for primer hybridization designed to minimize probe secondary structure.

The SMART probe is an engineered sequence (approximately 60-100 nucleotides) that anneals to the target RNA molecule centered at the location of the mutation. The last 20-40 nucleotides on either end of the probe, called the SMART probe "arms", are designed not to hybridize with the target RNA. These arms are adjustable as they are non-specific to the target RNA, allowing control over roughly two-thirds of the SMART probe sequence. This allows the use of these arms as flexible and specific

primers for efficient, sensitive amplification, that is not dependent on the target variability. The SMART probe can be engineered specifically to have favorable or unfavorable binding energies (e.g. ensuring it doesn't bind to other oligonucleotides in the mix). SMART requires only single time diffusion and binding of small molecules (SMART probes) into the RNA structure. Hence, diffusion is fast and less dependent on the RNA structure itself than in traditional NASBA. The amplification step of SMART uses an abridged version of NASBA, starting with the short SMART probe DNA template rather than the actual long RNA template. This crucial design feature completely eliminates the non-cyclic reverse transcription phase of NASBA and uses a very small amplicon (100 nucleotides) in comparison to traditional NASBA or PCR for amplifying RNA, resulting in faster and more accurate amplification and detection. SMART can be performed on a closed microfluidic chip device that utilizes isothermal heating in low temperature (41°C) without thermal cycling or preheating, thus driving cost down.

6.7. Details of SMART

SMART includes five chronological processes: (1) *Isolation* of sample RNA from a patient sample, (2) *Capture* of sample RNA onto magnetic beads and hybridization of SMART probes, (3) Microfluidic *separation* of bead bound RNA-SMART probe complex from free unbound probes, (4) *Amplification* of SMART probes using the abridged version of NASBA, and (5) Real time *detection* of probes. An overview of these processes is illustrated in figure 6.3 and detailed in the following sections, with the example of using SMART for the detection of the HIV-1 K103N mutation.

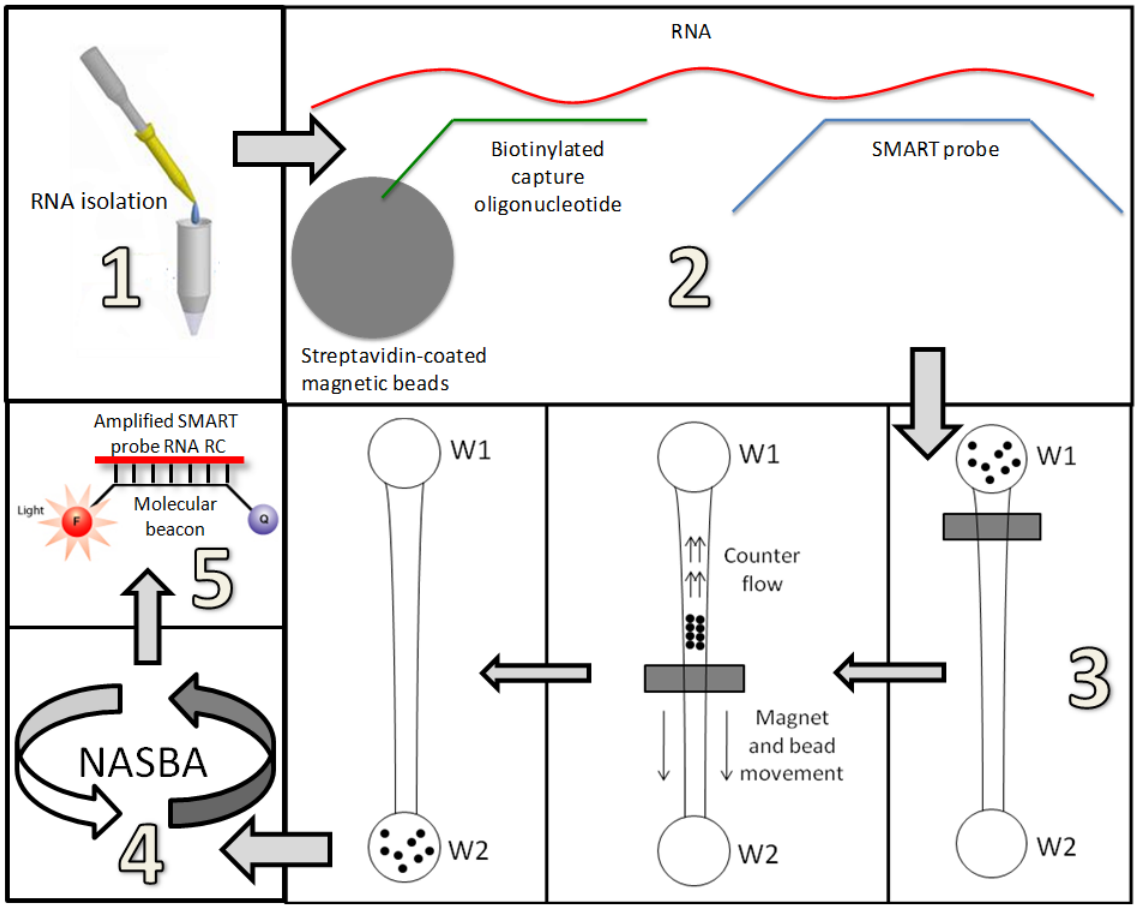

Figure 6.3. Overview of SMART from sample-to-result. 1) RNA sample is isolated from a clinical sample and put into a TE buffer solution. 2) Streptavidin coated beads conjugated with biotinylated capture oligonucleotides and SMART probes are added to the solution. 3) The solution is added to W1 of the SMART microchip and a magnet is used to separate the bead-bound complex from the unbound structures. 4) SMART probes are amplified via NASBA. 5) Sample is quantified in real time using molecular beacons.

6.7.1 RNA Isolation

The *isolation* of RNA from a patient sample needs to be integrated into the microchip platform and is currently being validated in our lab. This step typically involves using a lysis buffer to break apart any protein/cellular packaging and release of nucleic acids and a set of positively charged microbeads, such as silica beads, to bind all nucleic acids. The beads can be pelleted with a magnet and the supernatant waste can be

removed and replaced with elution buffer to free the isolated nucleotides for processing. The microfluidic method for RNA isolation uses a "Z-chip" shown in figure 6.4. The first buffer is the lysis binding buffer which runs from well 1 to well 2. This buffer consists of 5.4M GuSCN and 10mg/mL Na N-lauroylsarcosine. The second buffer is isopropanol running from well 2 to well 3 to serve as a washing step. The third and last buffer is 80% ethanol also serving as a washing step running from well 3 to well 4. The entire sample can then be transferred for elution using water or a TE buffer and processed (well 5).

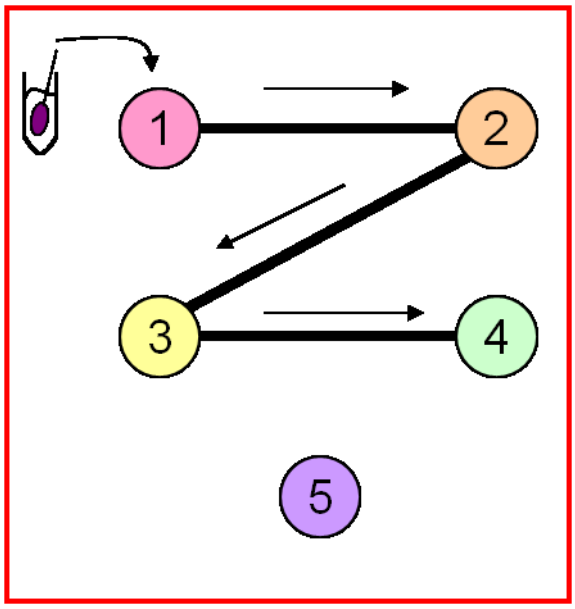

Figure 6.4. Z-chip for isolation of RNA from patient sample.

6.7.2. Capture

This step utilizes biotinylated oligonucleotides that are designed to hybridize with an upstream conserved *gag* sequence (responsible for encoding the HIV-1 protein capsid) of the isolated HIV-1 RNA, or in our experiments the conserved sequence of the sDNA. The 5' end of the biotinylated oligonucleotide contains the molecule biotin which readily binds to a streptavidin coated magnetic bead. This allows for the *capture* of sDNA containing the conserved sequence onto the beads (figure 6.5).

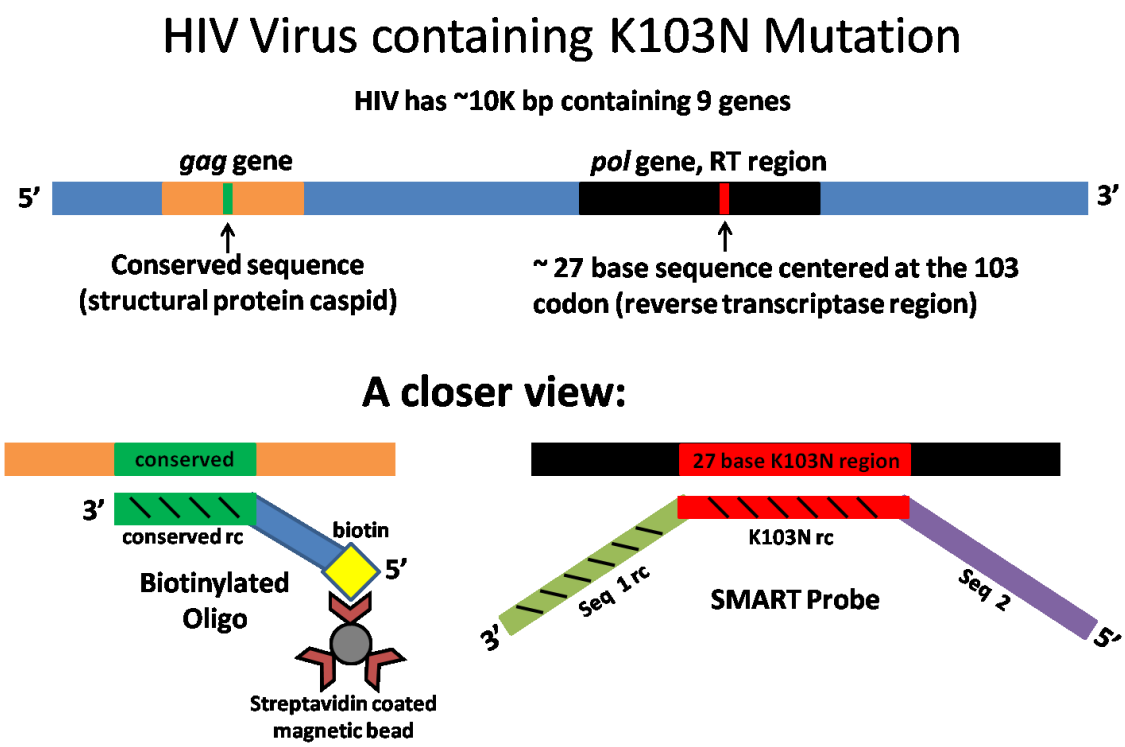

Figure 6.5. SMART capture step.

Simultaneously downstream on the sDNA, the K103N SMART probe molecule hybridizes with the sDNA. The K103N RC (dashed red) sequence of the SMART probe molecule (~25 nucleotides) is the reverse complement of a sequence centered at the mutation region (solid red) of the sDNA. The 25 nucleotide hybridization is highly specific without sacrificing the reaction kinetics or diffusive properties crucial to the SMART probe design. When an isolated patient sample will be targeted, a group of SMART probes with all potential variations of the K103N region will be used in order to capture all potential K103N variants. This does not sacrifice any amplification and detection efficiency because all of these SMART probes are the same length and contain the same 5' and 3' arm sequences, thus they use the same primers and molecular beacons for real-time detection. The final product of the capture step is a chain-linked molecule complex of streptavidin coated magnetic beads - biotinylated oligo- sDNA - K103N

SMART probe. At this stage of SMART there are still unbound K103N SMART probes within the mixture which need to be removed using a separation technique.

6.7.3. Microfluidic separation

Separation of the chain-linked molecule complex from any unbound K103N SMART probes occurs in the presence of a magnetic field. We are able to separate the bead bound complex through our microfluidic device (figure 6.6), a microchip, using a small magnet and wash away any unbound debris, unbound RNA, DNA and most importantly unbound SMART probe molecules.

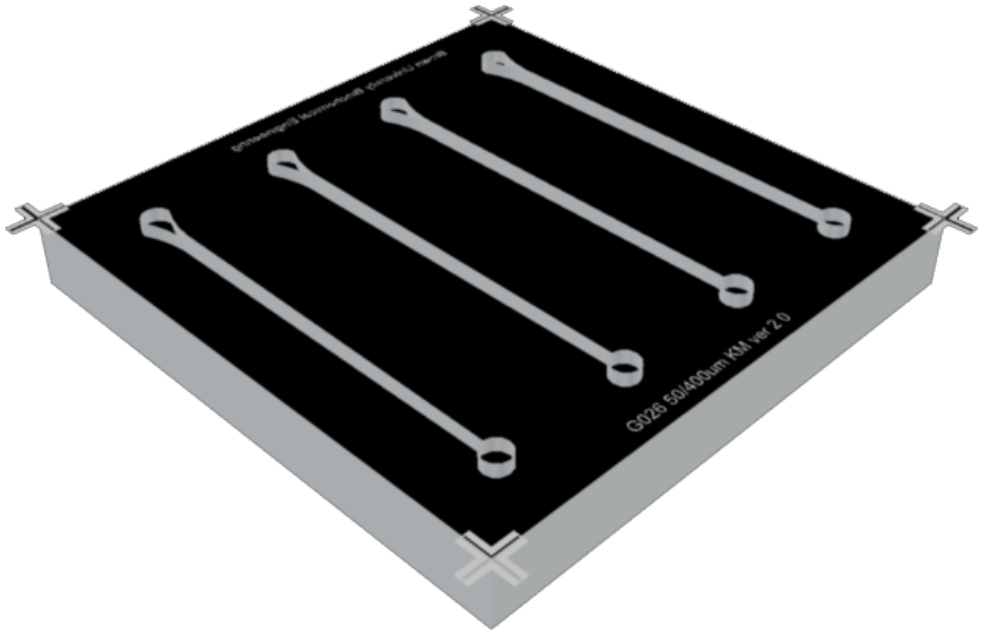

Figure 6.6. SMART microchip device.

The microchip is a simple and practical means of separating biomolecules and overcomes the inherent disadvantages of multistep bead washing assays, particularly involving loss of sample and/or inadequate washing. In addition, the microchip uses a tapered channel design. The dimensions decrease along the channel, such that the volume decreases as separation occurs, concentrating reagents for greater sensitivity. The end

product of the separation process is the chain-linked molecule complex, without the unbound SMART probes. There are several advantages to this separation technique: (i) The rapid motion of beads through fluid in the microchannels provide near zero carry-over of unbound molecules, (ii) motion of beads through a long microchannel is analogous to infinite washing of beads but takes only few seconds to accomplish, (iii) it does not require flow of sample solution (from W1 in figure 6.6) containing target molecules; the capture/binding of targets occurs in a reservoir, so that the method uniquely processes large amounts of sample for rapid separation, (iv) it can separate at high efficiency without using any membrane or pumps, thus it is quite useful for point-of-care (POC) use, and (e) to further reduce the carry over or diffusion of unbound molecules, a counter flow of clean buffer (from W2 to W1 in figure 6.6) can be created by a simple fluid volume differential.

6.7.4. Nucleic acid sequence based amplification of SMART probes

Amplification is required because the target sequences can exist in extremely small quantities, especially for HIV, and even more so when targeting drug resistant mutant variants. At the end of the *separation* step we either introduce primers, enzymes, molecular beacons, additional reagents and heat to W2 of the microfluidic device sample to catalyze the on-chip amplification process of the SMART probes; or we remove the separated sample for off-chip amplification and detection. The choice and reasoning for on-chip versus off-chip amplification and detection is detailed in chapter 9. The amplification step utilizes the cyclic phase of NASBA, and is truly isothermal (does not require a 65°C pre-heat) at 41°C because the SMART probes were designed not to exhibit significant secondary structure.

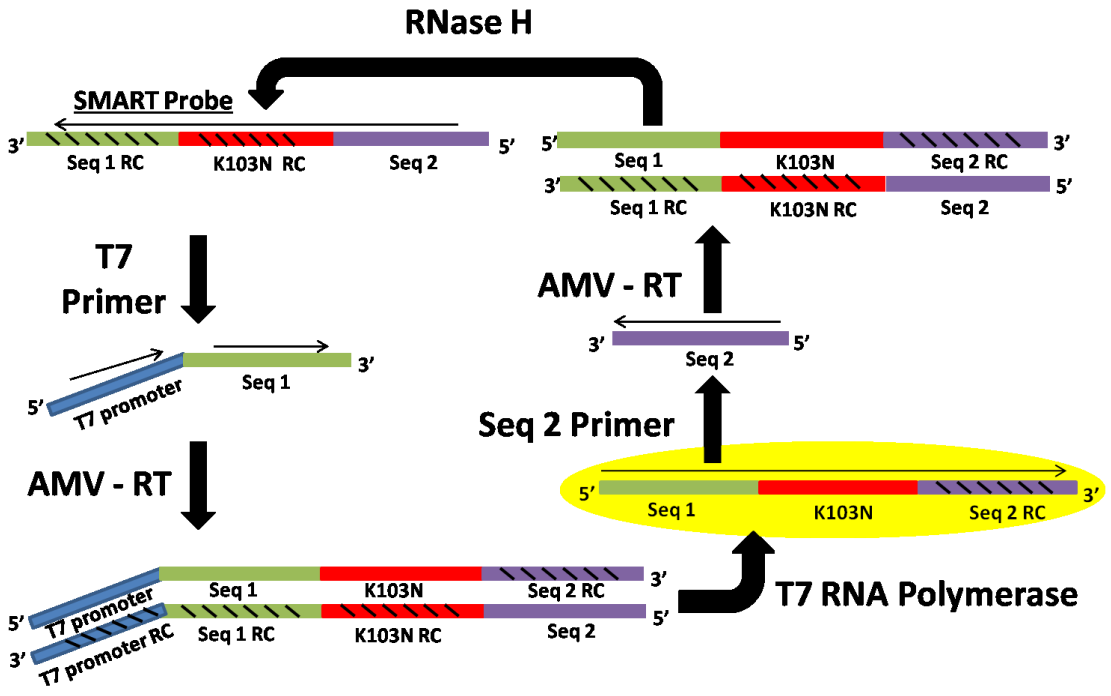

Figure 6.7. SMART amplification using cyclic only NASBA.

The abridged NASBA amplification step requires three enzymes: RNAseH, avian myeloblastosis virus reverse transcriptase (AMV-RT), and T7 RNA polymerase. When targeting an RNA sample, the cyclic phase initiates when the RNAseH selectively degrades the target RNA in the target RNA/DNA probe hybrid leaving behind the K103N SMART probes for amplification.

As seen in figure 6.7, the K103N SMART probes are used as templates, undergoing cyclic isothermal amplification to exponentially produce their RNA reverse complement (RC) products (highlighted yellow). The cycle begins when the K103N SMART probe binds with a primer containing a T7 promoter sequence (top-left). The primer is perfectly reverse complement to the 3' Seq1 region of the SMART probe, allowing for excellent hybridization kinetics. AMV-RT is then engaged and produces double stranded cDNA (bottom-left). In the presence of double stranded DNA containing

a T7 promoter sequence, T7 RNA polymerase transcribes large amounts of RNA RC (bottom-right), reverse complement of the original K103N probe. T7 RNA polymerase continues to transcribe RNA RC until either rNTPs or T7 RNA polymerase become exhausted. A second primer, Seq2, (middle-right) binds to the K103N RNA RC sequence. AMV-RT is engaged and produces cDNA/RNA hybrids (top-right). RNAseH specifically degrades the RNA in the cDNA/RNA hybrid leaving behind single stranded cDNA which is identical to the original K103N SMART probe (top-left). The end product of the amplification cycle is exponentially amplified copies of the K103N RNA RC.

6.7.5. Real time detection of K103N RNA RC

As K103N RNA RC products are amplified, corresponding molecular beacons, which were added at the beginning of amplification, hybridize with the products. The molecular beacons are designed to be a hairpin structure, containing a stem and a loop. In their natural state, they contain a CGCG-CGCG stem, which keeps the hairpin bound. The loop sequences are perfectly reverse complement to Seq2 RC, as shown in figure 6.8.

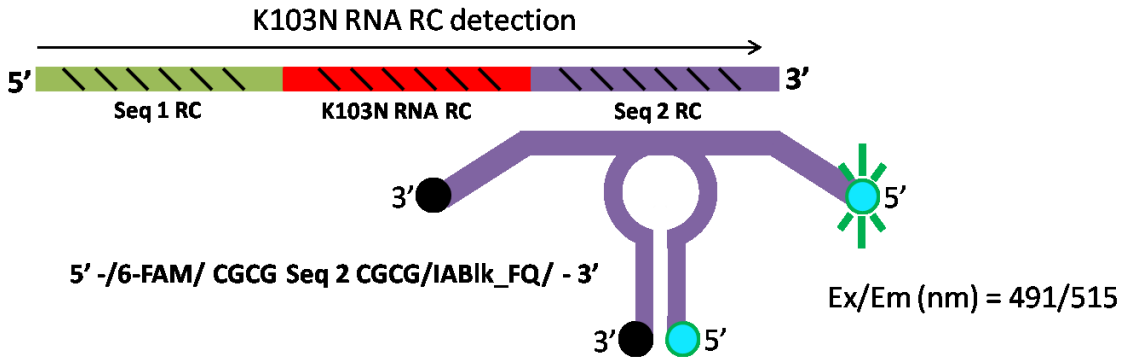

Figure 6.8. Molecular beacon hybridization and real-time detection.

In the process of real time detection of amplified SMART probes, the molecular beacons hybridize with their K103N RNA RC targets and change their conformation from a hairpin like structure to a linear structure, releasing the fluorophore from its quencher and allowing fluorescence to be emitted. The fluorescence is quantified as it occurs, resulting in real time K103N detection.

6.8. Development of SMART and applications in subsequent chapters

The following chapters focus on the development of the microfluidic separation and real-time amplification technique used for SMART, offering an excellent model for biomolecule separation (chapter 7) and insights on designing efficient amplifiable SMART probes (chapter 8). We then show SMART's capabilities by detecting synthetic samples of HIV-1 containing the K103N mutation and offer a method for a viral load assay(chapter 9). Finally, we use SMART to detect clinical samples of H3 influenza (chapter 10).

6.9. References

1 Thompson, W. W. *et al.* Estimating influenza-associated deaths in the United States. *American journal of public health* **99**, S225 (2009).

2 *Influenza (Seasonal) Fact Sheet*, <http://www.who.int/mediacentre/factsheets/fs211/en/> (2009).

3 Fouchier, R. A. M. *et al.* Characterization of a novel influenza A virus hemagglutinin subtype (H16) obtained from black-headed gulls. *Journal of virology* **79**, 2814 (2005).

4 Fiore, A. *et al.* Prevention and control of influenza: recommendations of the Advisory Committee on Immunization Practices (ACIP), 2008. *MMWR. Recommendations and reports: Morbidity and mortality weekly report. Recommendations and reports/Centers for Disease Control* **57**, 1 (2008).

5 Beigel, J. *et al.* Avian influenza A (H5N1) infection in humans. *The New England journal of medicine* **353**, 1374 (2005).

6 Mermel, L. A. Pandemic avian influenza. *Lancet Infect Dis* **5**, 666-667 (2005).

7 Fauci, A. S. Pandemic influenza threat and preparedness. *Emerg Infect Dis* **12**, 73-77 (2006).

8 Germann, T. C., et al.,. Mitigation strategies for pandemic influenza in the United States. *Proc Natl Acad Sci U S A* **103**, 5935-5940 (2006).

9 Bonner, A. B., et al. Impact of the Rapid Diagnosis of Influenza on Physician Decision-Making and Patient Management in the Pediatric Emergency Department: Results of a Randomized, Prospective, Controlled Trial. *Pediatrics* **112**, 363-367 (2003).

10 Woo, P. C. K., et al. Cost-Effectiveness of Rapid Diagnosis of Viral Respiratory Tract Infections in Pediatric Patients. *Journal of Clinical Microbiology* **35**, 1579-1581 (1996).

11 Levy, J. A., Autran, B., Coutinho, R. A. & Phair, J. P. 25 Years of AIDS: recording progress and future challenges. *Aids* **26**, 1187-1189, doi:Doi 10.1097/Qad.0b013e328354f602 (2012).

12 Clavel, F. & Hance, A. J. HIV drug resistance. *N Engl J Med* **350**, 1023-1035, doi:10.1056/NEJM2ra025195 350/10/1023 [pii] (2004).

13 Johnson, V. A. *et al.* 2011 update of the drug resistance mutations in HIV-1. *Top Antivir Med* **19**, 156-164 (2011).

14 Gilks, C. F. *et al.* The WHO public-health approach to antiretroviral treatment against HIV in resource-limited settings. *Lancet* **368**, 505-510, doi:S0140-6736(06)69158-7 [pii] 10.1016/S0140-6736(06)69158-7 (2006).

15 Gianella, S. *et al.* Detection of Minority Resistance during Early HIV-1 Infection: Natural Variation and Spurious Detection rather than Transmission and Evolution of Multiple Viral Variants. *J Virol* **85**, 8359-8367, doi:Doi 10.1128/Jvi.02582-10 (2011).

16 Gianella, S. & Richman, D. D. Minority Variants of Drug-Resistant HIV. *J Infect Dis* **202**, 657-666, doi:Doi 10.1086/655397 (2010).

17 Dunn, J. J., et al. Comparison of the Denka-Seiken INFLU A.B.-Quick and BD Directigen Flu A+B kits with direct fluorescent antibody staining and shell vial culture methods for rapid detection of influenza viruses. *Journal of Clinical Microbiology* **41**, 2180-2183 (2003).

18 Petric, M., L. Comanor, and C. A. Petti. Role of the Laboratory in Diagnosis of Influenza during Seasonal Epidemics and Potential Pandemics. *The Journal of Infectious Diseases* **194**, S98-110 (2006).

19 Gavin, P. J., and R. B. Thomson, Jr. Review of Rapid Diagnostic Tests for Influenza. *Clinical and Applied Immunology Reviews* **4**, 151-172 (2003).

20 Fiscus, S. A. C., B.; Crowe, S. M.; Demeter, L.; Jennings, C.; Miller, V.; Respess, R.; Stevens, W.; Altern, F. C. H. R. HIV-1 viral load assays for resource-limited settings. *PLoS Med* **3**, 1743-1750 (2006).

21 Chin, C. D. *et al.* Microfluidics-based diagnostics of infectious diseases in the developing world. *Nat Med* **17**, 1015-U1138, doi:Doi 10.1038/Nm.2408 (2011).

22 O'Connell, R. J. *et al.* Performance of the OraQuick rapid antibody test for diagnosis of human immunodeficiency virus type 1 infection in patients with various levels of exposure to highly active antiretroviral therapy. *J Clin Microbiol* **41**, 2153-2155 (2003).

23 Wang, S. Q., Xu, F. & Demirci, U. Advances in developing HIV-1 viral load assays for resource-limited settings. *Biotechnol Adv* **28**, 770-781, doi:DOI 10.1016/j.biotechadv.2010.06.004 (2010).

24 Cabrera, C. *et al.* Comparative evaluation of the TRUGENE HIV-1 envelope (gp41) genotyping assay on clinical samples. *Antivir Ther* **10**, S48-S48 (2005).

25 Church, J. D. *et al.* Sensitivity of the ViroSeq HIV-1 genotyping system for detection of the K103N resistance mutation in HIV-1 subtypes A, C, and D. *J Mol Diagn* **8**, 430-432, doi:DOI 10.2353/jmoldx.2006.050148 (2006).

26 Grant, R. M. *et al.* Accuracy of the TRUGENE HIV-1 genotyping kit. *J Clin Microbiol* **41**, 1586-1593, doi:Doi 10.1128/Jcm.41.4.1586-1593.2003 (2003).

27 Bile, E. C. *et al.* Performance of drug-resistance genotypic assays among HIV-1 infected patients with predominantly CRF02_AG strains of HIV-1 in Abidjan, Cote d'Ivoire. *J Clin Virol* **32**, 60-66, doi:DOI 10.1016/j.jcv.2004.07.008 (2005).

28 Halvas, E. K. *et al.* Blinded, multicenter comparison of methods to detect a drug-resistant mutant of human immunodeficiency virus type 1 at low frequency. *J Clin Microbiol* **44**, 2612-2614, doi:Doi 10.1128/Jcm.00449-06 (2006).

29 Li, J. Z. *et al.* Low-Frequency HIV-1 Drug Resistance Mutations and Risk of NNRTI-Based Antiretroviral Treatment Failure A Systematic Review and Pooled Analysis. *Jama-J Am Med Assoc* **305**, 1327-1335 (2011).

30 Li, J. Z. *et al.* Relationship between NNRTI adherence and low-frequency resistance mutations with the risk of virological failure. *Antiviral Therapy* **16**, A16-A16 (2011).

31 Wang, C. L., Mitsuya, Y., Gharizadeh, B., Ronaghi, M. & Shafer, R. W. Characterization of mutation spectra with ultra-deep pyrosequencing: Application to HIV-1 drug resistance. *Genome Res* **17**, 1195-1201, doi:Doi 10.1101/Gr.6468307 (2007).

32 Ellis, G. M. *et al.* Comparison of oligonucleotide ligation assay and consensus sequencing for detection of drug-resistant mutants of human immunodeficiency virus type 1 in peripheral blood mononuclear cells and plasma. *J Clin Microbiol* **42**, 3670-3674, doi:DOI 10.1128/jcm.42.8.3670-3674.2004 (2004).

33 Gale, H. B., Kan, V. L. & Shinol, R. C. Performance of the TruGene human immunodeficiency virus type 1 genotyping kit and OpenGene DNA Sequencing system on clinical samples diluted to approximately 100 copies per milliliter. *Clin Vaccine Immunol* **13**, 235-238, doi:Doi 10.1128/Cvi.13.2.235-238.2006 (2006).

34 Kapoor, A. *et al.* Sequencing-Based detection of low-frequency human immunodeficiency virus type 1 drug-resistant mutants by an RNA/DNA heteroduplex generator-tracking assay. *Journal of Virology* **78**, 7112-7123, doi:Doi 10.1128/Jvi.78.13.7112-7123.2004 (2004).

35 Palmer, S. *et al.* Multiple, linked human immunodeficiency virus type 1 drug resistance mutations in treatment-experienced patients are missed by standard genotype analysis. *J Clin Microbiol* **43**, 406-413, doi:Doi 10.1128/Jcm.43.1.406-413.2005 (2005).

36 Shi, C. *et al.* LigAmp: Sensitive detection of single nucleotide differences. *J Mol Diagn* **6**, 437-437 (2004).

37 Wang, B. *et al.* Sensitive detection of the K103N non-nucleoside reverse transcriptase inhibitor resistance mutation in treatment-naive HIV-1 infected individuals by rolling circle amplification. *J Virol Methods* **161**, 128-135, doi:S0166-0934(09)00274-2 [pii] 10.1016/j.jviromet.2009.06.004 (2009).

38 Kobayashi, N., Tamura, K. & Aotsuka, T. PCR error and molecular population genetics. *Biochem Genet* **37**, 317-321 (1999).

39 Dyer, J. R. *et al.* Quantitation of human immunodeficiency virus type 1 RNA in cell free seminal plasma: Comparison of NASBA(TM) with Amplicor(TM)

reverse transcription-PCR amplification and correlation with quantitative culture. *J Virol Methods* **60**, 161-170 (1996).

40 Vandamme, A. M. *et al.* Detection of Hiv-1 Rna in Plasma and Serum Samples Using the Nasba Amplification System Compared to Rna-Pcr. *Journal of Virological Methods* **52**, 121-132 (1995).

41 McCalla, S. E. & Tripathi, A. Microfluidic Reactors for Diagnostics Applications. *Annu Rev Biomed Eng* **13**, 321-343, doi:DOI 10.1146/annurev-bioeng-070909-105312 (2011).

42 Luebke, K. J., Balog, R. P. & Garner, H. R. Prioritized selection of oligodeoxyribonucleotide probes for efficient hybridization to RNA transcripts. *Nucleic Acids Res* **31**, 750-758, doi:Doi 10.1093/Nar/Gkg133 (2003).

43 Guatelli, J. C. *et al.* Isothermal, Invitro Amplification of Nucleic-Acids by a Multienzyme Reaction Modeled after Retroviral Replication. *P Natl Acad Sci USA* **87**, 1874-1878 (1990).

44 Deiman, B., van Aarle, P. & Sillekens, P. Characteristics and applications of nucleic acid sequence-based amplification (NASBA). *Mol Biotechnol* **20**, 163-179 (2002).

45 Compton, J. Nucleic-Acid Sequence-Based Amplification. *Nature* **350**, 91-92 (1991).

46 Gupta, P. *et al.* High viral load in semen of human immunodeficiency virus type 1-infected men at all stages of disease and its reduction by therapy with protease and nonnucleoside reverse transcriptase inhibitors. *J Virol* **71**, 6271-6275 (1997).

47 Vangemen, B. *et al.* A One-Tube Quantitative Hiv-1 Rna Nasba Nucleic-Acid Amplification Assay Using Electrochemiluminescent (Ecl) Labeled Probes. *Journal of Virological Methods* **49**, 157-167 (1994).

48 Vandamme, A. M. *et al.* Quantification of HIV-1 RNA in plasma: Comparable results with the NASBA HIV-1 RNA QT and the AMPLICOR HIV monitor test. *J Acq Immun Def Synd* **13**, 127-139 (1996).

49 Segondy, M., Ly, T. D., Lapeyre, M. & Montes, B. Evaluation of the nuclisens HIV-1 QT assay for quantitation of human immunodeficiency virus type 1 RNA levels in plasma. *J Clin Microbiol* **36**, 3372-3374 (1998).

50 Yao, J., Liu, Z., Ko, L. S., Pan, G. & Jiang, Y. Quantitative detection of HIV-1 RNA using NucliSens EasyQ HIV-1 assay. *J Virol Methods* **129**, 40-46, doi:DOI 10.1016/j.jviromet.2005.04.017 (2005).

51 Gulliksen, A. *et al.* Real-time nucleic acid sequence-based amplification in nanoliter volumes. *Anal Chem* **76**, 9-14, doi:10.1021/ac034779h (2004).

52 Gulliksen, A., et al. Parallel nanoliter detection of cancer markers using polymer microchips. *The Royal Society of Chemistry* **5**, 416-420 (2005).

53 Furuberg, L. *et al.* RNA amplification chip with parallel microchannels and droplet positioning using capillary valves. *Microsystem Technologies* **14**, 673-681 (2008).

54 Dimov, I. K. *et al.* Integrated microfluidic tmRNA purification and real-time NASBA device for molecular diagnostics. *Lab on a Chip* **8**, 2071-2078 (2008).

55 McCalla, S. E. *et al.* A Simple Method for Amplifying RNA Targets (SMART). *Journal of Molecular Diagnostics* **14,**, 328-335 (2012).

CHAPTER 7

CAPTURE AND SEPARATION OF BIOMOLECULES USING MAGNETIC BEADS IN A SIMPLE MICROFLUIDIC CHANNEL WITHOUT AN EXTERNAL FLOW DEVICE

7.1. Abstract

The use of microfluidic devices and magnetic beads for applications in biotechnology has been extensively explored over the past decade. Many elaborate microfluidic chips have been used in efficient systems for biological assays. However most fail to achieve ideal point of care (POC) status, requiring larger traditional external devices in conjunction with the microchip. This paper presents a simple technique for capture and separation of biomolecules using magnetic bead movement on a microchip without the use of an external flow device. The microchip consisted of two well reservoirs (W1 and W2) connected via a tapered microchannel. The bead motion was first analyzed on the microchip and a permanent magnet was moved alongside the microchip, dragging the beads at equivalent speed through the microchannel between the two wells. It was found that greater than 95% bead transfer from W1 to W2 occurred at a velocity of 0.7 mm/s. Prior to testing our microchip with enzymatic reactions, we characterized our

enzyme, alkaline phosphatase (AP), and substrate, 6-8-difluoro-4-methylumbelliferyl phosphate (DiFMUP), with an off-chip control. AP was used to dephosphorylate the non-fluorescent DiFMUP to fluorescent 6,8-difluoro-7-hydroxy-4-methylcoumarin (DiFMU). Next, three assays were performed using our microchip: non-specific adsorption of DiFMUP, capture of AP, and separation of AP. Biotinylated AP was immobilized on streptavidin coated magnetic beads for the capture and separation assays. Our non-specific adsorption assay indicated that the microchip was capable of transferring the beads with less than 0.002% carryover of DiFMUP. Our capture assay indicated that microchip efficiently captured and transferred biotinylated AP with our streptavidin conjugated magnetic beads. 100% of DiFMUP was converted to DiFMU within 15 minutes. Our separation assay showed effective separation of AP from the non-specific substrate and elucidated the binding capacity of the beads, wherein leftover unbound AP converted 100% of DiFMUP within 10 minutes and samples with less than full bead capacity (i.e. all AP was transferred) did not convert any of the substrate. The immobilization of AP on bead surface resulted in 32% reduced enzymatic speed as a result of altered protein conformation and/or steric hindrance of the catalytic site. Overall, this microfluidics platform was established as simple and effective means of separation on biomolecules without needed any flow apparatus.

7.2. Introduction

Experimental samples of RNA, DNA and proteins are often sparse and reagents used in biotechnology are often costly. Immobilized enzymes have reduced enzymatic activity due to steric hindrance and changed protein conformation.[1] New techniques to improve the isolation of biomolecules are always needed. An improved method for

moving magnetic beads on a microfluidic chip can help immobilized enzyme efficiency. Microchip devices allow the study of biomolecular reactions using sub-nanoliter quantities of reagents, substrates and sample for each assay.[2] Cell lysis[3], DNA extraction[3,4], polymerase chain reaction[5], sequencing by synthesis[6] and ELISA[7] are some examples of relevant batch process techniques that have been featured on microchips. Microchip devices are ideal for point of care (POC) applications because they have been shown to be effective in such biological assays.

Magnetic beads are also widely applied in biotechnology techniques such as magnet activated cell-sorting (MACS)[8] and detection combining magnetic beads with antibodies[9]. A newer technique is immiscible filtration assisted by surface tension (IFAST) which utilizes an immiscible phase for enhanced separation of cells[10] and nucleic acids.[11] The use of magnetic beads on a microfluidic chip is common, particularly when in a continuous flow microreactor.[12,13] A variety of magnetic magnetic bead systems have been used for capturing and separating biomolecules[14-16]. However, these systems are elaborate and are limited by their dependence on external equipment, such as pumps for regulation flow conditions and microscopes for precise optical based assays. A more basic approach utilizes capillary tubes combined with a syringe pump for an effective immunoassay platform[17].To our knowledge, there have been no basic microfluidic studies where beads were used as a mobile platform for capture and separation of biomolecules without the use of an external flow device. Here we demonstrate a simple magnetic bead based microfluidic system for capturing and separating biomolecules without the use of an external flow device.

We performed the following three assays: non-specific adsorption, capture and separation using mobile magnetic beads on our microchip platform. Fluorescence of 6,8-difluoro-7-hydroxy-4-methylcoumarin (DiFMU) was quantified through a simple assay combining microfluidic bead movement using a simple magnet, conjugation of alkaline phosphatase (AP) and dephosphorylation of 6-8-difluoro-4-methylumbelliferyl phosphate (DiFMUP). Magnetic beads coated with streptavidin were used to immobilize biotinylated AP. When in contact with DiFMUP, the AP causes dephosphorylation of DiFMUP producing DiFMU. DiFMUP is non-fluorescent however its product, DiFMU, can be quantified using fluorescence spectroscopy. Detection and quantification of DiFMU was used to investigate the three specific assays: non-specific adsorption of DiFMUP onto the streptavidin coated beads, capture of AP, and separation of AP from DiFMUP.

7.3. Experimental

7.3.1. Materials

Rare earth magnets (Grade N52) were purchased from K&J Magnetics (Jamison, PA). DiFMUP (14 000 cm^{-1} M^{-1}, excitation/emission = 358/450 nm), and spherical super-paramagnetic streptavidin coated Dynabeads® M-280 (Ø 2.8 µm, 10mg/ml) were obtained from Invitrogen (Carlsbad, CA). DiFMUP and DiFMU were dissolved in DMSO, calibrated by UV-absorbance (ND-1000, Nanodrop, Wilmington, DE) and stored as aliquots at -20°C. Calf intestinal alkaline phosphatase conjugated with biotin (AP-biotin) was acquired from Rockland Immunochemical (Gilbertsville, PA). The buffer used in the microchip contained 50 mM Tris pH 8.0 and 0.05% Tween 20. Buffer

reagents mentioned, including DMSO and chip components, were purchased from Sigma-Aldrich (St. Louis, MO).

7.3.2. Microchip device

A polydimethylsiloxane (PDMS) microchip was fabricated using soft lithography. PDMS was poured over the fabricated SU-8 structure on a silicon wafer and then incubated at 75°C for two hours. The PDMS was then removed from the mold, cleaned with ethanol and oxygen plasma (PDC-32G, Harrick Plasma Ithaca, NY)and bonded to a Pyrex® slip (1.4 mm thick). The microchannel used was a tapered lane of 400 μm wide down to 50 μm wide, 120 μm deep and 30 mm long. The depth of the channel was measured by surface profilometer (Dektak).

7.3.3. Microscope apparatus

A microscope apparatus was used to observe the movement of the magnetic beads during the experiment and to precisely change the magnet's position alongside the microchannel. The microchip was placed onto the slide plate of an inverted microscope (Eclipse TE2000-U, Nikon, Melville, NY). The magnet (bar magnet, 2.5 x 1.25 x 0.64 cm thick) was attached on the lens, directly beneath the chip and held approximately 1 mm in front of the main bead cluster during movement. The magnet was attached to the lens via a plastic brace in order to securely fix it in the correct position. The slide plate was then moved at a specific velocity, changing the chips position to the magnet. A schematic for the bead movement through the channel by magnetic force is shown in figure 7.1(a).

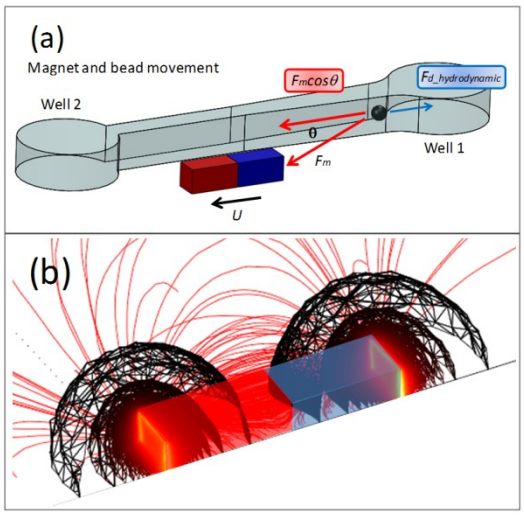

Figure 7.1. (a) Schematic showing the main forces acting on a magnetic bead **(b)** Comsol simulated magnetic field created by the permanent magnet.

The 3D numerical simulation using COMSOL (figure 7.1b) shows that a magnetic bead with a 1.4 μm radius located 1.4 mm (y = 1 mm, z = 2 mm) from the magnet as shown, perceives a force of Fm=-2.55 pN in the y direction. The relative permeability of iron μ_r = 600 and the magnetization of the magnet = 279600 A/m. The black surfaces are the iso-magnetic force surface and red lines are magnetic field streamline. If $F_m \geq F_d$, the beads will follow the magnet as it moves alongside the channel. If the velocity of the magnet is too high, $F_m < F_d$, then $u \to 0$ and the beads do not move with the magnet.

7.3.4. Percent bead transfer procedures

5 μL of buffer was pipetted into W1 and pressured into the microchannel using a disposable 1mL syringe. Excess buffer was then removed from the wells and 5 μL of additional buffer was pipetted into both wells. Procedures were then paused for 10 minutes to eliminate any hydrodynamic flow. Afterwards, 1 μL of 1 μg/μL streptavidin conjugated magnetic beads were pipetted into W1. Simultaneously, 1.5 μL buffer was added into W2 to prevent any hydrostatic driven flow. The beads were moved from W1

to W2 by changing the position of the slide plate on the microscope. The time required for the beads to pass through the microchannel was measured resulting in a range of bead velocities (0.5 - 1.4 mm/s). Counting the beads using a hemocytometer in solution pre-transfer and post-transfer and extrapolating the total amount of beads, in addition to manually counting any beads in W1/microchannel post-transfer allowed us to calculate the percent transfer of beads from W1 to W2.

7.3.5. Three assays: non-specific adsorption, capture and separation

The percent bead transfer versus velocity of the magnet experiment results yielded a maximum bead velocity (~0.7 mm/s) at which we could confidently predict that greater than 95% of beads would transfer. Since our motivation is to develop a simple assay using less equipment and to transfer 100% of the beads, we used 0.7 mm/s as our upper limit and manually moved the magnet along the 30 mm channel for about 1-2 minutes by hand (~0.25 - 0.5 mm/s) instead of using the microscope apparatus to transfer ~100% of the magnetic beads for our three bioassays. The three bioassays were used to evaluate non-specific adsorption, capture and separation conditions (shown in figure 2).

The non-specific adsorption assay was to ensure DiFMUP did not diffuse to W2 or non-specifically bind or carryover with the streptavidin coated magnetic beads. 1 µg of beads and varying concentrations of DiFMUP (1mM, 2mM, 4mM) were added to W1 and mixed for 30 seconds and AP (714±100µM) was added to W2. The fluorescence of each prepared supernatant solution (without beads) was measured using a spectrofluorometer (QuantaMaster™, Photon Technology International, Birmingham, NJ) and using a 10 µL quartz fluorometer cuvette (16.10F-Q-10, Starna cells, Atascadero, CA) before adding the samples to W1 and W2. Then the beads were transferred from W1

to W2 with the magnet. After the transfer W2 supernatant fluorescence was immediately measured for t = 0 minutes or was measured at 3 minutes interval endpoints up to 16 minutes total with the fluorometer by transferring the supernatant back to the quartz cuvette. Note that beads were not bound to AP in W1 but that AP was placed in W2 to initiate the conversion of any DiFMUP if carried non-specifically to W2.

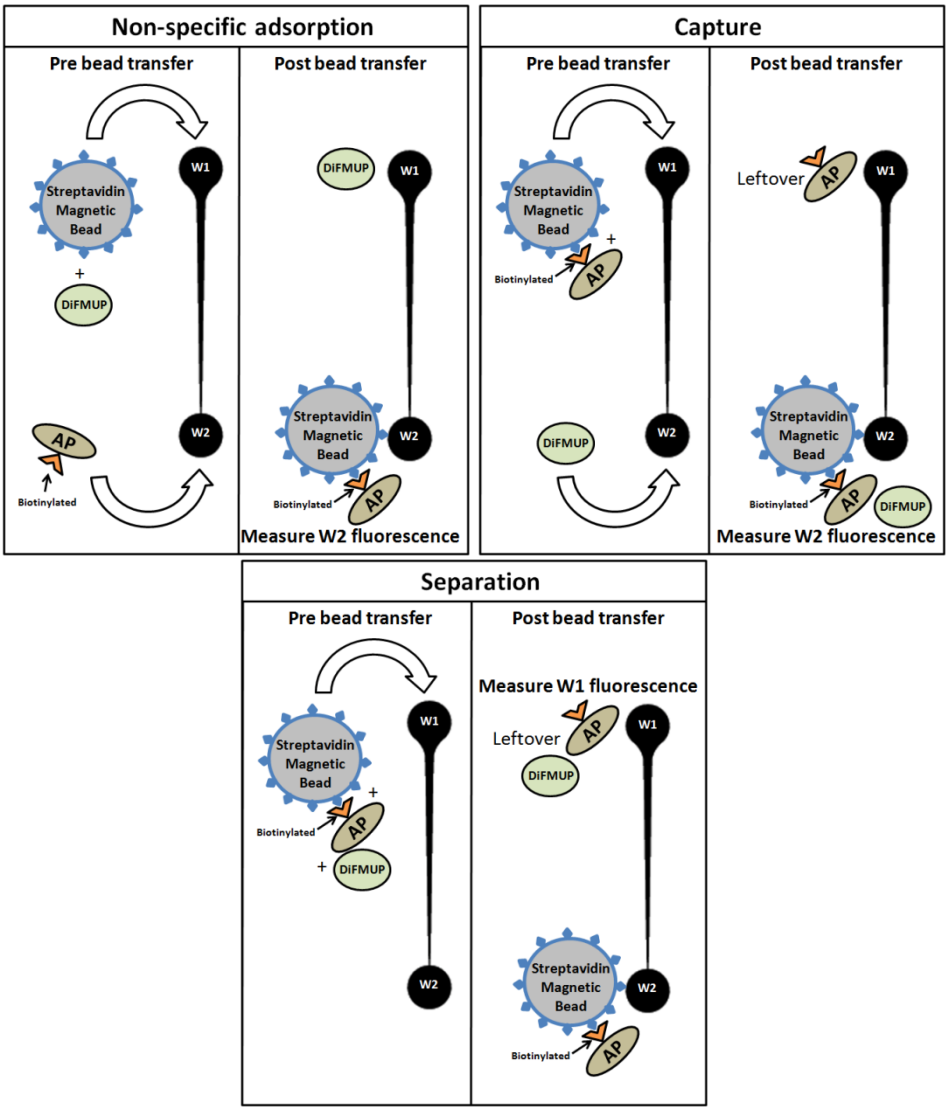

Figure 7.2. Substrate conversion assays. **(TOP-LEFT)** Non-specific adsorption assay. **(TOP-RIGHT)** Capture assay. **(BOTTOM)** Separation assay.

Capture consisted of adding 1µg of beads and varying concentrations of AP to W1 and mixing for 30 seconds and a fixed concentration of DiFMUP (4mM) to W2. AP concentrations were chosen relative to the theoretical binding capacity of the M-280 Dynabeads (table 1). Then the beads were moved to W2. This condition tested the ability of the beads to bind with AP and stay bound after transferring them from W1 to W2. The conversion of DiFMUP to DiFMU in W2 serves as an indicator of the capture process. After the transfer to W2 the supernatant fluorescence was immediately measured in cuvette for time = 0 minutes or was measured at 3 minute interval endpoints up to 16 minutes total.

Separation consisted of adding 1µg of beads, AP and DiFMUP (4mM) to W1 and then moving the beads to W2 with the magnet. This condition tested the ability of the beads to effectively separate AP from DiFMUP. After the separation W1 fluorescence was immediately measured for t = 0 minutes was measured at 3 minutes interval endpoints up to 16 minutes total. All conditions use 1uL of 1 µg/µL streptavidin conjugated magnetic beads. AP concentrations were again chosen relative to the binding capacity of the M-280 Dynabeads. DiFMUP concentrations were chosen to exhibit minimal photobleaching and illicit a quantifiable fluorescence response when exposed to AP.

7.4. Results and discussion

7.4.1. Magnetic bead movement

The movement of the magnetic beads through the microchannel was observed with consideration to velocity, quantity of beads used, shape of the SPS during movement and transfer rates between the wells. Actual bead movement through the channel is

shown in figure 7.3(a). The images clearly show that beads moved as a discrete plug of length around 1.6-2.0 mm through the tapered microchannel. Towards the end of channel beads were observed to be more closely packed compared to those in the plug at the start of the microchannel. There was no bead sticking observed in the microchannel.

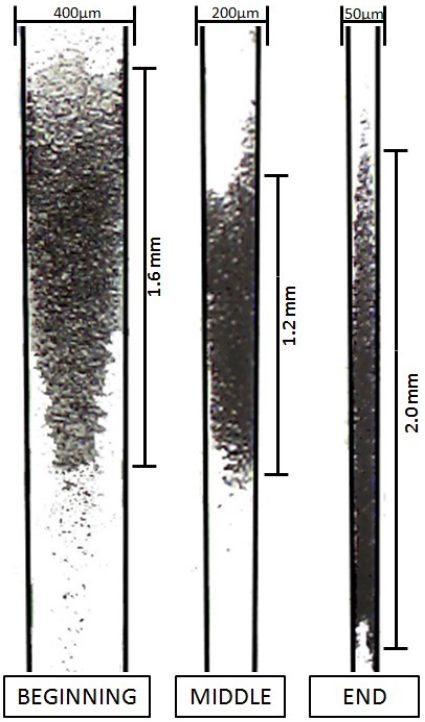

Figure 7.3(a). 1µL of 1µg/µL (~65,000 beads) magnetic beads progressing through the microchannel at 0.7±0.04 mm/s (images captured at 2x magnification). The magnet was temporarily removed to capture images. Beads were guided to the beginning of the channel (left, ~400µm width) just beyond the initial tapering from W1. Beads then were guided to the middle of the channel (middle, ~200µm width). Beads were finally guided the full duration of the channel30 (30 mm in total) and were located at the end of the channel (right, ~50µm width) about to enter W2.

An optimum movement of the beads included > 95 % bead transfer from W1 to W2 and an average bead velocity of 0.7 ± 0.04 mm/sec in the microchannel. The use of a cylindrical magnet (1.1 cm Ø x 0.64 cm thick) was also examined. This magnet also moved the beads at a comparable 0.6 mm/sec, but the bead transfer were not as high (70%) as with the bar magnet. The greatest bead velocities were obtained when the poles

of the bar magnet were placed parallel to the microchannel as shown in figure 7.1(b) simulation.

The percentage of magnetic beads transferred from W1 to W2 decreased with increasing magnet velocity. Moving the magnet faster than ≈ 0.7 ± 0.04 mm/s became too fast, resulting in inadequate magnetic force and caused the beads to remain in the microchannel and W1. Figure 7.3(b) shows this relationship.

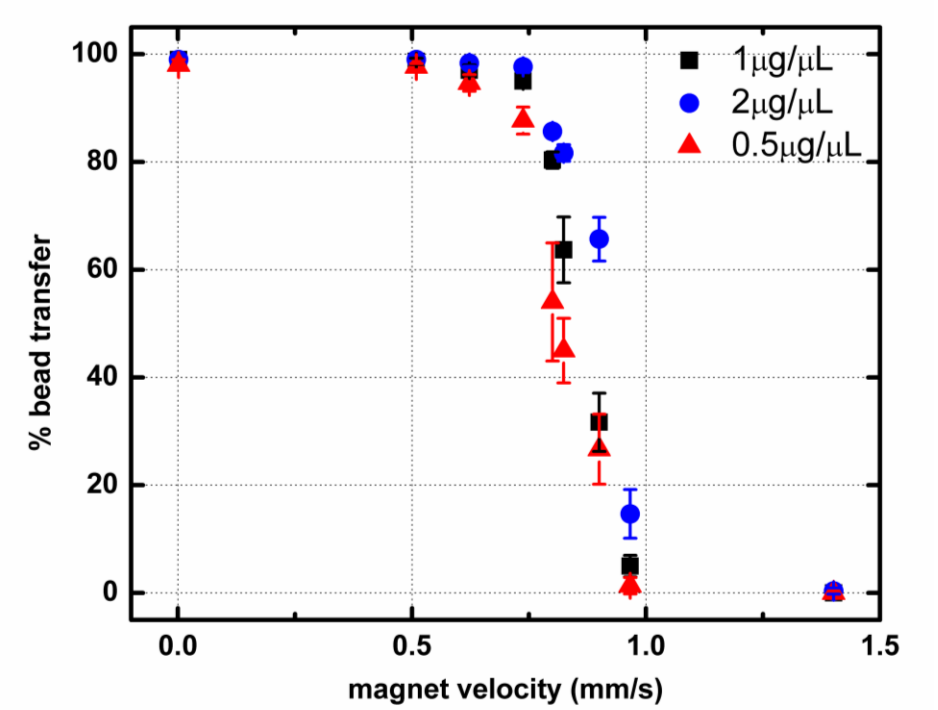

Figure 7.3(b). Percentage of magnetic beads transferred between the wells as a function of increasing velocity of the magnet**.** A lower concentration of magnetic beads at critical bead velocities (~0.6 - 1.0 mm/s) results in better transfer of beads. The plotted results are the average values for three individual experiments and the error bars are generated from the standard deviation of the data.

7.4.2. Alkaline Phosphatase (AP) kinetics

Substrate (DIFMUP) conversion assays were used to quantify non-specific adsorption and the efficiency of capture and separation after the bead motion in the microfluidic channel. As a control for the kinetics of these assays, solution phase and

magnetic particle bound AP kinetics were first assessed at a fixed DiFMUP concentration of 4mM and four different concentrations of AP. Table 7.1 shows the properties of the streptavidin coated beads and the theoretically calculated biotinylated AP binding capacity. Based upon the theoretical binding capacity of ~ 71.4±10 µM, four concentrations of AP were investigated: 0.1x bead capacity = 7.1±1µM, 0.5x bead capacity = 37±5 µM, 10x bead capacity = 714±100 µM, and 100x bead capacity = 7.14±1mM.

Dynabeads® M-280 Streptavidin		
Stock bead concentration	10	mg/ml
Biotinylated AP bead capacity	10	ug/mg of beads
Number of beads	6.50E+08	per ml
Bead radius	1.4	um
Volume per bead	11.49	um^3
Total bead volume	7.47E+09	um^3/ml
Total bead density	1.34E-09	mg/um^3
Experiment conditions		
Bead concentration	1	mg/ml
Bead volume	0.001	ml
Bead mass	0.001	mg
Biotinylated AP bead capacity	0.0100	ug of Biotinylated AP
Molar mass of biotinylated AP	1.40E+05	g/mol
Moles of bead bound biotinylated AP	7.14E-14	mol
Molarity of bead bound biotinylated AP	7.14E-02	mM

Table 7.1. Properties of streptavidin coated magnetic beads and binding capacity of AP = 71.4µM.

Baseline fluorescence of the DiFMUP substrate was measured in a 10 µL quartz cuvette filled to 5µL. Because biotin-streptavidin biochemistry was used to attach AP to the magnetic bead, the activity of free biotin conjugated AP proteins was measured as the control. The cuvette was maintained at 25ºC using a digital temperature controller. The temperature was kept constant at 25ºC to minimize the evaporation effects. Note that the experiments can be performed at any other temperature. After the baseline was

established, the fluorometer reading was paused and the DiFMUP substrate was removed and mixed with 5 µL of biotin-AP and then the entire well-mixed volume was returned to the cuvette for continued measurement. Following each measurement, the cuvette was thoroughly washed with DI water, rinsed with 95% ethanol, and dried under nitrogen such that the cuvette windows were free from streaks. Figure 7.4 shows fluorescence versus time plots for several runs. The fluorescence increase is proportional to the rate of production of the fluorescent DiFMU molecules. The data was collected over the first 15 minutes. Each experiment was carried out three times to obtain the respective error bars.

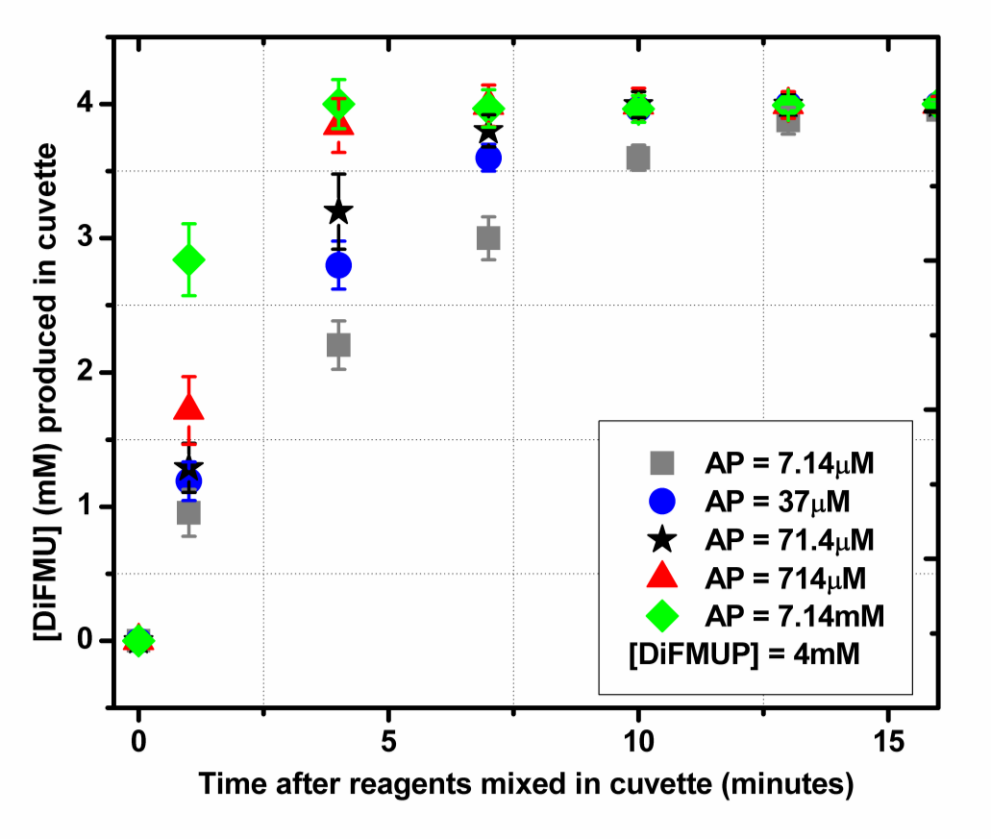

Figure 7.4. Off-chip DiFMUP added to AP in cuvette. DiFMUP was fixed at 4mM. The signal reached a plateau for all concentrations of AP, indicating that all DiFMUP had been converted to DiFMU. Raising the concentration of AP resulted in faster conversion of DiFMUP to DiFMU. 7.14µM AP was also included to exemplify the relationship of AP concentration and dephosphorylation of DiFMUP. The plotted results are the average values for three individual experiments and the error bars are generated from the standard deviation of the data.

The results here show that AP dephosphorylated 4 mM of DiFMUP within 15 minutes. As the concentration of AP decrease the conversion of DiFMUP to DiFMU became slower. Then the reaction velocities were estimated, $v = v_{\max}[DiFMUP]/K_m + [DiFMUP]$, by taking the derivative of the time plots. As expected maximum reaction speeds, $v_{\max}$, were observed at the start of the reaction. The Michaelis constant (K_m) is equivalent to the concentration of the substrate [DiFMUP] at which the reaction takes place at 1/2 its maximum speed. The K_m value was evaluated using the Lineweaver-Burke analysis[18] where the inverse of reaction velocities are plotted against the inverse of substrate (DiFMUP) concentrations. The Michaelis constants for solution-phase AP-biotin was evaluated to be K_m = 2.42 ± 0.04 mM and $v_{\max} = 0.955 mM/\min$. This K_m value is consistent with those reported previously using AP as enzyme for various substrates[12,19]. The quantitative range of our data limits the analysis, however a smaller concentration of AP could be used to determine K_m with greater accuracy or similarly a smaller timescale could be used with the higher concentrations of AP. This would allow for a more detailed modeling of the dephosphorylation of DiFMUP.

Finally, the immobilized phase kinetics was assayed using AP conjugated beads. Here only bead bound AP kinetics are of interest so only the three lowest [AP], 71.4 μM, 37 μM and 7.14 μM, which were less than equal to the binding capacity of our magnetic beads, were included . Similar to solution-phase (control) experiments, our analysis determined K_m = 1.48 ± 0.03 mM and $v_{\max} = 0.667 mM/\min$ for the bead-bound AP. This value is remarkably close to that obtained for free biotin-AP in the solution phase. However, the immobilization of AP on bead surface resulted in 32% reduced enzymatic

speed as a result of altered protein conformation and/or steric hindrance of the catalytic site. In addition, a diffusion layer around the immobilized bead can create resistance to mass transfer, which can limit the reaction rate.

7.4.3. Non-specific adsorption and/or carryover of DiFMUP

The non-specific adsorption assay was to ensure DiFMUP showed no signs of non-specifically binding to our streptavidin coated magnetic beads. Streptavidin coated beads and DiFMUP were added to W1 and AP to W2. Beads were then moved from W1 to W2. Note that beads were not bound to AP in W1 but that AP was placed in W2 to initiate the conversion of any DiFMUP if carried non-specifically to W2. Figure 7.5(a) shows the concentration of DiFMU produced in W2 as a function of time.

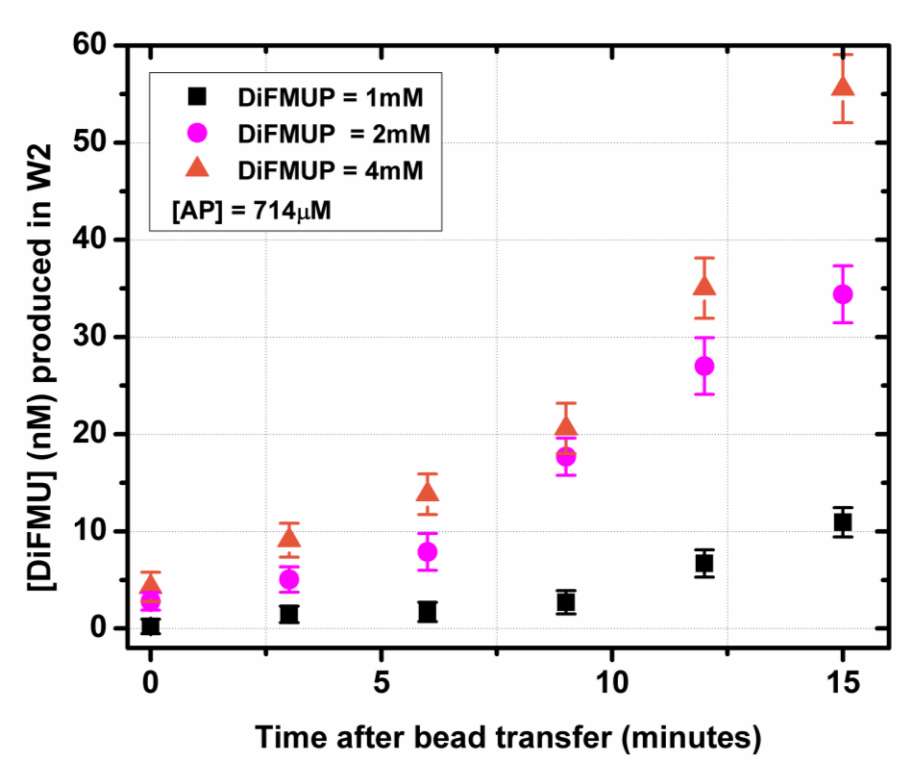

Figure 7.5(a). Non-specific adsorption assay. W1 fluorescence remained constant. [AP] was fixed at 714μM. W2 did not exhibit any considerable change in fluorescence after the bead transfer. The plotted results are the average values for three individual experiments and the error bars are generated from the standard deviation of the data.

Three different concentrations of DiFMUP (1 mM, 2 mM, 4 mM) were used to test non-specific adsorption or carryover of DiFMUP via the streptavidin coated beads with a fixed concentration of AP (714±100μM). Note that W2 contained AP at 10X concentration of bead capacity for AP immobilization. Hence, both immobilized and free solution AP enzyme was available to dephosphorylate any DiFMUP molecule carried or adsorbed via bead motion. Results from previous section show that 100% conversion would be achieved in 15 minutes if, hypothetically, all DiFMUP molecules were transferred from W1 to W2. The results show that less than 0.002% of DiFMUP molecules moved ($[DiFMU]/\{1-\exp(-v_{\max}t/K_m)\}$) with the beads to W2 for all concentrations of DiFMUP in W1. Since the diffusion time $t_{diff} \sim l^2/2D$ for DiFMUP in a $l = 30mm$ long microchannel is much longer than the total time of bead transfer $t_{BT} \sim 1\min$, we attribute the DiFMUP migration to either non-specific adsorption or carryover within the interstitial spaces of the bead cluster. Although adsorption-desorption kinetics of DiFMUP molecules onto the streptavidin coated bead surface is complex, some important experimental details can be established using a Langmuir isotherm model.[20] While this model is not applicable for multilayer adsorption, the purpose of this part of the exercise is to quantify adsorbed concentration $\Gamma\left[\frac{moles}{m^2}\right]$ of DiFMUP onto the streptavidin coated bead surface in the experiments. The adsorption rate is proportional to the number of available sites $(\Gamma_\infty - \Gamma)$ and the solute concentration in the well c, the desorption rate can be assumed to be proportional to Γ. Hence, the rate of surface accumulation of DiFMUP can be written as

$$\frac{d\Gamma}{dt} = -k_1 c\left(\Gamma_\infty - \Gamma\right) + k_{-1}\Gamma = -k_A\left[c\left(\Gamma_\infty - \Gamma\right) - K\Gamma\right] \quad (1)$$

Here k_1 $\left[\frac{m^3}{s.moles}\right]$ and k_{-1} $\left[\frac{1}{s}\right]$ denotes adsorption and desorption rate constants and Γ_∞ denotes total number of sited available on the bead surfaces. At steady state, equation (1) results in

$$K = \frac{k_{-A}}{k_A} = \frac{\left(\Gamma_\infty - \Gamma^{ss}\right)c}{\Gamma^{ss}} \quad (2)$$

where K is the adsorption-desorption equilibrium constant. Equation (2) can be used to describe the observed adsorption/desorption kinetics. The data in figure 7.5(a) shows that at 15 minutes the carryover/adsorbed DiFMUP concentration ($[DiFMU]/\{1-\exp(-v_{\max}t/K_m)\}$) in W2 is in linearly proportional, with slope $\Gamma_\infty/K = 7.9\times10^{-4}$, to the bulk concentration of DiFMUP placed in W1. This suggests that $K >> c$ and both adsorption and desorption of DiFMUP molecules was significant for the concentration range used on our experiments. In other words, DiFMUP molecules do not undergo strong adsorption onto the sphere. Hence, a possibility of simple carryover of molecules in zero-flow spaces between particles cannot be ruled out. Lastly, the fluorescence in W1 remained constant indicating that there was no diffusion of AP from W2 to W1.

Above experimental investigation clearly suggests that our technique for capture or separation of molecules via motion of beads though microchannel minimizes the carryover and non-specific adsorption of small molecules such as DiFMUP.

7.4.4. Capture of alkaline phosphatase (AP)

The aim of these experiments was to efficiently isolate AP from W1 to W2 without loss of activity of enzyme. Samples containing AP were first placed in W1. 1µg of beads were then placed in W1 and stirred with the magnet for 1 minute and subsequently beads were moved to W2. 4mM of DIFMUP was placed in W2 to initiate the reaction using captured AP bound to beads. Figure 7.5b shows a plot of DiFMU produced as a function of time for four sets of experiments with varying concentration of AP in W1. Note that 100% bead capacity for AP was 71.4±10uM.

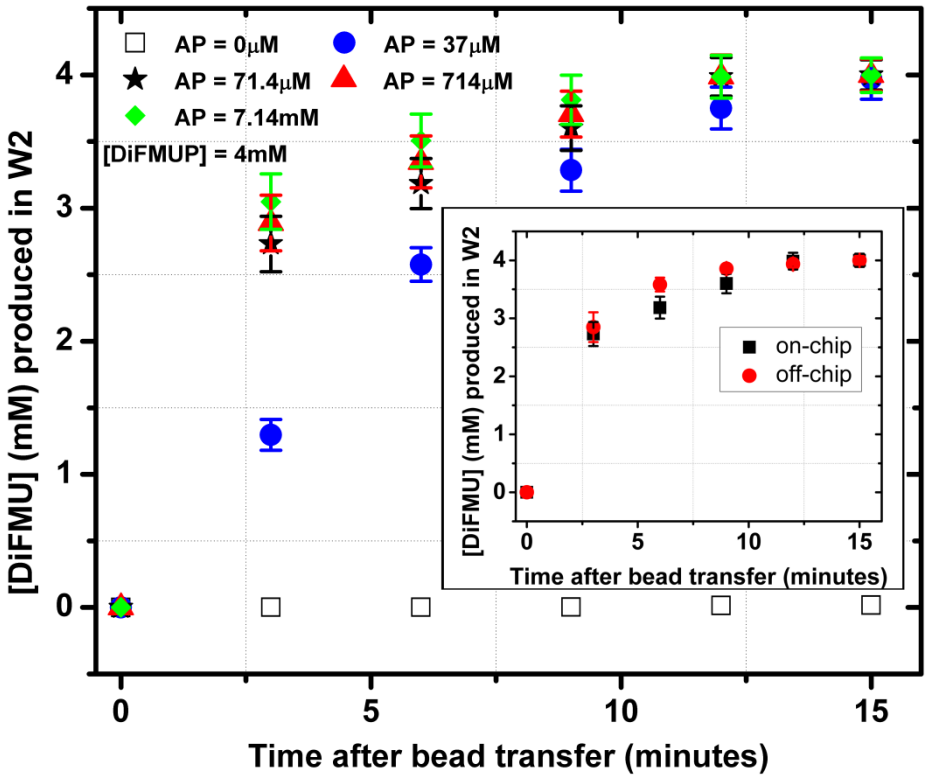

Figure 7.5(b). Capture assay. W2 exhibited a large increase in fluorescence indicating that the AP transferred from W1 to W2 and the DiFMUP had subsequently undergone dephosphorylation. The rate of DiFMU production for the varying [AP] is consistent with the off-chip cuvette results (inset) indicating a strong biotin-streptavidin bond. The plotted results are the average values for three individual experiments and the error bars are generated from the standard deviation of the data.

Our results show successful binding and capture of AP from W1. Biotinylated proteins, such as AP, have a very low dissociation constant of $K_d = 10^{-15}$ M with streptavidin coated beads, where $K_d = \frac{[protein][ligand]}{[complex]}$. The smaller the dissociation constant, the higher the concentration of ligand bound protein complex and the lower the concentration of unbound protein and ligand. Thus, a low K_d indicates a high affinity between ligand and protein such that they form a very strong bond. The diffusion time inside W1 = 2.5 seconds. All three concentrations of AP converted >75% of DiFMUP within 10 minutes and ~100% conversion within 15 minutes. Figure 7.5b (inset) also compares the reaction kinetics of captured AP with that obtained off chip for [AP]=bead capacity 71.4±10 uM case. The max reaction velocity $v_{max} = 0.667 mM/\min$ and K_m = 1.48 ± 0.03 mM well describe the plots. The rate of DiFMU production for the varying AP is consistent with the off-chip cuvette results indicating an efficient biotin-streptavidin binding to the pack of beads and supports the results of no loss of activity of AP.

These experiments clearly show that the microfluidic bead motion technique effectively isolate AP from the well and it does not deteriorate bound enzyme due to any shear or any magnetized bead compaction. Also, the microfluidic bead motion technique successfully isolate a reactive species from W1 to W2 without losing bound species inside the microchannel or onto the walls of microchannel.

7.4.5. Separation of alkaline phosphatase (AP)

Separation tested the ability of the beads to effectively separate AP from DiFMUP. Note that DiFMU production at time = 0 minutes initialized even prior to bead

separation, because all reagents were added to W1 stirred for 30 seconds and then transferred to W2. The separation results (figure 7.5(c)) yield a substantial increase in signal in W1 when working with concentrations of AP (714 μM and 7.14mM) above the bead capacity (71.4 μM). Obviously, the leftover enzyme molecules in W1 convert DiFMUP into DiFMU. Within 9 minutes these high concentrations of AP have converted ~100% DiFMUP. However for 37 μM approximately half the working bead capacity, the signal remains nearly constant throughout 15 minutes. Assuming linear dependence of $v_{\max}$ on enzyme concentration ($v_{\max} = \frac{0.668}{7.14}[enzyme]$) at least up to 7.14 μM, we estimate that only $7.14 \times K_m \ln(4/4 - [DiFMU]) \times time / 0.668 = 33.4nM$ (less than 0.5%) of enzyme remained in W1. Even at 100% bead capacity of 71.4±10μM, the results show infinitesimal production of DiFMU over time after separation.

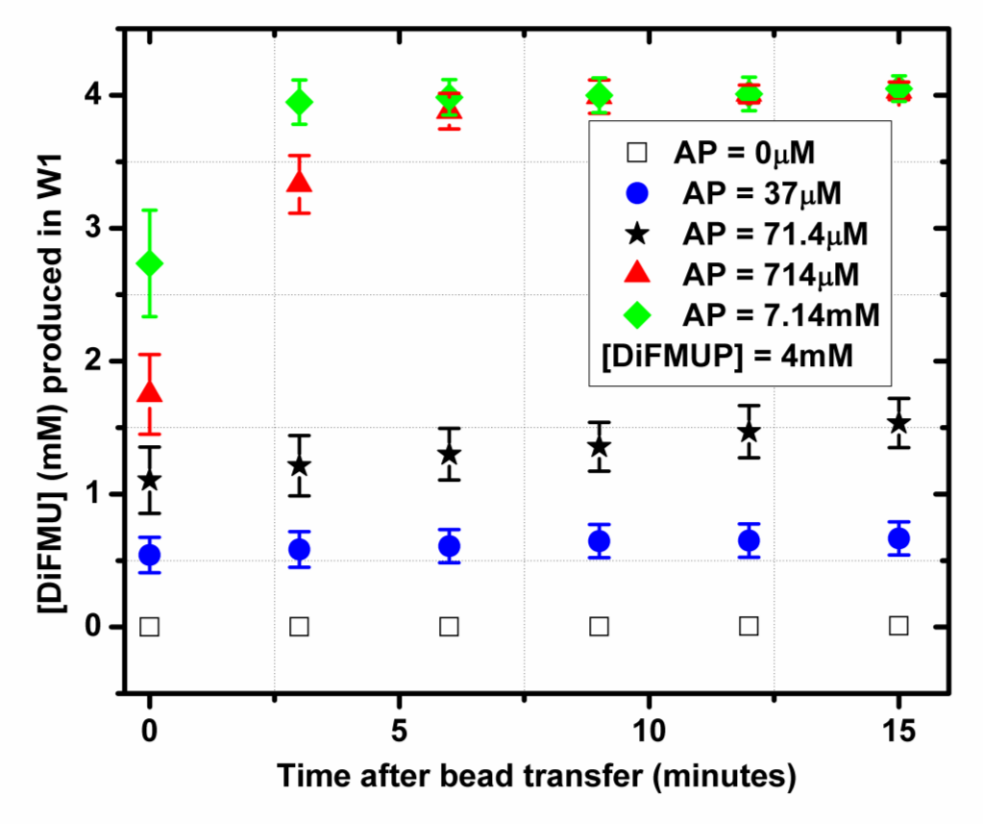

Figure 7.5(c). Separation assay. For [AP] = 37 μM and 71.4 μM W1 and W2 did not exhibit any considerable change in fluorescence after the bead transfer indicating that all of the AP available was bead bound. However when [AP] exceeded the capacity of the beads ([AP] =714 μM, 7.14 μM) the leftover AP in W1 was free to continue to produce DiFMU. The plotted results are the average values for three individual experiments and the error bars are generated from the standard deviation of the data.

This analysis shows that only 120 nM (less than 1.7%) of enzyme remained in W1. These results suggest that the magnetic beads are effective for separations dependent upon the streptavidin-biotin bond, so far as the binding events are within the capacity of the beads. The results also verify that there was a minimal quantity of beads remaining in W1 after separation.

7.5. Conclusion

Our work shows a novel separation technique with the following features **(a)** the rapid motion of beads through microchannel fluid provides near zero carry-over of

unbound molecules; **(b)** it does not require flow of sample solution (from W1) containing target molecules. The capture/binding of targets occurs in the reservoir, so that our method uniquely processes large amount of sample for rapid separation; **(c)** it can separate at high efficiency without using any membrane or pumps. Thus, it is quite useful for point of care devices.

Our chip design showed an insignificant amount of non-specific transfers, highly specific transfer of AP and high magnetic bead transfer percentages. The tapering of the microfluidic channel facilitatedtransfer of the beads from W1 into the channel and minimal diffusion from the channel into W2. The channel dimensions and the strength of the magnet can be customized depending on the desired total bead mass, transfer rate, diffusion sensitivity, and velocity in the microchannel. This investigation presents the parameters of this quick method on a microchip platform with many possible applications. The proposed technique can be used to improve a number of assays, including DNA isolation[4] and amplification, blood plasma separation[21] and peptide isolation.

Applying techniques from molecular biology on microchips has the possibility to make assays faster and cheaper. Microchips with zero flow conditions are simpler than a continuous flow micro-reactor and have a practical advantage in POC settings. Although zero flow reactors are very sensitive to hydrodynamic flow and bubble formation. A small assay kit with this technique would be easy to use in the field, where there is no need for an additional device applying a continuous flow though the chip. Our method would eliminate the need for continuous flow in established techniques for DNA isolation and blood plasma separation using a microchip. Although the optics used in our assays

are not ideal for POC applications, optical technologies are currently being developed for convenient POC applications such as cell phone based microscopes for monitoring cells[22],detection of waterborne parasites[23], and detection of infectious diseases[24].

The minimal diffusion of this microchip design could allow a multi-well system with different reagents in each well. Moving molecules such as RNA and DNA on the beads on beads between the wells would allow many steps (capture, separation, isolation, amplification and detection) to take place in one assay. Another example could be protein isolation and detection from a blood sample. Additionally, protein purification on a microchip format may be useful as a preparation step for analysis demanding low substrate contamination such as mass spectrometry. Some studies have been done for protein movement[25] and purification by isoelectric focusing[26] on microchips, but utilizing the method described in this paper method would be a novel simplified approach.

Investigating the effects of diffusion on more complex chip designs should be examined, since biological applications pull from a large pool of parameters. Diffusion rates at different SPS sizes and velocities would also be valuable to investigate further.

7.6. Acknowledgments

We would like to thank Tom Erkers for gathering preliminary data and Jinkee Lee for help on simulations. We acknowledge the support of the National Science Foundation (CBET 0653835), the National Health Institute (Grant No. 1R21 A1073808-01 A1), and the partial financial support of the NASA RI Fellowship for this research.

7.7. References

1 DeLouise, L. A. & Miller, B. L. Enzyme Immobilization in Porous Silicon: Quantitative Analysis of the Kinetic Parameters for Glutathione-S-transferases. *Analytical Chemistry* **77**, 1950-1956, doi:10.1021/ac0486185 (2005).

2 Wu, G. *et al.* Assay development and high-throughput screening of caspases in microfluidic format. *Combinatorial Chemistry & High Throughput Screening* **6**, 303-312 (2003).

3 Bienvenue, J. M., Duncalf, N., Marchiarullo, D., Ferrance, J. P. & Landers, J. P. Microchip-Based Cell Lysis and DNA Extraction from Sperm Cells for Application to Forensic Analysis. *Journal of Forensic Sciences* **51**, 266-273, doi:10.1111/j.1556-4029.2006.00054.x (2006).

4 Duarte, G. R. M. *et al.* Characterization of dynamic solid phase DNA extraction from blood with magnetically controlled silica beads. *Analyst* **135**, 531-537 (2010).

5 Giordano, B. C., Ferrance, J., Swedberg, S., Hühmer, A. F. R. & Landers, J. P. Polymerase Chain Reaction in Polymeric Microchips: DNA Amplification in Less Than 240 Seconds. *Analytical Biochemistry* **291**, 124-132, doi:10.1006/abio.2000.4974 (2001).

6 Yershov, G. *et al.* DNA analysis and diagnostics on oligonucleotide microchips. *Proceedings of the National Academy of Sciences of the United States of America* **93**, 4913-4918 (1996).

7 Eteshola, E. & Leckband, D. Development and characterization of an ELISA assay in PDMS microfluidic channels. *Sensors and Actuators B: Chemical* **72**, 129-133, doi:10.1016/s0925-4005(00)00640-7 (2001).

8 Grützkau, A. & Radbruch, A. Small but mighty: How the MACS®-technology based on nanosized superparamagnetic particles has helped to analyze the immune system within the last 20 years. *Cytometry Part A* **77A**, 643-647, doi:10.1002/cyto.a.20918 (2010).

9 Kim, B. C., Ju, M. K., Dan-Chin-Yu, A. & Sommer, P. Quantitative Detection of HIV-1 Particles Using HIV-1 Neutralizing Antibody-Conjugated Beads. *Analytical Chemistry* **81**, 2388-2393, doi:10.1021/ac802267u (2009).

10 Berry, S. M., Strotman, L. N., Kueck, J. D., Alarid, E. T. & Beebe, D. J. Purification of cell subpopulations via immiscible filtration assisted by surface tension (IFAST). *Biomed Microdevices* **13**, 1033-1042, doi:DOI 10.1007/s10544-011-9573-z (2011).

11 Berry, S. M., Alarid, E. T. & Beebe, D. J. One-step purification of nucleic acid for gene expression analysis via Immiscible Filtration Assisted by Surface Tension (IFAST). *Lab Chip* **11**, 1747-1753, doi:Doi 10.1039/C1lc00004g (2011).

12 Kerby, M. B., Legge, R. S. & Tripathi, A. Measurements of Kinetic Parameters in a Microfluidic Reactor. *Analytical Chemistry* **78**, 8273-8280, doi:10.1021/ac061189l (2006).

13 Gijs, M. A. M. Magnetic bead handling on-chip: new opportunities for analytical applications. *Microfluidics and Nanofluidics* **1**, 22-40, doi:10.1007/s10404-004-0010-y (2004).

14 Pamme, N. Magnetism and microfluidics. *Lab on a Chip* **6**, 24-38, doi:Doi 10.1039/B513005k (2006).

15 Choi, J. W. *et al.* An integrated microfluidic biochemical detection system for protein analysis with magnetic bead-based sampling capabilities. *Lab on a Chip* **2**, 27-30, doi:Doi 10.1039/B1077540n (2002).

16 Hahn, Y. K. *et al.* Magnetophoretic immunoassay of allergen-specific IgE in an enhanced magnetic field gradient. *Anal Chem* **79**, 2214-2220, doi:Doi 10.1021/Ac061522l (2007).

17 Yu, X. B. *et al.* mu FBI: A Microfluidic Bead-Based Immunoassay for Multiplexed Detection of Proteins from a mu L Sample Volume. *Plos One* **5**, doi:ARTN e13125 DOI 10.1371/journal.pone.0013125 (2010).

18 Segel, I. H. *Enzyme Kinetics: Behavior and Analysis of Rapid Equilibrium and Steady State Enzyme Systems* (Wiley, 1993).

19 Jouzi, M., Kerby, M. B., Tripathi, A. & Xu, J. Nanoneedle method for high-sensitivity low-background monitoring of protein activity. *Langmuir* **24**, 10786-10790, doi:Doi 10.1021/La703630a (2008).

20 Adamson, A. W. *Physical Chemistry of Surfaces*. 5th edn, (John Wiley & Sons, 1990).

21 Yang, S., Undar, A. & Zahn, J. D. A microfluidic device for continuous, real time blood plasma separation. *Lab on a Chip* **6**, 871-880, doi:10.1039/b516401j (2006).

22 Ozcan, A. & Demirci, U. Ultra wide-field lens-free monitoring of cells on-chip. *Lab Chip* **8**, 98-106, doi:10.1039/b713695a (2008).

23 Mudanyali, O., Oztoprak, C., Tseng, D., Erlinger, A. & Ozcan, A. Detection of waterborne parasites using field-portable and cost-effective lensfree microscopy. *Lab Chip* **10**, 2419-2423, doi:10.1039/c004829a (2010).

24 Mudanyali, O. *et al.* Integrated rapid-diagnostic-test reader platform on a cellphone. *Lab Chip*, doi:10.1039/c2lc40235a (2012).

25 Johansson, L. *et al.* A magnetic microchip for controlled transport of attomole levels of proteins. *Lab on a Chip* **10**, 654-661 (2010).

26 Jensen, K. F., Wen, J. A. & Albrecht, J. W. Microfluidic preparative free-flow isoelectric focusing in a triangular channel: System development and characterization. *Electrophoresis* **31**, 1606-1614, doi:10.1002/elps.200900577 (2010).

CHAPTER 8

ENGINEERING INSIGHTS IN MULTIPLEXING REAL-TIME NUCLEIC ACID SEQUENCE BASED AMPLIFICATION (NASBA).

8.1. Abstract

Nucleic acid sequence based amplification (NASBA) offers huge potential for low-cost, point-of-care (POC) diagnostic devices, but has been limited by high false-positive rates and the challenges of primer design. We offer a systematic analysis for NASBA design, with a view towards expanding its applicability. We examine the parameters that effect dimer formations, providing a framework for designing NASBA primers that will reduce false positive results and make NASBA suitable for more POC diagnostic applications. First, we present the theory behind primer dimerizations and the appropriate measures to avoid hybridizations that inhibit the NASBA reaction. We also examine the factors and parameters to consider when designing a real-time NASBA system using molecular beacon detection, particularly when multiplexing. Then we compare three different oligonucleotide sets to examine 1) the inhibitory effect of dimer formations, 2) false positives with poorly designed primers, and 3) the effect of beacon target location during real-time NASBA. The required T7 promoter sequence adversely affects the reaction kinetics, although the common abridged sequence canimprove

kinetics without sacrificing accuracy. We demonstrated that poorly designed primers undergo real-time exponential amplification in the absence of target RNA, resulting in false positives with a time to half of the peak value ($t_{1/2}$) of 50 minutes compared to 45 minutes for true positives. Redesigning the oligonucleotides to avoid inhibitory dimers eliminated false positives and reduced the true positive $t_{1/2}$ by 10 minutes. Finally, we confirm the efficacy of two molecular beacon design schemes, and discuss their multiplexing utility in two clinical scenarios.

8.2. Introduction

Since the early 90s [1], nucleic acid sequence based amplification (NASBA) has provided an attractive alternative to PCR for the amplification of RNA. It is routinely used in the clinical diagnosis of many single stranded RNA viruses including influenza A [2], foot-and-mouth virus [3,4], severe acute respiratory syndrome (SARS), coronavirus [5,6], West Nile virus [7], human bocavirus (HBoV) [8], and most importantly HIV [9,10]. NASBA offers huge potential for low-cost, portable diagnostic devices, because unlike PCR, NASBA is isothermal. NASBA often runs faster than PCR, it compares favorably with regards to sensitivity and convenience [11], and it is preferred over PCR for clinical HIV samples [10,12]. Recently, diagnostic NASBA assays integrated with microfluidic systems have shown improvements over conventional bench-top techniques [13]. Microfluidic hardware decreases the reagent use and energy consumption of the isothermal system by decreasing the reaction volume. Additionally, the small reaction volumes required by microfluidic chips (10nL - 2μL) concentrate the target molecule of interest to improve primer binding and reaction kinetics. Because of advances in microfluidics, NASBA is poised to offer major advantages in sequence-based diagnosis.

Despite these advantages, NASBA has not been used to its full potential because of the inhibitory secondary structure of RNA, which makes primer design and multiplexing difficult. Hybridization sites on long, viral RNA strands require rigid oligonucleotide design, and only a small fraction of oligonucleotides hybridize efficiently to RNA [14], making many conserved regions unsuitable as NASBA priming sites. Even heating NASBA reagents to 65°C before adding enzymes [15] and selecting primer sites 100-200 nucleotides apart fail to prevent inhibitory secondary structures [16]. Primer dimerization can significantly increase the rate of false positives, which is extremely dangerous in certain clinical tests. Furthermore, NASBA initiates with a non-cyclic phase, as shown in figure 1, which depends on primers hybridizing multiple times with an often tangled RNA structure and two relatively long initial reverse transcription steps in order to produce the amplicon used during the cyclic phase.

NASBA can yield end-point results or real-time results using fluorophores, making it analogous to PCR and real-time PCR, respectively. End-point NASBA is usually accompanied by a gel electrophoresis, which determines the size of nucleotides and detects size-specific sequences. Real-time NASBA is often advantageous because it does not require gel electrophoresis: it uses molecular beacons or other forms of fluorophores for sequence detection. The use of fluorophores is conducive to inexpensive diagnostic devices utilizing optics, such as LEDs and photodiodes. However, due to the lack of nucleotide size detection, real-time NASBA is more susceptible to false positives. When NASBA works properly, the product of the cyclic amplification is a portion of RNA antisense to the original RNA target, as shown in figure 8.1.

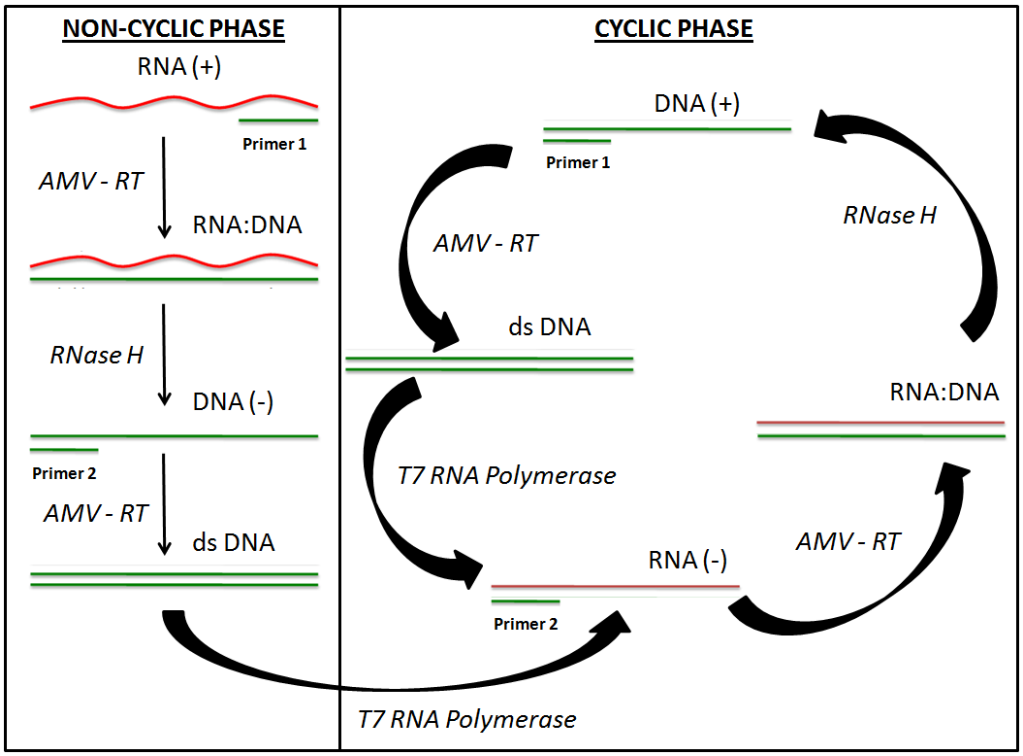

Figure 8.1. Traditional NASBA. Amplification begins with a non-cyclic phase which creates the RNA product (RNA -). RNA(-) is the product and template of the cyclic amplification phase and can be detected by end-point gel electrophoresis or in real-time NASBA using molecular beacons.

In real-time NASBA, molecular beacons hybridize with the RNA product as the amplification cycle progresses. Real-time NASBA can yield false positive results when the molecular beacon hybridizes with a non-specific DNA and/or RNA molecule. Furthermore, if the NASBA system is poorly designed, it may amplify non-target sequences that non-specifically hybridize with the molecular beacon, mimicking the expected time real-time exponential amplification profile. This is further complicated during multiplexing, when several targets are grouped, amplified and detected using one molecular beacon.

New RNA detection techniques[17,18] amplify a short probe molecule using NASBA. The short probe serves as an indicator and amplicon for the much longer target

RNA. These techniques overcome some of the traditional limitations of NASBA; (1) primers for the short amplicon are easy to design and use with excellent hybridization kinetics, (2) pre-heating is not required because there is no inherent secondary structure of the short probe, and (3) the relatively long non-cyclic phase of NASBA is bypassed because the short probe is the amplicon used during the cyclic phase, resulting in faster amplification and detection.

Although NASBA has been widely explored and developed for a variety of microfluidic diagnostic applications, the formation of inhibitory dimers and their effect on the reaction kinetics in traditional or short amplicon NASBA has not been adequately addressed. Most literature denotes the importance of avoiding dimer formations during PCR and NASBA, but a systematic description of dimer formations that occur in NASBA and design techniques to avoid such dimers is not yet available, nor for avoiding non-specific molecular beacon hybridizations.

In this chapter, we detail the cause and effect of dimer formations and we give examples of dimers that interfere with real-time NASBA and non-specific hybridizations of molecular beacons resulting in false positives. We suggest ways to avoid dimerizations and false positives caused by non-specific molecular beacon binding. Additionally, we discuss molecular beacon design parameters for effective multiplex NASBA assays.

8.3. Design constraints

8.3.1. Inhibitory and non-inhibitory dimer formations

Primer-beacon and other non-specific hybridizations are bound to occur in a dynamic system like NASBA. These non-specific and confounding hybridizations are considered non-inhibitory when their melting temperatures are well below the

amplification reaction temperature (41^{o}C). In most NASBA reactions, a denaturation step (65^{o}C) is used to loosen the secondary structure of the target oligonucleotide before amplification occurs. Any non-inhibitory dimer formations or target hair-pin structures are melted, so that the amplification can proceed uninhibited.

In contrast, inhibitory dimer formations involve non-specific hybridizations characterized by T_m values close, equal to, or exceeding the amplification reaction temperature. Inhibitory dimerization is a common source of false-positives. Of all of the possible dimer formations, the most likely to disturb normal reaction kinetics involves the primer containing the T7 promoter sequence, because this sequence is directly involved in the amplification process by way of T7 RNA polymerase. This article will focus on dimerizations caused by the T7 sequence.

8.3.2. Dimer formation caused by T7 promoter sequence

The T7 promoter sequence (figure 8.2), which must be incorporated into one of the primers, can be particularly cumbersome when designing NASBA primers because it is inherently prone to forming dimers. If the primer containing the T7 promoter sequence forms a dimer, the T7 RNA polymerase will act aberrantly, likely resulting in reduced reaction kinetics and/or a false positive.

Figure 8.2. T7 promoter sequence. The underlined sequence represents the abridged sequence and the +1 base is the first base incorporated into the RNA during transcription.

8.3.3. Optimizations to reduce inhibitory structures

The Mg^{++} concentration can be modified as a first attempt to reduce the potential hybridization energy of the T7 primer dimer, although it should be modified with caution.

Very slight modifications to [Mg^{++}] can result in drastically different hybridization energies for all oligonucleotides in the assay[19]. Thus reducing [Mg^{++}] in order to reduce the hybridization energy of the T7 primer dimer may negatively affect key hybridizations in the assay (i.e. primers + target oligonucleotide).

When primer sites are fairly abundant, primers should be redesigned to hybridize with the target oligonucleotide at a new location to achieve minimal dimer hybridization without significantly sacrificing the primer-target oligonucleotide hybridization energy. However, most new and next-generation sequencing applications—such as mutation detection and viral sub-typing—require primers for very specific oligonucleotide targets.

8.3.4. Molecular beacon design for NASBA

In NASBA, the molecular beacon is designed to either hybridize with (i) the primer 2 reverse complement (RC) region or (ii) the middle target region of the target RNA as shown in figure 8.3.

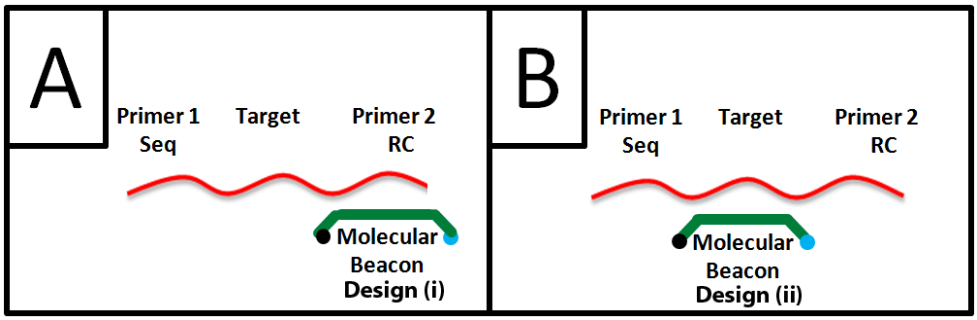

Figure 8.3. Molecular beacon designs. **(a)** Beacon design (i) is designed for multiplexing. A variety of probes can be used to target a group of individual sequences all of which are indicated with one molecular beacon. **(b)** Beacon design (ii) is designed for targeting a specific sequence rather than targeting a group of sequences.

In design (i), primer 2 is competitive with the molecular beacon to hybridize with the primer 2 RC region, sacrificing reaction kinetics. However, design (i) enables effective multiplexing—an unlimited number of potential target sequences may be used

while using only one molecular beacon. In design (ii), there is no competition in binding sites. However, because the beacons are target-specific, one beacon design may only be used for one sequence-specific target. Both beacon system designs have their ideal applications. For example, design (i) is ideal for HIV-1 mutation detection: a large number of HIV-1 mutations impart drug resistance so it is very important to screen for many mutations in parallel. Although design (i) can target all known mutations, a positive result does not indicate which mutation is present. This design does not yield sequence-specific results, but it nevertheless yields clinically relevant information in HIV drug resistance testing. Design (ii) is ideal for Influenza virus sub-typing. This design yields sequence-specific results, indicating which type(s) of influenza are present within a given sample, (H1N1, H3, H5, etc.) and it avoids premature transcription abortion by the T7 RNA polymerase, which has been observed in previous work[17].

8.4. Materials and methods

We engineered a HIV-1 oligonucleotide set without systematic consideration of primer design (OLD), a systematically designed SMART HIV-1 set (NEW) and an H3 Influenza set for SMART. Both HIV-1 sets were used for real-time NASBA detection using beacon design (i), while the H3 Influenza set used beacon design (ii). 1nM of amplifiable probe was used as the starting template for each set in our experiments. These synthetic oligonucleotides were purchased from Integrated DNA Technologies (Coralville, IA) and their nucleotide sequences are listed in table 8.1. Each oligonucleotide set was theoretically analyzed to predict hybridization energies and potential dimer formations and illustrated using DI-nucleic acid hybridization and

melting prediction (DINAMelt Server, RNA Institute, SUNY Albany, Albany, NY; available at http:// http://mfold.rna.albany.edu) [20].

Oligonucleotide	HIV-1 K103N Sequences (OLD)
Probe	5' - *TCAAGAGTAGACACCTGTTACCGAT* **TTGTTCTTCTTTAACCCTG** GTAATCAGATCAGAGCAATACGTCA - 3'
Primer 1 (P1)	5' - **taatacgactcactatagg** TGACGTATTGCTCTGATCTGATTAC - 3'
P1-Probe RNA Product	5' - **gg** UGACGUAUUGCUCUGAUCUGAUUAC **CAGGGUUAAAGAAGAACAA** *AUCGGUAACAGGUGUCUACUCUUGA* - 3'
Primer 2 (P2)	5' - *TCAAGAGTAGACACCTGTTACCGAT* - 3'
Molecular Beacon	5' - **/6-FAM/CGCG** *TCAAGAGTAGACACCTGTTACCGAT* **CGCG/3IABlk_FQ/** - 3'

Oligonucleotide	HIV-1 K103N Sequences (NEW)
Probe	5' - *TCAAGAGTAGACACCTGTTACCGAT* **TTGTTCTTCTTTAACCCTG** TATATTTTGGTGGTTGCAGAATAT - 3'
Primer 1 (P1)	5' - **taatacgactcactatagg** ATATTCTGCAACCACCAAAATATA - 3'
P1-Probe RNA Product	5' - **gg** AUAUUCUGCAACCACCAAAAUAUA **CAGGGUUAAAGAAGAACAA** *AUCGGUAACAGGUGUCUACUCUUGA* - 3'
Primer 2 (P2)	5' - *TCAAGAGTAGACACCTGTTACCGAT* - 3'
Molecular Beacon	5' - **/6-FAM/CGCG** *TCAAGAGTAGACACCTGTTACCGAT* **CGCG/3IABlk_FQ/** - 3'

Oligonucleotide	H3 Influenza Sequences
Probe	5' - *TCAACTCATCACACAGGATCAGCAT* **ACTCCAAATGGAAGCATTCCCAATG** ATTTTGGTGGTTGCAGAATCT - 3'
Primer 1 (P1)	5' - **taatacgactcactatagg** AGATTCTGCAACCACCAAAAT - 3'
P1-Probe RNA Product	5' - **gg** AGAUUCUGCAACCACCAAAAU **CAUUGGGAAUGCUUCCAUUUGGAGU** *AUGCUGAUCCUGUGUGAUGAGUUGA* - 3'
Primer 2 (P2)	5' -*TCAACTCATCACACAGGATCAGCAT* - 3'
Molecular Beacon	5' - /6-FAM/CGCG **AAATGGAAGCATTCCCAATG** CGCG/3IABlk_FQ/ - 3'

Table 8.1. Poorly designed HIV-1 K103N oligonucleotide set (OLD), redesigned HIV-1 K103N oligonucleotide set (NEW), and H3 Influenza oligonucleotide set. The Probe sequences contain an underlined sequence which hybridizes with P1. The P1 sequences contain the T7 promoter sequence (lowercase & bold). The transcribed P1-Probe RNA product hybridizes with P2 (italics). In the HIV-1 oligonucleotide sets, the molecular beacon (italics) competes with P2 to hybridize with the P1-Probe RNA product. In the Influenza oligonucleotide set, the molecular beacon (underlined & bold) is designed to be sequence specific and hybridizes with the target region (underlined & bold) of the transcribed P1-Probe RNA product.

The reagents used for real-time NASBA and their concentrations at the final reaction volume (80 µL) were 40 mM Tris(pH 8.0), 12.5 mM MgCl2, 73.5 mM CH3COOK (KOAc), 5.25 mM dithiothreitol, 1.05 mM dNTP, 2.1 mM rNTP, 0.21 µM each primer, 52.5 nM molecular beacon, 15.75% dimethyl sulfoxide, 1.68 u/µL T7 RNA polymerase, 0.34 u/µL AMV-RT, 0.005 u/µL RNase-H, and 0.11 mg/mL bovine serum albumin (BSA). Samples were amplified in real-time for 90 minutes in BRAND disposable UV micro cuvettes(Wertheim, Germany) using a Photon Technology International Quantamaster™ spectrofluorometer (Birmingham, NJ) maintained at 41°C.

Enzymes and reagents used for real-time NASBA were purchased from Promega (Madison, WI).

8.5. Results

Hybridization energies and melting temperatures for the T7 full sequence and abridged sequence were calculated to be ΔG=-9.7 J/mol, T_m=50.6°C and ΔG=-3.7 J/mol, T_m=22.9°C, respectively (figure 8.4).

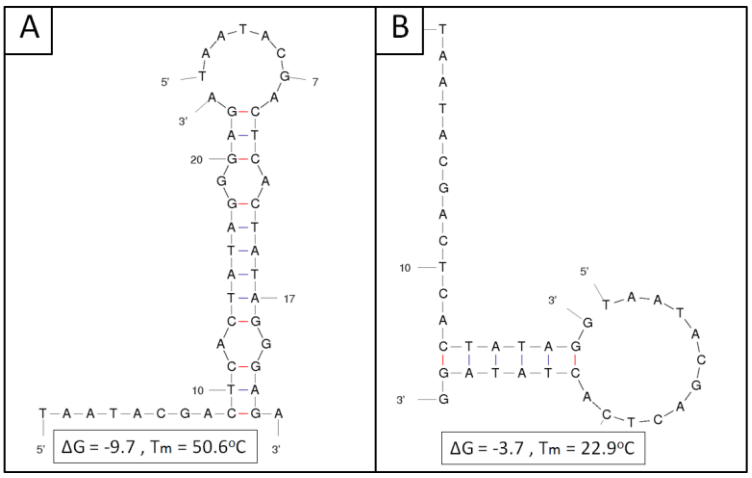

Figure 8.4. T7 promoter sequence dimer theoretical hybridization energies simulated with DINAMelt. Energy rules: DNA @ 41°C, C_T = 10µM, [Na^+] = 73.5mM, [Mg^{++}] = 12.5mM. **(a)** full sequence. **(b)** abridged sequence.

Hybridization energies for the OLD T7 primers were ΔG=-4.0 J/mol, T_m=7.3°C without any promoter sequence; ΔG=-7.6 J/mol, T_m=41.8°C with the abridged T7 promoter sequence; and ΔG=-11.3 J/mol, T_m=48.0°C with the full T7 promoter sequence.

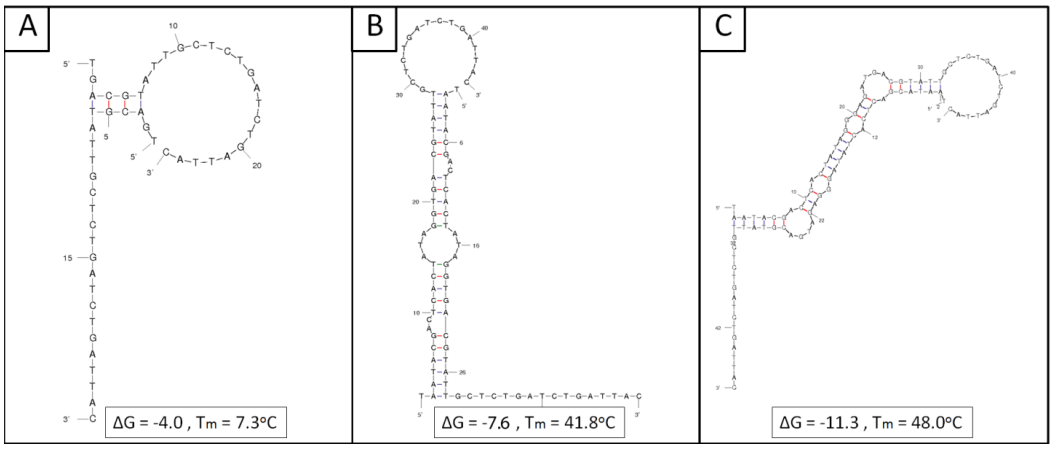

Figure 8.5. Primer dimer formations (OLD). Energy rules: DNA @ 41°C, C_T = 10µM, [Na^+] = 73.5mM, [Mg^{++}] = 12.5mM. **(a)** primer alone **(b)** primer with abridged T7 promoter **(c)** primer with full T7 promoter.

Table 8.2 outlines the hybridization energies and melting points for the OLD oligonucleotide set; notably primer 1 forms a dimer with ΔG=-9.2 J/mol, T_m=41.8°C.

HIV-1 Oligos (OLD)	P1		P2		Beacon		Probe	
	ΔG	T_m(°C)	ΔG	T_m(°C)	ΔG	T_m(°C)	ΔG	T_m(°C)
P1	**-9.2**	**41.8**	-6	28	-6	28	-24.7	70
P2			-2.1	-15	-3	-5.5	-3.4	20
Beacon					-5.7	32.4	-3.4	20
Probe							-3.6	5

Table 8.2. Theoretical hybridization ΔG and T_m values for all potential primer dimers and/or non-specific hybridizations in HIV-1 K103N oligonucleotide set (OLD). Energy rules: DNA @ 41°C, C_T = 10µM, [Na^+] = 73.5mM, [Mg^{++}] = 12.5mM.

Furthermore, this P1-P1 dimer was calculated to form a secondary hybridization to the beacon at ΔG=-14.0 J/mol, T_m=55.3°C (table 8.3).

HIV-1 Oligos (OLD)	P1		P2		Beacon		Probe		P1+P1 RNA		P1+Probe RNA	
	ΔG	T_m(°C)	ΔG	T_m(°C)	ΔG	T_m(°C)	ΔG	T_m(°C)	ΔG	T_m(°C)	ΔG	T_m(°C)
P1+P1 RNA	-9.3	45	-13	55.7	**-14**	**55.3**	-36	83.9	-5.6	-6.4	-9.9	33
P1+Probe RNA	-11	46.1	-38	88.2	-39	88.4	-110	99.5			-19	48.7

Table 8.3. Theoretical hybridization ΔG and T_m values for potential RNA product hybridizations with HIV-1 K103N oligonucleotide set (OLD). Energy rules for DNA/RNA & RNA/RNA: RNA @ 41°C, C_T = 0.001µM, [Na^+] = 1 M (fixed), [Mg^{++}] = 0 M (fixed). Energy rules for DNA/DNA: DNA @ 41°C, C_T = 10µM, [Na^+] = 73.5mM, [Mg^{++}] = 12.5mM.

In contrast, analysis of the NEW set of oligos only predicted a strong hybridization between primer 1 and the probe—ΔG=-22.4 J/mol, T_m=68.4°C (table 8.4). The H3 Influenza analysis also predicted only one significant hybridization between primer 1 and the probe—ΔG=-22 J/mol, T_m=71.0°C (table 8.5).

HIV-1 Oligos (NEW)	P1		P2		Beacon		Probe		P1+Probe RNA	
	ΔG	T_m(°C)	ΔG	T_m(°C)	ΔG	T_m(°C)	ΔG	T_m(°C)	ΔG	T_m(°C)
P1	-3.7	22.9	-3.7	4.5	-3.7	4.5	-22.4	68.4	-4.1	14.5
P2			-2.1	-15	-3	5.5	-4.3	16.9	-26.1	73.8
Beacon					-5.7	32.4	-4.3	16.9	-26.3	75.1
Probe							-3.9	19.5	-70.7	82.7
P1+Probe RNA									-11.9	39.1

Table 8.4. Theoretical hybridization ΔG and T_m values for all potential primer dimers and/or non-specific hybridizations using redesigned HIV-1 K103N oligonucleotide set (NEW). Energy rules for DNA/RNA & RNA/RNA: RNA @ 41°C, C_T = 0.001µM, [Na^+] = 1 M (fixed), [Mg^{++}] = 0 M (fixed). Energy rules for DNA/DNA: DNA @ 41°C, C_T = 10µM, [Na^+] = 73.5mM, [Mg^{++}] = 12.5mM.

H3 Influenza Oligos	P1		P2		Beacon		Probe		P1+Probe RNA	
	ΔG	T_m(°C)	ΔG	T_m(°C)	ΔG	T_m(°C)	ΔG	T_m(°C)	ΔG	T_m(°C)
P1	-4.2	32	-3.8	14.5	-3.2	8.1	-22	71	-5.9	36.6
P2			-2.9	12.4	-3	-9.3	-3.3	9.8	-27	74
Beacon					-5.3	24.8	-3.9	2.5	-21.3	69.9
Probe							-4.1	22.3	-79.4	86.4
P1+Probe RNA									-27	53.5

Table 8.5. Theoretical hybridization ΔG and T_m values for all potential primer dimers and/or non-specific hybridizations in H3 Influenza oligonucleotide set. Energy rules for DNA/RNA & RNA/RNA: RNA @ 41°C, C_T = 0.001µM, [Na^+] = 1 M (fixed), [Mg^{++}] = 0 M (fixed). Energy rules for DNA/DNA: DNA @ 41°C, C_T = 10µM, [Na^+] = 73.5mM, [Mg^{++}] = 12.5mM.

Real-time NASBA amplification of six oligonucleotide sets resulted in an exponential increase in signal from the New, Old, and H3 Influenza sets when probe was included; a similar exponential increase was observed in the OLD set when probe was not included (figure 8.6). The NEW and H3 sets failed to show a significant increase in

signal when probe was not included. Time to half of the peak value ($t_{1/2}$) was 45 minutes for OLD, 35 minutes for NEW, 18 minutes for H3 Influenza, and 50 minutes for Old without probe.

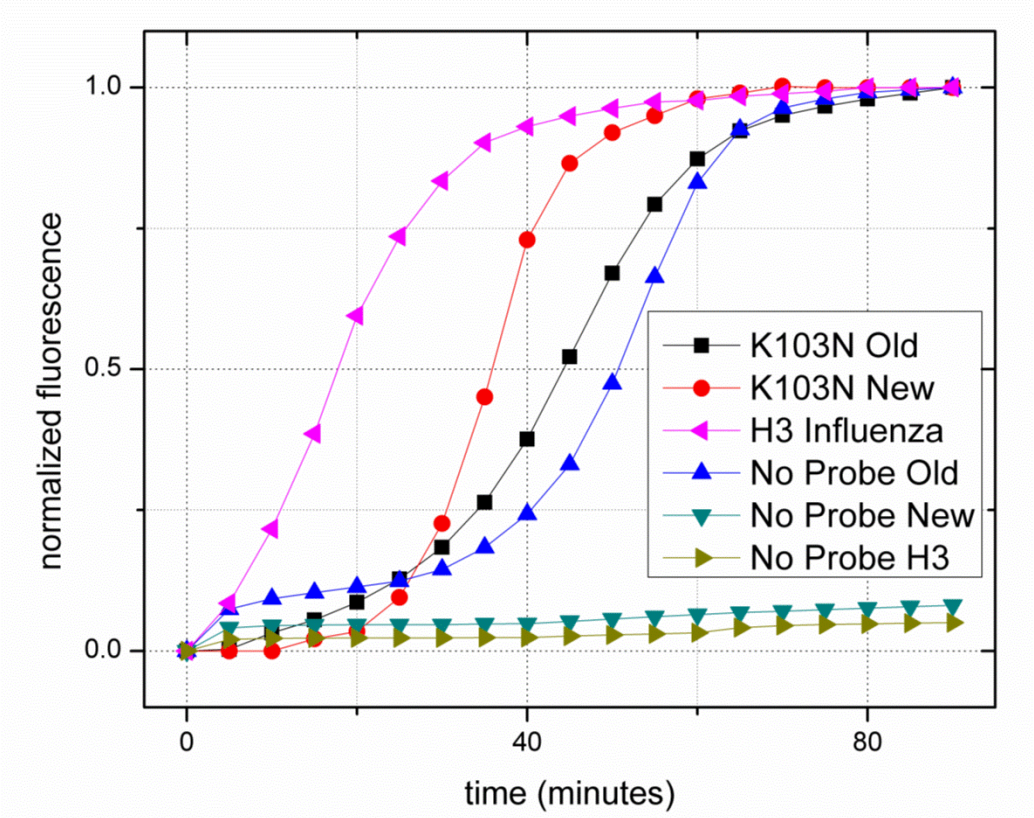

Figure 8.6. Real-time NASBA of poorly designed HIV-1 K103N oligonucleotide set (Old) vs. redesigned HIV-1 K103N set (New) vs. H3 Influenza oligonucleotide set. 1nM probes used and no probe controls included. Standard deviation was within 5% of results (error bars not shown).

8.6. Discussion

8.6.1. Thermodynamic evaluation of oligonucleotides using hybridization and melting predictions

Potential hybridizations/dimer formations were theoretically calculated. They are quantitatively represented by hybridization energy (ΔG) and melting temperature (T_m). A negative ΔG value indicates that the hybridization is energetically favorable and the T_m

represents the system in equilibrium at which half of the two oligonucleotides hybridize and the other half remains single stranded.

The T7 promoter sequence alone forms a very strong theoretical dimer with itself, even under optimal NASBA conditions. Although the T7 promoter sequence must be used to catalyze T7 RNA polymerase, the underlined sequence (figure 8.2), an abridged version, may be used for efficient transcription [21]. The abridged version significantly reduces the hybridization energy (increasing ΔG) and reduces T_m to the point where it would be considered non-inhibitory (figure 8.4).

Adding the T7 promoter sequence to the beginning of a primer adversely increases the self-hybridization energy and T_m of the primer. The example primer shown in figure 8.5 is from the poorly designed oligonucleotide set (OLD) for the NASBA amplification of a HIV-1 K103N sequence. This primer by itself is non-inhibitory, however the addition of the abridged T7 sequence causes an inhibitory dimer formation. This is further exacerbated by the full T7 promoter sequence.

A poorly designed primer will have inhibitory dimer formations and/or non-specific hybridizations. Screening for unwanted formations involves cross checking the ΔG and T_m values for all oligonucleotides used in the NASBA reaction at the appropriate reaction conditions. Table 8.2 shows these values for the poorly designed oligonucleotide set (OLD). The primer 1 (P1) and probe ΔG and T_m values (highlighted grey) show that P1 has a very strong affinity to its intended target probe. However, P1 also forms a strong self-dimer (highlighted grey & bold), albeit nowhere near as strong as the P1-Probe hybridization. In the presence of large quantities of probe, the P1 dimer will remain non-inhibitory. However as the concentration of probe decreases, the P1 dimer has a greater

inhibitory effect. For negative controls (i.e. no probe), the P1 dimer will become completely dominant in the reaction. The P1 dimer is capable of producing its own RNA product through NASBA amplification because it contains a T7 promoter region. As a result, not only is this P1 dimer RNA product detrimental to the reaction kinetics of NASBA, but it also has the potential to generate false positive results in real-time NASBA. It becomes impossible to distinguish between a false positive control (no probe) and a positive sample, because real-time NASBA results only indicate fluorescence values, not oligonucleotide lengths.

For the case of the poorly designed oligonucleotide set (OLD), an unexpected product emerges in addition to the expected P1-Probe transcribed RNA because of the presence of the T7 promoter sequence in the P1 dimer. Specifically, the P1 dimer is reverse transcribed to form a dsDNA template containing the T7 promoter region in two locations (figure 8.7a). Meanwhile, the P1-Probe hybrid is reverse transcribed and then T7 polymerase transcribes RNA as designed and expected (figure 8.7b). The transcribed RNA from the P1 dimer ds DNA template will interfere with the reaction kinetics because it contains two T7 promoter regions and misappropriates rNTPs. It also has the potential to hybridize with the beacon resulting in false positives.

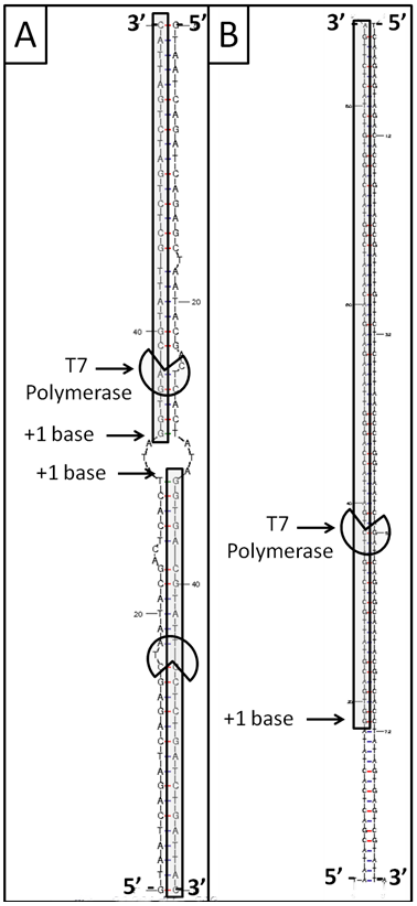

Figure 8.7. T7 polymerization of unexpected P1-P1 RNA. **(a)** There are two locations for the T7 polymerase to polymerize RNA since the T7 promoter exists on both strands 5'→3'. **(b)** T7 polymerization of expected P1-Probe RNA.

Table 8.3 demonstrates the theoretical hybridization of the expected P1-Probe transcribed RNA and the unexpected P1-P1 transcribed RNA with other. The P1+Probe RNA product is the desired RNA product of the NASBA reaction and it forms a strong bond with the molecular beacon (highlighted grey) indicating effective fluorescence detection. The P1+Probe RNA should also form a hybrid of similar strength with primer 2 (P2). This is also desirable and is required by the NASBA cycle shown previously in figure 1. However, DINAMelt analysis shows that the P1+Probe RNA actually forms its strongest bond with additional free-floating probe. This hybridization can be expected, because P1 and the probe are perfect reverse compliments. However, in practice the

much shorter and abundant P2 and beacon molecules are more likely hybridize with the P1+Probe RNA because of their relatively small size and much greater quantity than the probe.

The P1+P1 RNA product forms a relatively weak bond (highlighted gray & bold) with the molecular beacon. However, when there is a low concentration of probe, this relatively weak bond becomes strong and the molecular beacon will non-specifically hybridize with the P1-P1 RNA product resulting in false-positive fluorescence detection. Additionally, the P1-P1 RNA product forms a relatively strong bond (gray) with the probe which likely stifles the reaction kinetics.

8.6.2. Redesigning the primer avoids inhibitory dimer formation

The oligonucleotides can be redesigned to undergo fewer potential dimers and non-specific hybridizations. This is achieved by manually manipulating individual bases in the sequence of P1, so that there are fewer potential adenine-thymine and guanine-cytosine hydrogen bonds in the DINAmelt predicted hybridization. The required T7 promoter sequence gives primer 1 inherent minimum ΔG and T_m values that make it susceptible to dimerization (figure 8.5). After manipulating the original P1 sequence used, we achieve ΔG and T_m values for the P1 dimer matching those of the abridged T7 promoter sequence dimer alone ($\Delta G = -3.7$, $T_m = 22.9$ºC); thus we have designed P1 such that dimerization is as unfavorable as theoretically possible for our given reaction conditions. The probe sequence is modified in parallel for effective hybridization with the new P1 sequence. A cross-check of all potential dimers and/or non-specific hybridizations is shown in Table 4. Although there is a slight decrease in ΔG and T_m for the P1-Probe hybridization, the potential for P1 inhibitory dimerization has been

eliminated because the dimers dissociate far below the reaction temperature. Finally, H3 Influenza oligonucleotides were also cross-checked for potential dimers and/or non-specific hybridizations (Table 8.5). The P1-P1 dimer dissociates well below the reaction temperature and P1-Probe hybridization is relatively strong and occurs well above the reaction temperature.

8.6.3. Real-time NASBA using molecular beacon detection

Three real-time NASBA runs of each oligonucleotide set were performed (nine runs in total) and the average of the real-time fluorescence results for each of the samples are shown in figure 8.6. Controls without probe were included for each oligonucleotide set. The No Probe NEW and No Probe H3 conditions show negligible increases in fluorescence, while the No probe OLD negative control exemplifies the inhibitory effects and false positive result of the P1-P1 dimer in the HIV-1 oligonucleotide set. The OLD oligonucleotide set would certainly fail in practical applications such as point-of-care devices. The redesigned oligonucleotide set alleviates the issues of primer dimerizations and subsequent false positive results during real-time NASBA. Figure 8.6 shows that the poorly designed K103N oligonucleotide set does not exhibit optimal reaction kinetics for the amplification of 1nM probe in comparison to the redesigned set (NEW), because the new set has a lower $t_{1/2}$ value and a valid negative control. While the Influenza oligonucleotide set did not offer any significant improvements in predicted hybridization energies compared to the NEW oligonucleotide set, it did show dramatic improvements in NASBA reaction speed. The only significant difference in the H3 oligonucleotide design was the beacon hybridization location. The H3 Influenza set has the best kinetics

of all three sets, which indicates that the beacon location had a significant effect on reaction.

8.7. Conclusion

Careful considerations to ensure a weak ΔG (greater than -5) and low T_m (less than 35°C) for the T7 primer dimer and non-specific molecular beacon hybridizations should be taken when designing real-time NASBA systems. Poorly considered primers can not only decrease reaction kinetics, but can also increase the rate of false positive, which is dangerous in the context of clinical HIV testing. Two approaches to primer design significantly improve reaction kinetics and test accuracy—reducing the length of the T7 promoter sequence to the abridged version and reducing the potential number of adenine-thymine and guanine-cytosine hydrogen bonds in the primer. Furthermore, effective primer design requires DINAMelt analysis of the bond strength not only between primers and probes, but also between potential dimers and the beacon. A safe approach to improve reaction kinetics is to redesign the probes to avoid dimers at 41°C, because that is the optimal temperature of the reaction enzymes. Salt ion concentrations may also be altered but have significant implications for all hybridization energies and should be avoided if possible. The application of the NASBA assay is an important design parameter to consider since we have shown that a real-time NASBA system capable of detecting a group of sequences is less efficient than a real-time NASBA system only detecting one target. Successful primer design is not simply a matter of improving the efficiency of NASBA-based clinical assays, it is crucial to their accuracy as well.

8.8. Acknowledgment

We would like to thank Clay Wiske from the Warren Alpert Medical School for his help running NASBA assays, collecting results and providing edits.

8.9. References

1 Compton, J. Nucleic-Acid Sequence-Based Amplification. *Nature* **350**, 91-92 (1991).

2 Collins, R. A. *et al.* Detection of highly pathogenic and low pathogenic avian influenza subtype H5 (Eurasian lineage) using NASBA. *J Virol Methods* **103**, 213-225, doi:S0166093402000344 [pii] (2002).

3 Collins, R. A. *et al.* A method to detect major serotypes of foot-and-mouth disease virus. *Biochem Biophys Res Commun* **297**, 267-274, doi:S0006291X02021782 [pii] (2002).

4 Lau, L. T. *et al.* Detection of foot-and-mouth disease virus by nucleic acid sequence-based amplification (NASBA). *Vet Microbiol* **126**, 101-110, doi:S0378-1135(07)00335-5 [pii] 10.1016/j.vetmic.2007.07.008 (2008).

5 Chantratita, W., Pongtanapisit, W., Piroj, W., Srichunrasmi, C. & Seesuai, S. Development and comparison of the real-time amplification based methods--NASBA-Beacon, RT-PCR taqman and RT-PCR hybridization probe assays--for the qualitative detection of sars coronavirus. *Southeast Asian J Trop Med Public Health* **35**, 623-629 (2004).

6 Keightley, M. C., Sillekens, P., Schippers, W., Rinaldo, C. & George, K. S. Real-time NASBA detection of SARS-associated coronavirus and comparison with

real-time reverse transcription-PCR. *J Med Virol* **77**, 602-608, doi:10.1002/jmv.20498 (2005).

7 Lanciotti, R. S. & Kerst, A. J. Nucleic acid sequence-based amplification assays for rapid detection of West Nile and St. Louis encephalitis viruses. *J Clin Microbiol* **39**, 4506-4513 (2001).

8 Bohmer, A. *et al.* Novel application for isothermal nucleic acid sequence-based amplification (NASBA). *J Virol Methods* **158**, 199-201, doi:S0166-0934(09)00062-7 [pii] 10.1016/j.jviromet.2009.02.010 (2009).

9 Vandamme, A. M. *et al.* Quantification of HIV-1 RNA in plasma: comparable results with the NASBA HIV-1 RNA QT and the AMPLICOR HIV monitor test. *J Acquir Immune Defic Syndr Hum Retrovirol* **13**, 127-139 (1996).

10 Vandamme, A. M. *et al.* Detection of HIV-1 RNA in plasma and serum samples using the NASBA amplification system compared to RNA-PCR. *Journal of Virological Methods* **52**, 121-132 (1995).

11 Schneider, P. *et al.* Real-time nucleic acid sequence-based amplification is more convenient than real-time PCR for quantification of Plasmodium falciparum. *J Clin Microbiol* **43**, 402-405, doi:43/1/402 [pii] 10.1128/JCM.43.1.402-405.2005 (2005).

12 Dyer, J. R. *et al.* Quantitation of human immunodeficiency virus type 1 RNA in cell free seminal plasma: comparison of NASBA™ with Amplicor™ reverse transcription-PCR amplification and correlation with quantitative culture. *Journal of Virological Methods* **60**, 161-170 (1996).

13 Yobas, L. *et al.* in *Sensors, 2005 IEEE.* 4 pp.

14 Luebke, K. J., Balog, R. P. & Garner, H. R. Prioritized selection of oligodeoxyribonucleotide probes for efficient hybridization to RNA transcripts. *Nucleic Acids Research* **31**, 750-758 (2003).

15 Guatelli, J. C. *et al.* Isothermal, in vitro amplification of nucleic acids by a multienzyme reaction modeled after retroviral replication. *Proceedings of the National Academy of Sciences* **87**, 1874-1878 (1990).

16 Deiman, B., van Aarle, P. & Sillekens, P. Characteristics and applications of nucleic acid sequence-based amplification (NASBA). *Molecular biotechnology* **20**, 163-179 (2002).

17 McCalla, S. E. *et al.* A Simple Method for Amplifying RNA Targets (SMART). *The Journal of Molecular Diagnostics* **14**, 328-335, doi:10.1016/j.jmoldx.2012.02.001 (2012).

18 Ong, C. *et al.* Ligation with Nucleic Acid Sequence-Based Amplification. *J Mol Diagn* **14**, 206-213, doi:DOI 10.1016/j.jmoldx.2012.01.004 (2012).

19 Owczarzy, R., Moreira, B. G., You, Y., Behlke, M. A. & Walder, J. A. Predicting stability of DNA duplexes in solutions containing magnesium and monovalent cations. *Biochemistry-Us* **47**, 5336-5353, doi:Doi 10.1021/Bi702363u (2008).

20 Markham, N. R. (University at Albany: The RNA Institute College of Arts and Sciences, 2006).

21 Technologies, L. *The Basics: In Vitro Transcription*, <http://www.invitrogen.com/site/us/en/home/References/Ambion-Tech-Support/probe-labeling-systems/general-articles/the-basics-in-vitro-transcription.html>

CHAPTER 9

SMART ASSAY TO DETECT HIV-1 K103N MUTATIONS AND DEVELOP NOVEL VIRAL LOAD TECHNIQUE

9.1. Abstract

SMART was used to successfully detect synthetic K103N HIV-1 DNA. The SMART probe was amplified and detected both off-chip and in a microchip reservoir using a modified version of real-time NASBA; without the non-cyclic phase and 65°C pre-heat. We detected as little as 6 copies/μL of our synthetic K103N HIV-1 sample within 180 minutes of amplification. SMART had comparable sensitivity and was faster than commercially available viral load and HIV detection techniques, while using an inexpensive, practical and potentially more accurate isothermal amplification technique, in comparison to the traditional standard of polymerase chain reaction (PCR). However, SMART still needs further development to match the sensitivity of drug resistance monitoring assays. The use of molecular beacons resulted in relatively fast real time detection (< 180 minutes), however they were also shown to hinder the amplification process when compared to end-point detection using gel electrophoresis instead of molecular beacons. Finally, SMART probes were used for modeling and determining K103N mutant concentration of an unknown wild type (WT) sample. Within 90 minutes we were able to detect as low as 1% (6000 copies/μL) of K103N SMART probe within

the WT population (600,000 copies/μL). These results establish the groundwork for future drug resistance mutation detection and viral load quantification in clinical samples, which can revolutionize HIV patient care globally.

9.2. Introduction

In this chapter, we put into practice a new approach[1] for mutation detection, termed Simple Method for Amplifying RNA Targets (SMART), and use K103N as a model drug resistant mutation. We used previously isolated synthetic DNA (sDNA) in place of clinical HIV RNA samples, to establish the feasibility of this method. Future work will integrate isolation of RNA from an HIV-infected patient samples. There are a few minor variations to SMART, as detailed in chapter 6. These pertain to using SMART to target both K103N sDNA and wild type(WT) sDNA. This establishes the specificity of our assay, specifically the SMART probes, and helps us establish a new HIV-1 viral load technique. These deviations are detailed below in the remainder of the introduction.

9.2.1. Capture

When targeting an isolated patient sample, a group of probes with all potential variations about the K103N region is used in order to capture all potential K103N variants. The same process occurs for the capture of wild type (WT) RNA (figure 9.1).

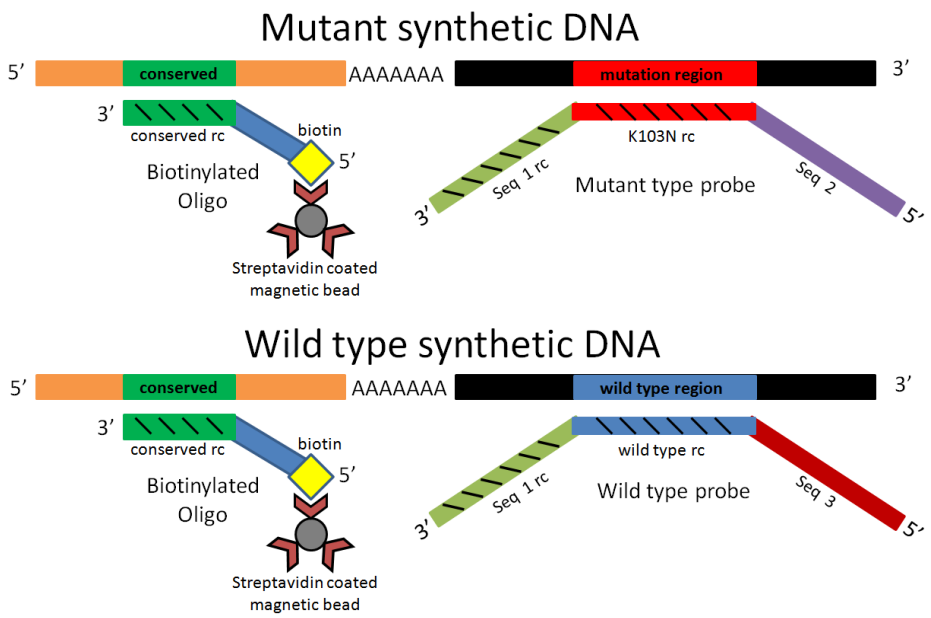

Figure 9.1. SMART capture using K103N and WT sDNA.

The biotinylated oligonucleotide hybridizes with all sDNA sequences(K103N and WT) and is conjugated to the magnetic beads through the streptavidin-biotin bond. Simultaneously, K103N and wild type probes hybridize with K103N sDNA and WT sDNA respectively. An important distinction is that the K103N and WT SMART probes each contain a unique arm sequence located at their 5' end, Seq 2 (TCAAGAGTAGACAC) and Seq3 (ACTAGCCTTCACGGT) so that during amplification they may be fluorescently tagged independently. By targeting both mutated and WT sequences, this assay will be able to not only detect and quantify drug resistance variants, but also quantify the total sDNA, and eventually the HIV-1 VL. The final product of the capture step is a chain-linked molecule complex of streptavidin coated magnetic beads - biotinylated oligo- sDNA - K103N/WT SMART probe.

9.2.2. Amplification

After microfluidic separation (chapter 6), the K103N/WT SMART probes are used as templates, undergoing cyclic isothermal amplification, to exponentially produce their RNA reverse complement (RC) products. As seen in figure 9.2, amplification begins when K103N and WT SMART probes bind with a primer containing a T7 promoter sequence (top-left). The primer is the RC of the 3' Seq1 region of both probes (GTAATCAGATCAGAGCAATAGGTCA), allowing for excellent hybridization kinetics. AMV-RT is then engaged and produces double stranded cDNA (bottom-left). In the presence of double stranded DNA containing a T7 promoter sequence, T7 RNA polymerase transcribes large amounts of RNA RC (bottom-right), reverse complements of the original K103N and WT SMART probes. T7 RNA polymerase continues to transcribe RNA RC until either rNTPs or T7 RNA polymerase become exhausted. Two second primers, Seq2 and Seq3, (middle-right) bind to their respective K103N and WT RNA RC sequences. AMV-RT is engaged and produces cDNA/RNA hybrids (top-right). RNAseH specifically degrades the RNA in the cDNA/RNA hybrids leaving behind single stranded cDNA which is identical to the original K103N and WT DNA SMART probes (top-left). The end product of the amplification cycle is exponentially amplified copies of the K103N and WT RNA RC.

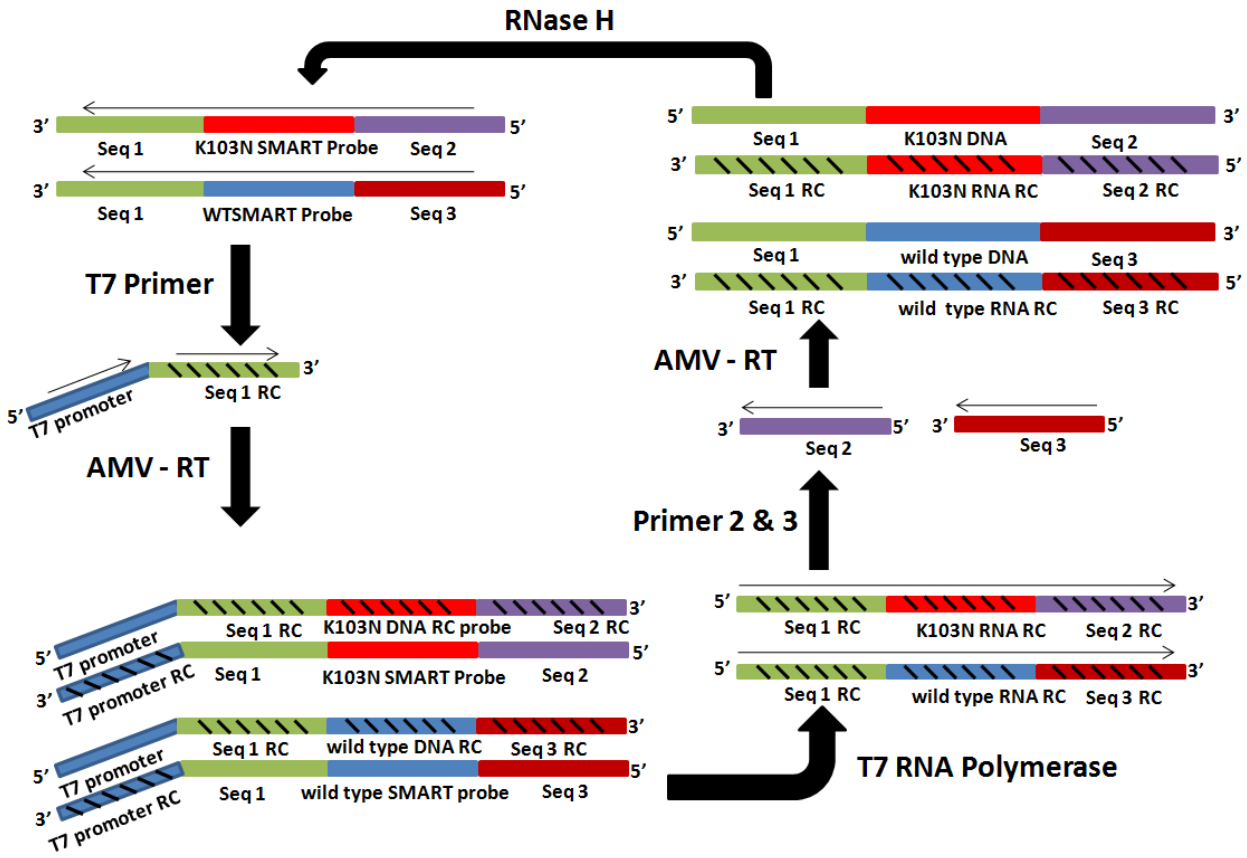

Figure 9.2. Modified real-time nucleic sequence based amplification (NASBA).

9.2.3. Real-time detection of *K103N and WT RNA RC*

K103N and WT beacons each contain different distinct fluorophores (6-FAM and CY5, respectively) with unique excitation/emissions so that they may be quantified simultaneously without signal interference. In the process of real time detection of amplified SMART probes, the molecular beacons hybridize with their K103N and WT RNA RC targets and change their conformation from a hairpin like structure to a linear structure, releasing the fluorophore from its quencher and allowing for fluorescence to be emitted. The fluorescence is quantified as it occurs, resulting in real time K103N and WT detection.

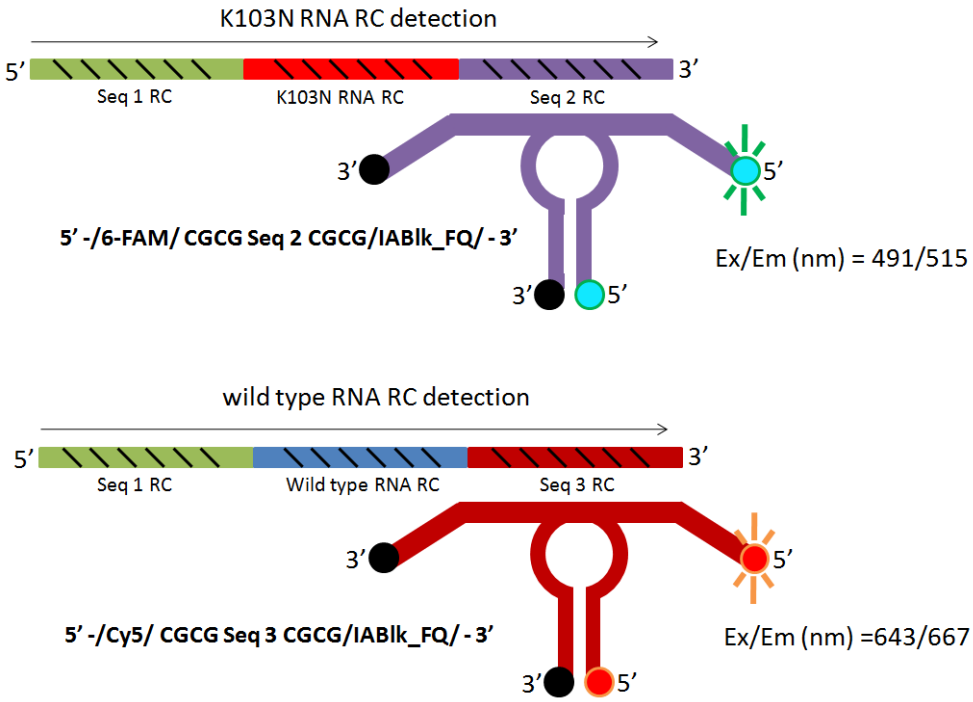

Figure 9.3. Real time fluorescence detection using molecular beacons.

A key design feature in this detection step is the hybridization of the beacons with Seq2 RC and Seq3 RC rather than targeting the K103N RC and WT RC hybridization sequences (figure 9.3). Although this creates a competition between primer 2 and molecular beacons during the amplification cycle, this design allows for a broad spectrum of K103N and WT SMART probe sequences to be used simultaneously in one assay. For example, 10 different K103N SMART probes could be used to target 10 different K103N mutation variations without adding any complexity, by design of the assay. Since all 10 SMART probes would have the same arm sequences (Seq1 and Seq2) and use the same two primers and a single molecular beacon, multiple SMART probes would not inhibit or change the amplification process at all. There would be a varying amount of each SMART probe at the start of amplification based upon which ones were successfully captured and separated, but this is inconsequential because all 10 SMART probes are

being amplified and detected as a group using one molecular beacon. During amplification 10 different K103N RNA RC sequences would be produced, but they all would contain the same Seq2 RC and only need one molecular beacon to detect all 10 sequences simultaneously. This design allows for screening a full panel of HIV WT and K103N sequences in parallel, achieved using only two molecular beacons. This is a more practical and cost effective design approach to screen for many mutations together with one beacon or many WT sequences together with one beacon than to use many beacons targeting specific K103N RC and WT RC hybridization sequences. Many beacons would be required to cover the full range of potential K103N RC and WT RC sequences if they were targeted individually, likely introducing non-specific primer and beacon hybridizations resulting in numerous false-positive results. Additionally, the cost of such a system would increase with the addition of each molecular beacon and with the optics required to simultaneously detect and differentiate >10 different fluorophores. We designed our assay to avoid such financial and reaction kinetic constraints.

9.3. Materials

9.3.1. Engineered oligonucleotide sequences

To design a comprehensive set of sequences that would represent the high variability of the HIV-1 K103N region, which is present in multiple HIV-1 subtypes and recombinant forms [2], we used a curated dataset of 300 K103N and 6100 WT sequences, obtained from the non-subtype B working group dataset [3]. The diverse regions adjacent to RT position 103 were examined in this multi-HIV-1 subtype dataset and the most conserved K103N mutated (AGAACAAATCGGTAAC) and WT sequences (AAAAAGAAAAAATCAGTAACA) were determined, covering ~75% of K103N and

~60% of WT sequences. . Any other sequence alignment method such as MUSCLE or Clustalw2 can be used for achieving same result. One K103N sequence and one WT sequence was chosen, both containing these conserved sequence respectively. A relevant portion of these individual sequences (~30 nucleotides which includes the respective conserved sequences) were used to engineer the K103N and WT sDNA. The K103N sDNA used (Table 9.1) came prepared in TE buffer solution and contained two distinct sequences representing the actual conserved region (*ATGGGTGCGAGAGCGTCAATATTAAG*) of the HIV-1 *gag* gene and a K103N mutation region sequence (**CAGGGTTAAAGAAGAACAAATCGGTAACAG**) separated by 10 adenine oligonucleotides to give ample space for hybridizations of the capture oligo and SMART probe. Table 9.1 also provides the WT sDNA sequence, SMART probes, primers, and molecular beacon sequences and the nucleotide length of these model sequences. All of these custom oligonucleotides were purchased from Integrated DNA Technologies, Inc. (Coralville, IA). Table 9.1 also shows the K103N and WT RNA RC sequences.

Sequence Name	Oligonucleotide sequence	Length (nt)
K103N sDNA	5' - aaaa **CAGGGTTAAAGAAGAACAAATCGGTAACAG** aaaaaaaaaa *ATGGGTGCGAGAGCGTCAATATTAAG* aaaa -3'	74
WT sDNA	5' - aaaa GGGTCTAAAAAAGAAAAATCAGTAAC aaaaaaaaaa *ATGGGTGCGAGAGCGTCAATATTAAG* aaaa -3'	72
Biotinylated oligo	5- /5BioTEG/*CTTAATATTGACGCTCTCGCACCCAT* -3	26
K103N SMART probe	5' - TCAAGAGTAGACAC **CTGTTACCGATTTGTTCTTCTTTAACCCTG** GTAATCAGATCAGAGCAATAGGTCA - 3'	69
WT SMART probe	5' - ACTAGCCTTCACGGT **GTTACTGATTTTTTCTTTTTTAACCCTG** GTAATCAGATCAGAGCAATAGGTCA - 3'	68
Primer 1 (K103N + WT)	5' - taatacgactcactataggg TGACCTATTGCTCTGATCTGATTAC - 3'	45
Primer 2 (K103N)	5' - **TCAAGAGTAGACACCTGTTACCGAT** - 3'	25
Primer 3 (WT)	5' - **ACTAGCCTTCACGGTGTTACTGATT** - 3'	25
K103N RNA RC	5' - TGACCTATTGCTCTGATCTGATTACCAGGGTTAAAGAAGAACAA **ATCGGTAACAGGTGTCTACTCTTGA** - 3'	69
WT RNA RC	5' - TGACCTATTGCTCTGATCTGATTACCAGGGTTAAAAAAGAAAA **AATCAGTAACACCGTGAAGGCTAGT** - 3'	68
Beacon 1 (K103N)	5 '- /6-FAM/ cgcg **TCAAGAGTAGACACCTGTTACCGAT** cgcg /3IABlk_FQ/ - 3'	33
Beacon 2 (WT)	5' - /Cy5/ cgcg **ACTAGCCTTCACGGTGTTACTGATT** cgcg /3IABlk_FQ / - 3'	33

Table 9.1. Oligonucleotides used in SMART assay. The ss K103N sDNA sequence was designed with a mutated sequence (bold) centered about the K103N codon (underlined) and the ss WT sDNA sequence was designed with a non-mutated sequence (regular) centered about the non-mutated lysine codon (underlined) (repetition of above). K103N and WT SMART probes have hybridization regions (bold) with their respective sDNA targets and a primer 1 region (underlined). Primer 1 was designed to hybridize with both

probes (underlined) and contains a T7 promoter region (lowercase). Primer 2 (K103N) and primer 3 (WT) were designed to hybridize (bold & underlined) with the K103N RNA RC and the WT RNA RC, respectively, and all potential SMART probe variations. Beacon 1 (K103N) and beacon 2 (WT) were also designed to competitively hybridize with the same regions (bold & underlined) of the K103N RNA RC and the WT RNA RC, respectively. Again, this is to ensure that only one K103N beacon and one WT beacon is necessary for all variations of K103N and WT probes.

9.3.2. Microchip device

The microchip was constructed using a glass substrate and a polydimethylsiloxane (PDMS) layer containing micro-channels and reservoirs. The microchip design (figure 9.4) is a simple tapered one-channel device designed for adequate separation of conjugated magnetic beads from unbound SMART probes using a magnetic bar. The microchip can process four samples simultaneously. The 2.8µm diameter M-280 magnetic beads were obtained from Invitrogen, Carlsbad, CA)

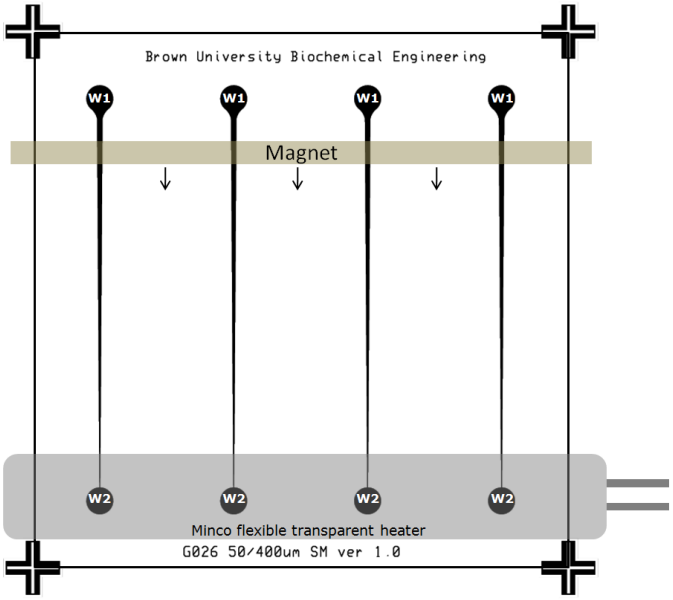

Figure 9.4. Microfluidic separation microchip design. A magnet is used to transfer the beads through a channel from W1 to W2. A transparent heater is attached for post-separation amplification.

9.3.3. NASBA reaction mix

The reagents used for NASBA and their concentrations at the final reaction volume were 40 mM Tris(pH 8.0), 12.5 mM MgCl2, 73.5 mM CH3COOK (KOAc), 5.25 mM dithiothreitol, 1.05 mM dNTP, 2.1 mM rNTP, 0.21 μM each primer, 52.5 nM molecular beacon, 15.75% dimethyl sulfoxide, 1.68 u/μL T7 RNA polymerase, 0.34 u/μL AMV-RT, 0.005 u/μL RNase-H, and 0.11 mg/mL bovine serum albumin (BSA). Enzymes and reagents used were purchased from Promega (Madison, WI).

9.3.4. Heating devices

On-chip amplification required an external RK-80H power supply (Matsusada Precision Inc, Kusatsu City, Shiga, Japan) providing 4-5V to the Minco flexible transparent heater to achieve 41°C in well 2 of the microchip. We validated the heating temperature using a thermocouple attached to our microchip wells.

Off-chip real-time amplification and detection used a single cuvette peltier (Photon Technology International, Birmingham, NJ) and off-chip amplification followed by off-chip end-point gel electrophoresis used a C1000 thermal cycler (Bio-Rad, Hercules, CA).

9.3.5. Optical equipment

On-chip detection used a Nikon Eclipse TE2000-U fluorescent microscope (Nikon Instruments, Inc., Melville, NY) with a blue filter set for 6-FAM (450-490nm excitation, 515 nm long pass emission), a red filter set for Cy5 (590-650nm excitation, 663-738 nm band pass emission), a 4x objective, a model 814 Photomultiplier Detection System with a gain of 700V (Photon Technology International, Birmingham, NJ), and an integrated high speed shutter (Melles Griot, Albuquerque, NM) set to open for 0.2s. A

custom in-house LabVIEW (National Instruments Corporation, Austin, TX) data acquisition program collected PMT output at a rate of 12-15 Hz.

Off-chip real time detection samples were prepared in disposable Uvettes (Eppendorf, Germany) and real-time fluorescence was measured using a Quantamaster spectrofluorometer (Photon Technology International, Birmingham, NJ). Off-chip post amplification detection used a 2100 Bioanalyzer and a small RNA gel cartridge (Agilent Technologies, Marshfield, MA).

9.4. Methods

9.4.1. Theoretical hybridizations

Theoretical hybridizations of sDNA to biotinylated oligos, sDNA to SMART probes, beacon dimers, and beacon to target RNA RC were calculated using the DINAmelt and mFold Web Server software (DINAMelt Server, RNA Institute, SUNY Albany, Albany, NY; available at http:// http://mfold.rna.albany.edu), for reaction conditions T=41ºC, (Na+) = 70mM and (Mg++) = 12mM. Oligonucleotide hybridizations are characterized by two properties: the gibbs free energy (delta G = ΔG), where a more negative delta G value represents a more energetically favorable state (higher probability of hybridization), and the melting temperature of the hybrid (T_m) at which 50% of the structures will have un-hybridized. The probability of hybridization can be expressed as $P \propto \exp(-\Delta G / RT)$ where R= a rate constant and T = hybridization temperature (constant). This equation shows that a more negative delta G exponentially increases the probability of hybridization.

9.4.2. SMART experiments

We used K103N and WT sDNA samples with a starting concentration ranging from 600,000 copies/μL to 6 copies/μL. This range of viral loads is only two orders of magnitude higher than the range of detection of most commercially available HIV-1 viral load assays (~0.05 copies/μL to 10,000 copies/μL)[4] ,thus most of these starting concentrations of sDNA are clinically relevant. Biotinylated oligos, sDNA sample, SMART probes, magnetic beads and hybridization buffer were incubated for 30 minutes prior to loading onto the microchip. The PDMS chip was pre-washed with nuclease decontamination solution (Integrated DNA Technologies, Coralville, IA) and pre-soaked with hybridization buffer(Tris, $MgCl_2$, NaCl, Tween-20, BSA). Microfluidic separation occurred after the incubation as biotinylated oligos, sDNA sample, SMART probes, magnetic beads and hybridization buffer were added to well 1 (W1 in figure 9.4) and moved through the channel by moving a neodymium magnet along the bottom of the channel at less than 0.6mm/s towards well 2(W2 in figure 9.4).

SMART experiments were initially performed for K103N detection using capture, separation and on-chip amplification for 180 minutes at 41°C, followed by off-chip end-point gel electropheresis. At the conclusion of the separation step the beads were <1cm from W2 and the flow was manually stopped by the removal of solution in both W1 and W2, and the addition of 12μL of paraffin oil to W1 to avoid evaporation of reagents. The NASBA reaction mix was then introduced for on-chip amplification (total volume of 5μL) and the on-chip amplification apparatus was connected. On-chip amplification was used to preliminarily demonstrate the ability of the assay to be used as a POC device. End point detection was used rather than real-time detection to validate the capture and separation steps; ensuring that the correct size oligonucleotide was amplified and visible

in the gel plot. Additionally, to evaluate the effect of the molecular beacons, amplification was performed with (B+) and without beacons (B-), to investigate if there was any inhibitory effect on amplification.

Subsequently, experiments were performed for K103N detection using capture, separation and off-chip real-time amplification and detection. Although on-chip detection can be performed by integrating better detection system, we used off-chip detection as a fluorometer was already equipped for more accurate, higher sensitivity fluorescence detection allowing us to better gauge the sensitivity of our assay. At the conclusion of the separation step, the magnetic bead complex was moved into W2. Then the W2 contents were transferred into a polypropylene tube and W2 was rinsed with an additional 6μL of hybridization buffer. The beads were then collected at the bottom of the tube and all but 2μL of solution was removed for off-chip NASBA amplification using a fluorometer. Fluorescence readings were taken every five minutes to yield real time fluorescence data. Off-chip amplification used the same ratio of NABSA reaction mix as on-chip with a larger total solution volume of 80μL.

9.4.3. Determining K103N concentration using SMART probes

As a final implementation step, we evaluated SMART as an effective means for estimating K103N concentrations of 'unknown' samples. The objective of this approach was to establish that we can simultaneously amplify and detect a multiple beacon system and that our SMART probes may be used in such a system as standards to determine K103N concentration of an unknown sample. We considered a group of samples with variable concentrations of WT and K103N SMART probes. We used a total of 1pM (600,000 copies/μL) of SMART probes (K103N + WT) to evaluate the efficacy of our

assay to generate linear models based upon K103N SMART probe concentrations. A variety of K103N SMART probe concentrations were used as our known standards and ranged from 100% (600,000 copies/μL) to 1% (600 copies/ μL). First, the SMART probes were added to the NASBA reaction mix for a total volume of 80 μL and detected with real-time amplification off-chip using the disposable cuvette/fluorometer apparatus. Second, the SMART probes were added to the NASBA reaction mix for a total volume of 5 μL, added to W2 in the microchip device and detected with real-time amplification on-chip using the fluorescent microscope/thin film heater apparatus.

The off-chip data were used to generate model fits capable of predicting starting K103N probe concentrations. This was achieved by rearranging and plotting the real time fluorescence data. The data were plotted as fluorescence at a given time point versus concentration on a two dimensional plane. The fluorescence of the standards was used to generate a linear model. Finally, the linear model could be used to interpolate and estimate the starting K103N concentration of the unknown sample. This modeling method to determine the starting K103N concentration was replicated for the on-chip data.

9.5. Results and discussion

9.5.1. Hybridization theory predications

The delta G and T_m shown in table 9.2, hybridization events 1&2 (bold), are -28.9 and 58.4ºC respectively. This is a very negative delta G and the melting temperature is safely above the reaction temperature (41 ºC) resulting in a very likely hybridization. However, events 5&6 in table 2 show more positive delta G values and the T_m falls well below 41ºC, thus the hybridization events are theoretically unlikely to occur. Additional

ΔG's and T_m's for key theoretical hybridization events were also calculated and shown in table 9.2.

Hybridization Event	Oligonucleotide(s)	Delta G Value (41°C)	T_m (°C)
1	**K103N sDNA + biotinylated oligo**	**-28.9**	**58.4**
2	**WT sDNA + biotinylated oligo**	**-28.9**	**58.4**
3	**K103N sDNA + K103N SMART probe**	**-32.0**	**59.4**
4	**WT sDNA + WT SMART probe**	**-25.3**	**51.7**
5	K103N sDNA + WT SMART probe	-10.8	31.1
6	WT sDNA + K103N SMART probe	-10.8	28.7
7	**Beacon 1 (K103N)**	**-1.1**	**49.9**
8	**Beacon 2 (WT)**	**-1.9**	**56.5**
9	Beacon 1 (K103N) + Beacon 1 (K103N)	-5.6	-14.7
10	Beacon 1 (K103N) + Beacon 2 (WT)	-6.4	12.8
11	Beacon 2 (WT) + Beacon 2 (WT)	-7.0	19.0
12	**Beacon 1(K103N) + K103N RNA RC**	**-26.2**	**55.3**
13	**Beacon 2(WT) + WT RNA RC**	**-27.2**	**56.8**
14	Beacon 1(K103N) + WT RNA RC	-5.3	-3.5
15	Beacon 2(WT) + K103N RNA RC	-8.1	11.0

Table 9.2. Theoretical hybridization energies.

Events likely to occur are shown in bold, while those unlikely to occur are shown in regular font. Events 7&8 indicate that the beacons alone form the desired hairpin structure at the reaction temperature of 41ºC and events 12&13 show that they form a very strong hybrid with their intended target without non-specific hybridization (events 14&15). Overall, we engineered our probes and targets to effectively hybridize while avoiding non-specific hybridizations.

9.5.2. Validation of SMART using on-chip amplification

Figure 3a summarizes the outcomes of the experiment, confirming that capture, separation and amplification reactions were occurring as expected. K103N Probe RC was expected to be ~69 nt in size. The dark bands in the K103N positive lanes (1,2,6 & 7)

correspond to this product. This K103N Probe RC band also occurred in K103N negative lanes (3,4,5,8,9 &10) but at very light intensity (low concentration), likely due to very low concentrations of K103N probe carryover during separation, which was expected[1].

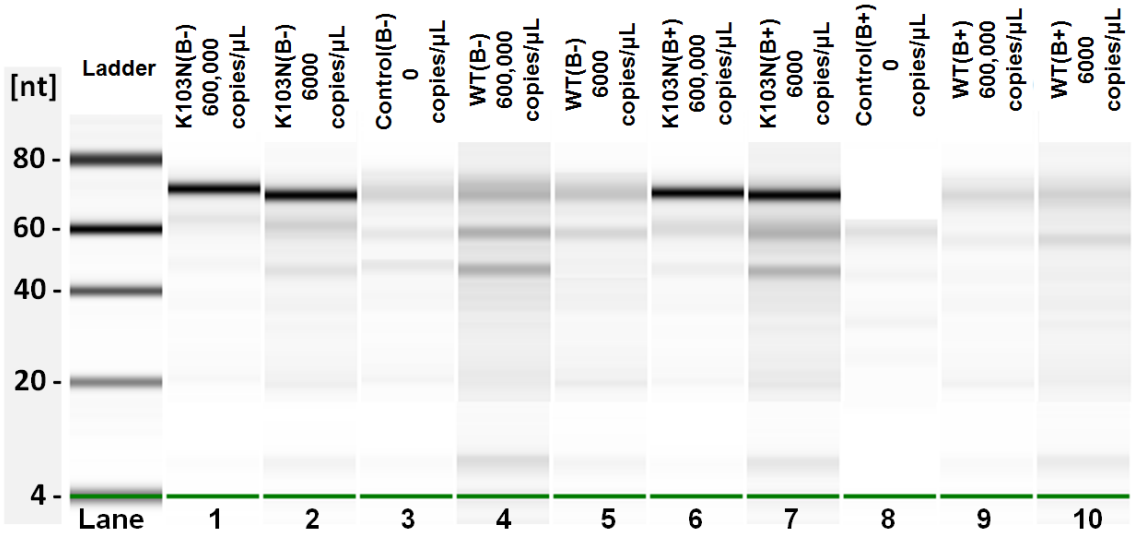

Figure 9.5. SMART gel plot after using on-chip amplification. No DNA, low and high concentration WT ssDNA controls were also included.

This minimal probe carryover currently limits the sensitivity of our assay and we will explore ways to further reduce carryover for even greater sensitivity. Light bands also occurred at ~45nt and ~22nt, likely attributed to the primers used. An unexpectedly produced light intensity band (~60 nt) may have occurred as the polymerase prematurely aborted transcription, resulting in RNA RC products that are shorter than expected. This prematurely aborted transcription was also observed in previous work [1] and does not have a negative impact on the assay with regards to sensitivity. Corresponding electropherogram data (figure 9.6) showed, as expected, that K103N sDNA at high starting concentrations yielded the highest fluorescence signal and that controls with no DNA and WT exhibited minimal fluorescence. Interestingly, the addition of molecular beacons had a significant effect on the amplification, particularly at the low

concentration. In figure 9.6, the area under the curve for the starting concentration of 600,000 copies/μL declined ~10% (lane 1 to lane 6) with the addition of beacon while decreasing ~45% for 6000 copies/μL (lane 2 to lane 7). This is likely attributed to the combination of two inhibitory events: (1) the competition between primer 2 and beacon 1 during the amplification cycle, and (2) the premature abortion of T7 polymerase. McCalla et al. reported that the premature abortion did not affect their detection methods as the beacon targeted the middle of the transcribed influenza RNA. However here, the beacon targeted the end of the transcribed RNA which would result in decreased beacon-RNA hybrids for the prematurely aborted RNA products. The several smaller peaks in the electropherogram support this suggestion. Targeting the end of the RNA RC product rather than the middle negatively impacts the speed of the assay, but is a necessary assay design trade-off for simultaneous detection of many K103N SMART probes while only using two primers and one molecular beacon.

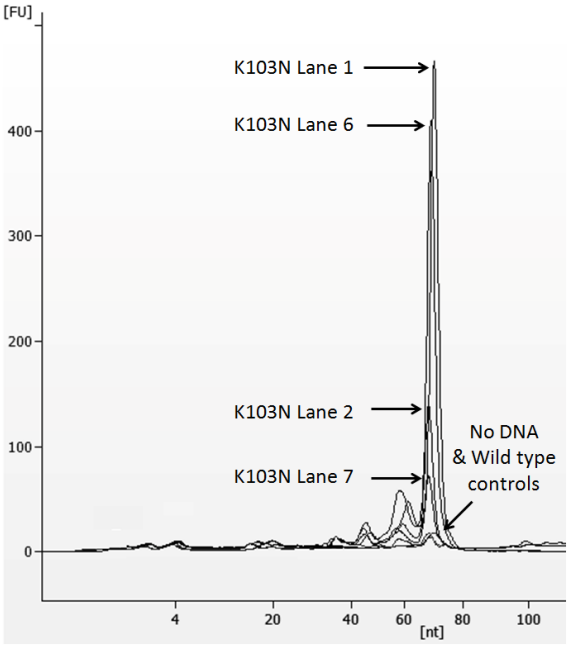

Figure 9.6. SMART electropherogram after using on-chip amplification.

A lower starting concentration of K103N sDNA yielded less hybridized K103N probe, as evident in the electropherogram when comparing 600,000 and 6000 copies/μL. Thus, a lower starting K103N sDNA concentration has a lower starting concentration of available K103N probe template for the NASBA cycle. Since the amplification cycle is exponential, the suggested inhibitory events are of a greater magnitude at lower K103N probe concentrations. This is directly supported by the data when comparing end-point amplification.

Results of with vs. without beacons experiments supported our hypothesis, that a beacon free system would amplify larger quantities of product. By our design, the beacons were in competition with Seq2 and Seq3 primers to hybridize with the RNA RC products during NASBA. When comparing the K103N samples containing 600,000 copies/μL, we saw approximately a 12% increase in fluorescence when the beacon was removed. For K103N samples containing 6000 copies/μL we saw approximately a 50% increase when the beacon was removed. Not only does this suggest that the beacon is inhibitory to the amplification cycle, but it supports the argument that inhibitory events are of a greater magnitude at lower K103N probe concentrations.

Nonetheless, the beacons are essential for detection in our assay and our POC design criteria, so the purpose of this comparison was to better understand the kinetics of the system, not to reach a decision point to eliminate/keep the molecular beacons. Our engineering efforts would be better spent further optimizing the NASBA buffer conditions for faster amplification and reduce carryover of unbound SMART probes for greater specificity.

9.5.3. SMART using off-chip amplification with real time detection

Upon verification of the amplified product using end-point detection, by interpreting the gel plot (figure 9.5) and electropherogram (figure 9.6), SMART was performed off-chip for real-time K103N detection. Figure 9.7. shows the real-time results:

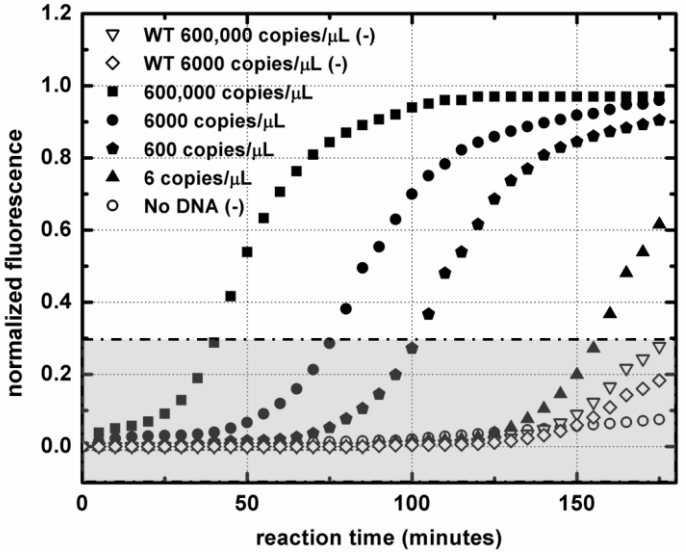

Figure 9.7. SMART assay results using off-chip amplification with real-time detection. WT sDNA and No DNA negative controls were included and plotted as background fluorescence (gray area). WT specific SMART probes, WT primers and WT molecular beacon were not included in this assay. The dashed black line indicates the threshold of detection or time to positivity (T_p) for positive samples. Standard deviation was within 5% of results (error bars not shown).

It is important first to note that the exponential curves plateau towards a maximum because the fluorescence represents the beacons hybridizing with the amplifying K103N RNA RC and there is a limited amount (52.5nM) of molecular beacons in the reaction mix. For the high concentration (600,000 copies/μL), 90 minutes of amplification yielded very distinguishable detection versus the controls with the amplification curve crossing the threshold of detection (i.e. time to positivity value (T_p) = 45 minutes). For the lower concentrations (6000 through 6 copies/μL), this level of

detection was achievable but required more time for amplification, consequently higher T_p values. This shows that detection is possible for very low, clinically relevant concentrations of K103N (≤ 1copy/μL) using SMART. A slightly longer amplification time is currently required (~4 hours) in order to achieve comparable results, although T_p is achievable within 180 minutes.

The linear model (figure 9.8) of time to positivity vs copies/μL (logarithmic scale) indicates that the current SMART assay is theoretically sensitive enough to detect as low as 1 copy/μL of K103N sDNA. Even more sensitive detection may be possible, but cannot be predicted with this linear model and would require further assay development. Figure 9.9 shows an endpoint analysis of these results, offering a clear illustration of all K103N concentrations tested to be well above the threshold of detection after 180 minutes of amplification.

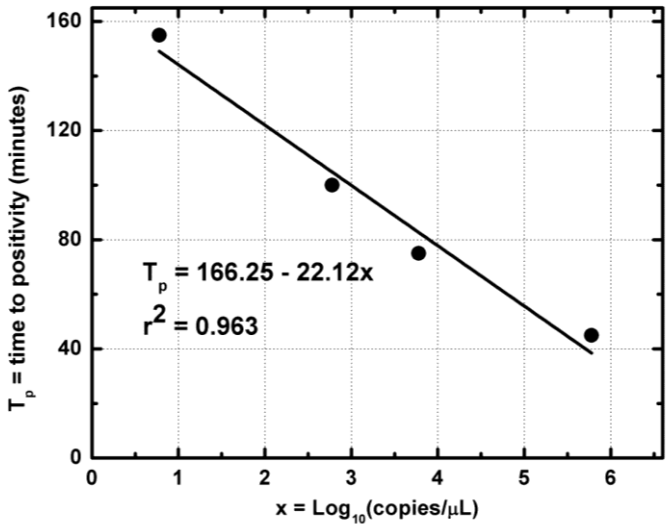

Figure 9.8. Time to positivity (T_p) values are plotted versus the logarithmic scale of starting K103N sDNA concentration. Standard deviation was within 5% of results (error bars not shown).

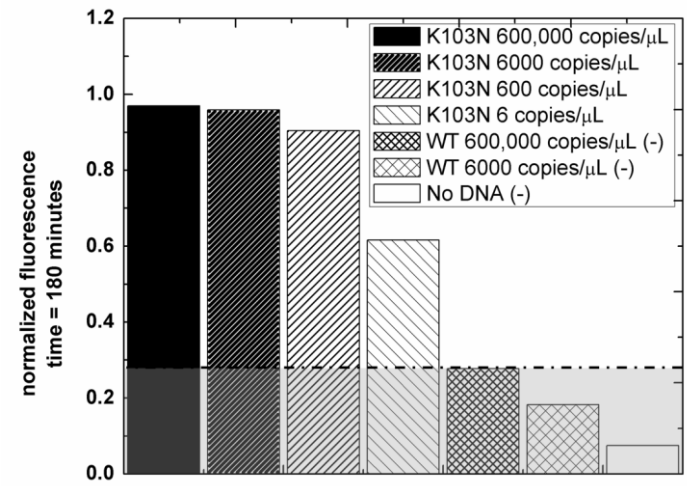

Figure 9.9. Histogram of normalized fluorescence of all sDNA and controls after 180 minutes reaction time. Standard deviation was within 5% of results (error bars not shown).

9.5.4. Determining K103N concentration using SMART probes

Figure 9.10 shows the real time detection of the K103N probe within varying K103N-WT probe samples. There was no considerable change in baseline K103N beacon fluorescence for samples containing no DNA and for sample containing only WT probe, confirming that the K103N beacon was stable and highly specific to its intended K103N RNA RC target. As the starting percentage of K103N probe increased, so did the rate of fluorescence. With a higher starting concentration of K103N probe, the reaction produced more K103N RNA RC in a given amount of time.

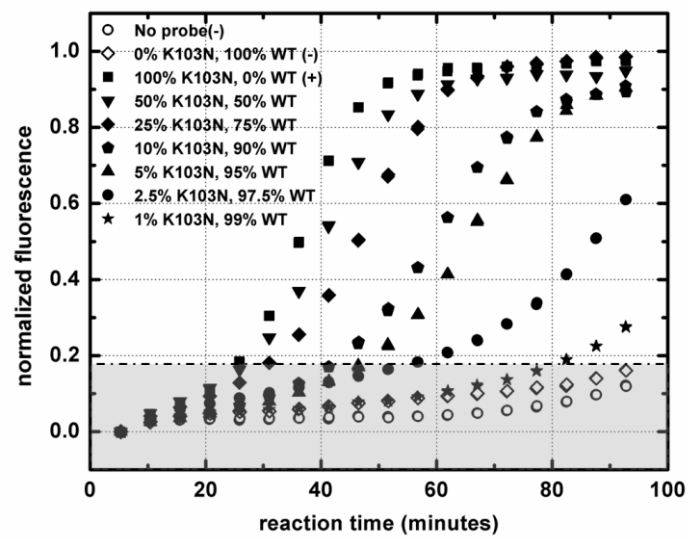

Figure 9.10. Off-chip real time fluorescence of amplified K103N probe as a function of time. Standard deviation was within 5% of results (error bars not shown).

Therefore with higher starting concentrations of K103N probe there was faster hybridization of K103N beacon with the K103N RNA RC target. This correlation can also be explained in its converse; as the starting concentration of K103N probe decreased, the resulting exponential fluorescence curve shifted with increasing time. These data correspond to the real time SMART results from figure 9.7, in which a higher concentration of starting K103N sDNA yielded more K103N probe, which in turn resulted in faster amplification.

Figure 9.11 similarly shows the real time detection of the WT probe within varying K103N-WT probe samples. There was no change in baseline WT beacon fluorescence for samples containing no DNA and for sample containing only K103N probe, confirming that the WT beacon was stable and highly specific to its intended WT target. For samples containing 50% to 100% WT probe, the WT beacon fluorescence increased exponentially reaching its beacon limited maximum after approximately 45 minutes. These data indicate that the WT beacon hybridized effectively with high concentrations of WT RNA RC target, however the concentrations were too high to

achieve any distinguishable resolution between the varying concentrations of probe in this timescale. This suggests that SMART, as it is currently designed, is not ideal for distinguishing concentrations above 300,000 copies/μL. This gives us a ballpark number for the upper VL limit of our assay, which compares well to commercially available VL kits (~10,000 copies/μL).

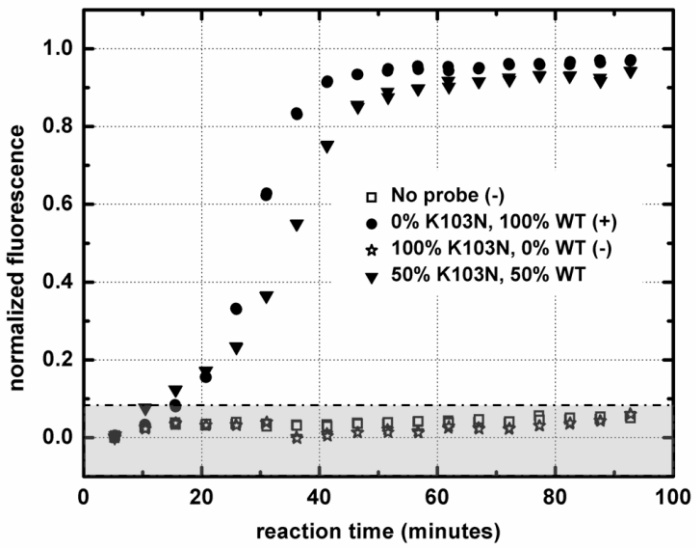

Figure 9.11. Real time fluorescence of amplified WT probe as a function of time. Standard deviation was within 5% of results (error bars not shown).

Figure 9.12. shows the model for high concentrations (30,000–150,000 copies/ μL) of K103N SMART probes. For high starting concentrations we are able to resolve fluorescence at an early time point during the amplification (45 minutes). These data fit a linear curve which can be used to interpolate for unknown high K103N SMART probe starting concentrations based upon these measured fluorescence standards values.

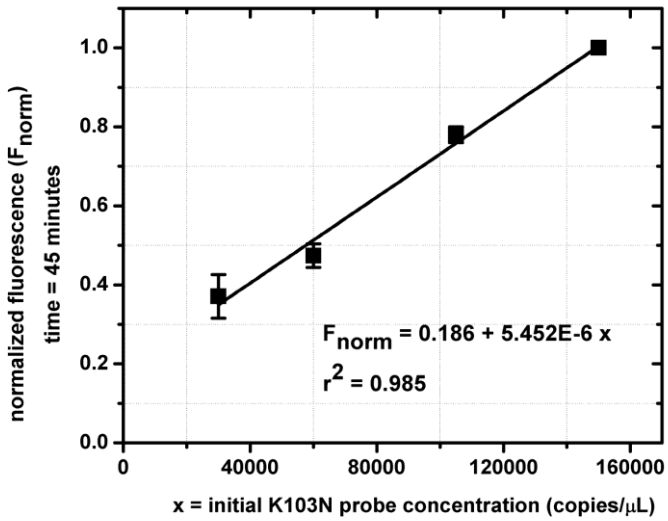

Figure 9.12. Off-chip modeling of fluorescence versus K103N SMART probe concentration at high concentrations (30,000 – 150,000 copies/μL K103N SMART probe).

For low concentrations (<30,000 copies/ μL) (figure 9.13) we are able to resolve the variations at a later time point during the amplification (90 minutes). These data fit a linear curve which can be used to interpolate for unknown low K103N SMART probe starting concentrations based upon measured fluorescence values. These data also show that K103N beacons hybridized effectively with high and low concentrations of K103N RNA RC target.

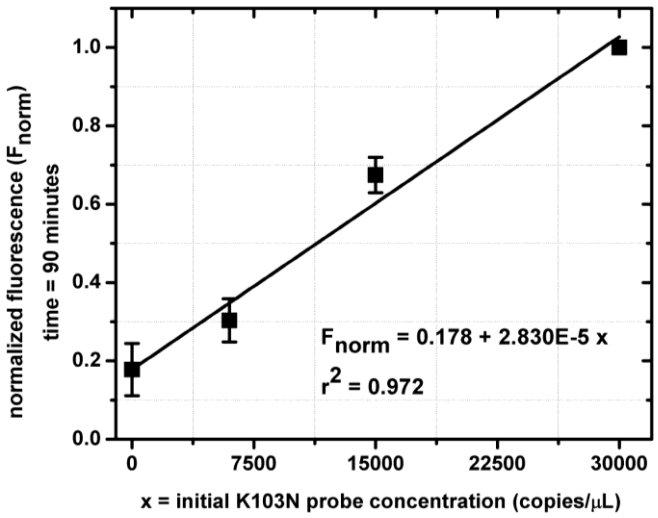

Figure 9.13. Off-chip modeling of fluorescence versus K103N SMART probe concentration at low concentrations (less than 30,000 copies/μL K103N SMART probe).

Using the real time fluorescence data from known standards (i.e. samples with known K103N probe concentrations), we were able to accurately predict the K103N probe concentration (copies/μL) of an unknown multi-probe sample. Off-chip amplification was used to establish this method of modeling, with a greater degree of sensitivity than could be achieved on-chip. However, the off-chip amplification was a less practical method since we could only amplify one sample at a time. For the case of on-chip amplification each PDMS chip contained four identical channels, such that three samples of known K103N concentration could be run in parallel with one unknown sample. However to establish our theoretical model we used all four channels with known sample quantities.

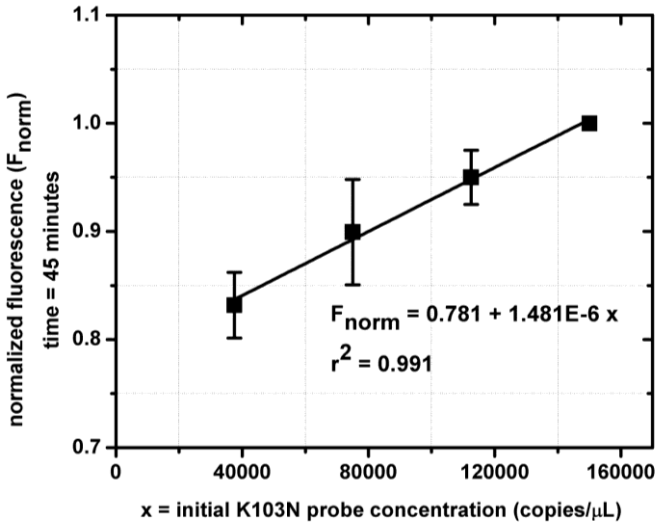

Figure 9.14. On-chip K103N viral load quantification at high concentrations (6.25% to 25% K103N).

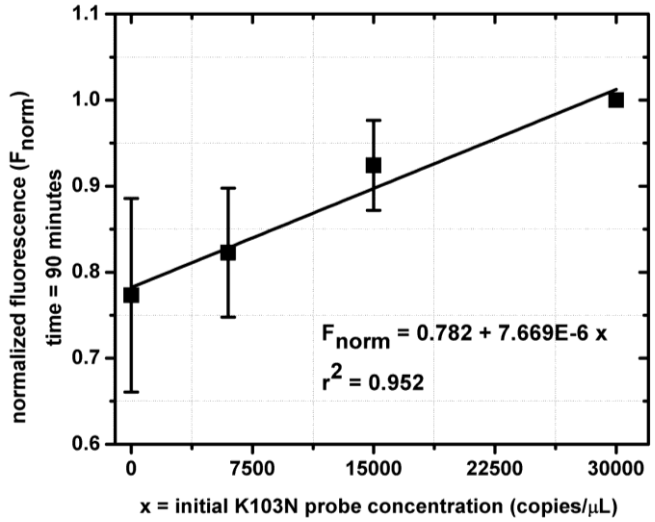

Figure 9.15. On-chip K103N viral load quantification at low concentrations.

Figures 9.14 and 9.15 show similar plots for on-chip modeling. Linear models were produced but with a larger standard error resulting in reduced specificity of the on-chip model.

9.6. Conclusion

We presented a novel method for RNA mutation detection, and apply it to HIV-1 drug resistance determination. We captured, separated, amplified and detected target K103N and WT sDNA sequences resembling an HIV-1 RT commonly mutated region, and engineered amplifiable SMART probes for optimal reaction kinetics rather than amplifying the target sDNA itself, utilizing both off-chip and on-chip amplification and detection systems. We show that the initial 65°C step of NASBA can be removed because of our novel design, making the amplification fully isothermal, thus providing significant advantages in field deployable and other POC settings. The hybridization of both a biotinylated oligonucleotide and amplifiable SMART probe instead of primers maintained the specificity of the assay when compared to traditional methods of mutation detection; and the use of magnetic beads instead of a tube-based multiple wash kit allowed for simple and efficient separation of the target-bead complex from unbound SMART probe. A simple microfluidic device to facilitate separation of the amplifiable SMART probes was incorporated, avoiding the need for a flow apparatus or major heating component. This resulted in a significantly reduced assay cost and is a promising practical platform for POC use.

On-chip real time detection of sDNA samples required a very small (only 5μL) amount of reaction volume as opposed to conventional PCR volumes, which usually starts at a minimum of 20μL. The small reaction volume concentrated the target and probe molecules, which may have decreased the time to positive results. Although evidence existed for non-specific carryover of K103N SMART probe at very low quantities, this started occurring after a very long (~135 minutes) amplification time. The

real-time fluorescence for most samples of K103N sDNA (600,000 – 600 copies/μL) crossed the threshold of detection in less than 100 minutes, Only the lowest concentration (6 copies/μL) K103N sDNA sample required more time (~155 minutes) for positive detection. 6 copies/μL was positively detected, but the result was close to our negative controls (on sDNA, WT sDNA), thus close to the current lower VL limit of detection.

Existing methods for HIV resistance mutation detection are not intended for POC use. Existing detection and emerging quantification methods, potentially suitable for POC use, do not incorporate drug resistance mutation determination. Existing detection and emerging quantification methods, potentially suitable for POC use, do not incorporate drug resistance mutation determination. Sensitive commercial VL non-microfluidic assays (TaqMan assay, NucliSens, Ultrasensitive p24 assay,etc.) are not specifically designed to detect drug resistance sequences and appear to lack the practicality for POC settings. Microfluidic methods, which are only developed using immuno-based chemistry, are very promising VL methods for POC use, however they fail to address drug resistance monitoring. Many drug resistance mutation detection assays are either commercially available (TRUGENE & ViroSeq) or used in the research setting (pyrosequencing, single genome sequencing, AS-PCR, LigAmp), but they are not yet fully viable for POC and do not take advantage of microfluidics. SMART is a promising means of merging these methods for POC settings; using a simple microfluidic platform for detecting resistance mutant sDNA with high specificity and distinguishing between mutant/WT sequences simultaneously. With further development, SMART could be used as a VL monitoring technique in addition to determining the concentration of K103N within a given sample.

SMART did exhibit a few limitations. First, the use of molecular beacons was shown to inhibit the amplification process, however the T_p values were similar to commercial and non-commercial PCR-based techniques. This is therefore only a minor issue and a worthwhile trade-off for the POC attributes that accompany the use of molecular beacons. Second, SMART assay design parameters may be adapted and further optimized for smaller T_p values that would reduce the reaction time beyond existing techniques. Third, SMART at its current stage lacks an integrated isolation step. This is an important aspect of its POC applicability and is currently in development. Fourth, the optics used for detection were laboratory grade and a transition to field deployable optics to achieve full POC and RLS status is still needed. Fifth, we only showed SMART to be effective for targeting one K103N and one WT sequence. We need to assay many sequences simultaneously to further prove the validity and applicability of our design. Lastly, the sensitivity of SMART is within the commercially relevant range (2 copies/μL – 10,000 copies/ μL), but additional work is needed to improve the sensitivity to match the lower VL limit of commercial kits for detection drug resistant mutations (~0.05 copies/μL). We anticipate achieving greater sensitivity by incorporating of our own on-chip isolation technique, in which larger volumes of starting sample containing RNA will be processed and concentrated into a smaller volume, effectively increasing the VL. Our synthetic samples did not have the benefit of a concentrating isolation step.

In summary, we introduce a novel HIV-drug resistance detection assay and show that it can theoretically detect, quantify and estimate unknown HIV RT K103N concentrations. The eventual applicability of these methods and this platform to clinical, global HIV-care is clear. We used sDNAs that were based on actual K103N and WT

HIV-1 RNA sequences at clinically relevant concentrations, and those were shown to hybridize efficiently with the SMART probes. The sample-to-result time of our assay meets or improves upon most commercially available assays[4]. The flexibility of the SMART probe sequence allows this method to be easily adopted for other HIV drug resistance mutations. Moving forward we would like to achieve similar results with clinical HIV samples, incorporate the RNA isolation step and use RLS capable optics. Our ultimate goal of providing costly, timely and effective POC HIV detection, VL and drug resistance monitoring in RLS with no mandatory laboratory support, will allow clinicians to more adequately and effectively treat HIV-infected patients, whether before or after exposure to antiretroviral therapy. The expansion of this concept to other RNA targets, including influenza and biothreats is only a matter of time.

9.7. Acknowledgments

Authors acknowledge the financial support of the National Institute of Health (Grants No. 1R21 A1073808-01 A1; and R01AI066922) and The RNA Institute, College of Arts and Sciences, State University of New York at Albany for use of their DINAMelt web server. We would like to thank Dr. Rami Kantor, Leeann Schreier and Mia Coetzer from Miriam Hospital for obtaining the HIV-1 K103N and wild-type sequences and for their scientific contribution and technical assistance. We would also like to thanks Stephanie McCalla, Aartik Sarma and Carmichael Ong for their previous work inventing SMART and developing the technology.

9.8. References

1 McCalla, S. E. *et al.* A Simple Method for Amplifying RNA Targets (SMART). *Journal of Molecular Diagnostics* **14,**, 328-335 (2012).

2 Kantor, R. Impact of HIV-1 pol diversity on drug resistance and its clinical implications. *Curr Opin Infect Dis* **19**, 594-606 (2006).

3 Kantor, R. *et al.* Impact of HIV-1 subtype and antiretroviral therapy on protease and reverse transcriptase genotype: results of a global collaboration. *PLoS Med* **2**, e112, doi:04-PLME-RA-0230R1 [pii]10.1371/journal.pmed.0020112 (2005).

4 Wang, S. Q., Xu, F. & Demirci, U. Advances in developing HIV-1 viral load assays for resource-limited settings. *Biotechnol Adv* **28**, 770-781, doi:DOI 10.1016/j.biotechadv.2010.06.004 (2010).

CHAPTER 10

SMART ASSAY TO DETECT ISOLATED H3 INFLUENZA SAMPLES

10.1. Abstract

SMART was used to successfully detect the presence of H3 influenza in isolated patient samples obtained from Memorial Hospital of Rhode Island. A critical design criteria was redesigning the biotinylated oligonucleotide for increased spacing between the 5' biotin end and the 3' hybridization end and a redesign of the molecular beacon form less fluorescence in the hair-pain unbound state with greater stability. After redesigning, the preliminary results show effective H3 influenza detection.

10.2. Introduction

In the previous chapter we showed SMART for effective detection of synthetic DNA analogous of HIV-1 containing the K103N mutation. Here we move one step further, and use SMART to detect clinically isolated samples of actual influenza. We have designed three SMART oligonucleotide sets based upon PCR primers shown to detect H3, H1 seasonal and H1N1 swine influenza with high specificity and sensitivity. In this chapter we detail our preliminary results which used SMART for H3 influenza detection.

10.3. Materials

10.3.1. Engineered oligonucleotide sequences

We designed three sets of biotinylated oligonucleotides and SMART probes based upon primers that were previously shown in our lab to successfully detect clinically isolated samples of H3, H1 seasonal and H1 swine influenza using polymerase chain reaction (PCR). The PCR primers are shown in table 10.1.

Subtype	PCR Primer 1	PCR Primer 2
H3	*5' - AATTTTGATGCCTGAAACCGTACCA* - 3'	5' - **ACTCCAAATGGAAGCATTCCCAATG** -3'
H1 seasonal	*5' - TCTGTAGTGTCTTCACAT* - 3'	5' - **CTCTACTCAGTGCGAAAG** - 3'
H1 swine	*5' - ATGCTGGATCTGGTATTAT* - 3'	5' - **CAATTTTGTGCTTTTTACATATT** - 3'

Table 10.1. Successfully used influenza PCR primers.

One PCR primer (italics) was copied as used for the biotinylated oligo and the other primer (bold) was copied and used for the SMART probe for each sub-type. These oligos along with the additional oligos required for SMART are shown in table 10.2. All oligonucleotides were purchased from Integrated DNA Technologies, Inc. (IDT) (Coralville, IA) except for the clinically isolated influenza samples obtained from Memorial Hospital of Rhode Island. A redesigned H3 biotinylated oligo and redesigned H3 molecular beacon were also designed and ordered from IDT (table 10.3).

Sequence	Oligonucleotide sequence
H3 biotinylated oligo	5' - BioTEG/*AATTTTGATGCCTGAAACCGTACCA*- 3'
H1 seasonal biotinylated oligo	5' - BioTEG/*TCTGTAGTGTCTTCACAT* - 3'
H1 swine biotinylated oligo	5' - BioTEG/*ATGCTGGATCTGGTATTAT* - 3'
H3 SMART probe	5' - TCA ACT CAT CAC ACA GGA TCA GCA T **ACTCCAAATGGAAGCATTCCCAATG** ATT TTG GTG GTT GCA GAA TCT C CTA TAG TGA GTC GTA TTA - 3'
H1 seasonal SMART probe	5' - TCA ACT CAT CAC ACA GGA TCA GCA T **CTCTACTCAGTGCGAAAG** ATT TTG GTG GTT GCA GAA TCT C CTA TAG TGA GTC GTA TTA - 3'
H1 swine SMART probe	5' - TCA ACT CAT CAC ACA GGA TCA GCA T **CAATTTTGTGCTTTTTACATATT** ATT TTG GTG GTT GCA GAA TCT C CTA TAG TGA GTC GTA TTA - 3'
NASBA Primer 1	5' - TAA TAC GAC TCA CTA TAG G AGA TTC TGC AAC CAC CAA AAT - 3'
NASBA Primer 2	5' - TCA ACT CAT CAC ACA GGA TCA GCA T - 3'
H3 molecular beacon	5' - /6-FAM/CGCGC **ACTCCAAATGGAAGCATTCCCAATG** GCGC/3IABlk_FQ/ - 3'
H1 seasonal molecular beacon	5' - /6-FAM/CGC **CTCTACTCAGTGCGAAAG** GCG /3IABlk_FQ/- 3'
H1 swine molecular beacon	5' - /6-FAM/CGCGC **CAATTTTGTGCTTTTTACATATT** GCGC/3IABlk_FQ/ - 3'

Table 10.2. Engineering oligonucleotide sequences for SMART influenza detection. SMART probes have hybridization regions (bold) with their respective influenza sub-type targets and a primer 1 region (underlined). Primer 1 was designed to hybridize with both probes (underlined) and contains a T7 promoter region. Primer 2 was designed to hybridize (regular font) with the SMART Trobe RNA RC for all sub-types. Contrary to chapter 9 designs, the molecular beacons are designed to be specific only to their sub-type target (shown bold).

Sequence Name	Oligonucleotide sequence
Redesigned H3 biotinylated oligo	5' - /5BioTEG/AAA AAA AAA AAA AAA AAA AAA AAA AC AAA AAA AAA AAA AAA AAA AAA AAA ACAA AAA AAA AAA AAA AAA AAA AAA *AATTT TGA TGC CTG AAA CCG TAC CA*- 3'
Redesigned H3 molecular beacon	5' - /6-FAM/CGCGC **ACTC**/ZEN/**CAAATGGAAGCATTCCCAAT** GGCGCG/3IABlk_FQ/ - 3'

Table 10.3. Redesigned oligonucleotide sequences for H3 SMART detection.

10.3.2. Microchip device

The microchip device was the same PDMS chip and the magnetic beads were the same M-280 beads as were used in chapter 9.

10.3.3. NASBA reaction mix

The reagents used for NASBA and their concentrations at the final reaction volume were the same as was reported in chapter 9. A total volume of 80μL was used for off-chip real-time amplification and detection.

10.3.4. Heating devices

Off-chip real-time amplification and detection used a single cuvette peltier (Photon Technology International, Birmingham, NJ) and off-chip amplification followed by off-chip end-point gel electrophoresis used a C1000 thermal cycler (Bio-Rad, Hercules, CA).

10.3.5. Optical equipment

Off-chip real time detection samples were prepared in disposable Uvettes (Eppendorf, Germany) and real-time fluorescence was measured using a Quantamaster spectrofluorometer (Photon Technology International, Birmingham, NJ). Off-chip post amplification detection used a 2100 Bioanalyzer and a small RNA gel cartridge (Agilent Technologies, Marshfield, MA).

10.4. Methods

10.4.1. Theoretical hybridizations

Similar to chapter 9's theoretical hybridizations of sDNA, here we determined the theoretical hybridization of RNA to the biotinylated oligos, and to the SMART probes. We also calculated potential primer dimers, beacon dimers, and beacon to target RNA RC to occur during the NASBA cycle. Theoretical hybridizations were calculated using the DINAmelt and mFold Web Server software (DINAMelt Server, RNA Institute,

SUNY Albany, Albany, NY; available at http:// http://mfold.rna.albany.edu). Energy rules for DNA/RNA & RNA/RNA: RNA @ 41°C, C_T = 0.001μM, $[Na^+]$ = 1 M (fixed), $[Mg^{++}]$ = 0 M (fixed). Energy rules for DNA/DNA: DNA @ 41°C, C_T = 10μM, $[Na^+]$ = 73.5mM, $[Mg^{++}]$ = 12.5mM. Theoretical hybridizations were only performed for the preliminary results' H3 influenza oligonucleotide set.

10.4.2. Redesigning the biotinylated oligonucleotide and molecular beacon

Initial results and supplemental experiments in our lab suggested that the biotinylated oligo was not capturing clinically isolated RNA with the same effectiveness as sDNA sample (chapter 9). The biotinylated oligo was redesigned to be much longer, spacing the hybridization region ~100 nm away from the biotin/streptavidin surface of the magnetic bead. This was for better targeting of the long RNA molecules, creating easier targets for them to form hybrids and to reduce any steric hindrance of the RNA with the magnetic beads.

Additionally, we discovered during experiments that our molecular beacon was not offering optimal quenching of fluorescence in its native hair-pin like structure and it appeared to be unbinding unpredictably resulting in clear false positives. The molecular beacon was redesigned using mFold to exhibit a stronger hair-pin like structure with increased quenching of fluorescence.

10.4.3. SMART experiments

SMART assays were performed using the same methods as in chapter 9, using the capture, separation and off-chip real-time amplification and detection method.

10.5. Results and discussion

10.5.1. Hybridization theory predications

Table 10.4 shows the delta G and T_m hybridization events 1&2 (bold) are -25.9, -27.5 and 73.1ºC , 74.7ºC respectively. This suggests that the designed hybridization of the magnetic bead - biotinylated oligo - H3 RNA - H3 SMART probe occurred. Additionally, hybridization event 6 (bold) shows that the redesigned biotinylated oligo forms a strong bond with the H3 RNA. We also checked the other hybridization events that would be considered inhibitory (regular font) and these all are predicted to melt well below the reaction temperature (41 ºC).

Hybridization Event	Oligonucleotide(s)	Delta G Value (41°C)	T_m (°C)
1	**Biotinylated oligo + H3 RNA target**	**-25.9**	**73.1**
2	**SMART probe + H3 RNA target**	**-27.5**	**74.7**
3	Biotinylated oligo + SMART probe	-5.9	30.8
4	Biotinylated oligo + Biotinylated oligo	-1.5	-1.1
5	SMART probe + SMART probe	-4.1	22.3
6	**Redesigned biotinylated oligo + H3 RNA target**	**-26.3**	**74.0**
7	Redesigned biotinylated oligo + SMART probe	-5.9	30.8
8	Redesigned biotinylated oligo + redesigned biotinylated oligo	-5.0	28.3

Table 10.4. Theoretical hybridization ΔG and T_m values for predicted H3 oligonucleotide set hybridization during capture phase of SMART.

After validating that acceptable hybridizations were predicted to occur during the capture/separation phase of SMART, we cross-checked all of the oligonucleotide hybridizations during the NASBA real-time amplification and detection phase of SMART. Table 10.5 shows the hybridization energies for the original oligos and table 10.6 shows the hybridization energies after redesigning the molecular beacon.

H3 NASBA Oligos	P1		P2		Beacon		Probe		P1+Probe RNA	
	ΔG	T_m(°C)	ΔG	T_m(°C)	ΔG	T_m(°C)	ΔG	T_m(°C)	ΔG	T_m(°C)
P1	-4.2	32	-3.8	14.5	-3.2	8.1	-22	71	-5.9	36.6
P2			-2.9	12.4	-3	-9.3	-3.3	9.8	-27	74
Beacon					-5.3	24.8	-3.9	2.5	-21.3	69.9
Probe							-4.1	22.3	-79.4	86.4
P1+Probe RNA									-27	53.5

Table 10.5. Theoretical hybridization ΔG and T_m values for predicted hybridizations of the original oligonucleotide set during NASBA.

H3 NASBA Oligos	P1		P2		Redesign Beacon		Probe		P1+Probe RNA	
	ΔG	T_m(°C)	ΔG	T_m(°C)	ΔG	T_m(°C)	ΔG	T_m(°C)	ΔG	T_m(°C)
P1	-4.2	32	-3.8	14.5	-4.8	18.3	-22	71	-5.9	36.6
P2			-2.9	12.4	-2.5	-10.1	-3.3	9.8	-27	74
Redesigned Beacon					-7.8	35.2	-5.3	30.2	-22.5	70.5
Probe							-4.1	22.3	-79.4	86.4
P1+Probe RNA									-27	53.5

Table 10.6. Theoretical hybridization ΔG and T_m values for predicted hybridizations during NASBA using the redesigned molecular beacon.

Tables 10.5 and 10.6 show that the expected P1-Probe and Beacon-P1+Probe RNA hybridizations are very likely to occur. No inhibitory hybridizations are predicted to occur at the reaction temperature (41ºC) and the redesign of the molecular beacon does not have any inhibitory effects on the predicted hybridizations.

10.5.2. Redesigned molecular beacon

The mFold prediction for the original molecular beacon folding (figure 10.1a) shows that the 6-FAM fluorophore (green) is not optimally positioned with the black hole quencher (black). Additionally the folding strength is weak (ΔG = -2.68, T_m = 55ºC) at the reaction conditions. The redesigned molecular beacon (figure 10.1b) has an optimal positioning of the 6-FAM fluorophore adjacent to the black hole quencher. We also incorporated an additional quencher(purple) called a ZEN quencher. This is a proprietary design by IDT for enhanced quenching in the hair-pain state without sacrificing fluorescence amplitude in the unbound/hybridized state.

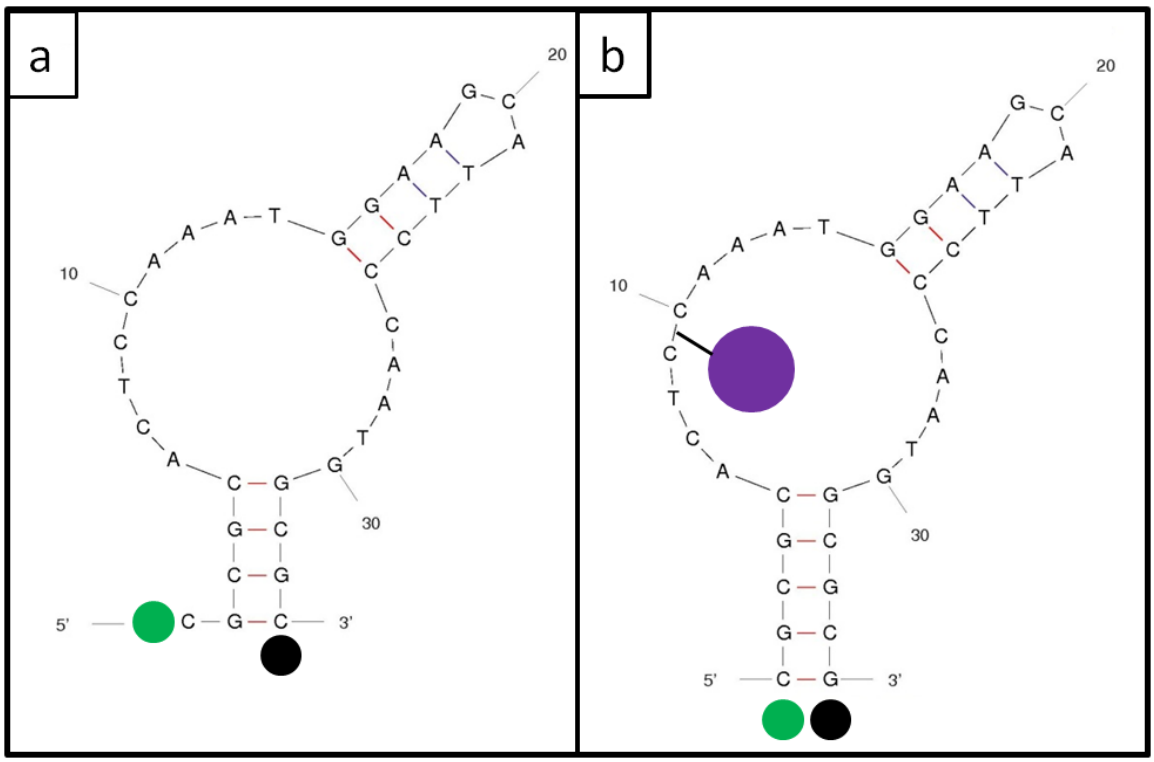

Figure 10.1. Comparison of hair-pin structure of molecular beacons. **(a)** Original H3 molecular beacon. **(b)** Redesigned H3 molecular beacon.

10.5.3. SMART detection of H3 influenza

SMART was used to detect isolated H3 influenza samples (figure 10.2). The original molecular beacon samples(purple and blue) exhibited a higher baseline fluorescence compared to the redesigned molecular beacon samples (green and red) indicative of the non-adjacent positioning of the original beacon's fluorophore and quencher in the hair-pin state. For the original beacon, the real-time amplification of the H3 positive sample (blue) amplified too quickly based upon the maximum amount of SMART probes present. Normally the amplification would take a minimum of 40 minutes for the signal to amplify so drastically and the sample would contain orders of magnitude more (~1000x) SMART probe as the starting template. Additionally, the original beacon negative control (purple) showed the same initial drastic jump in

fluorescence, but then declined and reached a plateau in signal. This result suggests that the molecular beacon is not stable and needed to be redesigned.

The redesigned molecular beacon was used in conjunction with the redesigned biotinylated oligo. The results show a credible amplification curve for the H3 positive sample (green) and the negative control (red). The negative control suggests, as was the case in chapter 9, that there is some inherent carry-over of SMART probe in the negative control which ultimately determines the sensitivity limit of our assay.

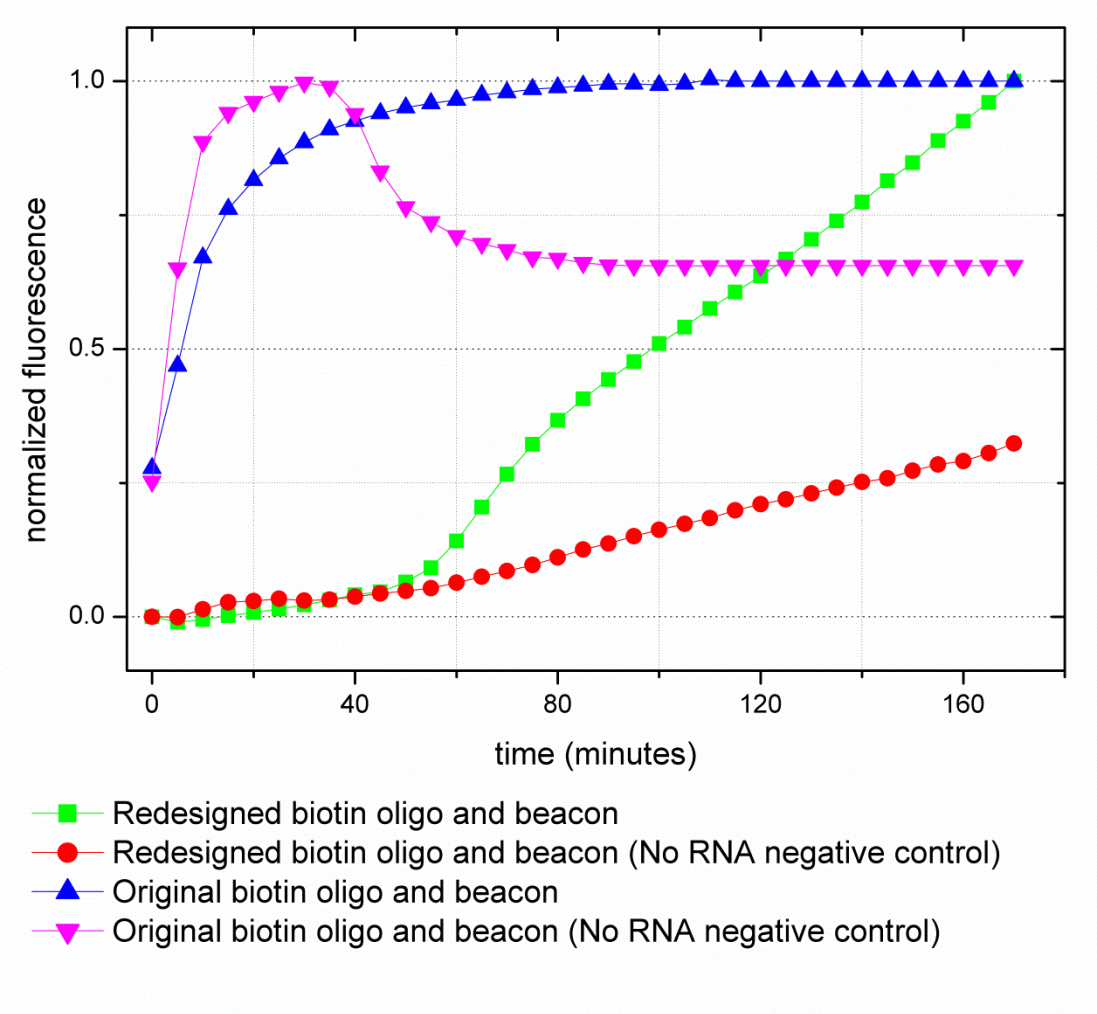

Figure 10.2. Original biotinylated oligo and molecular beacon vs. redesigned biotinylated oligo and redesigned molecular beacon. The redesigned oligo/beacon results have been reproduced and were represented by the average of the results.

10.6. Conclusion

We successfully detected isolated samples of H3 influenza using SMART. We anticipate similar results for seasonal and swine flu and look forward to using SMART to assay all three subtypes simultaneously, yielding influenza detection and sub-type information. We have established the feasibility of SMART for patient samples and now research is moving forward to use SMART on a large set of patient samples.

10.7. Acknowledgments

Authors acknowledge the financial support of the National Institute of Health (Grants No. 1R21 A1073808-01 A1; and R01AI066922) and The RNA Institute, College of Arts and Sciences, State University of New York at Albany for use of their DINAMelt web server. We would like to thank Dr. Stephen Opal from Memorial Hospital for supplying the isolated influenza samples and Stephanie Angione for supplying the PCR primer sequences.

CHAPTER 11

CONCLUSION AND FUTURE DIRECTIONS FOR SMART

Part two of this thesis started (chapter 6) by detailing the available point-of-care (POC) disease diagnostic assays for HIV and influenza detection. However none address the need for specific mutation or sub-type detection. Additionally, commercial assays designed for mutation detection and influenza sub-typing were thoroughly represented, but none were designed for POC or use in resource-limited-settings (RLS). To fill the void we engineered SMART, a novel diagnostic assay for effectively detecting HIV-1 mutations and influenza sub-types with POC design and RLS capabilities.

A simple microfluidic approach was used for the separation step of SMART and the development/validation of this simple yet effective separation technique was detailed in chapter 7 using a model biomolecule substrate. Chapter 8 elucidated the parameters involved in the complex microbiology during the amplification process of SMART. The results provide insights for successfully designing oligonucleotides for SMART and methods to optimize reaction kinetics and avoid inhibitory hybridization events.

SMART was shown to successfully detect clinically relevant concentrations of synthetic HIV-1 containing the K103N mutation (chapter 9). SMART probes were shown to be highly specific to the synthetic K103N samples within a wild-type population. SMART was also introduced in a multi-beacon platform as a means for viral load detection and determining the concentration of K103N variants within a K103N/wild-type mixed sample.

Finally SMART was shown to detect clinically isolated samples of H3 influenza. The biotinylated oligonucleotide was redesigned for better hybridization with the long clinical RNA samples. Additionally, oligonucleotide knowledge gained from chapter 8 was used to redesign a more stable molecular beacon for effective H3 detection.

In the very near future, we would like to replicate our H3 detection results for H1 seasonal and H1 swine flu. We would also like to compare clinically isolated sample results with our developing Z-chip isolation technique. Once we can achieve very sensitive detection of influenza samples at low starting concentrations (less than 10^3 copies/mL) we will have confidence to assay sparse clinical HIV K103N RNA samples.

In the near future we plan on integrating our own Z-chip isolation step on-chip and eventually using POC style optics, forming complete device as seen in figure 11.1.

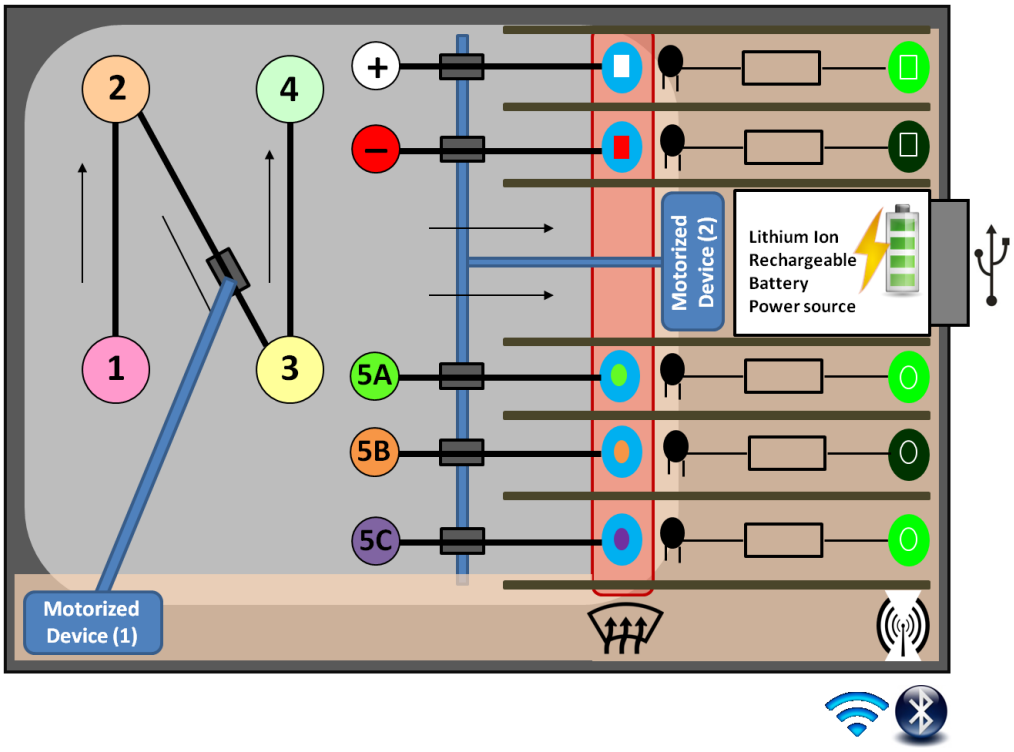

Figure 11.1. SMART disease diagnostic POC device.

The SMART device works as follows: **(1)** The sample patient sample is isolated using the Z-chip and an automated magnet attached to a motor from W1 to W4. **(2)** Next the sample is split (manually or automated) evenly among 3 wells (5A, 5B, and 5C). The (+) well contains a synthetic H3 positive sample and the (-) well contains nuclease free water, serving as parallel controls. **(3)** All of the samples are transferred through the SMART tapered channels in parallel using a second automated magnet attached to a motor. **(4)** Once the samples have reached the amplification wells (blue) they will solublize the freeze-dried NASBA reaction reagents which come pre-loaded in powdered form. **(5)** Next the thin-film heater (red) isothermally heat the amplification wells. Simultaneously, blue led's illuminate the samples causing fluorescence of hybridizing molecular beacons. The fluorescence is transduced to a current using photodiodes (shown in black). The current passes a set of resistors, which establish a current threshold of detection. If there is enough current (i.e. enough fluorescence from hybridized beacons) the photo-diodes (green) will illuminate indicating detection.

The device is designed to transmit results in real-time to a cell phone or laptop computer through a USB wired connection or wirelessly over a wifi network or through a Bluetooth wireless connection. Additionally, the device is powered by a lithium ion rechargeable battery which can be recharged through the USB connection.

We have been successful developing the molecular biology and microfluidics principles of the assay. We are now starting to invest resources into the device aspects with the goal of engineering a true POC diagnostics device.

Overall, we have made excellent strides in developing a POC assay for mutation detection and/or sub-typing. We look forward to integrating all the necessary missing

components (isolation, optics, device housing, etc.) into SMART for a complete POC diagnostic device.